Analyzing the complexity of ice with explainable machine learning for the development of an ice material model

Vom Promotionsausschuss der
Technischen Universität Hamburg

zur Erlangung des akademischen Grades

Doktor-Ingenieur (Dr.-Ing.)

genehmigte Dissertation

von

Leon Kellner

aus

Bremen

2022

Gutachter: Prof. DSc. (Tech.) Sören Ehlers
Prof. Dr. rer. nat. habil. Norbert Hoffmann

Datum der mündlichen Prüfung: 16.12.2021

ORCID Leon Kellner: 0000-0001-9722-7508
doi: 10.15480/882.4076

Preface

This thesis was mainly written in the first half of 2021. It is, however, the result of several years of research from 2016 to 2021, quite a journey. I am very grateful to a number of people who supported me throughout this journey, be it supervisors, colleagues, friends, family, or the examiners. I would like to thank some of you in particular, without claim to completeness.

I had the wonderful experience that the busiest researchers always took time to answer my questions, even in cases when they did not know me at all. I'd like to mention some in particular:

Sören, thank you for your supervision, guidance and discussions, and your view of the bigger picture. I am grateful for your open-mindedness and support, whether in terms of doing research abroad or new research approaches.

Franz, thank you for answering my countless questions on ice mechanics, sharing your knowledge with me, and for many enjoyable coffee breaks.

Prof. Düster, thank you for sparking my interest in numerical methods throughout my master's studies and for always taking the time to discuss specific topics with me during my doctoral research.

I would also like to thank the members of the examination board, specifically Prof. Hoffmann, thank you for agreeing to act as a the second examiner without hesitation.

I would furthermore like to acknowledge my colleagues and friends at the Hamburg University of Technology for their wonderful collaboration, Gyde, Annika, Moritz (both of you), Merten, Hauke, Bjarne, just to name a few. Thank you for your moral support, discussions, advice, good times in our laboratory, sharing experimental data, proof reading, and much more. You have made working here a very enjoyable experience.

I am also indebted to the people at NTNU in Trondheim for their support, Knut, Wenjun, Torodd, Runa, Julie, Martina, and many more. I felt very welcome among you and it was a pleasure to work with you.

Next, I would like to extend my gratitude to all those who make their work available as open source, be it software packages or freely available literature. Parts of this thesis would not have been possible without them.

I thank my friends and fellow students who were always there since the first semester. Merten, Thilo, Felix, Gunnar, and many more, you helped me make sense of the weirdest and most abstract topics during my studies without losing touch with the less theoretical aspects of life. The list of my supportive off-campus friends is too long to be included here, but you know you are meant. Thank you so much.

Finally special thanks to my parents and my brother, thank you for your loving and kind support. I am lucky to have you.

Abstract

Sea areas previously inaccessible due to year-round ice coverage are now only partially or seasonally covered with ice and have become attractive for various stakeholders, e.g., the oil and gas industry. Ships and structures operating in these areas must be designed to withstand ice-induced loads, for instance from ice floe impact. This is mostly done with empirical methods and model-scale ice tests. However, empirical methods only give estimates of global loads and are inflexible regarding, e.g., hull shapes, and model-scale ice tests require high effort. Numerical simulations are a desirable remedy, but their accuracy is limited because current ice material models only partially capture the behavior of ice. Yet the development of improved ice material models is impeded by gaps in ice mechanics theory and experimental data.

These issues are approached as follows. Many effects observed during full-scale interaction between ice and structures are also seen in small-scale tests, which are better studied and executed under more controlled conditions. Hence understanding and modeling ice behavior in small-scale is seen as a first step toward full-scale simulations.

So firstly, an analysis of a large database of small-scale tests with explainable machine learning (ML) is presented. It demonstrates that ML models can accurately predict ice behavior and strength, and that ML model explanations can improve our understanding of ice mechanics, e.g., through feature impact rankings. Such explanations help to make decisions on which and how to include features in numerical models, they may also serve as an alternative validation method.

Secondly, a material model for small-scale tests is presented with a focus on elasticity and fracture, since ice-structure interaction is predominantly elastic-brittle. In the context of material modeling, the 'small-scale first' approach introduces further scale-related problems. Homogenization of elasticity is often assumed but not evidenced or linked to microstructural length scales such as grain size. Here, it is shown that the effect of using a model with polycrystal elasticity and geometry is small globally but significant on a local scale. Moreover, about 300 grains per volume are necessary for representative elastic behavior, but this number depends on additional aspects such as the desired accuracy. Furthermore, the fracture process zone (FPZ) of ice can be large compared to specimen size, and mechanical properties can be scale-dependent. A fracture model based on the Cohesive Zone Method (CZM) was applied to an edge-cracked square plate of different sizes spanning several magnitudes. The study demonstrates that FPZ size depends on crack length and plate size and that the FPZ can span more than 60 % of plate size. Moreover, the CZM captures a size effect, i.e., the dependence of the nominal strength of similar structures on size. Lastly, simulations with the fracture- and polycrystal models combined are shown to match experimental results.

Overall, the present work supports the development of material models with a 'small-scale first' approach, complemented by ML data analyses.

Contents

1 Introduction

1.1 Motivation and objectives

Ice is relevant to many processes in geophysics and engineering. It is also a model material for the research of polycrystals because of its transparency and large grain sizes, among others. More specifically, sea areas that were previously inaccessible due to year-round ice coverage are now only partially or seasonally covered. As a result, activities in these areas have increased, e.g., shipping or setting up offshore wind turbines, and ocean engineering applications have come into focus. These are mostly related to the interaction between ice and structure, for instance between ships and bergy bits. Such applications necessitate the estimation of ice-induced loads and vibrations to assess the risk of damage to ships and structures.

However, experimental approaches are limited. Full-scale experiments of ice interaction require tremendous effort and results may not translate well to new designs with different geometries. In model-scale ice testing, model ice properties do not always scale as stipulated by scaling laws, which can introduce uncertainty. In addition, lead time for new test series is long and the costs are high. Small-scale tests are suboptimal for estimating ice loads because it is challenging to reproduce corresponding full-scale scenarios in the laboratory. Numerical models offer a low-cost, high-resolution alternative, but in contrast to, e.g., steel, there are no well-established ice material models. Hence, though today's numerical methods toolbox is vast, the ice material model has become the bottleneck to progress in ice-related numerical modeling.

The reasons are manifold. Ice is a complex material and ice mechanics theory is incomplete. Many topics are controversial and subject of ongoing research, e.g., scaling laboratory fracture tests to full-scale. Experimentally, the relationships between two parameters may be well-documented, e.g., how strength depends on temperature. Yet ice behavior should be imagined as an n-dimensional space where the dimensions represent numerous influencing and possibly interacting parameters. The multivariate studies necessary to investigate this require a high number of tests and are seldom done. These issues apply even more to full-scale scenarios, where studies are scarce and done in highly variable environments. By contrast, small-scale tests offer more controlled conditions, the observation of effects requires less effort, and consequently there is much more data. Furthermore, many effects observed during full-scale interaction between ice and structures are also seen in small-scale tests.

Due to this, one approach is to focus on material models for small-scale cases, which is seen as a first step toward full-scale models. However, this 'small-scale first' modeling approach introduces scale-related problems. Firstly, homogenization of properties is often assumed but not evidenced or linked to microstructural length scales such as grain size. In theory, the

larger the ratio of grain to specimen size, the stronger the influence of the microstructure. It is desirable to quantify this influence, particularly for 3D models. Secondly, if small-scale material models are to be extended to full-scale simulations, their ability to capture effects from small- to full-scale needs to be assessed, e.g., the dependence of nominal strength of geometrically similar structures on size. Moreover, ice is a quasi-brittle material, i.e., its fracture process zone (FPZ) can be large compared to the specimen size and hence influence test results. Consequently, it may be necessary to include the FPZ in the fracture model.

Lastly, improving ice mechanics knowledge through the classic process of *hypothesis - experiments - derivation of laws* is highly important but also tedious and slow. A complementary data-based approach is proposed. Large, high-dimensional data is desirable to capture complex behavior and make results less susceptible to variability. Under such circumstances, machine learning (ML) tools can help to identify patterns in the data. The idea is to link these patterns to ice mechanics to confirm and quantify known effects but also possibly reveal new relationships and rank parameters by influence. Moreover, validation with only univariate studies limits the transferability of models to different scenarios. In contrast, a machine learning analysis emulates a multivariate study, hence its results may be used as an alternative validation method.

This leads to two central ideas. Firstly, a 'small-scale first' numerical modeling approach for elastic-brittle behavior of ice with an emphasis on scalability, and secondly a data-based analysis to improve ice mechanics understanding and generate additional means of validating small-scale models. The following objectives are derived:

(i) Use a data-based approach to rank dominant features and identify interaction effects in experimental studies for an improved understanding of ice mechanics, and give an alternative means to validate models.

(ii) Develop and apply an ice material model for polycrystal elasticity and intergranular fracture to small-scale tests that reflect features of ice-structure interaction.

(iii) Identify the minimum size for an elastic representative volume element for polycrystal ice and quantify the influence of the microstructure.

(iv) Assess the scalability of the fracture model based on the Cohesive Zone Method and identify fracture process zone sizes for finite plates.

Specifically, (i) is tackled with a database of 4600 small-scale compression tests which are analyzed with gradient-boosted tree ML models. The predictions from the black-box ML models are then explained with an approach based on Shapley values from game theory, the SHAP method. Both predictions and explanations are discussed in terms of ice mechanics.

To address (ii) and (iii), an artificial polycrystal geometry is generated based on Laguerre tessellation with the existing software Neper. Subsequently, a tool is created that randomly assigns a different elasticity tensor to each grain. Intergranular fracture is modeled with Cohesive Zone Method elements on every grain boundary. The minimum representative volume element (RVE) size is identified with the polycrystal model for elastic behavior without fracture. The polycrystal and fracture models combined are applied to small-scale tensile-splitting- and compression tests.

Objective (iv) is approached by applying the Cohesive Zone Method to an edge-cracked square plate of different sizes spanning several magnitudes. The fracture process zone size and the nominal strength, i.e., the crack splitting load divided by the plate cross-sectional area, are identified and linked to crack length and plate size.

1.2 List of publications with author's contributions

This thesis is based on publications published as peer-reviewed journal articles and conference proceedings (P1, P2, P5-P7) as well as non-peer-reviewed conference proceedings (P3, P4). P1 and P2 review the state of the art of modeling ice-structure interaction and estimating ice loads. P3 and P4 were preliminary studies on numerical modeling of brittle failure of ice with elastic- and fracture models. P5 treats the numerical Cohesive Zone Method for single cracks in plates and the method's behavior under scaling. P6 and P7 describe data acquisition, data-based models and evaluation.

[P1] L. Kellner, H. Herrnring, and M. Ring. "Review of ice load standards and comparison with measurements OMAE2017-61735". In: *Proceedings of the ASME 2017 36th International Conference on Ocean, Offshore and Arctic Engineering*. ASME 2017. DOI: 10.1115/OMAE2017-61735.

Ring did a preliminary review of standards and created the initial scripts for their evaluation. Herrnring supervised the preliminary work and contributed with comments and guidance. Kellner did an in-depth review of standards, continued and expanded existing scripts, did postprocessing and visualization, and wrote the paper.

[P2] R. U. F. von Bock und Polach; M. Klein; J. Kubiczek; L. Kellner; M. Braun; H. Herrnring. "State of the Art and Knowledge Gaps on Modelling Structures in Cold Regions". In: *Proceedings of the ASME 2019 38th International Conference on Ocean, Offshore and Arctic Engineering*. ASME, 2019. DOI: 10.1115/OMAE2019-95085.

Each author wrote one part of the paper. Kellner contributed with a section on ice mechanics and ice material modeling.

[P3] H. Herrnring, L. Kellner, J. Kubiczek, S. Ehlers. Simulation of Ice-Structure Interaction with CZM-Elements. In: *Proceedings of the 18th German LS-Dyna Forum* (2018). Bamberg, Germany.

Herrnring and Kellner conceived the study. Herrning created most numerical models, ran simulations, and wrote parts of the paper. Kellner ran simulations, wrote several sections on the Cohesive Zone Method and contributed to the overall writing. Kubiczek contributed with comments and guidance. Ehlers supervised research.

[P4] H. Herrnring, L. Kellner, J. Kubiczek, S. Ehlers. A cohesive model for ice and its verification with tensile splitting tests. In: *Proceedings of the 12th European LS-Dyna Conference* (2019). Koblenz, Germany.

Herrnring and Kellner conceived the study. Herrning created most numerical models, ran simulations, and wrote parts of the paper. Kellner ran simulations, wrote several sections on the Cohesive Zone Method and numerical instability, and contributed to the overall writing. Kubiczek contributed with with comments and guidance. Ehlers supervised research.

[P5] L. Kellner, W. Lu, S. Ehlers, K. V. Høyland. "Study on the Cohesive Edge Crack in a Square Plate with the Cohesive Element Method". In: *International Journal of Fracture* (2021). DOI: 10.1007/s10704-021-00560-9.

Kellner and Lu conceived the study. Kellner created the numerical models, programmed the material models, did postprocessing and visualization, ran the simulations, and contributed to the writing. Lu provided most of the theoretical framework, provided the analytical solutions, and contributed to the writing. Ehlers and Høyland contributed to the writing and supervised research.

[P6] L. Kellner, M. Stender, R. U. F. von Bock und Polach, H. Herrnring, S. Ehlers, N. Hoffmann, K. V. Høyland. "Establishing a common database of ice experiments and using machine learning to understand and predict ice behavior". In: *Cold Regions Science and Technology* (2019). DOI: 10.1016/j.coldregions.2019.02.007.

Kellner and Stender conceived the study. Kellner collected the data and created the database, contributed to the programming, ran the analyses, did the postprocessing and visualizations and wrote most of the paper. Stender contributed to the programming and wrote subsections on the correlation analysis, the principal component analysis, and decision trees. von Bock und Polach, Herrnring, Ehlers, Hoffman and Høyland contributed with comments and supervised research.

[P7] L. Kellner, M. Stender, R. U. F. von Bock und Polach, S. Ehlers (2022). "Predicting compressive strength and behavior of ice and analyzing feature importance with explainable machine learning models". Submitted to: *Ocean Engineering*

This paper is an extension of [P6]. Kellner and Stender conceived the study. Kellner collected additional data, did most of the programming, postprocessing and visualization. Stender contributed to the programming, wrote subsections on computing feature importance and contributed to the overall writing. Ehlers and von Bock und Polach contributed to the overall writing and supervised research.

1.3 Original contributions

The contributions of this work to the state of the art, which are believed to be original, are listed below along with corresponding publications.

[C1] Establishment of a database of small-scale compression and tension tests on ice [P6, P7].

[C2] Identification of the most important parameters and interaction effects between these parameters in small-scale ice compression tests with explainable machine learning [P6, P7].

[C3] Establishment of a process for creating simulation models with polycrystal elasticity and geometry as well as intergranular fracture.

[C4] Based on [C3], the identification of the size of an elastic representative volume element for ice in 3D, linked to grain size.

[C5] Based on [C3], the simulation and validation, qualitatively and quantitatively, of small-scale compression- and tensile splitting tests.

[C6] Based on [C3], the evaluation of the influence of the polycrystal microstructure on the results of the simulations of [C5].

[C7] Establishment of a numerical model for the edge-cracked square plate with the Cohesive Zone Method for the identification of nominal strength and process zone size in dependence of plate size and crack length. Validation with analytical solutions and experimental results [P5].

[C8] With [C6], showing that the Cohesive Zone Method is able to capture a size effect [P5].

[C9] With [C6], computation of fracture process zone sizes for finite plates [P5].

1.4 Limitations

The thesis' limitations are summarized below. Detailed discussions are given in Sects. 6.9 and 8.5.

Data-based analysis

- The analysis is based on correlation and not causation. Precautions have been taken to ensure the generalizability of the model, but only causal modeling truly solves this issue.
- The analysis is based on parameters which do not necessarily represent effects such as wing-cracks. Ice mechanics needs to build the bridge between effects and parameters.
- The results are, strictly speaking, only valid for the input data used, i.e., small-scale compression tests of mostly uniaxial type with biases toward certain feature values.
- The results can only be directly used in modeling if the approach is empirical or phenomenological, i.e., through curves which are to a limited extent consistent with theory but not derived from it.

Numerical modeling

- Only brittle behavior has been modeled. No viscoelasticity or plasticity effects were included. The model is not applicable to the ductile regime.
- The model is only valid for granular freshwater ice. In saltwater ice, additional features such as pores and brine inclusions affect behavior. The model may be extended to columnar ice loaded along columns, but this was not tested.
- The fracture model is, strictly speaking, only valid for cases without confinement, namely tensile splitting tests, uniaxial tests, and for plane stress scenarios. An application to scenarios with significant confinement risks neglecting its influence on crack nucleation and propagation.
- The fracture model is phenomenological. It appears to be consistent with theory and experiment, but it does not reflect specific effects, e.g., wing-cracking.
- Only intergranular fracture has been modeled.
- At present, applying the polycrystal model to full-scale is not numerically feasible. Regarding elasticity, using representative volume elements is advisable. Regarding fracture, if there is no polycrystal structure, other means of achieving realistic crack-pathing are recommended.

1.5 Outline and structure

The structure of the thesis is illustrated in Fig. 1.1. In general, each chapter begins with a short paragraph (printed in italics) that connects the current to previous chapters and the overall leitmotif.

The current chapter points out the motivation for this research, presents the central ideas and indicates corresponding publications, original contributions but also limitations.

Part II puts the research into context and presents the underlying theory for ice mechanics and homogenization. Ch. 2 further motivates research on ice with a focus on ice-structure interaction and describes state-of-the-art modeling approaches. In particular, Sect. 2.4 substantiates the small-scale first approach. Ch. 3 discusses which features require modeling regarding brittle small-scale tests and how these features relate to ice-structure interaction. Ch. 4 outlines the theory for the identification of a minimum size representative volume element (RVE).

Part III comprises the application and results of the data-based- (machine learning, ML) and numerical models. Ch. 5 describes the necessary background for applying ML- and explanation models. Ch. 6 depicts the database, applies the ML and explanation models to it, compares the ML model to empirical and analytical formulas (i.e., classic prediction approaches), and discusses the results in terms of ice mechanics. Ch. 7 introduces the material models for polycrystal elasticity and geometry as well as fracture. In Ch. 8, these models are applied in in four studies: one on minimum elastic RVE size, one on scaling of the fracture

model, and two further studies on small-scale tests, namely tensile splitting- and compression tests.

Part IV concludes the thesis.

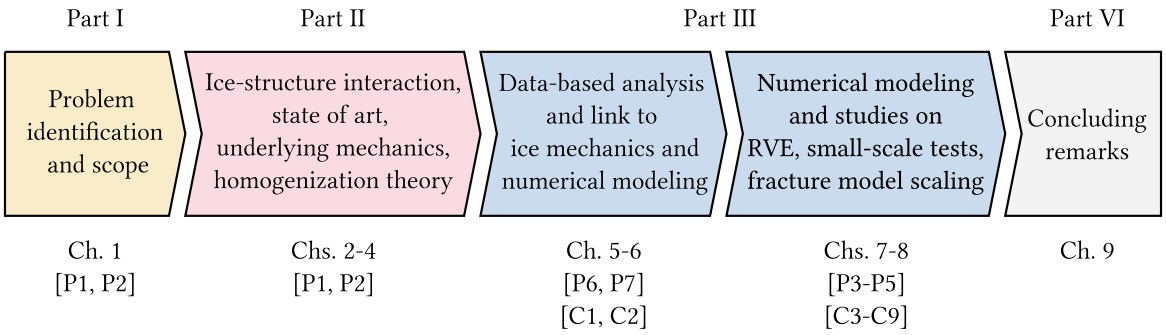

Fig. 1.1: Outline and structure of the thesis.

2 Ice-structure interaction

This chapter further motivates research on ice regarding ice-structure interaction (ISI). Full-scale processes of ISI are described. The immense challenge of going straight to modeling full-scale scenarios is illustrated. This is reflected in a review of state-of-art ISI models for ice loads and vibrations and their limitations. Further, it is explained why, though the motivation for the present work stems from full-scale scenarios, a small-scale first modeling approach is chosen. Fundamental ice mechanics and their link to ISI phenomena are discussed in the subsequent chapter (Ch. 3).

2.1 Background

Especially in the Arctic, the climate crisis results in a rapid sea ice decline, which will likely continue throughout this century. Sea areas that were previously covered by ice year-round are now only partially or temporally covered, see, e.g., [217, p. 4] and [238]. Such areas have become attractive for various stakeholders and activities are increasing. This has major implications for the local environment and native population, and for all further stakeholders, for instance oil and gas, navy, mining, fishing, and tourism [263]. Particularly opening the Northern Sea Route for high-volume traffic will have geopolitical consequences such as a substantial reduction in trade costs between Europe and Asia [238].

Increased shipping will put more pressure on the already threatened Arctic ecosystem and is criticized [98, 319]. Exploration of fossil resources in the Arctic also raises concerns due to the environmental risks [5]. The prospect of exploration also has a political dimension, as it is, e.g., opposed by the majority of US citizens [164, p. 45]. Moreover, and probably less controversial, is the surge in renewable energy in recent years and subsequent interest in offshore wind power in regions with at least seasonal ice cover such as the Baltic Sea [25, 85, 217].

Beyond the ecological, economical and political dimension of these developments, it is known that sea ice can damage ships [8, 105] and offshore structures [22, 132, 169]. For ships, consequences range from repairs to a critical loss of structural integrity and environmental disaster, e.g., oil spillage. Such catastrophes are exacerbated in the remote and ecologically fragile Arctic. Hence, besides the ecological, political and economical perspectives, safe shipping is imperative. Consequences from ice interaction to offshore structures are displacement or collapse, but also fatigue failure in secondary structures due to ice-induced vibrations.

Therefore, ships and offshore structures operating in these areas must be designed to withstand ice-induced loads, for instance from ice floe impact, and be as little susceptible to ice-

induced vibrations as possible. There is also a need to assess risks for existing non-ice class ships if their operation is extended to the marginal ice zone [165].

2.2 Underlying processes

Ice-structure interaction (ISI) is an umbrella term for processes involved in the interaction of ice with offshore structures and ships. These processes span several scales and illustrate the complexity of ice mechanics. Brittle failure, or crushing, is dominated by fragmentation and cracking. Forces between ship or structure and the ice fluctuate in space and time [224, 321] and can reach critical levels [132]. Ductile, or creep behavior, is unusual and results in lower forces and a more homogeneous pressure distribution. Other rare cases are, e.g., ice over-ride or adfreeze effects [207, pp. 136 and 151]. In this work, the focus is on the brittle regime, since this mode governs design loads [256, p. 337].

The overall process of brittle failure during ISI is multi faceted. On a local level, most of the global force is transmitted through small, constantly changing regions of the total interaction area, termed high-pressure zones. In these zones, ice is highly confined and transmits high local loads without cracking. Local pressures can reach up to 70 MPa and drive local design. Under lower confinement, farther away from the central area, ice tends to fail under compression. This results in cracks, spalling and extrusion of material. Simultaneously, the microstructure of ice changes due to microcracking and recrystallization, among others [139].

On a global level, ice may fracture in different patterns. Examples include bending or splitting (see Fig. 2.1 for a splitting example) depending on the scenario, e.g., structure geometry, confinement of the ice or indentation rate. These global (brittle) failures are dominated by fracture and act as load-releasing mechanisms in ISI [139, 176].

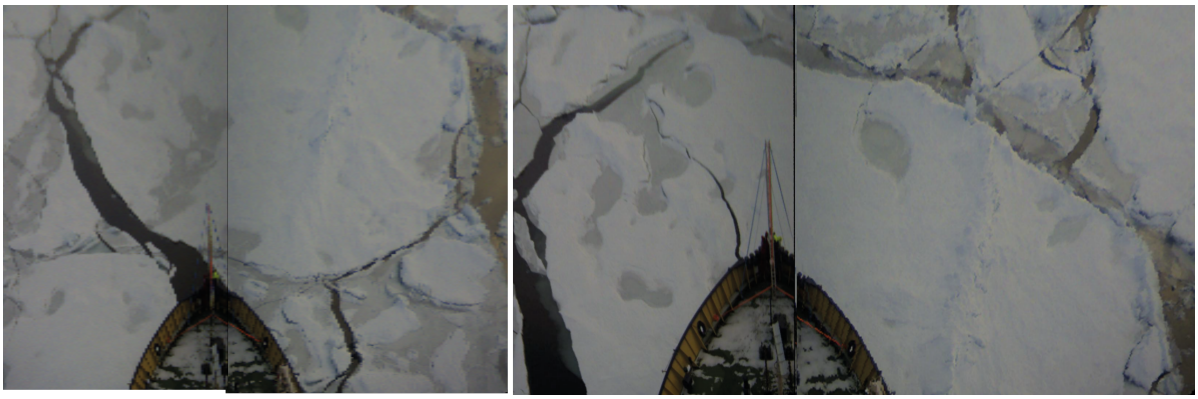

Fig. 2.1: Rectified images from a ship coming into contact with an ice floe (left), causing a single crack running through the ice floe and eventually splitting it (right). Taken from [176], with kind permission from Wenjun Lu and Elsevier.

The heterogeneity of sea ice adds to the complexity. Different ice types can be mixed, e.g., columnar and rubble ice, and grain sizes vary. Existing damage and cracks influence further crack nucleation and propagation. Thermal gradients within ice sheets affect porosity and

hence stiffness [256, p. 336]. Additionally, there remain knowledge gaps regarding properties of ice features such as ridges [287].

Above all, a complete understanding of ISI and its processes is made difficult by a lack of (available) full-scale data. Such full-scale testing requires tremendous effort, has long lead times, and achieving a high measurement resolution is a challenge, see, e.g., the Norströmsgrund campaigns [135] or overview in [207, pp. 162-167]. Local pressures in particular are difficult to measure, e.g., [74], even in the laboratory [117]. Moreover, there is debate on the interpretation of full-scale crushing data, e.g., [74]. Lastly, it is almost impossible to separate effects in full-scale where various processes act simultaneously in a heterogeneous and less-controlled environment.

In short, brittle failure in ISI is a highly complex process and also the most relevant mode in engineering. However, fully reproducing the overall process or estimating resulting loads either experimentally or through modeling approaches is a challenge. How this is currently done is treated below. A review of the mechanics related to the ISI processes is postponed to Ch. 3.

2.3 State-of-the-art methods

There exist various methods to model ice-structure interaction or estimate ice loads. These are summarized and briefly discussed below, a detailed review of methods can be found in [27, 209]. Here, *structure* is used as a general term for ships and offshore-structures. Moreover, no distinction is made between models that focus on local or global loads and pressures.

Empirical methods

Design against ice loads is currently mostly done with empirical or semi-empirical methods. These are based on experimental data and, in the case of semi-empirical methods, combined with principles that are derived from physical laws. An overview is given in [142] and [217, p. 35].

Methods of this group give estimates for static loads. Different structure geometries are not fully considered. Interaction with a deformable structure may change both the magnitude of forces and the mechanical response of the ice as well as the structure, see [116, 222] and [217, pp. 9-10], but this is usually not considered.

With regard to ships, current regulations do not fully reflect localized ice loads and may underestimate deformation of stiffened panels [64, 155]. Furthermore, localized loads or pressures for various ice conditions (e.g., level ice, broken ice, ridges) cannot be simulated accurately. As a result, ships operating in ice-infested waters are not designed according to physical measures, i.e., accurate stress state due to ice loading, but according to economic- and empirical design measures. Yet for a safe transport, a direct analysis is desirable [61].

For offshore structures, the situation is similar. To predict ice loads, regulations prescribe empirical formulas, e.g., [35, 130], which give static, global loads. There is some consensus with respect to how loads are estimated but the choice of input values such as ice compressive strength varies significantly [281]. The results of these estimations show scatter for the same

case [142, 281]. Dynamic loads are considered by multiplying static loads with amplification or safety factors as, e.g., in [130]. The influence of structure deformation on loads and ice behavior is typically not included. Ice-structure interaction is considered for the case of ice-induced vibrations with simplified approaches as, e.g., in [130].

In all, empirical methods can be used for quick estimates of ice loads. Nevertheless, for the design of ships and structures, more accurate and flexible approaches are desirable, e.g., regarding dynamic and localized loads.

Phenomenological models

Phenomenological models can be thought of as an extension of empirical formulas. They are defined as "[...] mathematical descriptions of empirical relationships, which are to some extent consistent with theory, but not derived from it" [217, p. 11]. They seek to model the interaction between ice and structure with time-dependent modeling approaches, to for instance capture a synchronization of structure and ice-crushing frequency. Examples for such models are the Matlock model from the 1960's [184] or the more recently developed Hendrikse model [100].

These models are more sophisticated than the empirical ones, but simpler than high-fidelity computational methods (see second-next section). As with other models, tuning of several parameters is required. They are less computationally demanding and coupling to other models, e.g., wave load models, is comparably straightforward. An overview of phenomenological models is given in [217, p. 36].

Model-scale ice tests

Another widely used option are model scale ice tests where a downscaled version of the ship or structure is tested in a model basin, see Fig. 2.2. Subsequently, parameters of interest, e.g., ice resistance, are scaled up to obtain full-scale values. Such tests are considered a state-of-the-art method to predict the performance of ships and structures in ice-infested waters [302, 303]. They are also recommended by standards or classification guidelines [35, 70, 82].

Nonetheless, they are subject of ongoing discussion, see, e.g., [6, 67, 208, 209]. Controversial topics range from scaling laws to variable ways of making artificially weakened model ice and its nonlinear behavior [28]. Adding to that, there are various understudied phenomena specific to the internal mechanics of model ice. This introduces uncertainties regarding the scaling of test results to full-scale. Case-based scaling, i.e., using different scaling laws for different scenarios, may be necessary but has been only recently proposed [303].

More generally, model-scale tests require high effort. Sophisticated testing capabilities are necessary, e.g., large cold rooms. The lead time for new test designs is long and the cost of repeated tests is high [29]. Moreover, changes in in model geometries may require building a new ship- or structure model and refreezing of the water surface.

Fig. 2.2: Ship model at Aalto Ice Tank prior to a resistance test. The model ice contains 0.3 % of ethanol for the adjustment and scaling of strength. The ship is towed through an open channel, while the carriage is pushing the ice orthogonally to the moving direction of the ship applying a compressive frictional force onto the hull. Image: R. U. F. von Bock und Polach, with kind permission.

Numerical methods and material models

Lastly, various numerical or computational methods are used [27]. These comprise 'classic' approaches for solving differential equations, such as the finite element method (FEM), e.g., [153], but also particle-based approaches such as the discrete element method (DEM), e.g., [7], and smoothed particle hydrodynamics (SPH), e.g., [210]. The benefits of numerical methods are their flexibility regarding model creation, for instance regarding boundary conditions or varying geometries, the low-cost repeatability of simulations, and a high-resolution of physical quantities such as pressure. As with the phenomenological models, different methods can also be coupled with tools such as *comana* [154], though this is not trivial. The main drawbacks of numerical methods are the long lead time to develop a validated model and the high computational effort compared to empirical and phenomenological models.

All the above-mentioned numerical methods require material models. However, compared to other well-researched materials such as concrete or steel, ice is understudied. This is mainly due to its complexity and gaps in knowledge and experimental data (see Ch. 3 below). This issue is tackled in different ways, depending on the model's purpose.

If local or global loads in collision scenarios are sought, e.g., between ship and iceberg [320], the material models typically focus on effective 'outside' behavior. Usually a semi-empirical approach is taken that combines experimental data with expected behavior. Often, different effects are combined into one approach, e.g., failure surfaces [55]. In some cases models for other materials are adapted, e.g., foam models [78]. These material models are usually efficient and considered accurate enough so long as contact pressures and loads are approximately of the right magnitude. This is reflected in the fact that empirical pressure-area curves are commonly used for validation [171, 320]. A use of these models in scenarios

to which they were not originally calibrated may require recalibration.

The second group are material models that aim to capture small-scale tests for a better understanding of ice mechanics. Compared to the effective models, their development process is usually reversed such that initially model creation stems from physical laws and validation with experimental data is done subsequently. Due to the involved modeling, they are usually limited to one or two specific phenomena, e.g., wing cracks [153] or recrystallization [172], and require a high computational effort. In the near future, it is unlikely that there will be holistic high-fidelity models, that is, models that accurately consider all necessary phenomena based on physical laws. Furthermore, these models are not and do not aim to be efficient enough for other than small-scale simulations [217, p. 42].

This is why some approaches seek to find a middle-ground between efficient but inaccurate and accurate but slow models, sometimes termed medium-fidelity models. The key idea is that the most influential effects likely require explicit modeling in order for the overall model to be accurate and generally applicable. This is for instance reflected in the fact that no reasonably sized representative volume element exists for large cracks [84], therefore necessitating a fracture model. On the other hand, some smearing or neglecting of effects might be possible without introducing a significant error. For example, as long as discrete cracks are modeled, it might be sufficient to do so with a reasonable degree of accuracy. These middle-ground models can still improve understanding of ice mechanics and support interpretation of full-scale data. Furthermore, such models may allow to study scenarios that are not accessible experimentally [96] and validate the effective models. In contrast to the accurate approaches, an upscaling of these models to full-scale scenarios may be challenging but possible.

2.4 Discussion of state of art and present approach

"A gap remains between ice mechanics and the prediction of forces on full-size structures."[1]

To sum up, various experimental or modeling approaches are used to estimate ice loads during ice-structure interaction (ISI). All of these methods have in common that their results entail uncertainty, at least to some extent [135, 217]. This results in high safety factors which can increase the cost of building ships and structures in sea areas with possible ice coverage [142, 207, 217, 281]. The main reasons are knowledge gaps in ice mechanics and experimental data, and the complexity of ISI phenomena. Hence, despite progress in the research of ice mechanics, most issues described by Dempsey more than twenty years ago [48] are still relevant today [27].

Here, the focus is on medium-fidelity numerical models, e.g., FEM-based, due to their flexibility, low cost, and high resolution of physical quantities. The key challenge is the development of ice material models that are validated with a range of tests that reflect ISI features and capture ice behavior on different scales. More specifically, the focus is on analyzing, understanding, and simulating ice behavior in small-scale tests for various reasons. Further-

[1] [207, p. 94]

more, since the brittle regime governs design loads in ISI [256, p. 337], the emphasis is on modeling elastic-brittle ice behavior.

Firstly, separating effects experimentally and hence in the validation of numerical models is desirable but almost impossible in full-scale where various processes act simultaneously in a less-controlled environment. Such a separation can partially be achieved in small-scale laboratory tests [95]. Nonetheless, using, e.g., ice strength parameters from small samples to predict full-scale processes is difficult [207, p. 162]. On the other hand, fundamental mechanisms underlying the heterogeneous process of ISI are expected to be the same as those observed in small-scale tests, see [256, pp. 336-337] and [95, 250, 253]. If a model includes these mechanisms, it is a first step toward reflecting the ISI processes described in Sect. 2.2.

Secondly, if the development of (material) models is based on small-scale tests, and if these models are to be used in full-scale scenarios in the future, scaling behavior of ice mechanical effects and properties and corresponding numerical models need thorough assessment. The larger the ratio of grain to specimen size, the stronger the influence of the polycrystal microstructure [63]. In addition to that, ice is a quasi-brittle material [18]: Its fracture process zone (FPZ) can be large and influence behavior. The magnitude of this effect depends on the size of the FPZ compared to the specimen size and is therefore important when scaling models or tests from small- to full-scale [175]. Furthermore, nominal strength was shown to depend on specimen size [51, 175]. To follow the small-scale first approach, such effects should be captured and quantified by the fracture model.

Given success, and if a model is able to reproduce experiments that reflect ISI features, extending the model to full-scale simulations is feasible. Furthermore, calibration with small-scale tests is possible once the scaling process is understood both mechanically and numerically. Current computational limitations may impede this process. Nonetheless, this approach can still be used for validation of the effective models and help to improve our understanding of ice mechanics [96].

This leads to the third aspect: An improved understanding of ice behavior is necessary for better modeling on all scales. As mentioned, this includes an emphasis on multivariate studies. Moreover, particularly with respect to validation of models, e.g., it is not enough to know that a higher temperature leads to more ductile behavior. It is desirable to quantify this with curves that average behavior over a range of experiments. Analyses with machine learning and explainable artificial intelligence are proposed as one way to achieve this.

To summarize, these points constitute the leitmotif of this thesis and are addressed in the following chapters. In the last chapter (Ch. 9) these threads are taken up again and concluded.

3 Ice mechanics

The previous chapter establishes brittle failure of ice during ISI as a dominant mode for engineering applications. Moreover, it motivates a small-scale-first approach with respect to simulation and modeling of full-scale ice-structure interaction (ISI). This chapter discusses in more detail what features need modeling when it comes to brittle small-scale tests and how these are linked to full-scale ISI phenomena. The aim is to lay the foundations for the micromechanical model which is to be used in the numerical simulations described in Ch. 8. Relevant ice mechanics are reviewed, including experimental knowledge, polycrystal microstructure and its impact on behavior, ice under compression, and fracture.

3.1 Experimental knowledge

The cornerstone of ice mechanics knowledge is experimental work. Investigations range from standard tests, e.g., uniaxial compression, to unique setups, such as the indentation experiments at Pond Inlet and Hobson's Choice [147] or the Norströmsgrund lighthouse measurement campaigns [134, 135]. The following outline of experimental knowledge focuses mostly on properties that influence ice behavior in the brittle regime. For a complete account the reader is referred to [71, 121, 256]. Here, *behavior* is the maximum stress ice sustains and whether it exhibits ductile or brittle deformation. Both points are critical in engineering and modeling.

First, the maximum stress, also called peak stress or strength, is related to the ice loads on a structure in limit stress scenarios [286]. That is, ice fails against a structure and its strength determines the maximum applied force [207, p. 109]. Maximum stress is used in material models to create failure surfaces, e.g., [55]. Furthermore, uniaxial strength is an input in empirical ice load formulas [142], though it should be interpreted as an "index of strength" rather than a material property such as, e.g., yield strength in plastic materials [285]. Second, the deformation mode, i.e., ductile or brittle, markedly influences the spatial and temporal distribution of loads, both during experiments and on real-world structures [207, 256].

Influential properties, or features, can be intrinsic, e.g., grain size, or external, such as confinement. Different features can be dependent [286]. A systematic overview of influential features begins with the material's history. Ice contains flaws and inclusions depending on formation, age and precursory stress [104, 284, 297], which cause crack nucleation [77]. Crack nucleation and propagation in turn considerably influence ISI processes [139]. The material's history also affects other intrinsic features, for example ice type, porosity due to gas and brine, salinity and temperature, which again influence its behavior. This becomes apparent by looking at strength, or peak stress, during experiments. Uniaxial tensile strength

depends on specimen size, grain size and brine content, but is less sensitive to temperature [110, 254, 259]. Uniaxial compressive strength appears to be insensitive to specimen size [256], but depends on grain size, porosity, temperature and ice type as well as prestrain or damage [157, 195, 251, 277]. These influential features are also seen in multi-year ice, which is often considerably stronger than first-year ice [297]. Therefore the distinction between 'old' and 'young' ice is also important with respect to forces and pressures during ISI.

Extrinsic influential features are related to testing conditions, that is stress state, strain rate and strain. Ice under uniaxial tension typically fails suddenly, under small strains about 0.01 % to 0.1 % and independent of strain rate [110, 254, 259]. Currently, there is no data on multiaxial tensile tests. Ice behavior under compression depends on strain rate [297] and, for multiaxial tests, also on stress state. Different combinations of stress state and strain rate result in different behavior. Generally, brittle(-like)[1] compressive failure is associated with small failure strains $\leq$ 0.5%, high strain rates $\geq 10^{-3}\ \mathrm{s}^{-1}$, low temperatures and low confinement. Ductile compressive failure is linked to high failure strains, low strain rates, high temperatures and high confinement. Especially for very low strain rates $\leq 10^{-5}\ \mathrm{s}^{-1}$ ice can sustain strains of more than one [256]. Such strains are commonly observed in the flow of glaciers and ice sheets, but are not relevant in engineering. More detailed behavior classifications include additional failure modes such as Coulombic- or Plastic faulting, see also Sect. 3.3 and [226].

Apart from these more or less well researched relationships, many aspects are known unknowns and under investigation. Examples are how damage and recrystallization alter ice properties [276], ice failure under high triaxial stress states [227], or ice-ice friction [249]. Also, though much data exists [297], there are gaps and available data is skewed towards simple tests. There is little data on shear and tensile strength of ice. A lot of data exists for uniaxial compression tests, but much less for bi- and triaxial compression tests. However, in reality ice is mostly under a multi-axial stress state. Lastly, the measurements and their correlations, e.g., between porosity and crack density [278], during experiments are less debated than the underlying physics, i.e., the cause for certain behavior.

Above all, ice behavior depends on a range of known and possibly unknown parameters. These parameters often interact, yet mutual influence is rarely investigated because studies of multivariate relationships require a high number of tests. Therefore many studies are limited to two or three parameters. For instance, the often-quoted relationship between flexural strength and brine volume

$$\sigma_\mathrm{f} = 1.76 \exp\left(-5.88\sqrt{\nu_\mathrm{b}}\right) \tag{3.1}$$

is a decent fit to data from various studies which show a distinct trend [296]. Nonetheless, the data shows considerable scatter of the flexural strength for the same brine volume. This suggests that there are further dependencies which are not captured by the one-parameter equation, or univariate studies, for that matter.

[1] So called Plastic or P-faulting is viewed as a brittle-like mode. The stress-strain curve displays a sudden drop upon formation of a fault, which is typical for brittle failure, but the damage within the fault comprises plastic deformation as well as recrystallized grains [253].

To sum up, numerous known influential parameters as well as various gaps in knowledge and experimental data are a manifestation of the material's complexity. This is exacerbated by a lack of multivariate studies. The impact of one parameter, e.g., on strength, in dependence of others remains unclear. As a result, initial modeling decisions such as which and how to include parameters are difficult. These thoughts and aspects are picked up again in Ch. 6, where machine learning methods are used for prediction and creating feature (parameter) rankings.

3.2 Crystal structure and elasticity

The microstructure influences the properties and behavior of polycrystals. The elasticity of ice is determined by both the single crystal elasticity as well as the distribution of c-axes of crystals (i.e., their orientation) in a polycrystalline aggregate. Grain size and shape also impact micro- and macro-response. For example, the strength and failure patterns of columnar ice depend on the loading orientation [133], and grain size influences strength (see Sect. 3.3). Grain size distribution affects behavior in metals [221], and possibly also influences ice behavior, but this has been little studied, see, e.g., for polar ice [159, 237].

Furthermore, cracks are often located on grain boundaries, and elastic mismatch between neighboring grains can cause stress concentrations which facilitate crack nucleation, this is discussed subsequently in Sect. 3.3. The larger the grains in comparison to, e.g., fracture features or specimen size, the more important the influence of polycrystalline inhomogeneities become. This is particularly true in ice, where grains are relatively large, see [53] and Sect. 3.3. On the other hand, the more grains in a volume, the more likely it is that homogenized elasticity can be assumed. In short, the microstructure is crucial when it comes to material models with representative behavior which are needed for efficient full-scale simulations, see Ch. 4.

Ice polycrystalline aggregates can be broadly classified in granular and columnar ice [242, p. 72]. In granular ice, the distribution of c-axes is random in all planes. Its macro-response is isotropic. In the case of columnar ice (often termed S2 ice) the distribution of c-axes is random in the plane of isotropy. The macro-response is transversely isotropic [63, 272]. Here, the focus is on granular ice and modeling (non-averaged) elasticity.

Ice single crystals are hexagonal (ice Ih) and transversely isotropic [316], see Fig. 3.1. To begin with, consider linear elasticity, where the second-order tensors for stress $\boldsymbol{\sigma}$ and strain $\boldsymbol{\varepsilon}$ are related through Hooke's law

$$\boldsymbol{\sigma} = \mathcal{C} : \boldsymbol{\varepsilon} \quad \text{or} \tag{3.2}$$

$$\sigma_{ij} = C_{ijkl}\varepsilon_{kl} \tag{3.3}$$

with $\mathcal{C}$ the fourth-order elasticity tensor. Due to the symmetry of the stress and strain tensors the originally 81 components of the elasticity tensor reduce to 36 independent constants. Material-specific elastic constants are almost always given in Voigt notation, which exploits

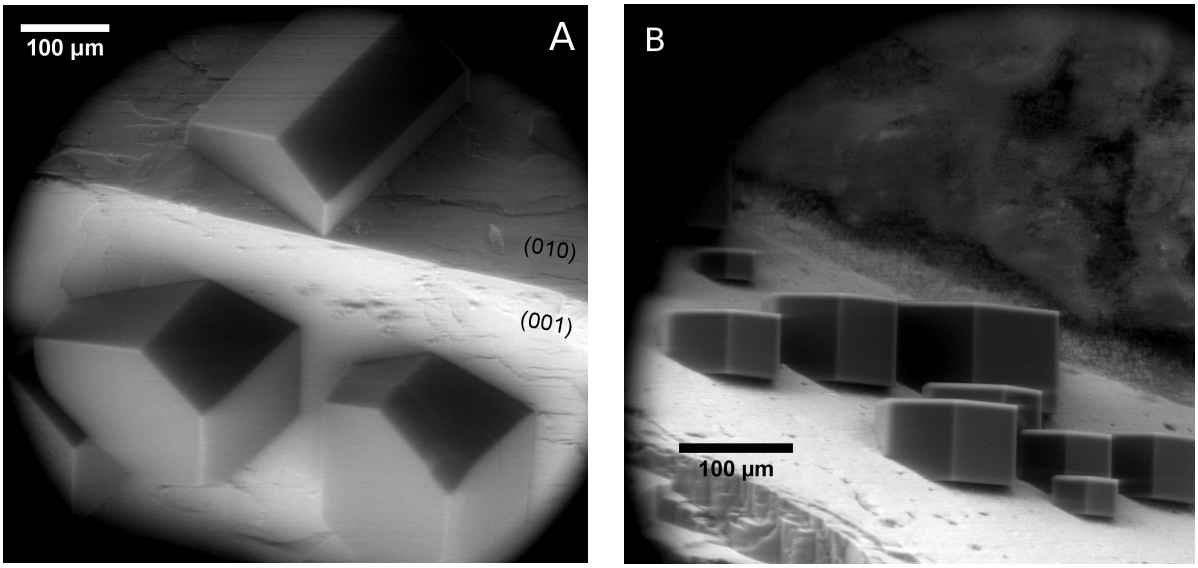

(a) (b)

Fig. 3.1: Environmental scanning electron microscope images of hexagonal ice crystals nucleated on the surface of feldspar mineral. In (**a**) the crystal faces of the feldspar are indicated with Miller indices. From [150], reprinted with kind permission from AAAS and Alexei Kiselev.

these symmetries with the mapping

$$p = \delta_{ij} i + (1 - \delta_{ij})(9 - i - j) \tag{3.4a}$$

$$q = \delta_{kl} k + (1 - \delta_{kl})(9 - k - l) \tag{3.4b}$$

$$\sigma_p = \sigma_{ij} \tag{3.4c}$$

$$\varepsilon_q = (2 - \delta_{kl})\varepsilon_{kl} \tag{3.4d}$$

$$C_{pq} = C_{ijkl} \tag{3.4e}$$

where δ_{ij} is the Kronecker delta, defined as

$$\delta_{ij} = \begin{cases} 1, & i = j \\ 0, & i \neq j \end{cases} \tag{3.5}$$

the $i, j, k, l \in \{1, 2, 3\}$ as the tensor indices and $p, q \in \{1 \dots 6\}$ as the Voigt notation indices [274, pp. 65-66]. Correspondingly, the second-order tensors for stress and strain reduce to

$$\boldsymbol{\sigma} = \begin{bmatrix} \sigma_{11} \\ \sigma_{22} \\ \sigma_{33} \\ \sigma_{23} \\ \sigma_{13} \\ \sigma_{12} \end{bmatrix} = \begin{bmatrix} \sigma_1 \\ \sigma_2 \\ \sigma_3 \\ \sigma_4 \\ \sigma_5 \\ \sigma_6 \end{bmatrix} \quad \text{and} \quad \boldsymbol{\varepsilon} = \begin{bmatrix} \varepsilon_{11} \\ \varepsilon_{22} \\ \varepsilon_{33} \\ 2\varepsilon_{23} \\ 2\varepsilon_{13} \\ 2\varepsilon_{12} \end{bmatrix} = \begin{bmatrix} \varepsilon_1 \\ \varepsilon_2 \\ \varepsilon_3 \\ \varepsilon_4 \\ \varepsilon_5 \\ \varepsilon_6 \end{bmatrix} \tag{3.6}$$

and Eq. (3.2) reduces to a matrix vector multiplication ($6 \times 6 \cdot 6 \times 1$).

For a single ice crystal, the number of independent, non zero constants in $\mathcal{C}$ reduces to five and the stiffness tensor in Voigt notation can be represented as a matrix

$$\boldsymbol{C} = \begin{bmatrix} C_{11} & C_{12} & C_{13} & & & \\ C_{12} & C_{11} & C_{13} & & & \\ C_{13} & C_{13} & C_{33} & & & \\ & & & C_{44} & & \\ & & & & C_{44} & \\ & & & & & \frac{1}{2}(C_{11} - C_{12}) \end{bmatrix} \tag{3.7}$$

where empty entries are zeros. These values are true elastic values based on sound wave measurements. Values based on stress-strain curves are always affected by the viscoelastic response of ice [256, pp. 54-55]. The C_{pq} constants are given in a cartesian coordinate system whose axes are defined in terms of the crystal's unit cell. For hexagonal ice, $\boldsymbol{x}_1$ and $\boldsymbol{x}_2$ are any pair of axes in the basal plane, $\boldsymbol{x}_3$ is parallel to the c-axis. Eq. (3.7) indicates direct effects of normal and shear stresses on the diagonal, and the Poisson's effect from the off-diagonal entries. In this basis, there is no further coupling between normal stress and shear strain, or shear stress and shear strains in orthogonal planes. In a generic basis, generally all anisotropic materials can have all coupling terms [300, pp. 26 and 39].

Overall, the elastic properties of single crystals barely change with temperature in the range from 0 °C to −50 °C [256, p. 56] and type of ice [79]. No variation within local homogeneous regions are expected [79]. Bulk elasticity on the other hand is lowered by damage in the form of microcracks and strain, at least in columnar ice. However, this only happens when there is sufficient time for extensive microcracking to develop, i.e., for low strain rates $\dot{\varepsilon} \leq 10^{-4}\ \mathrm{s}^{-1}$ [278].

3.3 Fracture

The motivation of understanding and modeling fracture stems from the fact that it is a dominant feature in brittle behavior of ice in failure ice-structure interaction (ISI) [139, 175, 176, 246, 291] as well as in tension and compression experiments [42, 149, 234, 241]. It is associated with scale, probabilistic effects, the distribution of flaws and inclusions as well as stress state dependency [69, 77, 291]. Friction (internal, ice on ice, static and kinetic) also influences fracture and brittle compressive failure of ice in general [250]. This section gives a brief overview on fracture in ice with a focus on brittle behavior.

To begin with, fracture can be explained in terms of crack nucleation and -propagation. This distinction is more important for ice under tension: Nucleation controls fracture for higher strain rates $\dot{\varepsilon} \geq 10^{-3}\ \mathrm{s}^{-1}$ and coarser grains $1\,\mathrm{mm} < \bar{d} < 10\,\mathrm{mm}$ with $\bar{d}$ the average grain size. Cracks propagate immediately after nucleation thereby causing brittle behavior, i.e., the stress required to nucleate a crack is also sufficient to propagate it. Tensile strength is governed by a Hall-Petch-type relationship (3.8a). For conditions reminiscent of ductile behavior, e.g., low strain rates $\dot{\varepsilon} \leq 10^{-3}\ \mathrm{s}^{-1}$ and finely-grained polycrystals, crack

propagation controls fracture. In that case, tensile strength is governed by Orowan-type relationships (3.8b). Hence

$$\sigma_\mathrm{t} = \begin{cases} \sigma_0 + \dfrac{k_\mathrm{t}}{\sqrt{\bar{d}}}, & \bar{d} > \bar{d}_\mathrm{c} \quad (3.8a) \\ \dfrac{K}{\sqrt{\bar{d}}}, & \bar{d} < \bar{d}_\mathrm{c} \quad (3.8b) \end{cases}$$

with the tensile strength σ_t, inherent resistance to lattice slip σ_0, and k_t a measure of how much grain boundaries impede the transmission of slip between grains. K factors in fracture toughness, microcrack geometry, and interaction of cracks [252]. The critical grain size $\bar{d}_\mathrm{c}$ marks the point where $\sigma^\mathrm{P} = \sigma^\mathrm{N}$, illustrated in Fig. 3.2, where to the left of the dashed line we have $\bar{d} > \bar{d}_\mathrm{c}$ with brittle behavior and vice versa.

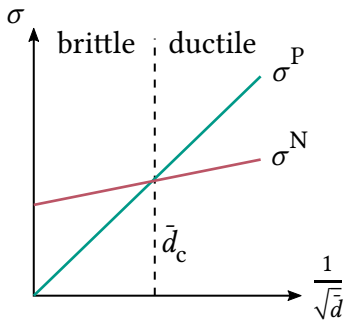

Fig. 3.2: Schematic sketch of the influence of grain size on the tensile stress required to nucleate (σ^N) or propagate (σ^P) cracks. Adapted from [246, 252].

For ice under compression, nucleation or propagation remain important but are superseded by consideration of additional mechanisms such as wing cracks [252]. Furthermore, crack growth under compression is a quasi-stable process, i.e., applied stress has to continue to increase to impact crack growth [253]. Ice specimens under uniaxial compression without lateral confinement fail through cracks aligned with the loading direction. Cracks nucleate on favorably oriented ($\approx$ 45° to the maximum principal stress) grain boundaries, see Fig. 3.3a. Then shear stress causes grain boundary sliding (GBS) along crack faces, which acts as a possible stress concentration mechanism [216]. The created tension at the crack tips leads to wing cracks and finally linking of these wing cracks results in axial splits [246].

Switching from uniaxial- to multiaxial stresses markedly raises failure stress. Normal stress across cracks increases which impedes frictional sliding and wing cracks tend to get closed. New types of cracks can be observed and result in two additional failure modes; Coulombic shear (C-)faulting and Plastic (P-)faulting. C-faulting is explained in terms of interaction of comb-like secondary cracks, which initiate from parent cracks, e.g., on a grain boundary, but can form transgranularly. Once the most favorably oriented microcolumns fail, the failure propagates through the specimen, developing a shear fault inclined by (30 ± 13)° with respect to the shortening direction [247], see Fig. 3.3b. It has been argued that splitting and shear faulting are end members of a continuous spectrum of one failure mode [304].

Upon further confinement still, frictional sliding is suppressed and no secondary cracks are visible anymore [89]. The above-mentioned P-faulting emerges as a localized plastic deformation on a plane of maximum shear, inclined by $\approx 45°$. The macroscopic brittle-like behavior under high confinement is really ductile flow on a microscopic level [247]. Crack interaction is not observed and seems to take no role in fault initiation [90]. The same compressive fault features develop in granular and columnar ice [88, p. 45].

Generally, the way ice compressive failure is influenced by cracking and confinement is at the heart of the ISI phenomena described in Sect. 2.2. In particular, going from high confinement at the center of the interaction area to low confinement at the free edges of the ice changes its behavior from microcracking to macrocracking and spalling as well as extrusion of crushed ice. Moreover, in medium-scale indentation tests macrocracks often lead to significant load drops [139].

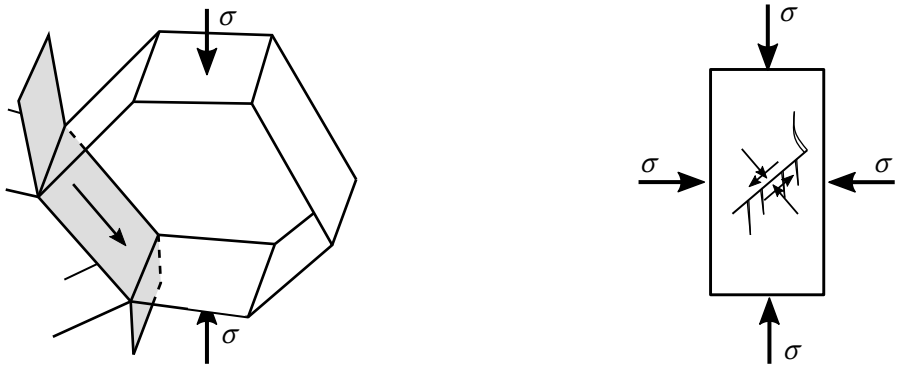

(a) Wing crack (b) Wing and comb crack

Fig. 3.3: (**a**) Schematic sketch of a wing crack (grey faces) on grain boundaries for a columnar-like grain shape, adapted from [77]. (**b**) Sketch of comb crack with indication of stresses normal and along the parent crack, adapted from [253].

Locally, the stress applied to the specimen reaches the cohesive strength of the lattice, also called theoretical cleavage stress. Yet crack nucleation is already observed at applied stresses below the cohesive strength, therefore some mechanism of stress concentration is required. Regarding tension, [246] stated that at higher rates of deformation, grain boundary sliding likely dominates crack nucleation. Frost analyzed possible causes for crack nucleation without referring to tensile or compressive failure but only for columnar ice. He stated that elastic anisotropy is not the main cause of crack nucleation. For moderate temperatures and higher strain rates, grain-boundary sliding is more likely. For low temperatures and high strain rates, crack nucleation from preexisting flaws and inclusions is "inevitable" as other mechanisms do not have sufficient time to emerge [77].

With respect to crack pathing, cracks in ice polycrystals run either through the grains, i.e., intra- or transgranular, or along grain boundaries, i.e., intergranular. Gold [86, 87] compressed columnar-grained ice cubes perpendicular to the column of the grains with an experimental setup similar to the numerical model in Fig. 8.2. The portion of at least partial grain boundary cracks increased with increasing strain rate, decreasing grain size and decreasing

temperature. For strain rates larger than $10^{-3}\,\mathrm{s}^{-1}$ and at a temperature of $-10\,^{\circ}\mathrm{C}$ almost all cracks were intergranular. Furthermore, few transgranular cracks propagated through a grain boundary into an adjacent grain. Yet non-propagating cracks are not expected to impact the overall ice failure in brittle experiments. To the author's knowledge, an analogous study for granular ice does not exist. Nonetheless, it is reasonable to assume that cracks that dominate ice failure are highly likely to be intergranular in the brittle regime.

The above-described knowledge on fracture mechanics is mostly based on small-scale studies due to the relatively low effort and the benefit of controlled conditions in the laboratory, see, e.g., [197]. Larger specimens are used in field tests but only with single tensile cracks, e.g., [52], and data is scarce due to the high effort required. Also, the proper way of testing is subject of ongoing debate [177]. To pursue the development of fracture models based on small-scale tests but with future applications to full-scale in mind, models must be valid on all relevant scales [196]. They have to capture the size effect, i.e., "the dependence of the nominal strength of geometrically similar structures on size" [18, 145]. The relationship between nominal strength and size can be described by different laws as illustrated in Fig. 3.4: Strength theory (which knows no size effect) for small geometries, linear-elastic fracture mechanics (LEFM) for large geometries and brittle behavior, and quasi-brittle scaling laws that asymptotically approach the two. If models *do* capture the size effect, they can be further used to extrapolate small-scale test results [175]. For a complete treatment of the size effect refer to, e.g., [14, 17, 196].

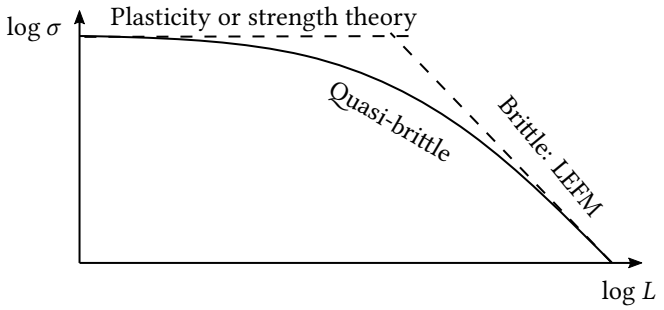

Fig. 3.4: Sketch of scaling of nominal strength vs. size with size-effect laws for limiting cases of strength criteria and LEFM, and transitional quasi-brittle scaling. Adapted from [16].

A size effect in compression has been shown in quasi-brittle materials such as concrete [18], thereby similar behavior can be expected in ice, at least for Coulombic faulting, i.e., lower confinement. With increased confinement and the switch to Plastic faulting, no size effect is expected [313]. For ice, to date, the few existing experimental studies have not found a significant size effect in compression for specimen sizes up to a couple of meters [157, 295], or at least not if the minimum cross-sectional diameter was $> 25\bar{d}$ [120]. However, it is always possible that specimens are too small for a size effect to become apparent [51, 163]. In addition to that, the majority of large-scale tests has been done in the ductile regime, where a size effect is not expected [295]. So these experimental studies by no means disprove a compression size effect. On the other hand, Schulson for instance argues that features of

compressive fracture generally look alike on different scales and suggests that fracture mechanics are scale independent [248, 253]. Nonetheless, as long as a model is only applied to small-scale simulations, it seems reasonable to postpone size-effect modeling in compression until more research is available. Moreover, the focus on small-scale models and tests is further justified by the similarity of fracture mechanics on different scales. A size effect in tensile fracture, on the other hand, has been shown experimentally for sea ice specimens with sizes ranging from 0.5 m to 80 m [51].

To conclude this overview on fracture in ice, the concept of fracture process zone (FPZ) and its link to specimen size and modeling approaches is treated. An unloaded (pre-)crack can be seen as having a well-defined crack tip. Upon loading, the crack has no well-defined tip anymore, but may be viewed as a traction-free crack which is attached to the FPZ. The FPZ is a space ahead of the crack tip, where voids and localized micro-cracks develop until they finally coalesce into the main (macro) crack [203, p. 105], see Fig. 3.5. Since no well-defined crack tip exists, a notional crack tip is assumed to be located at the point where the tensile stress equals the local tensile strength of the material, i.e., at the point of maximum tensile stress. Then, the FPZ spans the area between the traction-free crack tip, sometimes called physical crack tip, and the notional crack tip [52, 54]. Materials in which the FPZ size is not negligible in comparison to a cross-section dimension D are termed quasi-brittle [18], and modeling approaches should include the behavior within the FPZ. Ice is such material[2].

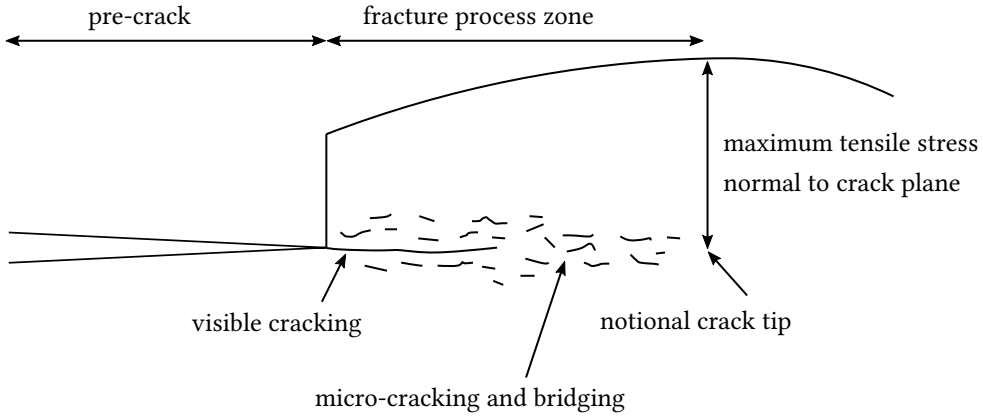

Fig. 3.5: Schematic of a crack and the fracture process zone. The curve above the crack indicates tensile stress acting on the crack. Reproduced based on [52, 54].

By contrast, modeling approaches that do not include the FPZ or assume it to be negligibly small, e.g., LEFM, should not be applied to sub-size specimens in terms of the small-scale yielding assumption [50]. This can be illustrated with the edge crack in a square plate: A load pushes the sides of a pre-crack apart, once this load is sufficient to propagate the crack it is called splitting load. As shown in [175] for sea ice, LEFM correctly predicts fracture in

[2] As mentioned, whether or not a material can be seen as quasi-brittle depends on the scale or size of the geometry. Sea ice can behave perfectly brittle on the scale of 1000 km [18], but this is far from any specimen sizes treated here.

three-point bending and edge-notched square plates if

$$L > 12\lambda_{\mathrm{L}} \tag{3.9}$$

is satisfied. Eq. (3.9) is recommended by [49, 197] and termed the process zone requirement. The characteristic length[3] λ_{L} is material-dependent and calculated as

$$\lambda_{\mathrm{L}} = \frac{EG_{\mathrm{c}}}{\sigma^2} \tag{3.10}$$

with E the Young's modulus of the bulk material, G_{c} the fracture energy and σ the maximum traction or tensile strength. Eq. (3.10) was established for isotropic materials, in other cases modifications may be necessary depending on the material or the fracture mode [106]. Eq. (3.9) is a requirement with respect to specimen size versus fracture process zone size. Additionally, for sea ice, the following homogeneity requirements in terms of grain size should be fulfilled

$$L > 200\bar{d} \quad \text{and} \quad A > 60\bar{d} \tag{3.11}$$

with L the specimen size in cracking direction and A the notional crack length [49, 197]. Below these size recommendations, the LEFM overpredicts the load, whereas methods based on the cohesive zone method or a fitted Bažant size-effect law indicate the correct trend or match experimental data, respectively [53, 175]. One reason for the limits of LEFM's applicability is the nonlinearity ahead of the crack in the FPZ. This needs consideration since grain sizes in ice can be of the order of several centimeters and Eqs. (3.11) result in large L and A [51].

To sum up, fracture in ice is an involved research area, so is the modeling of the underlying mechanics. Due to knowledge gaps and constraints regarding available numerical tools it is currently not possible to model full-scale events with multiple cracks and fragmentation [176]. However, we can focus on specific effects and corresponding appropriate treatment. All considered, it is desirable to include crack nucleation and crack propagation. Under compression, we expect confinement to have a strong influence, changing crack patterns from axial splitting to shear cracks that are oriented about 30° to 45° to the loading direction. At least for tensile cracks, some form of size effect should be captured by the model.

[3] A common alternative notation for the characteristic length is l_{ch}.

4 Homogenization of elasticity

This work proposes a modeling approach based on two pillars, elasticity and fracture, which are strongly connected through the polycrystal microstructure. The influence of the microstructure decreases with the size of observed volume. For large volumes, microstructural features can often be ignored, making modeling approaches based on representative or effective behavior possible. An open-ended question is the 'threshold' size below which the microstructure does have a big influence and should be explicitly modeled. Since the present work focuses on simulation models for small-scale tests it is paramount to choose the correct approach, i.e., modeling the microstructure if necessary. This chapter discusses how the threshold can be estimated. The described theory is picked up in Ch. 8, where a threshold or minimum size is investigated for modeling polycrystal elasticity.

All materials are heterogeneous at a small enough scale, owing to for instance domains of different materials or the same material in different states. Direct numerical simulations that include all heterogeneities are too computationally demanding for most domain sizes. Different multiscale techniques have been developed to overcome this. These can be categorized in homogenization methods in the case of sufficient separation of length scales between micro- and macrostructure, and concurrent methods in case of a strong coupling between scales [240]. Here, the former is assumed.

The aim of homogenization is to estimate effective macroscopic properties from the microstructure. This allows to substitute the heterogeneous material and its corresponding model with a homogeneous material and a much more efficient model. In the case of linear elasticity, the following relation is sought

$$\langle \boldsymbol{\sigma} \rangle = \mathcal{C}^* : \langle \boldsymbol{\varepsilon} \rangle \tag{4.1}$$

with the apparent stiffness $\mathcal{C}^*$, the stress and strain tensor fields $\boldsymbol{\sigma}$ and $\boldsymbol{\varepsilon}$ within a (statistically) representative volume element, and their spatial averages $\langle \boldsymbol{\sigma} \rangle$, $\langle \boldsymbol{\varepsilon} \rangle$ defined as

$$\langle \{\cdot\} \rangle = \frac{1}{V} \int_\Omega \{\cdot\} \, \mathrm{d}\Omega \tag{4.2}$$

whith V the volume of Ω [327]. Quantities such as $\mathcal{C}^*$ are relations between averages and not material properties, which is why they are called apparent properties [126].

Specific approaches to achieve this vary and can be classified in (semi-)analytical and computational methods. For an in-depth review of methods and applications refer to, e.g., [141, 240, 266, 327]. Here, computational homogenization with representative volume elements (RVE) and finite elements is chosen since the established models are to be further used in numerical simulations.

When it comes ice material models in engineering, granular ice is almost always modeled as isotropically elastic to reduce modeling- and computational effort. This assumes homogenized elasticity since ice single crystals are anisotropic (see Sect. 3.2). In theory, this assumption can be fulfilled because granular ice is indeed isotropically elastic, but this requires a volume element big enough to exhibit 'average' behavior. Based on a 2D numerical model, Elvin [63] stated that the minimum number of grains per volume should be about 230. For 3D, this number is not known. For a 2D quadrilateral element, 230 grains would mean at least $\approx$ 14 grains[1] along its edge.

For laboratory-grown ice, grain sizes are in the order of millimeters, whereas specimen sizes are in the order of centimeters. This puts unfeasible lower bounds on element sizes, at least when simulating experiments. A typical diameter for a cylindrical specimen could be 10 cm. With a grain size of 2 mm this would require element sizes of at least 2.8 cm and result in only three through-diameter elements. For standard formulations excluding high-order elements this is too few elements to resolve gradients or represent geometries. For sea ice, the model geometries are much larger, but so are grain sizes, resulting in the same issue.

Briefly, assuming and using homogenized elastic properties is desirable but strictly speaking often not correct. However, the minimum RVE size for polycrystal elasticity in 3D is not known, so is the error introduced by using elements smaller than the minimum RVE size. With the micromechanical elasticity model established in Sect. 3.2 the minimum RVE size in 2D and 3D can be confirmed or estimated, respectively, and the error of assuming homogenized elasticity with too small elements can be quantified. Below, basic concepts of homogenization are briefly reviewed in Sects. 4.1 to 4.3.

4.1 Representative volume element

The concept of a representative volume element (RVE) is at the core of computational homogenization. Several definitions exist [84], but in essence it is a volume whose "effective behavior is representative of that of the material as a whole" [10]. Research on RVE is concerned with (i) the existence of a RVE, (ii) its effective properties, and (iii) its size. Clearly defining a RVE is only possible for a unit cell in a periodic or regular microstructure, and for a volume containing a large number of microscale features such as grains with statistically homogeneous properties [205, 240]. Given its existence, the following separation of scales needs to hold

$$\left.\begin{matrix}\mathcal{L}^{\mu} \ll \\ \mathcal{L}^{\mu} <\end{matrix}\right\} \mathcal{L}^{RVE} \ll \mathcal{L}^{M} \tag{4.3}$$

where $\mathcal{L}^{\mu}$ is the characteristic length of the microstructural features or inhomogeneities, $\mathcal{L}^{RVE}$ the RVE size (if so justified) which is also called mesoscale, and $\mathcal{L}^{M}$ the characteristic size of the macroscopic body [10, 322]. As inequality on the left-hand side of Eq. (4.3) $\mathcal{L}^{\mu} < \mathcal{L}^{RVE}$ may be sufficient for microstructures with weak geometric disorder or mismatch in

[1] In [63], 230 grains are equivalent to a square model geometry with length 17.5 mm. Average grain area is 1.31 mm^2, which with Eq. (7.20) yields an average diameter of 1.29 mm, hence 17.5 mm/1.29 mm $\approx$ 14. Alternatively, we can compute $\sqrt{230} \approx 15$.

properties. The existence (and size) of a RVE strongly depends on the characteristics of the material and the properties we seek to average as for example discussed in [141, 205]. If damage or localization of deformation (e.g., macro fracture) has occurred, defining a RVE may be difficult or impossible, a RVE may not exist [84, 92].

The central issue is the trend of the mesoscale constitutive response, with

$$\delta = \frac{\mathcal{L}^{RVE}}{\mathcal{L}^{\mu}} \tag{4.4}$$

increasing, to a situation where the domain is structurally typical of the whole material on average (more precisely: spatially homogeneous and ergodic), and its effective response independent of its boundary conditions [204]. Mesoscale properties are termed *apparent*, as opposed to *effective*. The latter applies to $\delta \to \infty$ which signifies the passage to the RVE. On the other hand, any finite mesoscale implies statistical scatter and hence describes a statistical volume element (SVE).

Here, a RVE is sought for ice which, categorized after [10], is a non-porous grain polycrystal. The elastic properties resulting from the geometry and orientation of the single grains are to be averaged (see Sect. 3.2). Consequently, regarding the separation of scales in Eq. (4.3), $\mathcal{L}^{\mu}$ corresponds to the grain- and $\mathcal{L}^{M}$ to the specimen size.

The existence of an elastic RVE for ice has for instance been shown through very close Voigt-Reuss-bounds on the homogenized elastic constants [199]. Specifically

$$S^{V}_{ijkl} \leq S^{\text{eff}}_{ijkl} \leq S^{R}_{ijkl} \tag{4.5}$$

$$C^{R}_{ijkl} \leq C^{\text{eff}}_{ijkl} \leq C^{V}_{ijkl} \tag{4.6}$$

where S^{eff}_{ijkl} and C^{eff}_{ijkl} are the components of the compliance and stiffness tensor of the aggregate and $(\cdot)^{V,R}$ the solutions due to Reuss and Voigt, respectively. Furthermore, the effective properties are known because granular ice polycrystals are elastically isotropic.

The final step is RVE size determination. RVE size is defined as "a minimum size of a microstructural cell that fulfils the requirement of statistical homogeneity" [84]. It is always a lower bound, meaning that larger volumes behave similarly but smaller ones do not. Commonly, the size $\mathcal{L}^{RVE}$ is connected or proportional to the size of the constituents or inclusions μ. For polycrystalline ice, this is the average grain size $\bar{d}$, so $\mathcal{L}^{RVE} \propto \bar{d}$. Nonetheless, stating a single number of features in an element or along its edges is misleading. The size of a RVE, or the trend to go from SVE to RVE with increasing δ (Eq. (4.4)), depends on the material and its random geometrical and mechanical properties as well as the boundary conditions, which are treated in the next section. Above all, the RVE size also depends on the desired precision and the number of realizations [141].

4.2 Boundary conditions

The choice of appropriate boundary conditions (BC) is key to homogenization with RVE. BC have to be chosen such that they fulfill the macrohomogeneity or Hill-Mandel Condition

[118, 245]. For a linear elastic material, the condition can be expressed as

$$\langle \boldsymbol{\sigma} \,:\, \boldsymbol{\varepsilon} \rangle = \langle \boldsymbol{\sigma} \rangle \,:\, \langle \boldsymbol{\varepsilon} \rangle \tag{4.7}$$

with the strain and stress tensors $\boldsymbol{\sigma}$ and $\boldsymbol{\varepsilon}$, the double contraction ":", and $\langle \cdot \rangle$ the spatial average (4.2). Thus, the average of the product of stress and strain (representing the micro level) is the same as the product of their averages (macro level).

The condition (4.7) is fulfilled for finite bodies through a proper choice of boundary conditions, as shown by [114] and only briefly repeated here. Particularly, Eq. (4.7) can be rewritten as a surface integral over the boundary of the RVE

$$\int_{\partial\Omega} (\boldsymbol{t} - \langle \boldsymbol{\sigma} \rangle \cdot \boldsymbol{n}) \cdot (\boldsymbol{u} - \langle \boldsymbol{\varepsilon} \rangle \cdot \boldsymbol{x}) \, \mathrm{d}A = 0 \tag{4.8}$$

with the traction vector $\boldsymbol{t}$, the displacement $\boldsymbol{u}$, the normal vector of the boundary $\boldsymbol{n}$, and the position vector of a material point of the RVE $\boldsymbol{x}$ [113, 114].

Different BC that satisfy (4.8) exist which are briefly described below, for a detailed discussion refer to [240] or [205]. Kinematic uniform boundary conditions (KUBC) prescribe displacements $\boldsymbol{u}$ on the entire boundary $\partial\Omega$ of the RVE via

$$\boldsymbol{u}(\boldsymbol{x}) = \langle \boldsymbol{\varepsilon} \rangle \cdot \boldsymbol{x} \quad \forall \boldsymbol{x} \in \partial\Omega \tag{4.9}$$

Though straightforward to implement, the KUBC result in predicting a too stiff macroresponse. Static uniform boundary conditions (SUBC) prescribe tractions on the boundary such that

$$\boldsymbol{t}(\boldsymbol{x}) = \langle \boldsymbol{\sigma} \rangle \cdot \boldsymbol{n} \quad \forall \boldsymbol{x} \in \partial\Omega \tag{4.10}$$

Contrary to KUBC, with SUBC the macroresponse is predicted too soft. In the case of mixed-orthogonal uniform boundary conditions (MUBC) we have

$$(\boldsymbol{t} - \langle \boldsymbol{\sigma} \rangle \cdot \boldsymbol{n}) \cdot (\boldsymbol{u} - \langle \boldsymbol{\varepsilon} \rangle \cdot \boldsymbol{x}) = 0 \quad \forall \boldsymbol{x} \in \partial\Omega \tag{4.11}$$

The condition (4.11) can only be realized in materials with at least orthotropic elastic symmetry properties, where the axes of orthotropy are parallel to the axes of symmetry of a hexahedral volume element [114, 206]. KUBC and SUBC bound the apparent stiffness tensor [115].

If some finite scale periodicity of the microstructure can be assumed, a fourth option are periodic boundary conditions (PBC)

$$\boldsymbol{u}(\boldsymbol{x} + \boldsymbol{L}) = \boldsymbol{u}(\boldsymbol{x}) + \langle \boldsymbol{\varepsilon} \rangle \cdot \boldsymbol{x} \quad \boldsymbol{t}(\boldsymbol{x} + \boldsymbol{L}) = -\boldsymbol{t}(\boldsymbol{x}) \quad \forall \boldsymbol{x} \in \partial\Omega \tag{4.12}$$

with $\boldsymbol{L} = L\boldsymbol{n}$. PBCs require a periodic geometry and mesh topology. Regarding the geometry, this results in additional effort but can be handled by microstructure generation algorithms such as Neper [221]. Regarding the mesh, periodicity is easily achieved in the case of voxel discretizations resulting in grid-like meshes. The latter is often done when the microstructure is reconstructed from experimental data. However, the boundaries between constituents become stepped surfaces which are less suited for simulating phenomena at grain boundaries,

e.g., grain boundary sliding. Further, voxel-based meshes can lead to a large number of elements since the voxel size needs to be small enough to resolve the smallest feature within the RVE [266]. Tetrahedralizations are better at representing geometries such as curved entities, but achieving a periodic mesh topology is not straightforward.

Lastly, depending on the microstructure and its constituents, generating truly periodic RVEs might not be worth the additional effort [245]. An alternative that circumvents the drawbacks of PBC are approximate periodic boundary conditions [244, 245]. Combinations of the above are also possible [205, 245].

4.3 Apparent constitutive properties

Different options exist to compute overall stiffness. In general, 36 constitutive constants need to be determined via six independent load cases [327, p. 47]. Once the constants are determined, i.e., a completely defined stiffness, further averaged properties based on stiffness can be computed, e.g., Young's modulus.

The simplest way to obtain apparent elastic properties are via the stress and strain volume averages (4.2). In practice, this means summing element or integration point volume-weighted stress and strain components [206]. For one integration point per element, we have the averages

$$\langle \sigma_{ij} \rangle = \frac{1}{V} \sum_{n_{\text{elem}}} \sigma_{ij} V_{\text{elem}} \tag{4.13}$$

$$\langle \varepsilon_{ij} \rangle = \frac{1}{V} \sum_{n_{\text{elem}}} \varepsilon_{ij} V_{\text{elem}} \tag{4.14}$$

which constitute $\langle \boldsymbol{\sigma} \rangle$ and $\langle \boldsymbol{\varepsilon} \rangle$. If the effective response can be assumed to be isotropic, then instead of six only one loading case with non-zero dilatational and deviatoric components is required to define the apparent bulk and shear moduli [327, p. 46]

$$\kappa^* = \frac{1}{3} \frac{\langle \frac{\operatorname{tr} \boldsymbol{\sigma}}{3} \rangle}{\langle \frac{\operatorname{tr} \boldsymbol{\varepsilon}}{3} \rangle} \tag{4.15}$$

$$\mu^* = \frac{1}{2} \sqrt{\frac{\langle \boldsymbol{\sigma}^{\text{dev}} \rangle \,:\, \langle \boldsymbol{\sigma}^{\text{dev}} \rangle}{\langle \boldsymbol{\varepsilon}^{\text{dev}} \rangle \,:\, \langle \boldsymbol{\varepsilon}^{\text{dev}} \rangle}} \tag{4.16}$$

The above equations are valid for all boundary conditions[2]. Finally, with κ^* and μ^* known,

[2] Tarek Zohdi, personal communication, 08.02.2021.

the sought properties are

$$E^* = \frac{9\kappa^* \mu^*}{3\kappa^* + \mu^*} \tag{4.17}$$

$$\nu^* = \frac{3\kappa^* - 2\mu^*}{6\kappa^* + 2\mu^*} \tag{4.18}$$

Analytically, the bounds on properties can be calculated from a given stiffness (Eq. (3.7)) and compliance. Following Cowin [43], this can be done based on four tensors in matrix notation, namely the dilatational modulus tensor $\boldsymbol{C}_\mathrm{d}$, Voigt tensor $\boldsymbol{V}$, hydrostatic pressure modulus tensor $\boldsymbol{K}_\mathrm{h}$, and Reuss tensor $\boldsymbol{R}$ (not repeated here but given in [43]). To calculate the bounds, only the traces of these tensors are needed

$$\operatorname{tr} \boldsymbol{C}_\mathrm{d} = C_{11} + C_{22} + C_{33} + 2(C_{12} + C_{13} + C_{23}) \tag{4.19}$$

$$\operatorname{tr} \boldsymbol{V} = C_{11} + C_{22} + C_{33} + 2(C_{44} + C_{55} + C_{66}) \tag{4.20}$$

$$\operatorname{tr} \boldsymbol{K}_\mathrm{h} = S_{11} + S_{22} + S_{33} + 2(S_{12} + S_{13} + S_{23}) \tag{4.21}$$

$$\operatorname{tr} \boldsymbol{R} = S_{11} + S_{22} + S_{33} + \frac{1}{2}(S_{44} + S_{55} + S_{66}) \tag{4.22}$$

where the C_{ij} and S_{ij} are from the stiffness and compliance tensors in Voigt notation, for the former see Eq. (3.7). The Voigt and Reuss estimates for isotropic bulk and shear moduli are

$$\kappa_\mathrm{R} = \frac{1}{\operatorname{tr} \boldsymbol{K}_\mathrm{h}} \tag{4.23}$$

$$\mu_\mathrm{R} = \frac{15}{6 \operatorname{tr} \boldsymbol{R} - 2 \operatorname{tr} \boldsymbol{K}_\mathrm{h}} \tag{4.24}$$

$$\kappa_\mathrm{V} = \frac{1}{9} \operatorname{tr} \boldsymbol{C}_\mathrm{d} \tag{4.25}$$

$$\mu_\mathrm{V} = \frac{1}{30}(3 \operatorname{tr} \boldsymbol{V} - \operatorname{tr} \boldsymbol{C}_\mathrm{d}) \tag{4.26}$$

These estimates bound the actual effective moduli and, together with Eqs. (4.17) and (4.18), can be used to compute bounds on the Young's modulus and Poisson's ratio.

5 Data-based methods

As illustrated in Chs. 2 to 3, a big part of ice research is dedicated to either experimental work and the derivation of ice mechanics laws or translating these insights into numerical models. Alternatively, and as a step prior to numerical modeling, the idea of this chapter is to look at how a machine learning model, which has no access to physical laws, predicts experimental results based on data. These predictions possibly help to make decisions on which and how to include parameters in numerical models. Additionally, numerical models may require input parameters that are unknown, but can be substituted with predictions from machine learning models. Finally, results from a machine learning analysis could be used to validate other models, if, e.g., no suitable validation tests are available. The basic principles behind these ideas and the methods to realize them are discussed below. Subsequently, Ch. 6 applies the specific machine learning methods to a large ice test database.

Input-output relationships in ice tests are difficult to capture due to gaps in ice mechanics knowledge and the corresponding experimental data (see Sect. 3.1). As a result, modeling decisions such as the prioritization of effects are usually based on domain knowledge, which is incomplete, and a limited number of univariate experimental studies. Sometimes, no prioritization is done and various effects in the model act simultaneously, e.g., compressive- and flexural strength are combined as 'failure' strength [129] though the underlying mechanics are different. While not optimal, such approaches can be necessary due to the complexity of ice and are a feasible alternative as long as model limitations and assumptions are clear.

A closely related issue is the estimation of required but unknown input parameters to both numerical and phenomenological models. When no measurements are available for model inputs, it is common to fall back to empirical approaches. Taking compressive strength as an example, these formulas collapse multivariate relationships into simple equations with one or two inputs, see Sect. 6.5.1. Drawbacks are, for example, that they are often only valid for estimating uniaxial strength, and based on limited datasets, see, e.g., [136, 156]. In reality, strength depends on numerous parameters which may influence each other [285, 286]. In particular, multiaxial stress significantly impacts strength [294].

Briefly, current parameter estimation and prioritization approaches are based on limited data which risks overlooking influential effects or parameters as well as multivariate interactions between effects. It is desirable to complement these approaches with methods that are less affected by missing data or gaps in theory, and which are able to deal with multivariate nonlinear and higher-dimensional relationships. This points to evidence-based methods [19]. From a data-driven point of view, large- and high-dimensional data is needed to capture the complexity of ice. Since available data is often biased and contains missing values, machine learning is particularly useful [161]. The general process of a data analysis with machine learning is described in Sect. 5.1.

In addition to that, a high prediction accuracy for large datasets is often only achieved by complex models which are almost impossible to interpret. As a result, understanding why a model makes a specific prediction is often as important as the model's accuracy [179]. How such an understanding can be achieved is treated in Sect. 5.2.

This chapter describes key concepts and processes. The specific models and their parameters are described in Ch. 6. For a detailed background and theory of machine learning and the applied concepts, refer to [83] for an application-oriented perspective, and [108] for the underlying mathematics.

5.1 Data science process

A machine learning model essentially represents a mathematical formula that seeks to approximate a general input-output relationship using data [162] and is part of a general data science process that seeks to obtain insights from data in various formats, e.g., tabular data or images. There are various ways to describe the data science process, the one used here is the OSEME or OSEMN process, short for *obtain, scrub, explore, model, explain or iNterpret* [183, 282].

The first step is obtaining the data. Instances of data are termed observations or samples, which in turn are composed of several features. Having compiled the data, the second step is scrubbing. Scrubbing means filtering, cleaning and transforming the data to comply with the machine learning model's requirements and the problem formulation, e.g., outlier detection and treatment of missing values. In the end, the model can only be as good as the data, or put more colloquially: 'garbage in, garbage out'.

The next step is an exploratory analysis of the cleaned data. Patterns and relationships may emerge through visualizations, e.g., histograms can reveal imbalanced data. This often goes hand in hand with feature engineering which for instance comprises the removal of redundant or irrelevant features or selecting the most 'useful' features, i.e. those with the most predictive power. Dimensionality reduction, e.g., with a principal component analysis, can also be part of the the exploring stage.

Subsequently, one or multiple models are selected based on, for instance, input and output data type or desired accuracy, see Sect. 6.6. Then, the data is fed to the model for learning, also called training. Training is done on a subset (training data) of the complete dataset. If the data includes both a set of features, the predictors, and the solution to be predicted, the targets, the process is called supervised learning. Furthermore, if the targets are distinct classes (labels), the learning task is classification. If the target is a numerical value to be predicted out of a continuous range, the task is called regression. [83]

Training a model means finding the model architecture or parameters that minimize the prediction error (loss) of the model for the observations in a training set. The training set typically comprises 80 % of observations. The generalizability of the model is usually evaluated with the validation dataset. The performance of the final model is assessed with the testing dataset. The underlying question is 'how well does the model perform on new or unseen data?'.

The subsequent step of explaining and interpreting highlights that concerns of predicting

are not necessarily the same as model interpretation. On the contrary, they may conflict, see Fig. 5.1. Therefore the last step is to study the model and its predictions with the aim of understanding the input-output correlations hidden in the data and discovered by the model.

These steps are often repeated. For instance, the explain step might include a feature ranking which reveals that certain features are essentially ignored by the algorithm. This would justify going back to the feature engineering and subsequent removal of those features. Once the model building based on historic data is complete, the model deployment begins where predictions are made based on new data.

5.2 Explainability

Generally, there is a trade-off between model complexity, accuracy and explainability[1], see Fig. 5.1. The more complex the data and its hidden underlying patterns are, the more 'sophisticated' or complex the models need to be for accurate predictions, e.g., (deep) neural networks [282, p. 51]. By contrast, a too simple model is not able to learn the underlying pattern and will be inaccurate (underfit). On the other hand, a complex model applied to noisy and small datasets will likely overfit and, e.g., detect patterns in the noise itself. These patterns will not generalize to new data instances (overfitting) [83, p. 28].

Moreover and equally important, complex models are not explainable per se. That is, there is no direct way for a human to see the importance of features and understand the rules and relations between features that resulted in the model's prediction. Neural networks, for example, can be represented as a set of equations but these equations are not intuitively accessible to the human brain. In contrast to this, simpler models such as decision trees follow rules of the form $x > a$ so x belongs to class y. Linear regression models inherently show their decision rules through the magnitude and direction of weights attached to the input variables.

The trade-off between better model performance, i.e., more accurate predictions, and model explanation conflicts with knowledge discovery. One major point of criticism is "the lack of novel laws, understanding, and knowledge arising from their use" [243], see also [33, 122]. Such criticism sparked discussions and research under the umbrella term of *eXplainable AI* (XAI), see e.g. [103, 168, 239]. Understanding why a model made a prediction has become a central challenge in ML. Here, the approach goes even further along this argument: accurate predictions are important, but the explanation of the predictions is much more interesting. The aim is to see how a data-based model, without access to physical laws, predicts the outcome of ice tests, and what patterns these predictions are based on.

Fortunately, various XAI methods have been developed that seek to shift the complex models in Fig. 5.1 to the right, i.e., increase their level of explainability. Essentially, these

[1] Different definitions of explainability and interpretability have been proposed [11, 56, 103, 192] but often both terms are used interchangeably. More recent publications tend to define interpretability as a passive characteristic of a model which refers to the "level at which [it] makes sense for a human" [11, p. 84], i.e., its transparency. Explainability is seen as an active characteristic, denoting, e.g., a procedure of the model that clarifies its decision rules. It is linked to post-hoc methods that convert a black-box, non-interpretable model into an explainable one. Here, I stick to the term explainability.

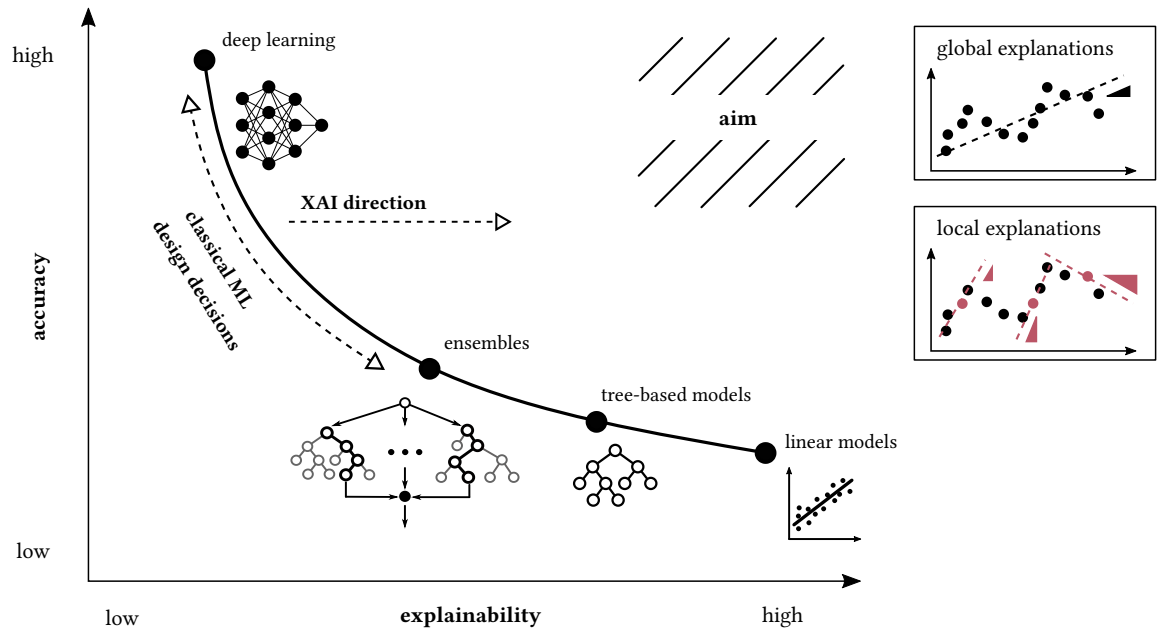

Fig. 5.1: Relationship between accuracy, explainability and complexity of models. Explainability approaches help to shift models towards higher explainability while keeping the model complexity constant. Right: difference between global and local explanations. Sketch adapted from Merten Stender [282], with kind permission.

methods view the explanation of a model's prediction as a model in itself. These explanation models can explain machine learning (ML) models globally, i.e., give the average impact of a feature over a dataset, or locally, i.e., the impact of input features on single samples [180]. This is depicted in the right of Fig. 5.1 with two plots: The global explanation plot gives the slope of a linear fit over all data points whereas the local explanation gives the slope for each single sample. Global explanations are constructed by combining all local, individual SHAP values [283].

Perturbation methods relate slight changes in inputs to the model outputs, e.g., LIME [229]. Additive feature attribution methods seek to approximate a complex model by a simpler and hence explainable model [179]. Alternatively, approaches based on Shapley values from game theory can be used [178, 179].

Shapley values are a way to answer the question "What is a fair way for a coalition to divide its payoffs?". They consider the marginal contribution of an agent, i.e., the difference in (overall) payoffs the coalition would obtain with and without the agent. This marginal contribution is averaged over all different sequences according to which the coalition could be built, i.e., in which order the agents are joining the coalition. In particular, the *SHapley Additive exPlanation* (SHAP) values draw a parallel between dividing payoffs to agents of a coalition and attributing model outcome to input features [179]. SHAP values have a solid theoretical foundation in game theory, which contrasts other, more heuristic approaches [192]. Using SHAP values was shown to be superior to other feature attribution techniques, e.g., gain or split count [178]. Most importantly, SHAP values are consistent, which means

they cannot decrease with increasing feature importance [178]. Furthermore, the method has been successfully applied to various problems ranging from medical to acoustic applications [180, 282, 283]. Therefore, in this work, explanations based on SHAP values are chosen.

To compute SHAP values, the following definitions hold: f is the model, $f(\boldsymbol{x})$ a prediction for the features in input vector $\boldsymbol{x}$. $f_x(S)$ is defined as the expected value of the function conditioned on a subset S of the input features, so $f_x(S) = E[f(\boldsymbol{x}) \mid \boldsymbol{x}_S]$. This is the expected value of $f(\boldsymbol{x})$ when only those elements of $\boldsymbol{x}$ in the subset S are known and used as input. Without conditioning, $E[f(\boldsymbol{x})]$ would be the expected value of the model, i.e., the average output of the model over a dataset. Further, M is the number of input features in N, which is the set of all input features, and S is a subset of N. Finally, the SHAP value is computed such that

$$\phi_i = \sum_{S \subseteq N/\{i\}} \frac{|S|!(M - |S| - 1)!}{M!} \left(f_x(S \cup \{i\}) - f_x(S) \right) \tag{5.1}$$

Essentially, ϕ_i is the difference between $E[f(\boldsymbol{x})]$ and $E[f(\boldsymbol{x}) \mid x_1]$, which is the expected value of the model given the information stored in the first element of input feature vector $\boldsymbol{x}$. In general, the sum of SHAP values for one observation is equal to the model output, so for $\boldsymbol{x}$ for one observation k the following holds

$$\sum_{i=0}^{M} \phi_i = f(\boldsymbol{x}) \tag{5.2}$$

As an example, take a binary classification task (classes 1 or 0) with an expected value $E = 0.5$, where the model predicts 0.9 for one observation. The SHAP value ϕ_i attributed to feature x_i could take any reasonable value. For example, ϕ_i for x_i may be 0.3, indicating that this feature is responsible for increasing the model's output by 0.3 compared to the expected value. Other features may carry negative values, hence individually would cause a reduced prediction value. Yet Eq. (5.2) would always yield the difference between $f(\boldsymbol{x})$ and E which is 0.4. Hence SHAP values have the unit of the prediction space [192]. Generally, ϕ_i gives a local explanation, but the SHAP values can be combined for several samples resulting in global explanations. For tabular data with N features and K rows, all SHAP values would be a $K \times N$ matrix $\boldsymbol{\phi}$. The information stored in $\boldsymbol{\phi}$ can be used for further downstream analyses, e.g., visualizations [178].

Notably, Eq. (5.1) has an exponential complexity[2] and efficiently estimating $E[f(\boldsymbol{x}) \mid x_S]$ is challenging. The different ways of estimating $E[f(\boldsymbol{x}) \mid x_S]$ can be broadly grouped in model-agnostic and model-specific methods. The former rely on post-hoc 'modeling of the model' with an additional function which can be slow and exhibit sampling variability. Additionally, convergence checks have to be done and some level of noise in the estimates has to be accepted. By contrast, model-specific methods leverage the model structure to improve on these points.

[2] $\mathcal{O}(TL2^M)$ with T the number of trees, L the maximum number of leaves in any tree and M the number of features. M is prescribed by the number of meaningful features in the data, i.e., those features with (high) predictive power. T and L can be limited by the user.

Here, two methods within the SHAP framework were used. Firstly, the 'TreeExplainer' which is specific to tree-based models. It enables fast[3] and exact computation of SHAP values and comes with additional benefits, for instance no estimation variability [180]. Secondly, the 'KernelExplainer' was used. It is an approximate model-agnostic approach that builds a weighted linear regression. This regression is based on the data, the predictions, and the model [179]. The basic idea is to estimate the contribution of a feature by evaluating the model output with and without the feature and for different (theoretically all) feature combinations. Due to its approximate nature, variability in the results can be expected. Furthermore, a background dataset is required to represent missing values during the toggling process. Different options of background datasets exist, e.g., a data subset, a k-means summarized dataset [4], a zeros-only observation, or, for image classification, a black image. Naturally, the choice of background dataset affects the explanation.

5.3 Tools and metrics

Below, some specific tools to evaluate the performance and assess the data are described. This includes methods for outlier detection, performance or error metrics, as well as methods for checking the generalizability of models and preventing overfitting.

Error metrics and loss functions

For the regression model, the following metrics were used:

$$MAE = \frac{1}{n}\sum_{i=1}^{n}|y_i - f(x_i)| \tag{5.3}$$

$$RMSE = \left[\frac{1}{n}\sum_{i=1}^{n}(y_i - f(x_i))^2\right]^{1/2} \tag{5.4}$$

with true value y_i and prediction $f(x_i)$ given the input x_i. The root-mean-square error (RMSE) is a standard metric. Additionally, the mean absolute error (MAE) can be used for its straightforward interpretation as average error [314]. Also, if the data distribution is skewed, squared error metrics can strongly increase mean errors if observations in the tail are badly predicted.

For binary classification, a straightforward metrics is the accuracy

$$ACC = \frac{TP + TN}{TP + TN + FP + FN} = \frac{TP + TN}{\text{all predictions}} \tag{5.5}$$

which is the fraction of correct predictions. Moreover, for imbalanced datasets, Matthews Correlation Coefficient is useful since it only scores high if the classifier does well on both

[3] $\mathcal{O}(TLD^2)$ with T the number of trees, L the maximum number of leaves in any tree and D the maximum depth of any tree. T, L and D can be limited by the user. In most cases M is much larger than 2, whereas usually $D \leq 6...8$, thereby $\mathcal{O}(TLD^2)$ is preferable to $\mathcal{O}(TL2^M)$.

classes [38, 186].

$$MCC = \frac{TP \cdot TN - FP \cdot FN}{\sqrt{(TP + FP)(TP + FN)(TN + FP)(TN + FN)}} \tag{5.6}$$

It takes the following values:

$$MCC = \begin{cases} +1 & ; \text{complete agreement} \\ 0 & ; \text{prediction no better than random} \\ -1 & ; \text{complete disagreement} \end{cases} \tag{5.7}$$

Furthermore, the SHAP method can be applied to the log-loss of the classifier. For a binary classification with a true label $y_i \in \{0, 1\}$ and a probability estimate of the model $p(y_i)$ that $y_i = 1$ the log loss for one sample is [83, p. 144]

$$L_{\log}(y_i, p(y_i)) = -\left[y_i \log(p(y_i)) + (1 - y_i)(\log(1 - p(y_i)))\right] \tag{5.8}$$

Outlier detection for skewed data

In regression, squared error metrics may place too much emphasis on observations with large residuals $|y_i - f(x_i)|$ during training [108, p. 349]. Such metrics can be ill-suited for long-tailed error distributions or mismeasured y-values termed outliers. Different options exist to tackle outliers: More robust criteria can be used, e.g., absolute error or Huber criterion, or learning methods that are less susceptible to outliers, e.g., tree-based methods. [108, pp. 349 and 351]

Alternatively, outliers are removed before training. This can be done based on outlier-detection criteria or domain knowledge, e.g., identifying unphysical values. For the former, a common approach is to classify all points outside the interval

$$[Q1 - 1.5\text{IQR}, Q3 + 1.5\text{IQR}] \tag{5.9}$$

as *potential* outliers. Where IQR is the interquartile range

$$\text{IQR} = Q_3 - Q_1 \tag{5.10}$$

and Q_i the quartiles. For a normal distribution, only 0.7 % of observations are expected to exceed (5.9), however for skewed distributions the exceedance probability using this criterion is usually too high. In this case, adjusted Hubert-Vandervieren (HV) whiskers can be used: Taking the medcouple (MC), defined in [32], as a measure of skewness of a univariate distribution, the HV-whiskers are

$$[Q1 - 1.5\text{e}^{-4\text{MC}}\text{IQR}, Q3 + 1.5\text{e}^{3\text{MC}}\text{IQR}] \quad ; \text{MC} \geq 0 \tag{5.11}$$

$$[Q1 - 1.5\text{e}^{-3\text{MC}}\text{IQR}, Q3 + 1.5\text{e}^{4\text{MC}}\text{IQR}] \quad ; \text{MC} < 0 \tag{5.12}$$

Outlier detection based on domain knowledge is done during the exploratory data analysis in Ch. 6.

Overfitting and generalizability

A good prediction performance is desirable, but needs to be double-checked for two aspects. First, the generalizability, i.e., whether by chance the random selection of test data resulted in a performance that would not hold when the model is applied to new unseen data. To assess the generalizability of the model, k-fold cross-validation (CV) can be used [108, 225]: The training data is divided into k segments, then, k iterations of training and validation are done. In every iteration a different fold of the data is held-out for validation while all remaining $k - 1$ folds are used for training. This simulates a repeated input of unseen data to the model. Having completed the iteration, k samples of the performance metric are available. The average and spread of metric values indicate the expected prediction performance of the model and its generalizability, that is, the sensitivity of the model training process to the data selection.

Secondly, it needs to be checked whether the performance is 'too' good due to overfitting: The model memorized the data instead of identifying universal patterns or the identified patterns are noise. Complex models come with an incredible amount of freedom due to their many parameters, therefore the more complex the model, the more prone it is to overfitting. Typically, the learning objective is regularized, that is, the objective rewards simple and predictive functions [37]. Besides regularization of the objective, a straightforward and efficient method is early stopping of the training process. If the model validation score does not improve over several training rounds, training is stopped. The optimizer probably found a local minimum which however does not necessarily coincide with a global minimum [83, p. 144].

6 Application of data-based methods to ice test data

This chapter applies the machine learning principles described in Ch. 5 to a database of small-scale tests. Two targets, compressive strength and behavior type (ductile or brittle), are predicted with a black-box machine learning model and its results compared to existing empirical- or analytical models. An additional explanation model is used to understand the machine-learning model predictions, i.e., how and why the black-box model made its decisions. Finally, the explanations are connected to ice mechanics theory. Known effects are confirmed and quantified, previously less visible and discussed effects are explored. Possible links to the material model are discussed in the next chapter, Sect. 7.1.

Some results of the study presented below are part of a submitted but not yet published manuscript[1] and [144]. Here, the results are reassessed and extended with additional data.

6.1 OSEME process applied to compression test data

In the following, the principles described in Ch. 5 are applied via the workflow illustrated in Fig. 6.1. The process follows the *obtain, scrub, explore, model, explain* (OSEME) process described in Sect. 5.1. A large database of small-scale compression tests was collected (Sect. 6.2), scrubbed (Sect. 6.3), and explored (Sect. 6.4). Four machine learning (ML) models were trained to predict compressive strength and behavior type for saltwater and freshwater ice, and compared to existing prediction methods.

The first target, compressive strength, is a numeric value target which is predicted through regression. It was chosen as a target because it is a required input for all types of ice-related models (numerical, empirical, analytical, and phenomenological), e.g., wave-ice interaction [107], ice-propeller interaction [148], and ship speed prediction in ice-covered seas [190]. It is also used in all standards for predicting ice loads such as the ISO 19906 [130], see also the overview by the author in [142]. Further, ice-structure interaction is thought to be dominated by the same mechanisms as for small-scale compression experiments [256, pp. 266 and 336]. Therefore an improved understanding of compression in the laboratory is thought to help develop models for full-scale ice-structure interaction. As comparison, existing empirical formulas are used as described below (Sect. 6.5.1).

The second target, behavior type, can be fundamentally different [254] and thereby desirable to predict [256, p. 320], e.g., to choose an appropriate constitutive model. This is for

[1] See [P7] in Sec. 1.2

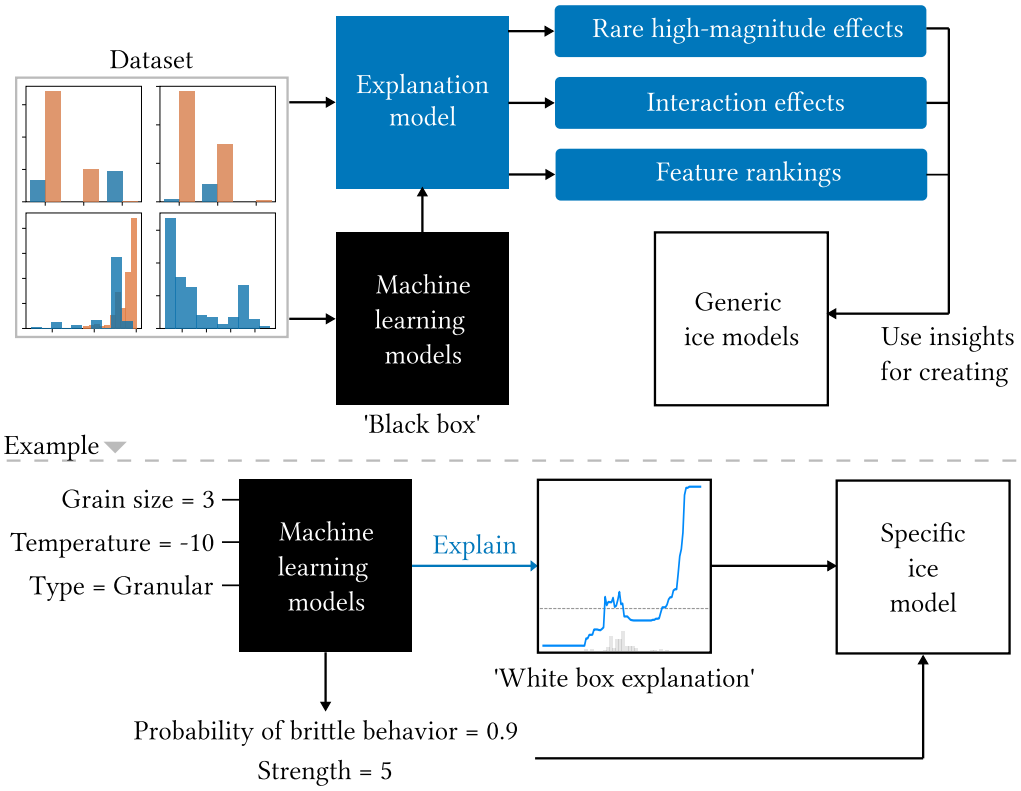

Fig. 6.1: Data analysis process for generic ice models (top) and applied to a specific ice model (bottom). Adapted from a submitted manuscript[2].

instance done in [129], where the actual strain rate $\dot{\varepsilon}$ compared to a critical strain rate $\dot{\varepsilon}_{cr}$ results in different constitutive models. Mostly, the foremost interest is to discriminate broadly between ductile and brittle behavior, though there are sub-types such as Coulombic faulting. In particular, the transition from ductile to brittle behavior in terms of a 'transition strain rate' has been studied extensively, for instance in [277], but its prediction remains challenging. To the author's knowledge, the only available tool is the analytical model by Renshaw and Schulson [228, 256], briefly described below (Sect. 6.5.2).

Once the predictions are made, the explanation model, also termed explainer, is applied with the input of both the data and the ML model (Fig. 6.1). Local explanations, i.e., for one observation, are combined for a whole set of data to generate global model insights. In turn, these are discussed in terms of ice mechanics (Sects. 6.7.4 and 6.8.4), and possibly used in the creation of further (non-data-based) ice models. Examples for such uses are scalar input values such as the compressive strength but also curves, e.g., from partial dependence plots. It is possible to validate models with results and curves from the ML and explanation models.

[2] See [P7] in Sec. 1.2.

6.2 Obtaining data

A high-dimensional dataset is needed to capture the complex ice properties and interactions. Here, the dataset comprises data from a broad range of small-scale laboratory and field ice tests. This includes different ice types, testing conditions, specimen sizes etc. The data sources are: [3, 41, 44, 45, 89, 90, 91, 93, 109, 110, 111, 112, 117, 128, 137, 138, 158, 167, 187, 191, 198, 218, 219, 231, 232, 235, 236, 251, 254, 255, 258, 261, 268, 269, 273, 275, 293, 297, 312, 318, 323, 326]. Additionally, data from the University Centre in Svalbard (UNIS) project from 2004 to 2011 is included, see, e.g., [123, 195, 286].

The key features that were used in the analysis are listed below. Their choice is based on the review on ice mechanics and influential features in Ch. 3. The type of data is indicated along with its range of values. For categorical data, the range of values is a set of categories, for numerical data the minimum and maximum values are given. For more details on specific features cf. [144]. The data is continuously updated, in this work, database version 1.16 was used.

- **Type of test**. *Categorical data* ∈ {uni-, bi- and triaxial compression}. Tension tests are part of the data but not used in this analysis.
- **Type of ice**. *Categorical data* ∈ {granular, columnar, ridge}. Ridge means ice samples taken from ice ridges found in nature.
- **Type of water**. *Categorical data* ∈ {saltwater, freshwater}. The water type of which the ice was made.
- **Columnar loading**. *Categorical data* ∈ {along, across, 45°}. For columnar and ridge ice, this indicates loading across or along the columns, and in rare cases in a 45° angle. For natural ice, this usually coincides with specimens from cores taken horizontally (loading across the column) or vertically (loading along) out of the ice sheet [195, 297].
- **Porosity**. *Numerical data* ∈ $[0.01, 84.3]$ %. This is total porosity of the ice, including air, and brine for saltwater ice.
- **Salinity**. *Numerical data* ∈ $[0.02, 20]$ ‰. Bulk salinity of saltwater ice.
- **Volume**. *Numerical data* ∈ $[252, 6283185]\,\mathrm{mm}^3$. The specimen geometries are included through volume.
- **Grain size**. *Numerical data* ∈ $[0.6, 23]$ mm. This is the average grain size for granular ice.
- **Strain rate**. *Numerical data* ∈ $[1.94 \cdot 10^{-8}, 3.50 \cdot 10^{1}]\,\mathrm{s}^{-1}$. A global strain rate typically calculated based on the global strain at peak stress, i.e., strength. This contrasts local strain rates, which can vary significantly [94].
- **Temperature**. *Numerical data* ∈ $[-50, 0]$ °C. Temperature of the specimen during testing.

- **Triaxial stress state**. *Numerical data* $\in [-507, 0.33]$. Measured with triaxiality η, which relates hydrostatic, σ_h, to shear stress, which can be represented as von Mises stress σ_vM, to give $\eta = \sigma_\mathrm{h}/\sigma_\mathrm{vM}$, see, e.g., [60]. Note that these values are not always available before the experiment. For extrusion tests, see [117], triaxiality was estimated with a FEM model[3].

6.3 General data scrubbing

An all-purpose data scrubbing was done before further analysis. Strain rate was logarithmized with base ten. For some numerical features, only values inside certain intervals were retained and all other values were set to Not a Number (NaN). The intervals where: for logarithmized strain rate $-10\,\mathrm{s}^{-1}$ to $10\,\mathrm{s}^{-1}$, for triaxiality -20 to 1, and for temperature $-100\,^\circ\mathrm{C}$ to $0\,^\circ\mathrm{C}$. In all cases values outside these intervals are unlikely to be correct, at least for the studies currently included.

For some categorical features, categories were replaced with higher-level categories, for example Coulombic faulting with brittle behavior. Categorical values not shown in Figs 6.2 and 6.3 were also set to NaN. Some of these categories are not well defined whereas for others the number of observations is too small to have any impact, e.g., single crystal ice. Extrusion tests were interpreted as triaxial compression tests. Additional scrubbing was done after the exploratory analysis and prior to the application of the ML models, firstly shear and tensile tests were excluded since this study aims at compression tests, and secondly observations with missing target values were excluded. Moreover, no distinction between laboratory and natural saltwater ice was made.

Categorical features were handled with ordinal encoding, i.e., consecutive numerical values for each category. This may lead the machine learning algorithm to assume a relationship between values, which is generally not the case in my data, e.g., a test is either biaxial or uniaxial, but there an in-between value does not make much sense. Nevertheless, how to do the encoding is subject of discussion [315]. In preliminary studies, the models performed better when categories where ordinally encoded compared to one-hot encoding. Hence the former was used.

Furthermore, the compressive strength data was analyzed regarding potential outliers since the data is skewed, see Fig. 6.4. Both freshwater and saltwater ice strength values include outliers in the right tail. For freshwater ice the following values stand out: 105 MPa, 104 MPa, 88.9 MPa, 79.6 MPa and 75.6 MPa. Toward lower strength, the values are continuously distributed. For saltwater ice, there are several outliers between 61.2 MPa and 38 MPa but all other values are smaller than 28 MPa and continuously distributed.

From a physical perspective, very low strength values are common due to testing at high temperatures or premature failure, whereas very high values are due to optimal conditions, see, e.g., [191, 235] for freshwater ice. For instance, the freshwater strength value of 105 MPa is from a test at $-40\,^\circ\mathrm{C}$, with a strain rate of almost $1\,\mathrm{s}^{-1}$, a high triaxial stress state, and a

[3] Computations done by Sarah Schreiber at the Institute of Ship Structural Design and Analysis, Hamburg University of Technology.

small grain size. All of these aspects are known to increase strength. For the highest saltwater ice strength values the situation is similar: high strain rates, low temperatures and a high triaxial stress state. So these measurements do not appear to be unphysical or true outliers.

From a statistical point of view, adjusted Hubert-Vandervieren (HV) whiskers were used to identify potential outliers, see Sect. 5.3 and [125]. The upper adjusted whiskers were 65.6 MPa for freshwater and 27.2 MPa for saltwater ice. Lower whiskers are not of interest since low compressive strengths are common. These statistically determined outliers are in line with those identified visually from Fig. 6.4. In short, there are several potential outliers in the data. These should not be ruled out prematurely but their removal could improve the performance of machine learning models.

6.4 Exploratory analysis

The next step after obtaining the data is the exploratory analysis. The aim is to identify patterns, imbalanced data, and features with a large fraction of missing values prior to applying the machine learning (ML) models.

Fig. 6.2 shows key predictor features with histograms and bar charts, where orange bars are saltwater and blue bars freshwater ice tests. About 90 % of the saltwater tests are done on natural ice specimens, the remaining 10 % are laboratory-grown. These plots indicate that many features are biased toward certain values or types: To begin with, test type is dominated by uniaxial compression (UC) tests because they are comparatively straightforward to do. Due to including extensive field test campaigns at the University Centre in Svalbard (UNIS) the UC data is biased toward saltwater ice. This is also reflected in the ice type bar chart, where most saltwater ice tests are done with columnar- or ridge ice, whereas freshwater ice tests are often done with granular ice. Next, when columnar ice is tested, it is overwhelmingly loaded along or across its columns, whereas 45° tests are the exception.

In the second row of plots in Fig. 6.2, regarding strain rate, the majority of tests is done at rates between 10^{-5} s^{-1} and 10^{-1} s^{-1} with a large number at 10^{-3} s^{-1}. This is firstly due to the UNIS campaigns, which were done at 10^{-3} s^{-1}, and secondly this value is often a transition strain rate between ductile and brittle behavior [144], and therefore of interest to researchers. Testing temperatures are mostly between −20 °C and 0 °C where saltwater ice tests tend to be executed at higher temperatures compared to laboratory tests. Grain size is seldom measured for saltwater ice tests, though in the corresponding histogram all measurements for columnar ice were excluded since there are different ways to define grain size in columnar ice.

In the third row, the triaxiality histogram shows a strong bias toward high triaxiality values. Uniaxial tests dominate with a value of −0.33, tests with values < -2 exist but are rare. The next two plots to the right show porosity. Saltwater ice porosity can be quite high with extreme values around 80 %, whereas the (mostly laboratory-grown) freshwater ice has a very low porosity.

The first plot in the bottom row indicates that salinity is centered around 5 ‰ and values rarely go above 10 ‰, which are typical values [297]. The middle- and right plots in the last row indicate that the majority of specimens are relatively small, where the largest dimension rarely goes above 200 mm.

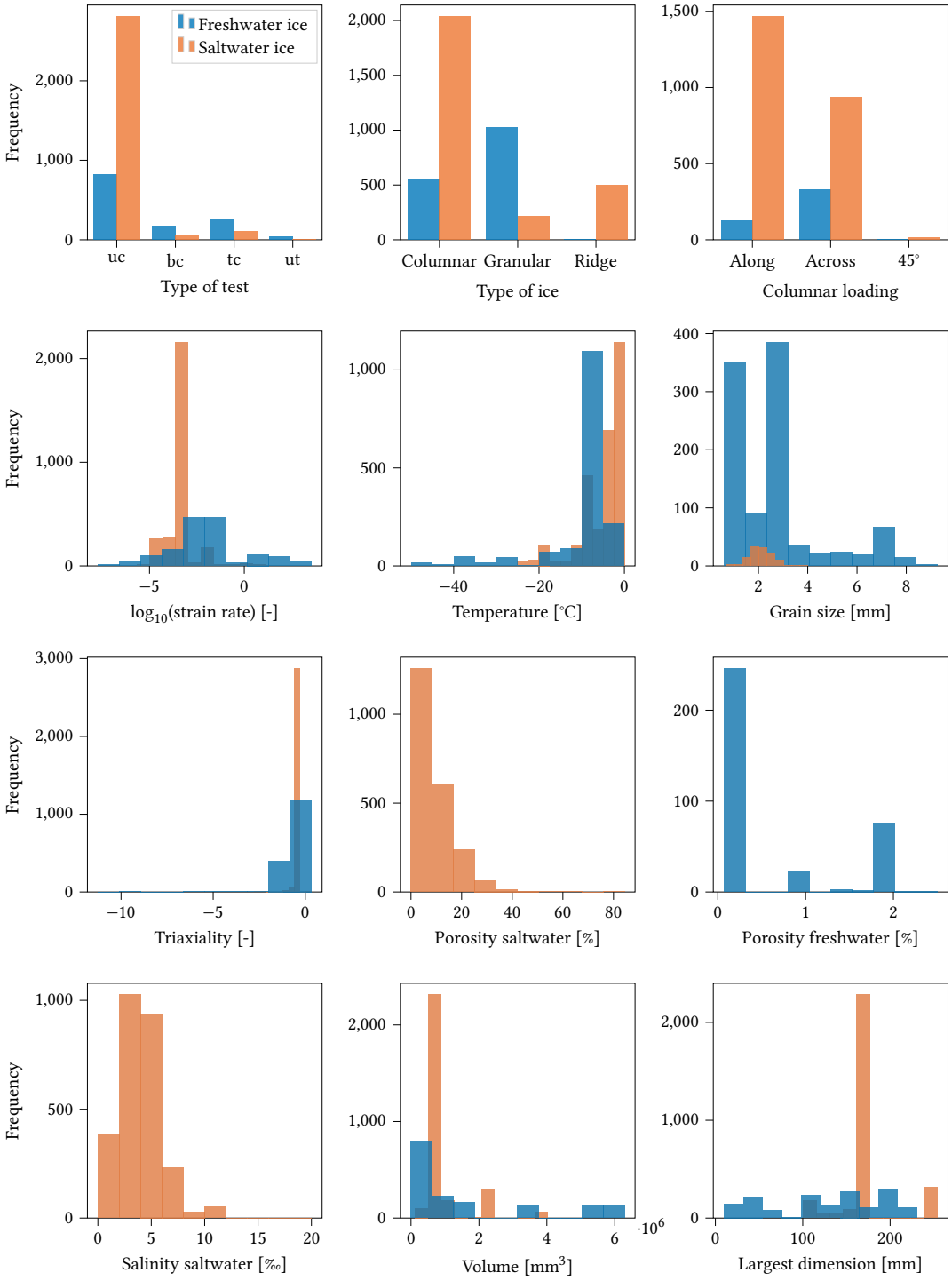

Fig. 6.2: Histograms and bar charts of the key features in the database. Top left; uc/bc/tc is uniaxial-, biaxial-, and triaxial compression, ut is uniaxial tension. Logarithmized strain rate has no unit according to [185].

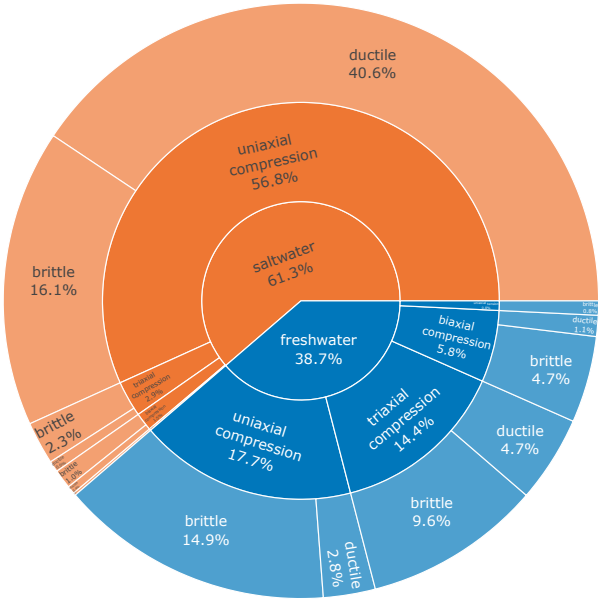

Fig. 6.3: Sunburst chart indicating hierarchical fraction of tests sorted (i) in the inner circle by freshwater or saltwater ice, (ii) in the middle circle by type of test, and (iii) in the outer circle by behavior type. Fraction is shown by width of slice and indicated in percentage of total data excluding missing values.

The target feature behavior type is visualized in more detail with the sunburst chart in Fig. 6.3. To begin with, it shows that there is more saltwater than freshwater ice data. It also underlines the bias of saltwater ice tests toward uniaxial compression, whereas for freshwater ice the test types are more balanced. Moreover, ductile behavior appears more common in saltwater than in freshwater ice tests and vice versa for brittle behavior. Hence behavior type is an imbalanced target. Note that these are only statements about the observations in the database, not necessarily conclusions about how ice behaves in general.

The second target, the compressive strength, is shown in Fig. 6.4. The data exhibits skewness and a long right tail with potential outliers. The values roughly follow log-normal distribution fits[4]. The saltwater ice data is better described by the log-normal fit than the freshwater ice data, possibly due to more available data. These fits match combined data from various studies relatively well, yet data from one study might be better described with a different distribution, e.g., Weibull [140].

In addition to biases and the distribution of target data, the percentage of missing values per feature requires consideration during machine learning applications. In Table 6.1 the percentage of missing values is given for key features. The most affected features are the strains, grain size and porosity.

[4]Fitted with SciPy [301]. The probability density function is $f(x, s) = \frac{1}{sx\sqrt{2\pi}} \exp -\frac{\log^2(x)}{2s^2}$ with shape parameter s. For freshwater ice, $\sigma = 0.947$, $\mu = 1.901$, whereas for saltwater ice, $\sigma = 0.927$, $\mu = 0.953$. σ and μ are for logarithmized data. For transforms see Eqs. (7.22) to (7.24).

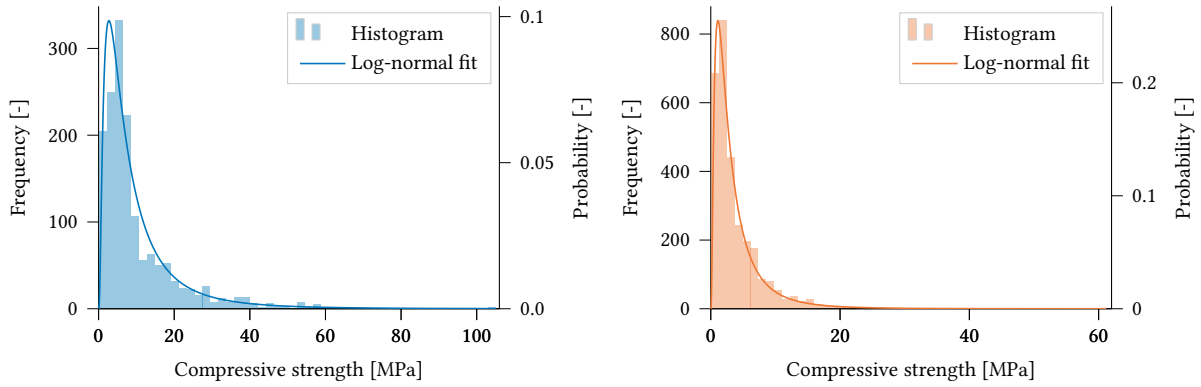

(a) Freshwater ice

(b) Saltwater ice

Fig. 6.4: Distribution of compressive strength for (**a**) freshwater and (**b**) saltwater ice and log-normal distribution fits. Vertical axes are inverted by multiplying negative compressive strength with −1.

Table 6.1: Percentage of observations with missing values per feature

Features	All (n = 4591)	Saltwater ice (n = 2978)	Freshwater ice (n = 1613)
Type of behavior	27.2	36.3	10.3
Strain ε_1	71.8	68.2	78.5
Strain ε_2	90.1	63.9	100.0
Strain ε_3	82.9	42.5	100.0
Grain size	18.0	58.9	5.3
Porosity	44.5	26.3	78.2
Salinity	-	10.5	-
Columnar loading	10.7	9.7	15.7

Only data with > 5 % missing data are shown. Strains are in principal test directions. The number of samples given in the first row might change depending on the feature, e.g., the grain size measurement only makes sense for tests with granular ice and in that case n is lower than indicated.

6.5 Classic prediction methods

Below, current approaches other than machine-learning-based are given for a later comparison to the machine learning model. These include the prediction of compressive strength with empirical formulas as well as two strain rate models for predicting ductile- or brittle behavior.

6.5.1 Compressive strength

The state-of-art tool to estimate compressive strength are empirical formulas. Various formulas exist, briefly described in the following. Ince et al. [129] suggest two fits which reflect the relationship between strength σ and temperature T:

$$\sigma = \begin{cases} -0.35T + 1.65 & ; \text{freshwater ice} \\ -0.40T + 0.90 & ; \text{saltwater ice} \end{cases} \tag{6.1}$$

No limits regarding the applicability of Eq. (6.1) are stated. The strength of freshwater ice in dependence of strain rate $\dot{\varepsilon}$ is given by Jones [136] as

$$\sigma = \begin{cases} 24.8\ \dot{\varepsilon}^{0.196} & ; \dot{\varepsilon} \leq 2 \cdot 10^{-3}\ \mathrm{s}^{-1} \\ 8.23\ \dot{\varepsilon}^{0.072} & ; \dot{\varepsilon} > 2 \cdot 10^{-3}\ \mathrm{s}^{-1} \end{cases} \tag{6.2}$$

The threshold strain rate in Eq. (6.2) could be seen as a transition strain rate between ductile and brittle behavior, but no such statement is made by the author. Eq. (6.2) is only valid for uniaxial strength. A case-based, two-parameter approach for sea ice strength is given by Timco and Frederking [295] based on total porosity ν_T in parts per thousand (ppt), ice type, and loading direction:

$$\sigma = \begin{cases} 37\ \dot{\varepsilon}^{0.22} \left(1 - \sqrt{\frac{\nu_\mathrm{T}}{270}}\right) & ; \text{horizontally-loaded columnar ice} \\ 160\ \dot{\varepsilon}^{0.22} \left(1 - \sqrt{\frac{\nu_\mathrm{T}}{200}}\right) & ; \text{vertically-loaded columnar ice} \\ 49\ \dot{\varepsilon}^{0.22} \left(1 - \sqrt{\frac{\nu_\mathrm{T}}{280}}\right) & ; \text{granular ice} \end{cases} \tag{6.3}$$

Eq. (6.3) is stated to be valid for uniaxial strength, and for strain rates $10^{-7}\ \mathrm{s}^{-1} \leq \dot{\varepsilon} \leq 10^{-4}\ \mathrm{s}^{-1}$, but may be used up to strain rates of $10^{-3}\ \mathrm{s}^{-1}$ risking an overprediction of strength.

Lastly, Kovacs [156] gives the following equation for uniaxial compressive strength of saltwater ice with the bulk ice porosity ϕ_B, and also based on strain rate:

$$\sigma = 2.7 \cdot 10^3 \frac{\dot{\varepsilon}^{\frac{1}{3}}}{\phi_\mathrm{B}} \tag{6.4}$$

While not clearly stated, Eq. (6.4) appears applicable to strain rates between approximately $10^{-6}\ \mathrm{s}^{-1}$ and $10^{-3}\ \mathrm{s}^{-1}$.

Except the formula by Ince et al., all of the above should only be applied to the prediction of uniaxial compressive strength. However, uniaxial strength should be seen as an index strength [286], meaning this will generally not be the strength in other loading situations [295] but still serves for comparison and estimation purposes.

6.5.2 Behavior type

The classification of behavior type is done by comparing the actual strain rate to a transition strain rate between ductile and brittle behavior. Two transition strain rate models exist: one for Coulombic (C-)faulting under low to moderate confinement by Renshaw and Schulson [228, 256], and one for plastic (P-)faulting under higher degrees of confinement by Renshaw, Golding and Schulson [226].

Briefly, C-faulting, also termed frictional faulting, is characterized by macro faults which consist of a narrow band of microcracks. It has been explained in terms of initiation and interaction of secondary cracks (comb cracks). P-faulting, termed non-frictional faulting, is characterized by macroscopic faults, which consist of a band of recrystallized grains, and local heating. Once significant heat diffusion is prevented by rapid loading, thermal softening overcomes hardening effects which results in increased localized plastic deformation. This leads to brittle-like behavior though on the microscopic level there is ductile flow. [89, 90, 247]

The transition between these two modes depends on the confinement R defined as the ratio between the least and greatest principal compressive stress. According to experimental results, the transition takes place at $R \approx 0.3$ [89, 226], but it can also be calculated using the coefficient of internal friction μ such that

$$R_\mathrm{t} = \frac{\sqrt{1+\mu^2} - \mu}{\sqrt{1+\mu^2} + \mu} \tag{6.5}$$

which for instance yields $R_\mathrm{t} = 0.3$ with $\mu = 0.6$. Yet μ is often not known and has to be estimated.

C-faulting

For $R \leq 0.3$ the transition strain rate is

$$\dot{\varepsilon}_\mathrm{t} = \frac{25BK_\mathrm{Ic}^3}{\bar{d}^{\frac{3}{2}}\left[(1-R) - \mu(1+R)\right]} \tag{6.6}$$

with the creep parameter B, the critical stress intensity factor K_Ic, the average grain size $\bar{d}$, the friction coefficient μ, and the confinement parameter R.

Regarding its applicability, B, μ and K_Ic are usually not known in advance. Strictly speaking, R is also sometimes not known in advance but this depends on the test setup. Nevertheless, the information behind R is similar to the triaxiality η which is used to train and predict

behavior type with the machine learning model later on. Therefore R was also treated as a known input with respect to Eq. (6.6).

This leads to two different approaches for unknown input values for Eq. (6.6): they can be estimated (Eqs. (6.7) to (6.10)) or substituted with reasonable fixed values. Fixed values are taken from the literature, namely [256, pp. 326-330] and [242, pp. 79-80]: K_{Ic} barely changes with temperature and grain size, measured values center around 0.1 MPa $\mathrm{m}^{0.5}$, which was the value used here. B was taken as $4.3 \cdot 10^{-7}$ $\mathrm{MPa}^{-3}\mathrm{s}^{-1}$ for freshwater and $5.1 \cdot 10^{-6}$ $\mathrm{MPa}^{-3}\mathrm{s}^{-1}$ for saltwater ice. A common value for μ is 0.5. Unknown saltwater ice grain sizes were estimated with $\bar{d} = 6$ mm.

Regarding estimates, B is temperature-dependent and, given a known reference value B_{ref} at a temperature T_{ref}, can be calculated with

$$B_0 = \frac{B_{\mathrm{ref}}}{\exp\left(\frac{-Q}{R_{\mathrm{gc}} T_{\mathrm{ref}}}\right)} \tag{6.7}$$

$$B(T) = B_0 \exp\left(\frac{-Q}{R_{\mathrm{gc}} T}\right) \tag{6.8}$$

In Eqs. (6.7) and (6.8), T is the temperature, Q is the apparent activation energy taken as 78 kJ mol^{-1}, R_{gc} is the universal gas constant, and lastly μ is the kinetic friction coefficient which mostly depends on sliding velocity and temperature but does not change much with ice type [146]. As an alternative to using the fixed value ($\mu = 0.5$), the following equation can be used:

$$\mu(\log_{10}(v_{\mathrm{s}}), T) = -0.4814 - 0.3413 \log_{10}(v_{\mathrm{s}}) - 0.00672T - 0.03005(\log_{10}(v_{\mathrm{s}}))^2 \tag{6.9}$$

which is a polynomial fit[5] of μ in dependence of logarithmized sliding velocity V_{s} and temperature T. This fit is based on several freshwater ice studies, namely [73, 146, 194, 257], and has an RMSE of 0.22. Due to a lack of data regarding μ and $\bar{d}$ for saltwater ice, the fit is strictly only valid for freshwater ice. The sliding velocity in Eq. (6.9) can be estimated as

$$v_{\mathrm{s}} = 2\dot{\varepsilon}\bar{d} \tag{6.10}$$

with the average grain size $\bar{d}$ [251].

Eqs. (6.6) to (6.10) show that if necessary parameters are available, the Renshaw-Schulson model is straightforward to use. Even if most of the parameters have to be estimated, it can still serve for roughly estimating the transition strain rate. In addition, it is comparatively well-studied, see, e.g., [226, 228, 256, 277].

[5] Reproduced from [P7] (see Sec. 1.2).

P-faulting

For $R > 0.3$, a critical strain rate required for P-faulting is given as

$$\dot{\varepsilon}_\mathrm{c} = \frac{-2\sqrt{2}\kappa m w_\mathrm{f}}{l w_\mathrm{d}^2 \frac{\partial \sigma}{\partial T}} \tag{6.11}$$

with thermal conductivity $\kappa = 2.3\,\mathrm{Wm^{-1}K^{-1}}$, work-hardening exponent $m \approx 0.4$, a fault width w_f assumed to be 2 mm and the same as w_d, l a characteristic length taken as the largest dimension of the specimen, and $\partial\sigma/\partial T$ the thermal softening estimated as $-0.55\,\mathrm{MPaK^{-1}}$ [89, 90, 226].

Alternatively to using a fixed value, $\partial\sigma/\partial T$ can also be calculated. This was not done here since it would introduce additional, generally unknown parameters. Furthermore, to the author's knowledge, Eq. (6.11) was developed based on tests of freshwater ice and may not give accurate results for saltwater ice, at least not for the above-given parameter values. Overall, similarly to the C-faulting model, various parameters are required which often have to be estimated. Nonetheless, Eq. (6.11) has been validated with experiments and can serve to estimate a transition strain rate in case of higher confinement.

6.6 Machine learning models

There is an abundance of available machine learning algorithms and in most cases different algorithms perform similarly well on the same task. Nonetheless, several points should be considered in the choice of algorithm. To begin with, the type and size of data should be taken into account. The original, non-scrubbed database consists of tabular data with about 4600 rows and 30 columns. For tabular data, tree-based algorithms outperform other methods, at least on this size of data [152, 180].

Furthermore, the features in the data showed a variety of nonlinear interactions. To capture these, usually complex nonlinear models are required. Moreover, earlier work by the author and colleagues yielded mixed results with classical statistical tools and simple decision trees [144].

All considered, two algorithms were used. The XGBoost implementation of gradient-boosted trees [37] since it is able to deal with missing data and due to its excellent integration in the explanation framework SHAP, see Sect. 5.2. Gradient-boosted trees are ensemble-models that additively build up simpler models which are fit to the gradient loss at each data point. Boosting means that models are built sequentially where each addition learns from mistakes made earlier - it is fit to the previous predictor's residuals. The underlying idea is that if residuals form a pattern, this pattern may be exploited to fit a model. See also [83, p. 205] and [37]. Additionally, for comparison, feed-forward artificial neural networks (ANN) were used as described in the Appendix, Sect. A.5. This was done to ensure that a different but equally sophisticated and flexible method yields similar results with respect to predictions and their interpretation.

Further tools used were parts of the scikit-learn package for pre- and postprocessing [213] and as explainers the above-described (Sect. 5.2) SHAP TreeExplainer and KernelExplainer. The former is the natural choice for tree-based models. The latter was used to explain the ANN model and furthermore validate the results from the TreeExplainer with a different approach. With respect to explaining the predictions, the 'true to the data' approach was used as explained in [36]. This means that the focus is on the data-generating process which may be well-represented by different models, and not so much in explaining the model itself.

6.7 Compressive strength prediction

6.7.1 Preliminaries

Only compression tests were analyzed. Shear and tensile tests were excluded. A preliminary study was done on outliers and logarithmizing target values to obtain a more normal distribution. For the tree-based model this barely affected results which is in line with expectations [108, p. 351]. Furthermore, for freshwater ice the five highest compressive strength values were excluded, i.e., values > 75 MPa. Including these rare values decreased performance but gives little additional value with respect to the desired output: accurate and explainable results. For saltwater ice, excluding outlier values did barely affect results, therefore all values were used.

As input data, there were 2970 saltwater and 1561 freshwater ice observations. Input features were: strain rate, temperature, grain size, porosity, triaxiality, volume, type of test, type of ice, columnar loading, and additionally for saltwater ice the salinity.

The following parameters were used for strength prediction: 500 trees, a learning rate of 0.07, a maximum number of leaves of eight and a subsample size of 50. These parameters are loosely based on [76, 108]. Early stopping was used with a patience of five rounds. Squared error was used as an early stopping metric and root-mean-squared error (RMSE) as a learning objective. A hyperparameter optimization was done with the Tree-structured Parzen Estimator approach [20, 21] but did not improve performance compared to the above-given parameters.

In the following, the main results are presented for the tree-based machine learning (ML) model, hereafter simply called 'model' if not stated otherwise. ANN-specific data scrubbing, model architecture, and results are presented in the Appendix, Sect. A.5.

6.7.2 Performance and generalizability

To begin with, the generalizability and model performance were evaluated. Table 6.2 gives root-mean-squared- and absolute error (RMSE and MAE, Eqs. (5.4) and (5.3)) for the cross-validation (CV) and the final model. The CV and final model performance is similar and the standard deviation of the CV fold performance values is low, thereby generalizability is confirmed. The absolute values in Table 6.2 appear large compared to typical compressive strength values but relative performance is good.

Table 6.2: Performance of ML strength regression model

Metric	Unit	Freshwater ice	Saltwater ice
RMSE CV average	MPa	4.34 ± 0.76	2.32 ± 0.40
RMSE final model	MPa	4.16	2.14
MAE CV average	MPa	2.67 ± 0.36	1.45 ± 0.11
Relative MAE CV average	%	3.91 ± 0.53	2.37 ± 0.20
MAE final model	MPa	2.68	1.39
Relative MAE final model	%	3.92	2.27

Sample sizes: freshwater ice final model $n = 313$, CV fold $n = 125$, saltwater ice final model $n = 594$, CV fold $n = 237$. CV values are average ± SD, $n = 5$ (number of CV folds). Relative values are in percent of range of values where freshwater and saltwater ice strength values range from 0.23 MPa to 68.6 MPa and 0.03 MPa to 61.2 MPa, respectively.

Table 6.3: Mean average error in predicting uniaxial strength

	Freshwater ice		Saltwater ice	
Method	MAE [MPa]	rel. MAE [%]	MAE [MPa]	rel. MAE [%]
Ince et al., 2016 [129]	3.48	6.0	1.91	6.8
Jones, 2007 [136]	4.01	6.9	-	-
Kovacs, 1996 [156]	-	-	1.28	4.5
Timco et al., 1990 [295]	-	-	2.37	8.4
ML model	1.24	2.1	1.29	4.6

Comparison is made for uniaxial data only. Sample sizes: freshwater ice $n = 313$, saltwater ice $n = 594$. Relative values are in percent of range of values where freshwater and saltwater ice strength values range from 0.23 MPa to 58.4 MPa and 0.03 MPa to 28.2 MPa, respectively. Blank cells means not applicable.

However, since the target data is roughly log-normally distributed, the information behind mean errors is limited. In Fig. 6.5a, true vs. predicted strength is plotted for freshwater and saltwater ice. In both cases there is some scatter, but the majority of predictions are close to the true values, i.e., near the $x = y$ line. This shows that the model performs well over the whole range of values for both freshwater and saltwater ice. Overall, the strength ML model performance merits further analysis and explanation of predictions. However, before moving on to the explanation, the ML model is compared to the empirical formulas for strength prediction.

These formulas are given in Sect. 6.5.1, they are only applied to the prediction of uniaxial strength. Average errors are compared in Table 6.3. In all, the ML model's performance on uniaxial strength is better or equals the performance of the empirical formulas.

Moreover, Figs. 6.6a and 6.6c show true vs. predicted values of the empirical formulas and the ML model. For freshwater ice, the ML model is more accurate and seems to generalize

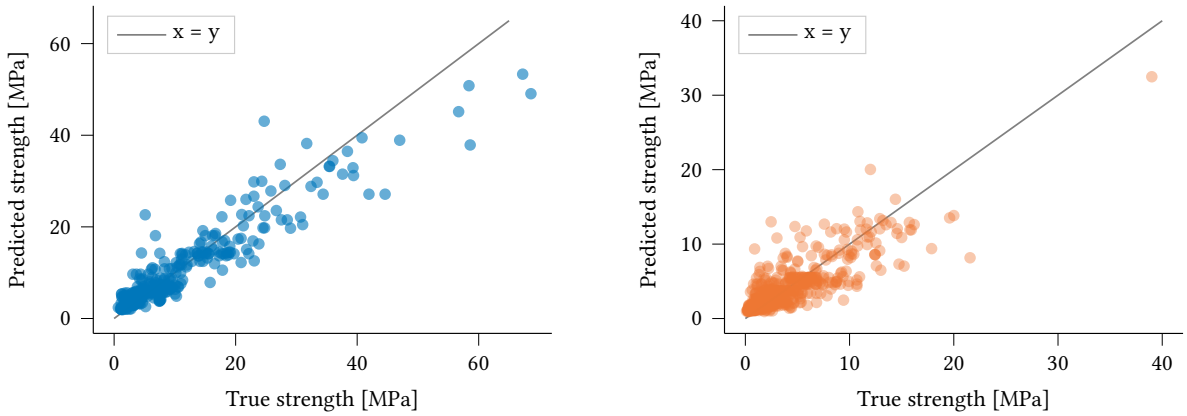

(a) Freshwater ice

(b) Saltwater ice

Fig. 6.5: True vs. predicted values for test data (including all compression test types) for freshwater and saltwater ice. Grey lines indicate where true and predicted values are equal. Density is indicated through color transparency.

better as most points are close to the $x = y$ line. The empirical formulas on the other hand keep predicting similar values despite increasing true values, resulting in points to the right of the $x = y$ line. For saltwater ice (Fig. 6.6c), the overall impression is similar. However the ML model also underpredicts several high strength values and there is much more scatter in the results. Nevertheless, the ML model's average performance remains good, see Table 6.3.

Figs. 6.6b and 6.6d show for each method a kernel density estimate[6] of errors along with quartiles and medians. Most errors are in the range of 0 MPa to 10 MPa. In the freshwater ice case the ML model outperforms the empirical approaches regarding overall distribution as well as median of error. For saltwater ice, the method by Kovacs performs equally well and does not exhibit a long tail of large errors. All other methods are not very accurate.

6.7.3 Data-based explanation

The ML model was not only created to accurately predict strength values, but to deliver insight into the data and feature relations. This section shows explanations of the model predictions. A discussion and comparison to ice mechanics knowledge is presented in the subsequent section. As an explanation data set, the whole (cleaned) data is fed into the SHAP explanation model. We generally look at global and local feature impact. Here global refers to the average impact of a feature over all observations in the explanation data set, i.e., the mean of absolute SHAP values. Local refers to the explanation for a single observation. Moreover, the influence of single features can be further analyzed with (partial) dependence plots. In general, SHAP values have the prediction space unit, here MPa.

Furthermore, encoded labels are necessary to understand impact. These are as follows. For freshwater ice columnar loading is encoded as $45° = 0$, across $= 1$, and along $= 2$, for test type, 0 is biaxial-, 1 is triaxial-, and 2 is uniaxial compression. Other categorical features

[6] Done with the statistical visualization package seaborn [310].

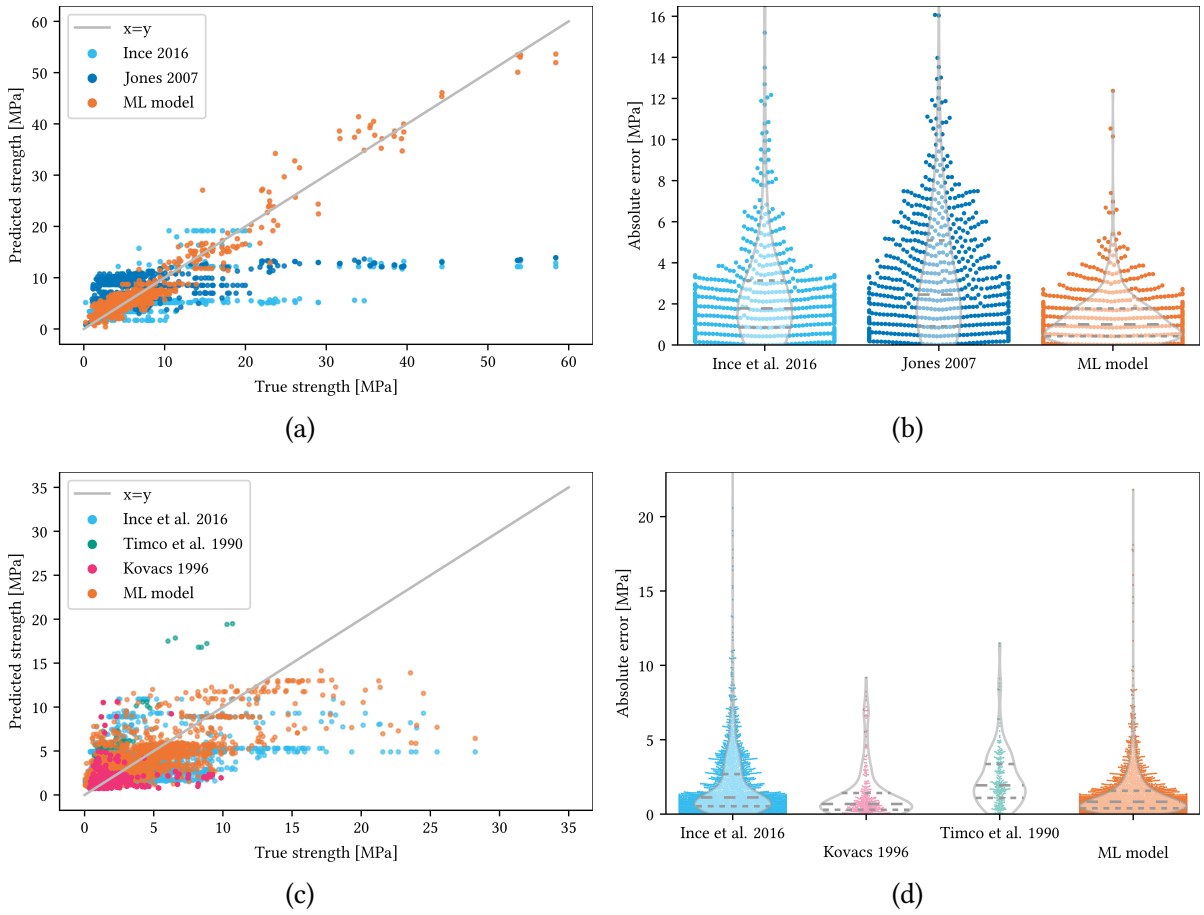

Fig. 6.6: Prediction of uniaxial compressive strength for ML model (trained on all data) and empirical formulas. (**a, b**) freshwater ice with $n = 824$, and (**c, d**) saltwater ice with $n = 2812$. (**a, c**) Predicted vs. true values, and (**b, d**) violin plots with kernel density estimates of absolute errors. Dashed lines indicate median and quartiles of error distribution, errors are indicated with underlying beeswarms.

have negligible impact. For saltwater ice, columnar loading is encoded as 45° = 0, across = 1, and along = 2, type of ice is encoded as columnar = 0, granular = 1, and ridge = 2. Other categorical features have negligible impact.

Freshwater ice

For freshwater ice, the bar chart in Fig. 6.7a gives the average (global) feature impact. More precisely, the horizontal axis is the the mean of the absolute SHAP values, the vertical axis ranks features by impact. Temperature, triaxiality, strain rate and volume exhibit an average impact between 2.5 MPa to 4 MPa, for other features the average impact is less than 1 MPa. It seems that only the first three to four features dominate.

The beeswarm plots in Figs. 6.7b offer further insights as this plot type does not conflate magnitude and prevalence. It gives SHAP value and feature value per observations (i.e., one dot) in the same order as in the impact bar chart. For freshwater ice, the beeswarm plots show a tendency toward positive SHAP values, i.e., a positive impact on strength. That is, there are many observations where features pushed the prediction toward higher strength, but fewer observations where features pushed the prediction toward lower strength. Furthermore, the majority of observations are clustered around certain SHAP values, often zero, whereas many others constitute long tails of values.

More specifically, temperature and strain rate have a long tail of high SHAP values for low feature values, i.e., a low temperature is rated to strongly increase compressive strength prediction whereas high temperatures slightly decreases it. This observation indicates that for most samples these features do not have a big impact, but for a smaller group the impact is exceptionally high. By contrast, the distribution of SHAP values for strain rate is more continuous with the exception of a few outliers. Regarding volume, low values have a tendency to push predictions toward higher strength values. Lastly, for categorical variables, a high or low feature value corresponds to the encoding given above. For instance, the beeswarm plot indicates that specimens loaded along columns are stronger than those loaded across. The case of 45° loading is rare and has negligible overall influence.

Besides the ranking and beeswarm plots, interaction effects are of interest for understanding ice mechanics as well as for material modeling. This is done with SHAP dependence plots (see Fig. 6.8 and [178]) which enrich traditional partial dependence plots described in [75]. Essentially, we are looking for secondary features, termed interaction features, which amplify or dampen the impact of the initial feature. Distinct vertical color patterns hint at possible interaction effects. Also, inflection points are feature values which, when passed, strongly decrease or increase the feature's impact.

The number of possible interactions is features × (features-1) × model, and hence high. Nonetheless, for freshwater ice, few clear interaction effects were found. Fig. 6.8a shows how a low triaxiality value, i.e., a high triaxial stress state, increases the prediction of strength. As expected, this is strongly linked with the type of test. For temperature, Fig. 6.8b shows a trend where values < -10 °C push the prediction toward higher strength, whereas between -10 °C to 0 °C the influence of temperature is relatively low. Using strain rate as a secondary feature does not reveal any clear pattern.

For strain rate as a main feature, Fig. 6.9a shows a global trend where the higher the

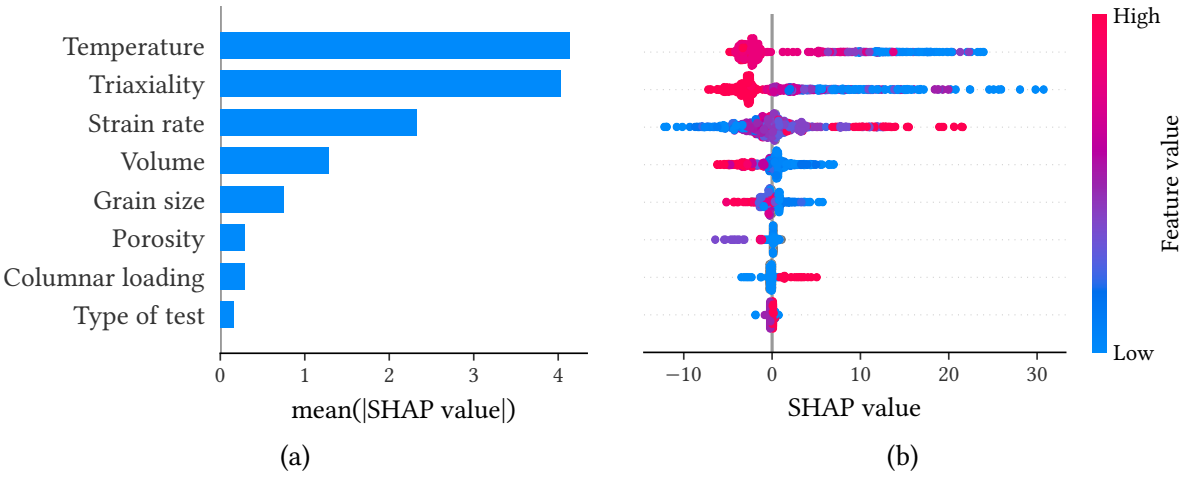

Fig. 6.7: Explanation of the ice strength prediction for the eight most impactful features for freshwater ice. (**a**) Average SHAP value indicating global feature importance. (**b**) Local explanation with beeswarm plots, vertical feature order is the same in both figures. Each dot is one observation, its color corresponds to its feature value. The dot's position on the horizontal axis shows the impact the feature has on the model output for that observation. Multiple observations with similar impact pile up to indicate density.

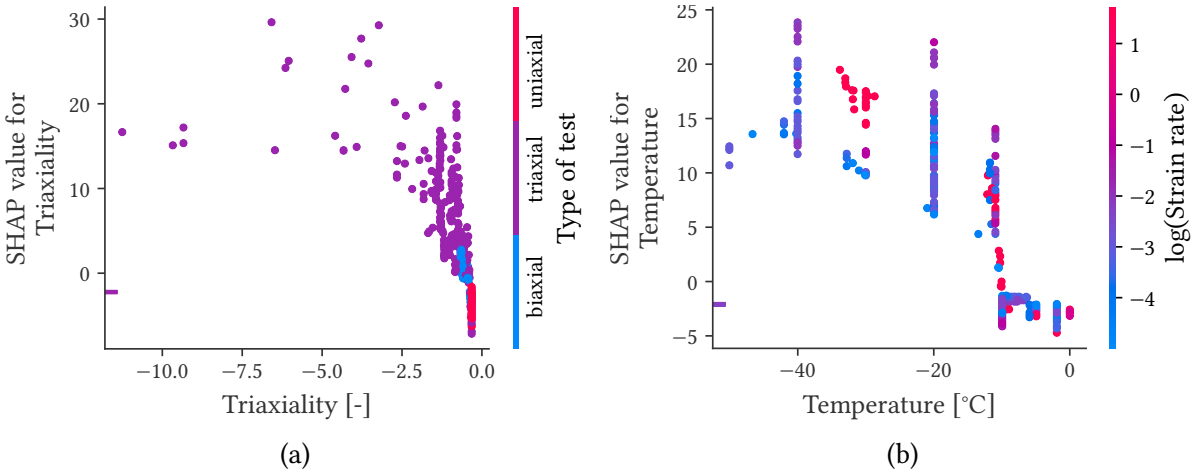

Fig. 6.8: Selected SHAP dependence plots for freshwater ice strength. Each dot is one observation, its feature value given on the horizontal axis and its corresponding SHAP value on the vertical axis. Additionally, the dot's color corresponds to another feature that possibly interacts with the original one. Observations with a hyphen-marker close to the vertical axis indicate NaN feature values, which are nonetheless used by the tree-based models and where a SHAP value can be estimated by the explainer. (**a**) Triaxiality and interaction feature type of test, (**b**) strain rate and triaxiality.

strain rate the higher the SHAP values. Furthermore, there is a vertical pattern regarding the interaction feature of triaxiality, but the data is scattered. In some cases, a low triaxiality appears to amplify- and in others to dampen the effect of strain rate. A clearer picture is presented with the strain rate partial dependence plot in Fig. 6.9b: It shows the marginal effect strain rate has on the predicted model outcome, cf. [75, 192]. In other words, it gives the average model output if all data points are forced to assume a prescribed strain rate. Specifically, from 10^{-5} s^{-1} to $10^{2.5}$ s^{-1} strain rate mostly increases strength though for about 10^{-3} s^{-1}, where most observations lie, the relationship mirrors the scatter shown in Fig. 6.9a. Outside of 10^{-5} s^{-1} to $10^{2.5}$ s^{-1} there are few observations so though the trend in Fig. 6.9a makes sense, more data is needed.

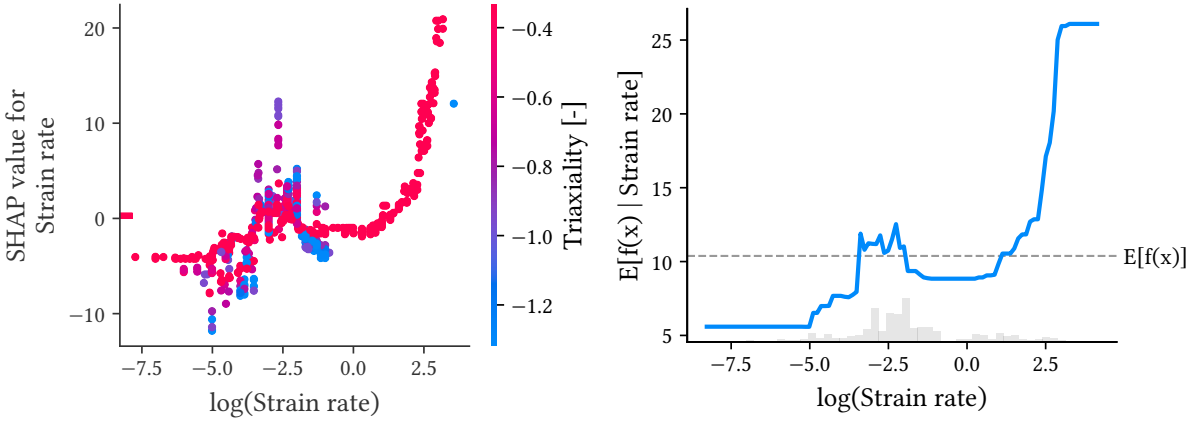

Fig. 6.9: Dependence plots for freshwater ice strength. (**a**) Same plot type as in Fig. 6.8 but for strain rate and triaxiality. (**b**) Partial dependence plot for strain rate, vertical axis is expected value given the strain rate, grey horizontal line represents expected value of the model $E[f(\boldsymbol{x})]$ (see Sect. 5.2) applied to the dataset, blue line is the average value of model output when strain rate is prescribed and varied, grey bars on horizontal axis are a histogram of logarithmized strain rate values.

Saltwater ice

For saltwater ice, the ranking is given in Fig. 6.10a. Average SHAP values are all less than 1 MPa which is low compared to freshwater ice, even considering the overall range of possible strength values (0 MPa to 60 MPa). Nonetheless the maximum (local) SHAP values are also lower, i.e., about 15 MPa for saltwater ice compared to 30 MPa for freshwater ice. The influence of features on saltwater ice strength is distributed more evenly over more features.

The beeswarm plots (Fig. 6.10b) show a picture similar to the one for freshwater ice but there are some differences. Type of ice for example has a negative impact for ridge ice and a positive impact for columnar ice. Porosity has a small impact albeit with a clear trend: Higher porosity decreases strength. For volume and salinity, there are no clear trends. In

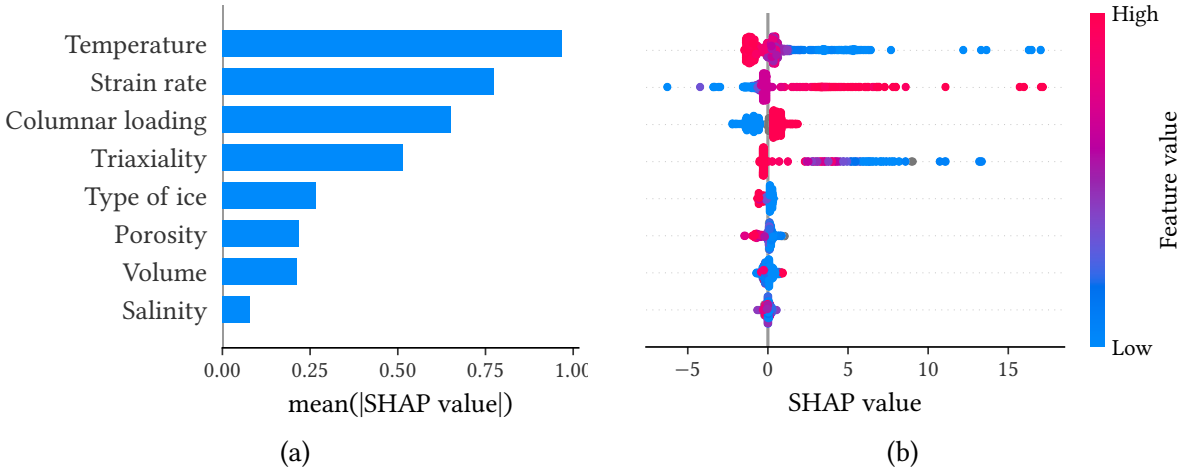

Fig. 6.10: Explanation of the ice strength prediction for the eight most impactful features for saltwater ice. (**a**) Average SHAP value indicating global feature importance. (**b**) Local explanation with beeswarm plots.

most cases, the beeswarm plots are asymmetrical, i.e., there is a tendency toward positive impact on strength, but almost no trend toward lower strength.

Selected SHAP dependence plots for saltwater ice strength are given ins Fig. 6.11. Overall, there were few clear interaction effects. Fig. 6.11a for instance shows in more detail the basis of the columnar loading beeswarm plot in Fig. 6.10b: Along-column loading increases strength (positive SHAP values) and vice versa, for 45°-loading there are too few observations to make conclusions. In addition, there appears to be a vertical color pattern.

The triaxiality plot in Fig. 6.11b is similar to the one for freshwater ice. A lower triaxiality increases strength but this effect seems to plateau for values < -1. Again there is no clear color pattern except for a few outlier points.

Next, Fig. 6.11c depicts the impact of strain rate paired with test type. Below $10^{-3}\ \mathrm{s}^{-1}$, the impact of strain rate is almost zero, whereas above it increases with increasing strain rate. Furthermore, there is a branch of a few triaxial observations with high SHAP values. The last plot in Fig. 6.11d is an example of two correlating features, temperature and porosity. A higher temperature means a higher porosity but there is no clear vertical color pattern.

6.7.4 Discussion of results

Two aspects were studied, how well a machine learning (ML) model predicts compressive strength and how this prediction can be explained. In terms of performance, the ML model accurately predicts strength for a wide range of different tests including bi- and triaxial tests. The ML model is also accurate when predicting uniaxial strength only, though it would likely perform better still if only trained on uniaxial data. For rough estimates of uniaxial strength, the use of empirical formulas is an alternative. This is particularly true when considering their simplicity compared to running a (pre-trained) ML model. Nevertheless, if strength in tests is dominated by a feature that is not included in the empirical formulas, they risk

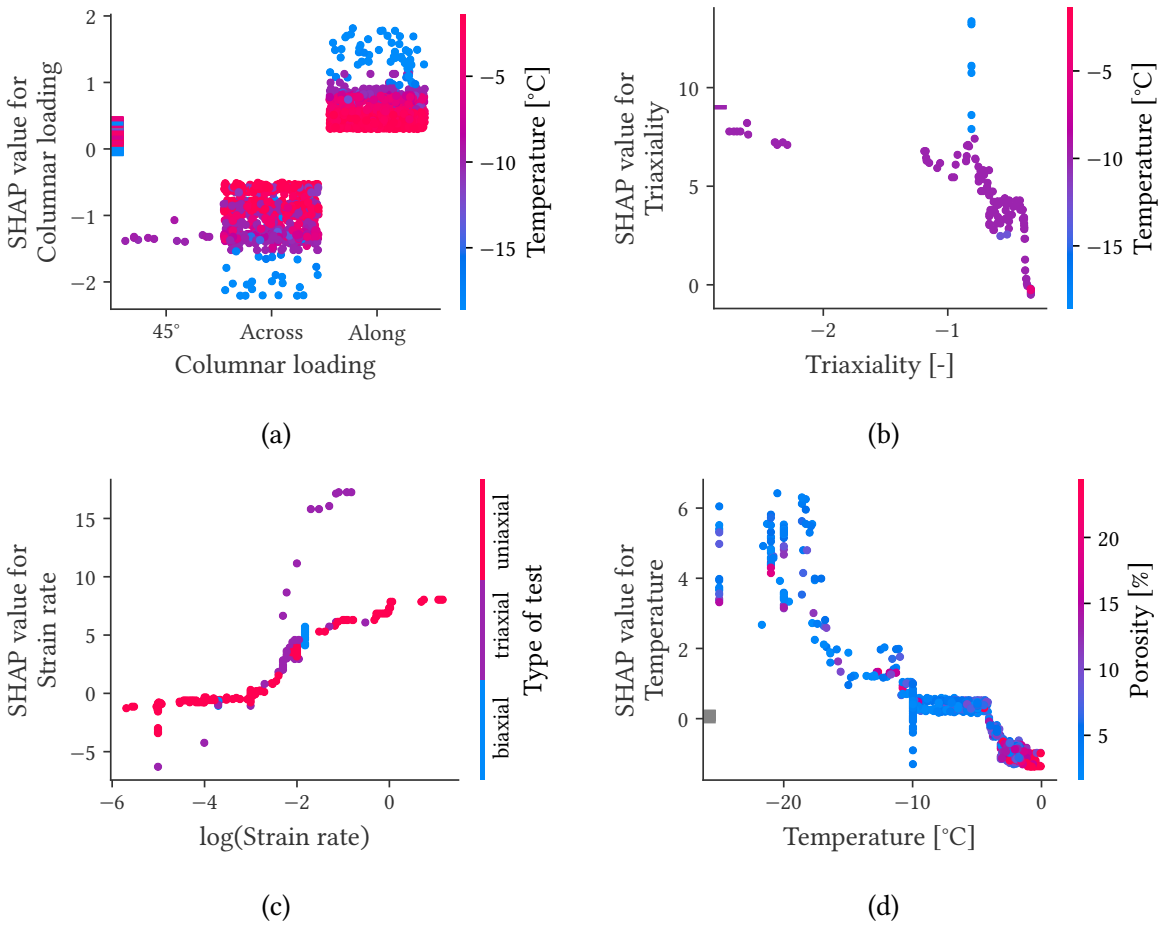

Fig. 6.11: Selected SHAP dependence plots for saltwater ice strength. (**a**) Columnar loading and temperature, (**b**) triaxiality and temperature, (**c**) strain rate and type of test, (**d**) temperature and porosity.

consistently giving inaccurate estimates. This is a likely cause for the horizontal scatter in Figs. 6.6a and 6.6c.

Overall, the explanation results are as expected. The rankings confirm influential features that have been documented in earlier studies. Dependence on single features are mostly in line with current ice mechanics theory and experimental studies. Similarity of mechanisms is expected between granular- and columnar ice, in particular when columnar ice is loaded across the columns [77, 193, 251], therefore specific effects of ice type are only discussed where necessary. Furthermore, not all effects are equally well-understood in both the ductile- and brittle regime. Hence this distinction cannot always be done. Below, the explanation results are linked to experimental studies and ice mechanics in more detail.

Freshwater ice

For freshwater ice, temperature, ranked first, influences strength through different mechanisms. Friction is temperature dependent and, in turn, influences compressive failure for instance through the wing-crack mechanism (see Fig. 3.3). This was discussed and also shown experimentally in, e.g., [215, 250, 251, 254] and [256, p. 24]. Furthermore, for brittle(-like) behavior, plastic faulting [90] is related to thermal softening which is expected to be influenced by temperature. In the ductile regime, temperature generally influences deformation processes, for an overview see [58].

The effect of bi- or triaxial stress on freshwater ice strength has been shown in experiments, e.g., in [191, 312]. It is related to the suppression of crack propagation, though this plays out differently in the ductile- and brittle regime and depending on the degree of confinement, see, e.g., [189, 254, 260].

Strain rate was ranked third place. Increasing strain rate is known to positively impact strength, though it has been suggested that this effect subsides at higher strain rates, see [137] and [256, p. 243]. Similarly to temperature, one likely reason is that strain rate influences sliding speed of crack faces which is critical to cracking processes. Nevertheless, the discussion on underlying mechanisms is ongoing, see, e.g., [41, 215, 254, 256].

Furthermore, the ML model explanation indicates a weak size effect where a small volume pushes the prediction toward higher strength values (Fig. 6.7b). A size effect for (quasi-)brittle materials under compression in general is discussed in [313]. For ice the existence of a size effect is an open-ended question, but so far there have only been few studies [256, p. 250]. At least in the ductile regime, specimen size does not appear to be a significant factor [158].

Grain size influences strength through stress concentration processes, see [251] or [256, p. 258-261], but here its impact is relatively small. In the ductile regime, grain size is not expected to have a visible effect for strain rates as low as $10^{-6}\ \mathrm{s}^{-1}$ [41, 246]. In [251] grain size was varied in the brittle regime with strain rates of $10^{-3}\ \mathrm{s}^{-1}$ and higher. A seven-fold increase in grain size from 1.1 mm to 7.3 mm reduced strength by about 30 %. A significant effect but comparably small in the context of the ML model and current input data, which explains the lower rank. Nevertheless, looking at full-scale scenarios, grain size can strongly vary within the same ice sheet, see, e.g., [326] or [209, p. 35]. Due to this a seven-fold change in grain size is more relevant than for instance a similar change in temperature.

The impact of the remaining features is negligible. That is not to say that from a mechanical

perspective these features are not important but it appears that the ML model did not attribute significant predictive power to these features. For columnar loading and porosity, the impact on saltwater ice strength is more pronounced and these effects are discussed below. For type of test, the impact is even smaller and the beeswarm plot is inconclusive. This feature is likely confounded with triaxiality but may have less predictive power since it contains only three categories whereas triaxiality is a continuous measure of stress state.

The beeswarm- (Fig. 6.7b) and dependence plots (Figs. 6.8a and 6.9b) reveal additional trends and inflection points. The influence of triaxiality (Fig. 6.8a) for values < -0.4 increases strongly but plateaus again for values < -2.5, which is similar to results of experimental studies, e.g., [138]. This is likely related to a change in failure mechanisms, see discussions by, e.g., [226, 227].

For temperature (Fig. 6.8b), the general trend is in line with studies where temperature was varied, e.g., [215, 251] and [256, p. 246]. The reason is that, as mentioned above, temperature is crucial to several mechanisms of ice deformation in both ductile and brittle regime [254, 256]. In addition, there is an inflection point where changing temperature has almost no impact between 0 °C to −10 °C. To the author's knowledge, there is no specific effect which suddenly dominates for temperatures < -10 °C, most effects come into play gradually.

Saltwater ice

Secondly, for saltwater ice strength, the top features and how they influence model outcome are also mostly in line with the literature. In general, similarity regarding fundamental mechanisms is expected between freshwater and saltwater ice [137, 246, 256, 258] and behavior during testing is often alike [157]. Therefore, below only those influential features specific to saltwater ice are discussed in more detail.

The effect of temperature, again ranked first place, has been shown in various experimental studies, e.g., in [157, 195, 326] and is confirmed by the data-based explanation. The influence of strain rate is for instance described in [157] and occurs in both the ductile and the brittle regime.

The impact of columnar loading, ranked third, is well-documented [133, 137, 195, 264, 294] and merits a closer look: The beeswarm plots show that along-columnar loading is linked to higher strength compared to across-columnar loading, which is in line with the literature and also the same for freshwater ice. For ductile behavior, this has been explained in terms of the basal planes on which crystallographic slip occurs [42, 157]. For ice loaded across the columns, there is always a high resolved shear stress on the basal planes of some grains (at least). For ice loaded along the columns, the shear stress resolved on to the slip planes is much smaller.

For brittle behavior, the majority of testing that emphasizes failure mechanisms in columnar ice has been done with across-column loading. In this case, the mechanisms are similar to those of granular ice [256, p. 246]. Hence, to the authors' knowledge, it remains to be clarified which effects lead to higher strength for ice loaded along columns and in the brittle regime.

Triaxiality, in fourth place, likely has similar effects as described above for freshwater ice. These effects have been studied experimentally in biaxial and triaxial tests on both columnar-

and granular ice, cf. [128, 293]. The next feature is type of ice, where granular and ridge ice (encoded as 1 and 2) slightly push the prediction toward lower strength. This is possibly a confounding variable whose underlying mechanism is similar as for columnar loading described above. The more 'granular' ice is, the less stiff it becomes, which generally reduces strength.

Porosity is ranked in sixth place. The corresponding beeswarm plot indicates that the higher the porosity, the lower the strength. Such behavior confirms existing studies, e.g., [326]. In sea ice, less porous ice is stiffer [256, p. 63]. Further studies, albeit for freshwater ice, show that fracture toughness increases with decreasing porosity [256, p. 201]. In the ductile regime, porosity is known to decrease strength whereas in the brittle regime, at least for values about 5 %, porosity has little impact on the strength [256, p. 249]. Yet in [306] both columnar and granular ice was tested in the brittle regime where columnar ice was slightly weakened by porosity but for granular ice there was no clear effect. Nonetheless, in both cases the data is scattered.

Next, the influence of other features as shown in the dependence plots (Figs. 6.11a to 6.11d) is mostly in line with expectations. A high temperature seems to override any effect of columnar loading (Fig. 6.11a) which is supported by the higher average impact of temperature (Fig. 6.10a). The overall trend for triaxiality is similar to the one for freshwater ice. The few observations with a high SHAP value and a low temperature belong to tests from the same laboratory [89, 90] which yielded relatively high strengths values of up to 47 MPa. This behavior might not be representative, but it hints at an amplification of strain rate by test type for triaxial tests. The trends regarding temperature, and strain rate are similar to those for freshwater ice discussed above.

To summarize, though material and testing data for freshwater and saltwater ice exhibit differences, the overall explanations are alike. This supports statements on the similarity of, e.g., failure mechanisms in columnar and granular ice as well as freshwater and saltwater ice. In all, the explanation model appears to agree with the literature.

6.8 Behavior prediction

6.8.1 Preliminaries

Only compression tests were analyzed and shear and tensile tests were excluded. Similarly to the strength model, a hyperparameter optimization was done but optimized parameters did not improve results. Hence the tree parameters were the same as for strength prediction with the exception of necessarily different performance metrics. Log-loss error was used as an early stopping metric and as a learning objective. As input data, there were 1820 saltwater and 1128 freshwater ice observations. Input features were: strain rate, temperature, grain size, porosity, triaxiality, volume, type of test, type of ice, columnar loading, and additionally for saltwater ice the salinity.

As for the strength prediction, the main results are presented for the tree-based machine learning (ML) model, hereafter simply termed 'model', if not stated otherwise. ANN-specific data scrubbing, model architecture, and results are presented in the Appendix, Sect. A.5.

Table 6.4: Performance of boosted tree behavior classification model

Metric	Freshwater ice	Saltwater ice
ACC CV average	0.98 ± 0.01	0.84 ± 0.03
ACC final model	0.99	0.87
MCC CV average	0.94 ± 0.04	0.62 ± 0.07
MCC final model	0.96	0.69

CV values are average ± SD, $n = 5$ (number of CV folds).
Final model values are for testing data.

Table 6.5: Performance of analytical behavior classification model

	Freshwater ice		Saltwater ice	
Metric	Fixed values	Estimated values	Fixed values	Estimated values
ACC	0.84	0.81	0.37	0.72
MCC	0.65	0.57	0.15	0.33

6.8.2 Performance and generalizability

First of all, the generalizability and model performance was evaluated. Table. 6.4 gives accuracy (ACC) and Matthews correlation coefficient (MCC) for the cross-validation (CV) and the final model. The performance during CV and the final model is similar, the standard deviation (SD) of the CV fold performance is small. This shows the generalizability of the model. Further insight is given by the confusion matrices in Fig. 6.12. The freshwater ice confusion matrix (Fig. 6.12a) confirms excellent performance on both classes. The saltwater ice confusion matrix (Fig. 6.12b) shows that most misclassifications occur when the model predicts ductile behavior when the true class is brittle. Due to this, the saltwater ice MCC is lower than the ACC (Table 6.4).

In all, the performance of the behavior model is very good, even for saltwater ice where much more variability in the data is expected due to its natural origin. The ML model also performed significantly better than a recently used single decision tree model [144]. Therefore the model predictions merit further analysis and explanation.

Before continuing with the explanation of the predictions, the performance of ML model and the analytical model described in Sect. 6.5.2 was compared. The analytical model's performance, given in Table 6.5, is acceptable for freshwater ice, but mediocre for saltwater ice. For freshwater ice, using estimated values worsens performance whereas for saltwater ice it is the opposite. Furthermore, for saltwater ice the MCC is low indicating the model does not perform equally well on both classes. Naturally, the choice of values for fixed parameters or the way they are estimated strongly influences results. Nonetheless, particularly in the case of freshwater ice, the analytical model may be used as a first estimate of transition strain rates.

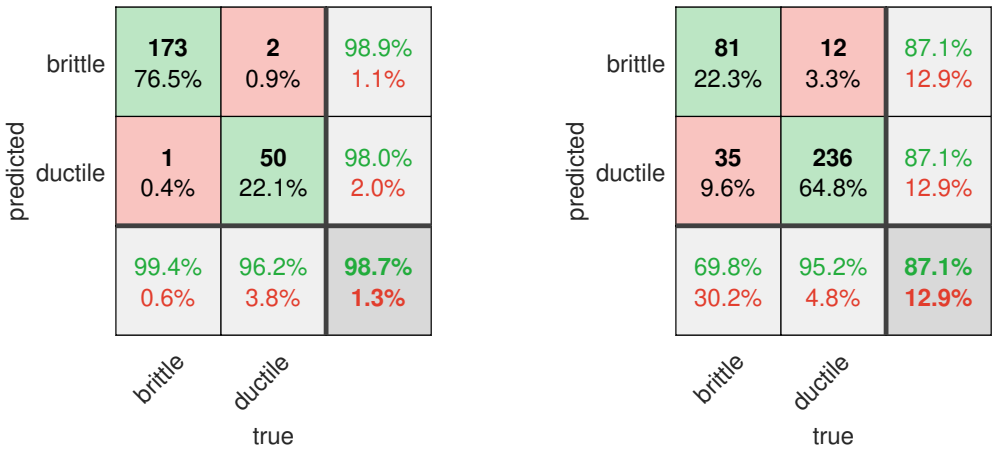

Fig. 6.12: Confusion matrices for (**a**) freshwater and (**b**) saltwater ice behavior prediction. Columns correspond to the true- and rows to the predicted class. Cells on the diagonal indicate correctly- and cells on the off-diagonal incorrectly classified observations.

6.8.3 Data-based explanation

Similarly to the ML strength model, the ML behavior model was not only created to predict behavior but also to deliver insight into the data and feature relations. This section presents the results from the SHAP explanation for the behavior prediction. As before, the explanation data set which is fed into the SHAP explanation model is the whole (cleaned) data. Though the model output is probability of ductile behavior, SHAP values are currently implemented to correspond to log-odds

$$\log\left(\frac{p}{1-p}\right) \tag{6.12}$$

with probability p of the observation belonging to class 1. Ductile behavior is binarized as class 1, brittle behavior as class 0, therefore Eq. (6.12) becomes

$$\log\left(\frac{p(\text{ductile behavior})}{p(\text{brittle behavior})}\right) \tag{6.13}$$

However, this does not change the interpretation of SHAP values as impact on model output as the transformation from probability to log-odds is monotonic, i.e., higher log-odds signify a higher probability of ductile behavior.

As before, for the beeswarm plots, encoded labels are necessary to understand impact. For freshwater ice, there are no categorical features that have a significant impact and their description is omitted. For saltwater ice, columnar loading is encoded as across $= 0$, and along $= 1$, 45° observations do not exist. Type of ice is encoded as columnar $= 0$ and ridge $= 1$, observations with granular ice are not present.

Freshwater ice

For freshwater ice, global and local feature impact is shown in Figs. 6.13a and 6.13b. Strain rate and triaxiality dominate, where high strain rates and high triaxiality values (in compression: low triaxial stress state, e.g., uniaxial tests) push the prediction toward brittle behavior (class 0). A low grain size correlates with ductile behavior and vice versa. For these three features the beeswarm plots indicate a more or less continuous impact. The last feature with some influence is volume, where a higher volume appears to slightly correlate with brittle behavior, but the impact is very small and the corresponding beeswarm plot exhibits no clear tendency.

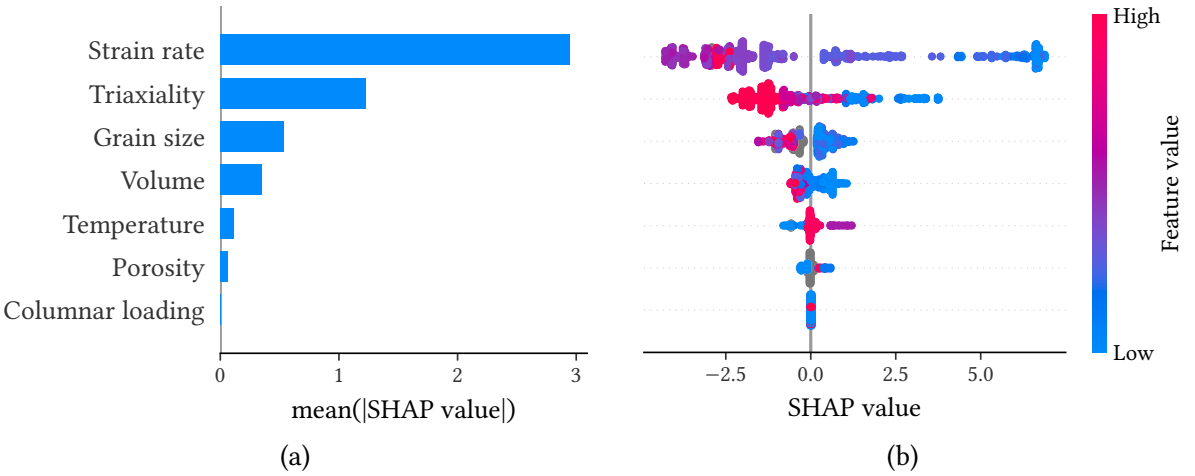

Fig. 6.13: Explanation of the freshwater ice behavior type prediction, (**a**) average SHAP value indicating global feature importance. (**b**) local explanation with beeswarm plots.

Again, possible interaction effects are visualized with dependence plots as explained in Sect. 6.7.3. For freshwater ice, there were no clear interaction effects. For grain size and triaxiality, the dependence plots did not give further insight compared to the beeswarm plots: A lower grain size and a lower triaxiality increases the probability of ductile behavior. For strain rate, Fig. 6.14a is a SHAP dependence plot as used before (e.g., Fig. 6.9a) which shows no clear interaction effect with triaxiality but a distinct overall trend of a S-shaped curve. This is further illustrated in the partial dependence plot in Fig. 6.14b. There appear to be two plateaus with respect to the influence of strain rate, however the histogram (grey bars) shows that the data beyond a strain rate range of 10^{-5} s^{-1} to 10^{-1} s^{-1} is scarce.

Saltwater ice

For saltwater ice, the ranking and beeswarm plots (Figs. 6.15a and 6.15b) indicate that there are more influential features with less influence per feature. This is similar to the saltwater ice strength ranking. The top features are temperature, columnar loading, and strain rate. A high temperature or a low strain rate pushes the prediction toward ductile behavior. The corresponding beeswarm plot shows a mostly continuous impact over the range of tempera-

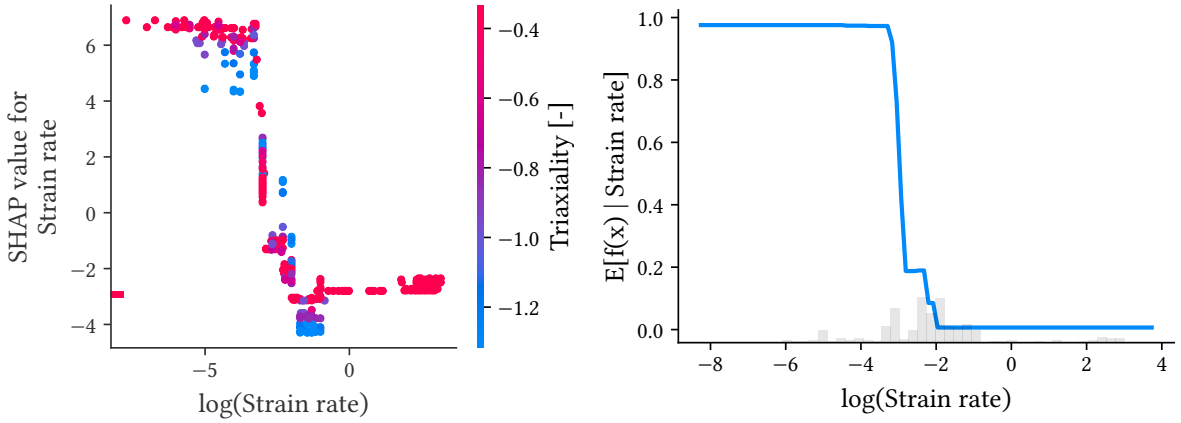

(a) (b)

Fig. 6.14: Dependence plots for freshwater ice behavior for strain rate. (**a**) SHAP dependence plot with secondary feature triaxiality and (**b**) partial dependence plot for strain rate, vertical axis is expected value or model output as a probability given the strain rate, blue line is the average value of model output when strain rate is prescribed and varied, grey bars on horizontal axis are a histogram of logarithmized strain rate values.

tures. For strain rate, the beeswarm plot indicates a high impact for a few observations with high strain rate values and a rather low impact for the majority of observations.

Regarding columnar loading, a high feature value (i.e., 1 for along-column) makes the model predict brittle behavior and vice versa. In this case, the beeswarm plot shows a distinct impact of each feature due to its categorical nature. A high porosity appears to make the specimen more ductile. Moreover, there seems to be a tendency for low salinity to correlate with ductile behavior but there is no clear trend. For type of ice, ridge ice (encoded as 1) pushes the prediction toward ductile behavior. Lastly, there is no clear tendency for the impact of volume.

Next, the emphasis is on possible interaction effects for saltwater ice behavior. Few clear interaction effects were found, which are all related to the categorical features type of ice and columnar loading. In Fig. 6.16, two possible interaction effects between ice type are shown via SHAP dependence plots. In Fig. 6.16a a low temperature apparently decreases the impact of ice type for columnar ice. There seems to be no interaction between temperature and ice type for ridge ice. Fig. A.7 in the Appendix indicates a similar effect for porosity. In Fig. 6.16b observations loaded across columns seem less influenced by ice type.

Two possible interaction effects with the columnar loading feature are given in Fig. 6.17. When loaded across columns, porosity does not interact, when loaded along columns, a higher porosity pushes the prediction toward ductile behavior or lowers the impact of the columnar loading feature, respectively (Fig. 6.17a). Regarding strain rate (Fig. 6.17b), there seems to be an interaction for across-column loading, where a higher strain rate pushes the prediction toward brittle behavior (i.e., lower log-odds). For along-column loading, there is no visible effect.

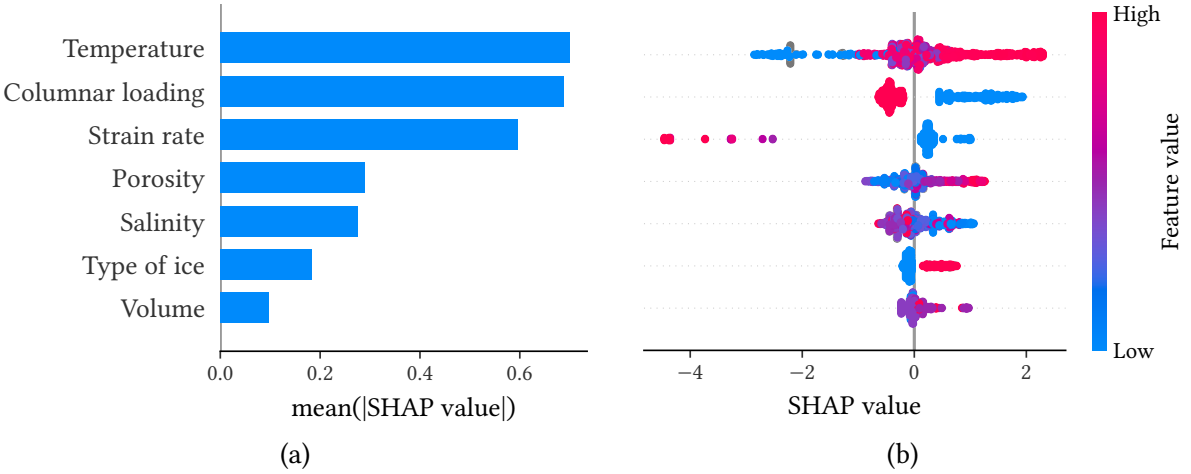

Fig. 6.15: Explanation of the saltwater ice behavior type prediction, (**a**) average SHAP value indicating global feature importance. (**b**) local explanation with beeswarm plots.

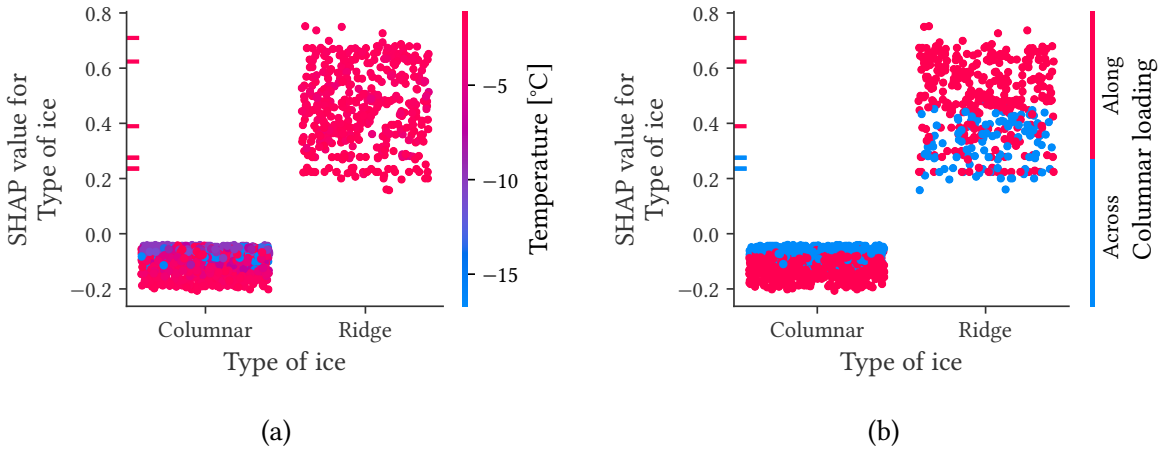

Fig. 6.16: SHAP dependence plots for saltwater ice behavior for type of ice and (**a**) temperature, and (**b**) columnar loading.

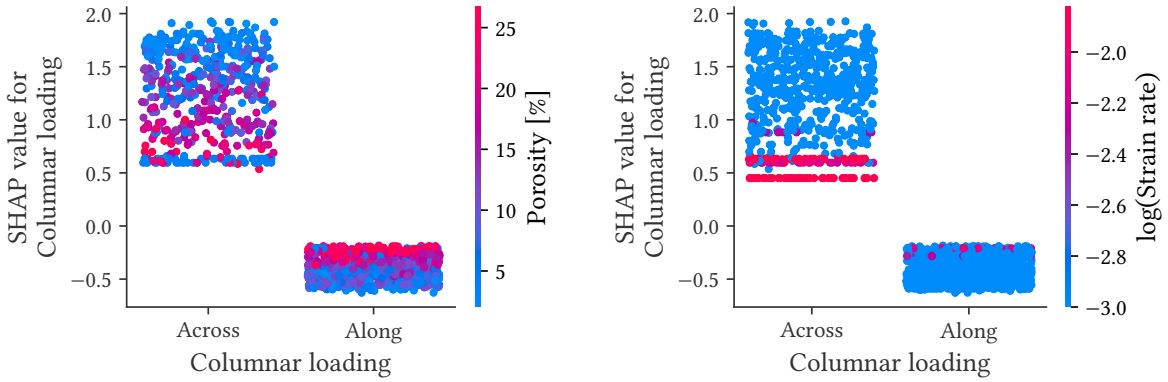

(a) (b)

Fig. 6.17: SHAP dependence plots for saltwater ice behavior for columnar loading and (**a**) porosity, and (**b**) strain rate.

An example where two features correlate but not necessarily interact is given in the plots in Fig. 6.18b. The SHAP dependence plot (Fig. 6.18a) indicates no distinct vertical color pattern, but a horizontal one. This suggests that warm ice is often more porous but porosity cannot (physically) cause warmer ice. As before, the trend indicated in the partial dependence plot is most reliable where the histogram indicates a lot of observations. However, there is a clear trend toward ductile behavior with higher temperature as indicated in the ranking (Fig. 6.13).

Lastly, Fig. 6.19 shows two plots for strain rate, a SHAP dependence plot (Fig. 6.19a) and a partial dependence plot (Fig. 6.19b). The overall S-shape resembles the one for freshwater ice (Fig. 6.14). However, for saltwater ice the variability of strain rate values is very limited as the majority of tests is done at 10^{-3} s^{-1}. This is also reflected in the grey bars of the underlying histogram.

6.8.4 Discussion of results

In all, the ML model predicted behavior with remarkable accuracy for a range of tests. Even for saltwater ice the performance was good, though due to its mostly natural origin more variability is expected. Notably, the ML model had a lower performance for predictions on the subset of true brittle saltwater ice samples, but no clear reason was found for this.

For initial estimates about behavior or transition strain rates, respectively, the Renshaw-Schulson model may be used. However, once the ML model is trained, applying it to single observations is equally fast and straightforward.

Regarding the explanations, many results are as expected but other aspects are new or have been little discussed until now. Generally, the rankings and beeswarm plots confirm influential features that have been identified in experimental studies.

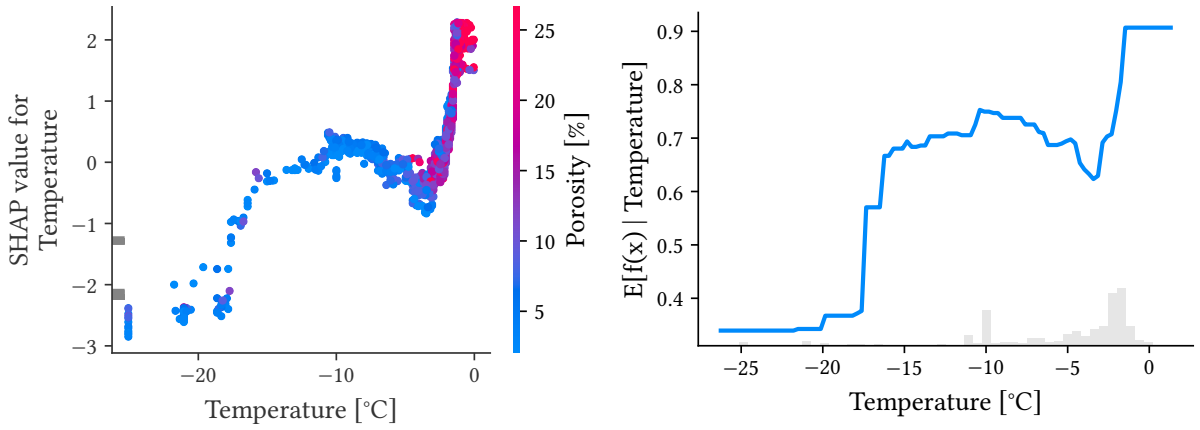

Fig. 6.18: Dependence plots for saltwater ice behavior for temperature. (**a**) SHAP dependence plot with secondary feature porosity and (**b**) partial dependence plot with underlying histogram of temperature values.

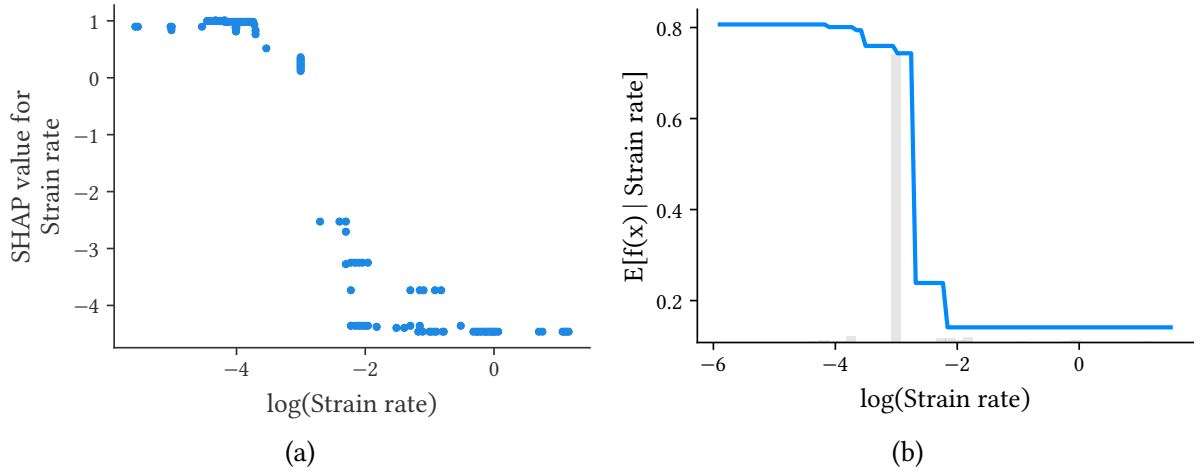

Fig. 6.19: Dependence plots for saltwater ice behavior for strain rate. (**a**) SHAP dependence plot and (**b**) partial dependence plot for strain rate with underlying histogram of strain rate values.

Freshwater ice

The freshwater ice behavior ranking and beeswarm plots (Figs. 6.13a and 6.13b) indicate four influential features. Unsurprisingly, strain rate leads the ranking as its impact is well-documented, e.g., in [242, 256, 297]. This can be understood in terms of the competing mechanisms of build-up and relaxation of stresses at favourably oriented cracks. At high strain rates, stress build-up dominates and vice versa [254, 260]. The SHAP values further confirm that observations predicted to be ductile exhibit strain rates lower than $10^{-3}\,\mathrm{s}^{-1}$ and vice versa for observations predicted to be brittle. This is in line with commonly given transition strain rates around $10^{-4}\,\mathrm{s}^{-1}$ to $10^{-3}\,\mathrm{s}^{-1}$ at $-10\,°\mathrm{C}$, see, e.g., [254, 277]. Furthermore, the strain rate dependence plots (Fig. 6.14a) also show a steep slope around this value. On the other hand, the underlying histogram of strain rate values shows that likely more data is necessary to confirm the S-shaped curve.

Along a similar line of reasoning, triaxiality influences behavior: The more compressive triaxial stress, the more crack propagation is suppressed and ice tends toward ductile behavior [251, 260].

The influence of grain size, ranked in third place, on material behavior is described in detail in [12, 40, 41]. An overview is given in [42]. Briefly, the coarser the grains, the lower the strain rate at which the material undergoes the transition to brittle behavior. This is exactly what is seen in the strain rate beeswarm plot.

The impact of volume is inconclusive, similar to results of an earlier study [144]. To date, the influence of volume on ductile or brittle behavior remains to be elucidated [256, p. 329]. In any case, the effect is small and more data is needed for further insight.

Temperature, ranked fifth, barely influences the behavior. A temperature effect on the ductile-to-brittle transition has been discussed in e.g. [226] or [256, p. 328]. Typically, a higher temperature is expected to result in more ductile behavior. Nonetheless [220, 254] stated that there is almost no change in transition strain rate with temperature for temperatures above $-20\,°\mathrm{C}$, and there are few observations with a temperature below this threshold. Hence it makes sense that the ML model attributes less predictive power to this feature.

The last two features with any influence, porosity and columnar loading, are mostly investigated for saltwater ice and a discussion is postponed to the next section. Lastly, no clear interaction effects were found for freshwater ice. This shows that, from a data-based perspective, the used features act on their own. That is, the impact of one feature is not significantly amplified or dampened by a secondary feature.

Saltwater ice

The saltwater ice behavior ranking and beeswarm plots (Figs. 6.13a and 6.13b) give several influential features. Here, contrasting the freshwater ice ranking, temperature is highly influential. At first glance, this is unexpected, as the above-quoted study [220] included saltwater ice. However, sea ice exhibits greater thermal sensitivity due to the influence of temperature (and salinity) on porosity and brine volume. Also, its compliance is more temperature-sensitive [256, p. 62].

Moreover, temperature correlates with porosity (ranked fourth) which in turn tends to

cause ductile behavior [195]. Likely reasons are that pores lower the resistance to creep deformation [256, p. 25] and that if a crack can run longer before hitting a pore, termed 'crack arrest', the sample is more likely to behave brittle [123, 195]. This behavior is confirmed by the porosity feature, ranked fourth place, and the corresponding beeswarm plot.

Columnar loading was ranked second place. This matches experimental studies which indicated a relation between behavior (or transition strain rate) and columnar loading, e.g. [157, 189, 195, 264]. This is likely due to similar mechanisms that account for an increased strength for along-columnar loading (see discussion above). It is also possible that this is related to brine channels which tend to run in parallel to columns. Since propagating cracks deviate from straight paths into these channels, they appear to facilitate crack propagation, and, more generally, cracks preferably run perpendicular to the c-axis alignment direction [42]. If crack propagation is not impeded, the overall behavior is likely more brittle. Fig. 6.16b furthermore shows that the type of ice feature is less important when loading is across columns, that is, when in loading direction the ice can be seen as granular.

The effects of strain rate, ranked third place, are similar to those described above for freshwater ice. Various studies have shown and discussed strain rate effects for saltwater ice too [157, 255].

Salinity is in fifth place. Various properties are brine volume dependent [264], but the influence of salinity on behavior is mostly discussed in terms of porosity or brine pockets within the ice [256, pp. 62, 217, 224]. It is conceivable that inclusions, whether measured as porosity, brine volume, or salinity, play a similar role such that they arrest cracks and lead to more ductile behavior [195]. Also, a lower brine volume correlates with cold sea ice, which in turn has a tendency to behave more brittle [311].

In sixth place, type of ice influences behavior such that ridge ice behaves more ductile. Ridge ice is described in detail in [123, 124, 286]. It is more heterogeneous than level ice and typically consists of both columnar and granular ice. In [195] the horizontal samples (loaded across columns and hence more granular-like behavior) all failed in the ductile regime. Possibly, ridge ice behaves more like granular ice, and therefore has an overall tendency toward ductile behavior compared to columnar ice. This is supported by the SHAP dependence plots for type of ice (Fig. 6.16) where ridge ice seems to tend to more ductile behavior. Clearly, columnar ice can also be loaded across columns and show more granular-like behavior, but that information should already be taken into account by the ML model with the columnar-loading feature.

Finally, volume is the last feature with some average influence, but the corresponding beeswarm plot is inconclusive. In addition, as described above for freshwater ice, the influence of specimen volume on behavior is understudied. Hence linking this to a mechanical effect is currently not possible.

6.9 Discussion of data-based analysis

The data-based approach was done to see how a machine learning model predicts experimental results without access to physical laws. The idea was to gain further insight into ice mechanics and predict properties to support modeling processes such as developing constitu-

tive models. The preceding results and corresponding discussions in terms of ice mechanics show that the models delivered on these objectives. This section discusses the concept in general terms.

To begin with, there are various sources of error and uncertainty. From a machine learning (ML) model perspective, the error can be broken down into three parts: bias-, variance-, and irreducible error. The latter is introduced in the way a prediction problem is framed, it may be caused by variables that are influential but unknown. We cannot control it. Bias originates from erroneous assumptions by the learning algorithm. Since decision trees make almost no assumptions they are usually not susceptible to high bias. Variance originates from a high complexity. In single decision trees this can be an issue as splits closer to leaves are based on less and less observations. Yet the method used here is based on an ensemble of trees where each tree is pruned to control variance. [108, pp. 37 and 308]

Hence due to the choice of learning algorithm, these errors should have a reduced impact. Additionally, model performance was high and cross-validation was successful in all cases, indicating that the models generalize well and should not suffer from either high bias or high variance.

Furthermore, ML and explanation model results depend on the choice of algorithms. ANN-based models (see Appendix, Sect. A.5) were trained to assess the influence of this. Generally the ANN models gave the same influential features as those from the tree-based ones but the feature ranking was different. Likely reasons are that the input data for ANN models requires standardization, and that there are significant differences between the employed explanation models. Whereas the explainer for the tree-based models is exact, the one for the ANN models is not and its results exhibit variability.

Next, 'garbage in, garbage out' is especially true for ML models. As already indicated by the exploratory analysis (Sect. 6.4) two issues emerge time and again: Features that are biased toward certain values, i.e., a lack of variability, and features with a lot of missing data. In both cases the model might not generalize well to circumstances that are not reflected in the current training data. For instance, the explanation model might attribute more predictive power to temperature than to grain size, yet grain size is seldom measured or there is too small a range of included grain sizes to generate a pattern to learn from. In reality, grain size might be more important than temperature. Such issues can only be dealt with through either more and representative data or by closely examining how the data influences results and explanations.

Nonetheless, the majority of results are in line with experimental studies and ice mechanics theory. Therefore it is unlikely that global trends are misidentified by the ML models. Yet when it comes to quantifying the impact of single features, e.g. through partial dependence plots, the underlying distribution of feature values and how the original studies were made should be taken into account.

Lastly, the created ML models are based on correlation and not causal. Applying an explanation model on top does not change this. Due to this confounders can be an issue. Confounders are associated with an independent (input) variable, but also causally related to the dependent (output) variable. Hence confounders may erroneously make it seem that a causal relationship exists where it does not [325]. Relations based on confounders often only hold in narrow settings, i.e., the ML models risk to generalize badly. Here, a high performance

during cross-validation shows that this is probably not a significant issue. Nevertheless, ultimately this can only be checked by looking closely at ice mechanics phenomena that underlie the results of the ML and explanation model.

To conclude, the proposed concept works well, but error sources should be kept in mind. The ML models successfully identify pattern in the data and complement the slow classic process of *'hypothesis - experiments - derivation of laws'*. The ML models emulate multivariate input-output studies and enable an analysis of all features in parallel, something that cannot be done experimentally. The rankings add objectivity to the process of selecting influential features for further modeling. Beeswarm plots identify one-sided impacts of features which may also lead to simpler-to-formulate but valid modeling assumptions. For instance, temperature was shown to positively impact strength but rarely decreases it.

Regarding the impact of single features, experimental studies often give curves such as strength in dependence of grain size. Yet these are strictly speaking only valid for the conditions of a specific study and the overall notion that increasing strain rate increases strength remains qualitative and hazy. Partial dependence and SHAP plots are an alternative way to reflect and quantify the influence of single features with a distinct curve, which is valid over a whole range of tests. Such plots can possibly be used for validation of other models if there is no suitable experimental data available. Practically, if a model seeks to capture a temperature dependency over a range of uniaxial tests, various tests with different temperatures can be simulated and results compared to a partial dependence plot for temperature as generated by a ML model.

On the other hand, a direct transfer of results to other models, e.g. analytical or constitutive, is not straightforward. In some cases, predictions, explanations, and ice mechanics knowledge can be combined to generate unknown input for a model or base modeling decisions on a broader foundation. In other cases, the influence of one parameter, e.g. grain size, is linked to various micromechanical processes and does not reflect one phenomenon only. In other words, though grain size might not be influential, the grain structure is. Furthermore, the range of possible feature values influences the impact as quantified by the ML models. That is, though one feature might be more influential than another, this only captures reality if the range of values of these features is realistic. For example, a larger sample of very low-temperature observations likely increases the impact of temperature, which is correct for the given dataset. On the other hand, temperatures below $-50\,°C$ are seldom measured in sea ice, and for a smaller range of values the feature impact could be less.

Lastly, sometimes both experimental studies as well as the ML and explanation model output show a relationship, but there is no physical explanation for it. Consequently, modeling this relationship can only be done empirically. As a result, further insight into ice mechanics can be obtained but a transfer to other models is not an automatic consequence.

To conclude, the proposed concept is a useful extension of 'classic' approaches, but should not stand on its own. Linking the identified patterns to ice mechanics helps to improve our understanding of ice behavior. Within the ML-based approach, the influence of model, explainer, and data on the output merits further investigation. Overall, the objective of an improved understanding of ice mechanics through a data analysis with explainable machine learning was achieved. However, domain knowledge and testing remain key to advancing research in this area.

7 Numerical methods

The discussions in Ch. 2 and 3 together with the data analysis in Ch. 6 suggest that it is not necessary to model every known phenomenon or parameter dependency. This is particularly true when the model purpose is limited to a specific scenario or behavior. This chapter synthesizes the results of this discussion and maps them to numerical methods. This includes the choice and description of methods as well as a review of required parameters. Subsequently, Ch. 8 applies these methods to firstly determine the minimum volume for applying effective material models, secondly simulate small-scale experiments, and thirdly assess the scalability of the fracture model.

This chapter describes the (micro-)mechanical model of polycrystalline ice. Based on previous chapters, namely the review of ice mechanics and material models for ice-structure interaction (Chs. 2 and 3), the focus is on elastic-brittle behavior under low confinement.

In addition to the ice mechanics perspective, the data analysis of ice compression tests (Ch. 6) is put into the context of material modeling. This is discussed in Sect. 7.1.

Two submodels are established: one for polycrystal elasticity and geometry, and a fracture model. The aim of the elasticity model is to identify the length scale below which the assumption of homogeneous elasticity is violated, and, in doing so, how big the resulting error is. To achieve this, an elastic polycrystal micromechanical model is needed and described in Sect 3.2.

Fracture in ice is modeled with the Cohesive Zone Model. This is described in Sect. 7.4. The micromechanical elasticity model extends well to the fracture model when it comes to crack nucleation and propagation in ice. For higher strain rates the majority of cracks form on grain boundaries [87]. Moreover stress concentrations due to elastic anisotropy are taken into account naturally, though they probably do not significantly contribute to crack nucleation. In contrast, existing flaws and inclusions are expected to lead to crack nucleation [77].

Lastly, a central issue of laboratory testing is scaling the results to full-scale. Section 7.4.3 discusses how the Cohesive Zone Model behaves under scaling and presents a model for testing this.

7.1 Link to data-based analysis

Establishing a link between the data-based analysis and material modeling is not straightforward (see Sect. 6.9). Nonetheless, the results can be put into context of the chosen modeling approach, namely focusing on micromechanics and fracture. Below, the underlying assumption is that whatever drives compressive strength is important for the material model. Furthermore, since the focus is on brittle behavior, results for ductile failure and in general for

the behavior prediction are secondary.

To begin with, temperature does not significantly affect elastic properties of ice, but is strongly related to frictional and plastic faulting. This supports the focus on fracture modeling. However, current fracture models are far from achieving the level of detail required to for instance make a distinction between Coulombic- and Plastic faulting. Hence in this case the processes are mostly understood, but the transfer to modeling is limited by fracture models, and also to a lower degree by numerical limitations.

How triaxiality affects brittle failure is well-documented and can be analytically modeled as described in Sect. 6.5.2. This information is theoretically usable in a fracture model. The Cohesive Zone Model is a 2D model which knows no 3D stresses, but could numerically access that information from neighboring volume elements. This is currently not possible with the software I used[1] but generally conceivable, e.g., through subroutines. Due to this, the proposed material model should not be applied to tests where triaxial stresses dominate.

The influence of strain rate on brittle compressive strength is subject of ongoing discussion (Sect. 6.7.4). Therefore if this effect is to be included, this would currently be possible only through empirical- or phenomenological approaches. The same applies to the volume feature, where there is an impact but its origins remain unclear.

Next, columnar loading and type of ice are related to the micromechanical structure, e.g., through stress concentrations at grain boundaries. The information of grain size, however, was not very impactful according to the ranking, though grains influence crack initiation and propagation. Possibly, as long as grain-related effects are modelled per se, their size is not crucial. This is acknowledged by explicitly modeling grains and anisotropic elasticity. Using columnar-shaped grains or mixed type structures such as ridge ice is possible. Applying different distributions of grain sizes and shapes is conceivable but should have a lower priority. Moreover, using cohesive elements on the grain boundaries enables the incorporation of grain-boundary phenomena.

Porosity and salinity are connected to fracture effects such as crack arrest by pores or more generally stress concentrations. These effects could be part of a very detailed modeling or incorporated through, e.g., random deletion of elements [26]. Nonetheless, based on the ranking, these effects do not need be a priority in modeling. Finally, because there were few interaction effects, a focus on single features is mostly justified.

To summarize, the link from the data-based analysis to material modeling is not automatic. However, limits apply due to a lack of data, an incomplete physical understanding, and numerical limitations, and less due to the limitations of the machine learning approach (discussed in Sect. 6.9). The latter can in fact alleviate some of these limitations, but not circumvent them completely.

7.2 Randomly oriented crystal elasticity

In order to map the anisotropy of polycrystalline aggregates the stiffness tensor of each crystal, given in Eq. (3.7), needs to be rotated randomly. Here, random rotation means rotating

[1] As simulation software, the general purpose finite element program LS-Dyna was used.

about a random vector in a 3D unit sphere with a random angle. The former can be created with Marsaglia's method [182]: Two numbers v_1, v_2 are generated independently and uniform on $(-1, 1)$ until

$$s = v_1^2 + v_2^2 < 1 \tag{7.1}$$

is satisfied. Then the random unit vector is

$$\boldsymbol{a} = \begin{bmatrix} 2v_1\sqrt{1-s} \\ 2v_2\sqrt{1-s} \\ 1-2s \end{bmatrix} \tag{7.2}$$

With this method, all points are uniformly and randomly distributed on a unit sphere (and vectors of length one) as shown in Fig. 7.1. Though it may not be the most efficient method, its implementation is straightforward and since only one random vector per grain is needed, the overall number of random vectors is relatively small. The angle is a uniform random number $0° \leq \theta < 180°$.

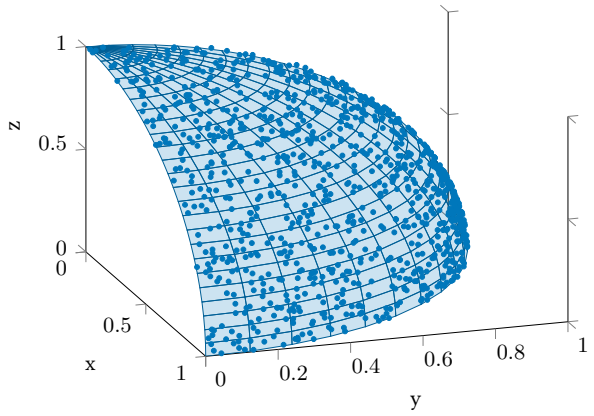

Fig. 7.1: Points on a sphere generated with Marsaglia's method [182] shown along with the surface of a unit sphere, only points on one eighth of the sphere with $x, y, z \geq 0$ are shown.

For transversely isotropic columnar ice, a rotation of the c-axis in the plane of isotropy can be done by rotating about for example the $\boldsymbol{x}_1$-axis with

$$\boldsymbol{Q}_{\boldsymbol{x}} = \begin{bmatrix} 1 & 0 & 0 \\ 0 & \cos\theta & -\sin\theta \\ 0 & \sin\theta & \cos\theta \end{bmatrix} \tag{7.3}$$

A general rotation about an arbitrary vector $\boldsymbol{a}$ can be done with the Euler-Rodrigues formula

$$\boldsymbol{Q}_{\boldsymbol{a}} = \boldsymbol{I} + \sin\theta \boldsymbol{A}_{\boldsymbol{a}} + (1-\cos\theta)\boldsymbol{A}_{\boldsymbol{a}}\boldsymbol{A}_{\boldsymbol{a}} \tag{7.4}$$

with the identity matrix $\boldsymbol{I}$ and

$$\boldsymbol{A}_{\boldsymbol{a}} = \begin{bmatrix} 0 & -a_3 & a_2 \\ a_3 & 0 & -a_1 \\ -a_2 & a_1 & 0 \end{bmatrix} \tag{7.5}$$

where a_i are the components of $\boldsymbol{a}$ [46]. The rotation matrices from Eqs. (7.3) and (7.4) are active rotations of a vector within a fixed coordinate system, as opposed to changing the coordinate system, see also [279].

Two possibilities to execute the rotation exist, one in Voigt notation[2] and one in tensor notation. For the former $\boldsymbol{Q}$ can be transformed to a rotation matrix for 6×6 stiffness tensors such as in Eq. (3.7) with

$$\boldsymbol{K} = \begin{bmatrix} Q_{11}^2 & Q_{12}^2 & Q_{13}^2 & 2Q_{12}Q_{13} & 2Q_{11}Q_{13} & 2Q_{11}Q_{12} \\ Q_{21}^2 & Q_{22}^2 & Q_{23}^2 & 2Q_{22}Q_{23} & 2Q_{21}Q_{23} & 2Q_{21}Q_{22} \\ Q_{31}^2 & Q_{32}^2 & Q_{33}^2 & 2Q_{32}Q_{33} & 2Q_{31}Q_{33} & 2Q_{31}Q_{32} \\ Q_{21}Q_{31} & Q_{22}Q_{32} & Q_{23}Q_{33} & Q_{22}Q_{33} + Q_{23}Q_{32} & Q_{21}Q_{33} + Q_{23}Q_{31} & Q_{21}Q_{32} + Q_{22}Q_{31} \\ Q_{11}Q_{31} & Q_{12}Q_{32} & Q_{13}Q_{33} & Q_{12}Q_{33} + Q_{13}Q_{32} & Q_{11}Q_{33} + Q_{13}Q_{31} & Q_{11}Q_{32} + Q_{12}Q_{31} \\ Q_{11}Q_{21} & Q_{12}Q_{22} & Q_{13}Q_{23} & Q_{12}Q_{23} + Q_{13}Q_{22} & Q_{11}Q_{23} + Q_{13}Q_{21} & Q_{11}Q_{22} + Q_{12}Q_{21} \end{bmatrix} \tag{7.6}$$

The rotation for stress and stiffness is

$$\boldsymbol{\sigma}^{(\theta)} = \boldsymbol{K}\boldsymbol{\sigma} \tag{7.7}$$

$$\boldsymbol{C}^{(\theta)} = \boldsymbol{K}\boldsymbol{C}\boldsymbol{K}^{\top} \tag{7.8}$$

with $\boldsymbol{C}^{(\theta)}$ being the rotated stiffness. The procedure for strains is the same, though with a different $\boldsymbol{K}$ as described in [274, pp. 87-91]. A rotation of stress and stiffness in tensor notation is

$$\sigma_{mn}^{(\theta)} = Q_{mi}Q_{nj}\sigma_{ij} \tag{7.9}$$

$$C_{mnop}^{(\theta)} = Q_{mi}Q_{nj}Q_{ok}Q_{pl}C_{ijkl} \tag{7.10}$$

see, e.g., [305].

Lastly, a rotation (7.10) does not change the principal invariants, which can be derived from the eigenvalue problem

$$(\mathcal{C} - \lambda\mathcal{I}) : \boldsymbol{M} = \boldsymbol{0} \tag{7.11}$$

with the fourth-order identity tensor

$$\mathcal{I}_{ijkl} = \delta_{ik}\delta_{jl} \tag{7.12}$$

and the second-order eigentensor $\boldsymbol{M}$. Examples of invariants are

$$\boldsymbol{I}_{\mathcal{C}} = \operatorname{tr}\mathcal{C} \tag{7.13}$$

$$\boldsymbol{II}_{\mathcal{C}} = -\frac{1}{2}\left(\operatorname{tr}\mathcal{C}^2 - (\operatorname{tr}\mathcal{C})^2\right) \tag{7.14}$$

$$\boldsymbol{III}_{\mathcal{C}} = \frac{1}{3}\left(\operatorname{tr}\mathcal{C}^3 - \frac{3}{2}\operatorname{tr}\mathcal{C}^2\operatorname{tr}\mathcal{C} + \frac{1}{2}(\operatorname{tr}\mathcal{C})^3\right) \tag{7.15}$$

[2] For Eq. 7.6 to work, the ordering must be as in Eq. 3.6. If this is not the case, either a different matrix $\boldsymbol{K}$ has to be used or the ordering has to be switched before and after rotation. See Appendix, Sect. A.2.

The trace and power of a fourth order tensor are

$$\operatorname{tr} \mathcal{C} = C_{klmn} C_{klmn} \tag{7.16}$$

$$\mathcal{C}^n = \underbrace{\mathcal{C} : \mathcal{C} : \cdots : \mathcal{C}}_{n} \tag{7.17}$$

where $\mathcal{C}^0 = \mathcal{I}$ and $\mathcal{C}^1 = \mathcal{C}$. The double contraction is

$$\mathcal{C} : \mathcal{C} = C_{ijmn} C_{mnkl} \tag{7.18}$$

For a full list of invariants and definitions see, e.g., [131]. The correctness of the rotation can be checked by comparing Eqs. (7.13) to (7.15) for $\mathcal{C}$ and $\mathcal{C}^{(\theta)}$.

7.3 Generation of artificial polycrystal morphology

A second modeling task besides the constitutive behavior is the geometry, e.g., the distribution and shape of the grains. Generally, three methods exist: (i) experimental reconstruction of the microstructure, (ii) physics-based simulation of the formation process, and (iii) geometry-based methods that focus on the morphology and ignore the physics behind the formation process. The first approach requires tremendous effort and is not feasible since homogenization is based on the creation of multiple models. In contrast, physics-based methods can be automated and are able to reproduce valid geometries. Nonetheless, they are more demanding than the third option of artificial creation; the geometry-based methods. Among them, many state-of-the-art methods are based on Voronoi/Laguerre tessellations. These generate geometries with properties that are very similar to actual polycrystals, the computational effort is acceptable, and they can also be automated. [10]

Here, a geometry-based method based on Laguerre tessellation was used due to its efficiency and flexibility regarding input parameters such as the grain size distribution. The algorithm is included in the open-source package Neper. For a detailed description of the algorithm see [221], and for tessellations in general [10] and references therein.

Polycrystalline morphologies are described with average and distribution of grain sizes and sphericity. Grain size is commonly measured with the equivalent diameter d. It is calculated by equating the true grain size with a circle or sphere as

$$d = 2 \left(\frac{3}{4\pi} v \right)^{\frac{1}{3}} \tag{7.19}$$

$$d = 2 \left(\frac{1}{\pi} a \right)^{\frac{1}{2}} \tag{7.20}$$

with d the equivalent grain diameter, and v or a the volume and area of the polyhedron or polygon, respectively. For ice experiments, typically only average grain diameters are given, measured with different methods [40]. Distributions of grain sizes are rarely recorded. One

exception is [140] who fitted a Weibull cumulative distribution function to sizes measured from 50 grains in the cross-sectional area of columnar sea ice:

$$F(d; k, \lambda) = 1 - \exp\left(-\left(\frac{d}{\lambda}\right)^k\right) \tag{7.21}$$

with d in mm, shape parameter $k = 3.323$ and scale parameter $\lambda = 9\,\text{mm}$. They give $16\,450\,\text{m}^{-2}$ grains per unit area, which with Eq. (7.20) yields a relatively high average (cross-sectional) column diameter $\bar{d}$ of 8.8 mm. All considered, this may not compare well to lab-grown granular freshwater ice.

On the other hand, grain sizes in polar ice are often log-normally distributed [237], as is the case for metals and other polycrystalline materials [221, 266]. Furthermore, the Weibull distribution given by [140] resembles the shape of a log-normal distribution. All considered, a log-normal distribution is chosen with the probability density function

$$f(d; \sigma, \mu) = \frac{1}{d\sigma\sqrt{2\pi}} \exp\left(-\frac{(\ln(d) - \mu)^2}{2\sigma^2}\right) \tag{7.22}$$

with d in mm, μ and σ the expected value (mean) and standard deviation of the logarithmized grain sizes [72, p. 131]. These are related to the mean $\bar{d}$ and standard deviation σ_d of the non-logarithmized grain sizes as given by [151, p. 117] through

$$\mu_X = \exp\left(\mu + \frac{1}{2}\sigma^2\right) \tag{7.23}$$

$$\sigma_X^2 = \left(\exp\left(\sigma^2\right) - 1\right) \exp\left(2\mu + \sigma^2\right) \tag{7.24}$$

with $\mu_X = \bar{d}$ and $\sigma_X = \sigma_d$. The values for $\bar{d}$ and σ_d are chosen depending on the model, see also Chapter 8. Fig. 7.2 exemplarily compares the desired and resulting probability density for grain sizes for a morphology created with Neper.

Secondly, the sphericity s is the ratio between the surface area of the sphere of equivalent volume and the surface area of the polyhedron. In 2D, the circularity is the ratio between the perimeter of a circle of equivalent area and the perimeter of the polygon. It takes a maximum value of one for a spherical grain [221]. To the author's knowledge, there is no research on sphericity for ice, hence for $1 - s$ a log-normal distribution with $\mu_X = 0.145$ and $\sigma_X = 0.03$ for 3D and for the circularity $\mu_X = 0.1$ and $\sigma_X = 0.03$ were used (Eqs. (7.22) to (7.24)), which are values for an alloy from [280].

7.4 Fracture modeling in polycrystals

As discussed in Sect. 3.3, the modeling of fracture in ice is key to simulating brittle behavior and obtaining forces and pressures. Since macrocracking is a strongly localized phenomenon, crack initiation and propagation requires explicit modeling. That also means homogenization is not possible within practical scales. Here, the Cohesive Zone Model (CZM) is chosen based on the discussion in Sect. 7.4.1. The model itself is depicted and discussed in Sect. 7.4.2. Subsequently, Sect. 7.4.3 treats size effect modeling with the CZM.

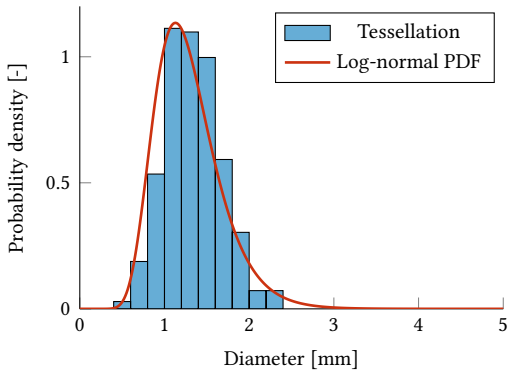

Fig. 7.2: Comparison of log-normal PDF and a probability density histogram based on tessellation data for grain size for a cube of 0.008 m edge length with 346 grains. The histogram was created with Matlab's 'auto' binning algorithm.

7.4.1 Choice of fracture model

Various methods exist to simulate crack initiation and propagation with discrete models, i.e., incorporating a separation of crack faces. However, simulating multiple arbitrary fracture paths with acceptable computational effort is a challenge and an ongoing area of research [223]. The XFEM for example has the potential to deal with arbitrary crack paths, see, e.g., [176], but it is difficult to apply to multiple fracture and fragmentation [233]. The phase field method has been successfully used to model fracture in a range of applications, but does not explicitly handle discontinuities [2]. Fragmentation or crack faces can only be represented during postprocessing by hiding highly damaged areas to show cracks, as, e.g., done in [80]. Fracture is predicted but not modeled explicitly.

Alternatively, discontinuous particle-based methods are used, e.g., Smoothed Particle Hydrodynamics (SPH) or the Distinct Element Method (DEM). With these meshfree methods, capturing arbitrary crack propagation is straightforward. Nevertheless, drawbacks are for example high computational cost and difficulties in implementing boundary conditions in the case of SPH. Additionally, due to the completely different way of representing material compared to continuum approaches, calibration and parameter identification is often comparatively difficult [66, 170]. For a more complete review of particle-based methods see [166].

Here, the Cohesive Zone Model (CZM) was used for several reasons, regarding both physical and numerical aspects: If the fracture process zone (FPZ, see also Sect. 3.3) is small, i.e., the assumption of small-scale yielding is valid, linear-elastic fracture mechanics concepts can be applied [175]. However, ice is a quasi-brittle material where this assumption does not generally hold, especially not for small specimens [18]. Therefore cohesive forces that exist in the FPZ should be considered by the model [31], which is intrinsically the case with the CZM. Due to this, the CZM has proven successful in modeling quasi-brittle materials [196]. Additionally, the CZM is easily incorporated in existing FEM models, for which the implementation of boundary conditions is straightforward. Consequently, the method is commonly used in several studies to model (quasi-)brittle fragmented fracture, e.g., in ceramics [223], metals [267], or composites [212], for an overview see [265]. In short, at least

for single-crack problems, CZM-based simulations are able to successfully reproduce experiments.

From a numerical perspective, the CZM is comparably robust and a good compromise between conceptual simplicity and efficiency on the one hand, particularly if potential crack paths can be defined a priori [233], and computational effort on the other hand [62]. Not least, the CZM is scalable regarding parallel computation [223], which is relevant for future full-scale applications. However, the CZM also comes with several drawbacks which are discussed in the next section.

7.4.2 Cohesive Zone Model

The Cohesive Zone Model (CZM) describes crack initiation and propagation. It models accumulated and localized damage as effective behavior ahead of the crack tip in the Fracture Process Zone (FPZ). In the process- or cohesive zone the crack is represented as a separation of two virtual surfaces (lines in 2D) resisted by traction between these surfaces. The traction is governed by a phenomenological traction-separation law (TSL) that can be thought of as a spring with a non-linear stiffness, see Fig. 7.3. It is a simple model, yet through different TSL it is able to generalize behavior in the cohesive zone for different types of material bonding [15]. The CZM is typically used in combination with the continuum technique termed finite-element-method (FEM), thus enhancing it with explicit fracture modeling.

Numerically, a rectangular cohesive element is an eight-noded, four-point element as schematically shown in Fig. 7.3, six-noded pentahedral elements are also possible. Tractions are evaluated on the mid-surface based on the differences of displacements between node-pairs on the top- and bottom surface. Two different approaches exist: An intrinsic CZM means the TSL has a finite initial stiffness or slope K_{coh}. Hence the cohesive element's response is reversible up to reaching the maximum traction Σ_0. Upon further separation the element is damaged and its response is irreversible. The initial stiffness is necessary to maintain momentum transfer and compatibility across elements. The reason is that cohesive elements already exist in the model prior to fracture. The extrinsic approach on the other hand assumes an initially rigid response which requires the dynamic insertion of cohesive elements during simulation [265]. Here, the intrinsic approach was used since it is already implemented in the FEM solver. Known issues with the CZM are discussed below with respect to brittle fracture in polycrystalline ice. How cohesive elements behave under scaling is discussed subsequently in Sect. 7.4.3.

To begin with, cracks can only propagate along cohesive elements. Due to this, cracks may follow paths that require more energy per unit crack extension than a crack with complete freedom of pathing [233]. Quasi-arbitrary crack pathing can be achieved by inserting cohesive elements along all interelement boundaries of solid elements, though trajectories will still depend on mesh type and element size [317]. Yet a large number of cohesive elements increases computational effort, exacerbates the problem of artificial compliance[3] and can cause numerical instabilities[4]. Moreover, realistic fracture paths are only obtained when the discretization resembles a disordered structure. Nevertheless, globally, the influence of

[3] Artificial compliance and its influence on, e.g., wave speed is discussed at length in [23, 24, 265, 289, 298].

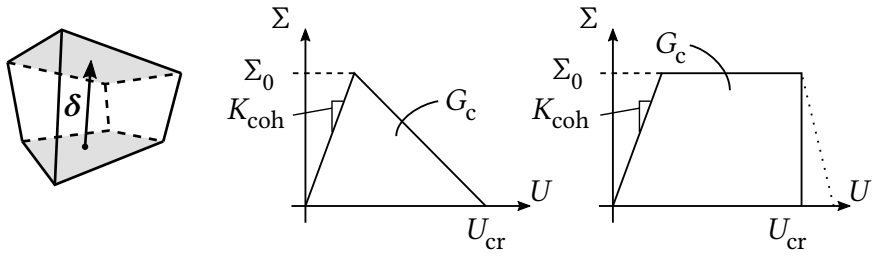

Fig. 7.3: Left: schematic drawing of separation process with separation vector $\boldsymbol{\delta}$. Middle: intrinsic linear softening law, i.e., a bilinear TSL, right: intrinsic rectangular softening law, dotted line is an alternative option for the descending branch. Σ_0 is the maximum traction, K_{coh} the initial stiffness, U_{cr} the critical separation, and G_{c} the fracture energy.

the discretization on the fracture path is expected to be less pronounced [292].

These issues are largely tackled with explicit modeling of a random, disordered microstructre and only considering intergranular cracks. In this thesis, the former is achieved with the generation of a artificial polycrystal morphology, see Sect. 7.3 and Fig. 8.4. The latter is a valid assumption for ice as discussed in Sect. 3.3. Inserting cohesive elements only on grain boundaries greatly reduces the number of elements required and mostly alleviates numerical issues. However, a true solution to artificial compliance has to overcome the violation of consistency and stability of the classic cohesive element formulations. Recently, discontinuous Galerkin approaches have been shown to achieve this [201, 223], but are not yet available in commercial codes.

Applying the CZM requires various parameter values. The TSL is assumed to be a material property, but it is identified on the lab-scale, the same curve does not necessarily coincide with the TSL that corresponds to full-scale behavior [53]. The TSL is commonly defined through the fracture energy G_{c}, the maximum traction σ and, in the case of intrinsic modeling, the initial stiffness K_{coh}, see Fig. 7.3, but the choice of TSL or cohesive model may introduce additional parameters. Usually, a different TSL is used for shear and normal separation of the virtual surfaces, thereby doubling the number of parameters. Furthermore, these parameters are connected to the above-mentioned numerical issues. For instance, a high K_{coh} is desirable to decrease artificial compliance, but this lowers time step size which is, among other aspects, controlled by the elastic modulus of the material [34]. Above all, a generic calibration procedure does not exist. Experimental determination of the TSL is highly difficult due to inherent difficulties in producing a single stable crack in brittle materials [62, 106], and often experimental studies are limited to mode I cracking, as, e.g., in [212]. This is exacerbated in sea ice due to viscoelastic and scale effects [52, 196, 197]. Consequently, parameters are either fitted to experimental results or identified by trial and error, see, e.g., [62, 96, 197, 212]. Ideally, a set of chosen parameters would be suitable for different experiments without a priori calibration to the experimental results.

With respect to the shape of the TSL, various options exist as, e.g., reviewed in [265,

[4] Personal experience from the author and colleagues with LS-Dyna. See [P3] and [P4] in Sec. 1.2.

pp. 359-365] and [211]. It has been argued that for brittle materials, the shape of TSL is more important than the maximum traction [31]. For describing progressive failure in brittle materials, linear softening laws are often used whereas for instance trapezoidal shapes resemble ductile failure [288, p. 233]. Also, bilinear cohesive laws appear to be better regarding artificial compliance [289]. Hence here, a bilinear TSL as described in [47] was used.

Another important aspect of fracture modeling is the fracture process zone (FPZ) size described in Sect. 3.3. Initially, three terms should be clarified. The true size of the FPZ is rarely known due to experimental difficulties in obtaining it. Its model equivalent is the (numerical) cohesive zone length, which is defined as the length along the crack over which cohesive elements lie on the softening part of their TSL, see Fig. 7.4. The terms FPZ and cohesive zone length will be used interchangeably and relate to numerical simulations if not stated otherwise. When the tensile stress along the crack reaches the maximum stress of the cohesive element, i.e., the peak of the TSL, the FPZ is termed 'fully developed'. Thirdly, a characteristic length is often introduced, which is a material property and typically of the form given in Eq. (3.10) and is generally different from measured fracture process zone sizes [101].

The stress distribution can have high gradients, that is, the stress along the crack can change abruptly, particularly close to the physical (traction-free) crack tip [145, 299]. In this regard, Fig. 7.4 is not accurate as the stress distribution is stretched horizontally for a better visualization. A 'sufficient' number of cohesive elements is needed in the cohesive zone to resolve this stress distribution. Firstly, this requires knowing the cohesive zone length. If this value is not known, the characteristic length (3.10) is commonly used as a substitute to estimate the required mesh density but was shown to overpredict the cohesive length [106]. Secondly, how many elements are sufficient is subject of ongoing research, suggestions range from two to ten elements [24, 299]. Additionally, at least for delamination problems, it is possible to lower the interface strength (maximum traction) to accommodate the same number of elements in the cohesive zone for a coarser mesh [106, 299].

To sum up, several issues require attention during the application of the CZM. The identification of parameter values of the cohesive model is closely related to numerical considerations. Many of the above-mentioned problems were so far mostly researched for single-crack mode I problems. Furthermore, a complete study including all dependencies of parameters, possible shapes of TSLs, and numerical issues would strongly increase the number of required simulations (or experiments). We can only treat specific aspects at a time and make reasonable assumptions for unsolved issues.

All considered, the CZM appears to be suitable for modeling multiple fracture and fragmentation in quasi-brittle materials such as ice. Therefore, in the present work, the emphasis is on the applicability of the CZM to multiple fracture in ice and not on an optimal set of parameters or highly accurate simulation results.

7.4.3 Cohesive zone size, splitting force and size effect

This section treats in more detail the links between specimen size, the forces required for crack propagation, and the cohesive zone size. The aim is to put the numerical study of the size effect and cohesive zone size in Sect. 8.4 in context. Because little is known about size

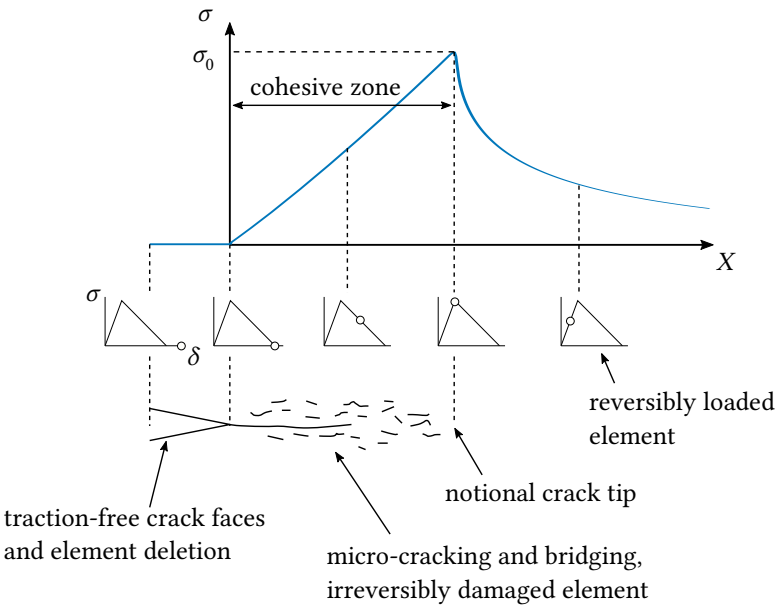

Fig. 7.4: Top: sketch of the stress σ along the crack at position X with cohesive zone size (fully developed FPZ). Middle: dot indicates current state of exemplary cohesive elements along the crack with respect to the TSL. Bottom: physical state of the material.

effects for ice in compression and under shear from the laboratory- to full-scale, the focus is on single tensile cracks as an initial step.

As described in Sect. 3.3, the small-scale yielding assumption is only valid for specimen sizes where the fracture process zone (FPZ), or cohesive zone, is much smaller than the geometry's characteristic length. Vice versa, the larger the FPZ size in comparison to the geometry, the more important the processes within the FPZ become. Since the Cohesive Zone Model (CZM) resolves these processes, albeit in a simplistic manner, it is theoretically applicable to all scales and it should be able to capture the size effect. This is important when simulating small-scale experiments such as the tensile splitting test and for the scaling of results from such experiments to full-scale. Moreover, ideally one set of CZM parameters is valid for different scales.

Generally, research on the CZM with focus on the size effect and the cohesive zone size is scarce. From numerical tests, e.g., [101], and analytical considerations [175], it es expected that the cohesive zone size increases with specimen geometry but converges to a constant value. For a single edge crack in an infinite plate, it was shown analytically that there is a limiting case as the plate size $L \to \infty$ [308]. For finite plates, the cohesive zone size has been unknown until recent studies by the author and colleagues [145]. For single edge notched bending tests and for compact tension tests it was shown that the cohesive zone size depends on the parameters of the traction separation law. Furthermore, for these two test types the converged value of the cohesive zone size was almost the same, hence it was suggested to be a intrinsic material property [101].

In theory, the same traction-separation law parameters should be applicable to different

sizes. In [102], experiments on the interfacial fracture between concrete and fiber reinforced polymer are described along with simulations based on the CZM. The fracture energy, calculated based on the experimental results, varied but values for different specimen sizes were similar. Parameters other than the fracture energy were fixed. The simulation results captured a size effect as predicted based on the work by Bažant [13]. Furthermore, from experimental studies on sea ice the fracture energy is expected to be size-independent [196].

Lastly, various mesh dependency studies have been done, but to the author's knowledge there has been no systematic research on the relations between the parameters, element size, and model size. Theoretically the element size is considered since the element-level equations are integrated over the area of the cohesive mid layer between the surfaces of the cohesive elements (grey areas in Fig. 7.3) [174, pp. 5-2 to 5-7]. Nonetheless, more research is needed.

7.4.4 Cohesive Zone Model parameters

The previous section illustrates the various dependencies between ice mechanics, testing possibilities, and numerical considerations. As mentioned, a complete study on all parameters and their impact is beyond the current work. However, some bounds on parameter values can be given based on the literature. This section gives an overview, the specific values used are stated in the corresponding numerical investigations chapter (Ch. 8).

Key parameters with respect to a bilinear traction-separation law (TSL) are tractions in tangential and normal direction, τ and σ, their ratio, and the fracture energy G_c. Some exemplary values are given in Tab. 7.1. The values for the maximum tractions vary, but all are in the order of 1 MPa. No definitive σ/τ-ratio has been identified for ice so far [96], but commonly $\sigma/\tau > 1$. The fracture energy G_c varies significantly, though within one test series it is expected to be size-independent [196]. Around 30 Pa m appears to be an upper bound, most values are between 3 Pa m and about 15 Pa m.

Several points account for the scatter in the given values: Some of the values were back-calculated, whereas others were identified by trial-and-error fits to experimental data. The back-calculation may additionally incorporate a viscoelasticity model. Furthermore, a range of testing or simulation setups is covered. Generally, all values are tentative pending additional research. In-depth discussion of features that influence the cohesive parameters during experiments are, e.g., given in [51, 52, 53].

Table 7.1: CZM model parameter values in the literature

Source	σ [MPa]	τ [MPa]	τ/σ [−]	G_c [Pa m]	Comment
[196, 197]	1.1	-	-	13.5	Tensile edge crack, $L = 0.5$ m, sea ice
[52]	0.5	-	-	15	Tensile edge crack, $L = 3 \ldots 80$ m, sea ice
[53]	2.5 4	-	-	17 31	Reversed-taper, freshwater ice, $L = 1.41$ m $L = 4.42$ m
[97]	0.12	0.14	1.167	3	Torsion and bending, L-shaped beam, sea- and freshwater ice
[95]	1.0	1.5	1.5	30	Bending, freshwater ice
[160]	0.85	0.91	1.07	30	Crushing, 2D, freshwater ice
[96]	0.4	1.5	3.75	30	Compression and tension, freshwater ice
	0.6	1.2	2	4	Values used in our research group from simulations of tensile splitting tests

8 Numerical investigations and applications

The hypothesis and objectives of this work evolve around models for simulations of small-scale tests and possible subsequent upscaling. To this end, the previously established numerical methods (Ch. 7) are finally used. Firstly, the scale-dependence of the polycrystal elasticity- and Cohesive Zone Model is investigated. The underlying question is at which scale the proposed numerical methods are appropriate and feasible, and whether they require adaption to different model sizes. Secondly, the models are applied to small-scale test setups. Ideally, the simulations should match the experiments without tweaking of model parameters. Qualitatively, the foremost aim is to reflect the expected ice behavior, e.g fracture patterns. Quantitatively, the models should reproduce the correct magnitude of, e.g, forces, but since the focus is not on calibration, obtaining exact results is secondary.

8.1 Minimum size of elastic RVE

An investigation of representative volume element (RVE) size that considers all possible dependencies described in Sect. 4.1 is beyond the scope of this work. Here, the aim is firstly to validate the modeling process described in Sect. 3.2, which is to be used to simulate experiments with specimens that are certainly too small for the use of RVE. The approach from statistical volume element (SVE) to RVE as a function of $\delta = \mathcal{L}^{RVE}/\mathcal{L}^{\mu}$ is evaluated. The expected result is a decrease in statistical scatter for repeated simulations with an increase of δ. The second aim is to confirm the RVE size in 2D as stated by Elvin [63] and estimate the RVE size in 3D for one set of boundary conditions and material properties.

Two cases are considered. First, the two-dimensional case based on [63], which corresponds to looking at a cross-section of columnar ice perpendicular to the columns and rotating the c-axes in plane with an angle $0° \leq \theta < 180°$. Secondly, a three-dimensional case, where c-axes are rotated about all axes. Generally, the homogenized isotropic elastic Young's modulus E^* and Poisson's ratio ν^* are computed for several cases and check convergence by looking at the spread of the homogenized properties.

The path from pre- to postprocessing is illustrated in Fig. 8.1. A polycrystal geometry is created with Neper and saved as a tessellation file (described in Sect. 7.3). The corresponding tessellation commands in Neper are given in the Appendix, Sect. A.10. Subsequently, a python script generates a tcl file that is executed in HyperMesh to reproduce the geometry based on faces. The faces are meshed with 2D elements, followed by a meshing of the thereby created closed volumes with 3D solid elements. Next, a simulation file is cre-

ated, which is manipulated with a python script to include one material model per grain (fewer are also possible) and additional information that is necessary to run the simulation (Sect. 7.2). The updated simulation file is passed to the simulation software LS-Dyna for solving. Lastly, several postprocessing files are combined to compute the apparent properties E^* and ν^* (Sect. 4.3). This process is repeated several times for every model size and number of grains, respectively.

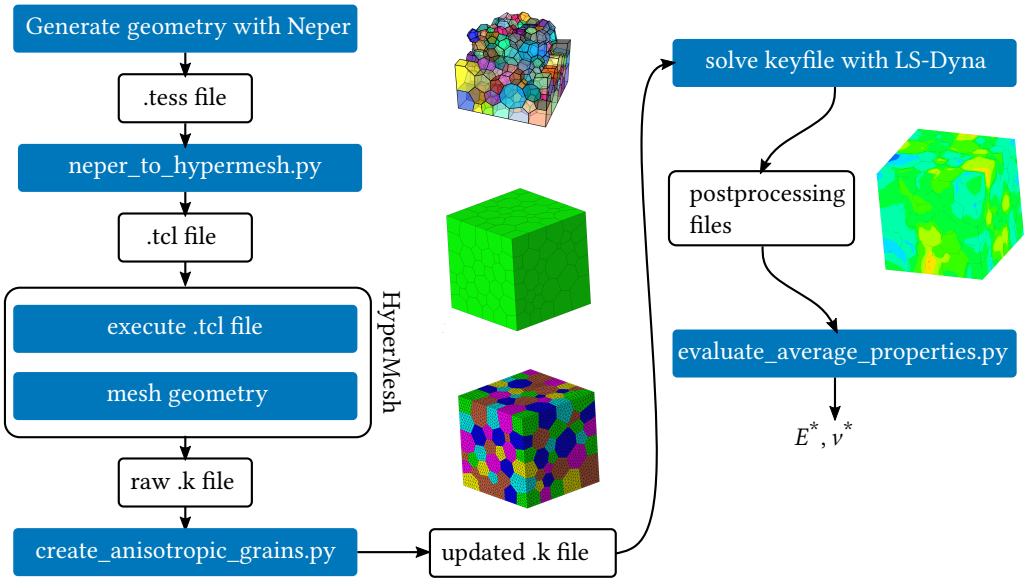

Fig. 8.1: General path from pre- to postprocessing of polycrystal models with randomly orientated elasticity tensors per grain.

8.1.1 RVE size in 2D

As an initial validation of the anisotropic elasticity model, the minimum RVE size in 2D for a polycrystal was analyzed with a quasi-2D model. That is, the model was discretized with solid elements, where the depth t consists of only few layers of elements. The aim was to compare this to the work by Elvin from 1996, who numerically determined the number of grains required for homogeneous elastic behavior of transversely isotropic columnar ice [63].

Preliminaries

Elvin assumed plane stress in the plane of isotropy, which is a cross-section perpendicular to the columns. Displacements were prescribed on two opposite sides, one moving and one fixed in x_3-direction, to create a uniaxial stress state (Fig. 8.2). Nodes at $(x_1, x_2, 0)$ were also fixed in x_2-direction to suppress any rigid body movement. On the remaining sides neither displacements nor tractions[1] were prescribed with the exception of one fully fixed node at $(0, 0, 0)$ to suppress the model from shifting. In the framework of boundary conditions (BC) for RVEs, these are considered mixed type, see [240] or example in [205]. Periodic BC were

not used since ice is a random medium as opposed to periodic, and this type of BC is not expected to be worth the additional modeling effort [245]. Lastly, it is assumed that grain interfaces are ideal, i.e., perfect bonding as defined in [204].

Elvin determined average properties based on forces and displacements on the boundaries. With respect to the coordinate system in Fig. 8.2 the homogenized constants are defined as

$$E^* = \frac{\bar{\Sigma}_3}{\bar{\varepsilon}_3} \quad \text{and} \quad \nu^* = -\frac{\bar{\varepsilon}_2}{\bar{\varepsilon}_3} \tag{8.1}$$

with the average normal stress component in x_3-direction

$$\bar{\Sigma}_3 = \int_A \frac{F_3(x_3 = h)}{wt} \mathrm{d}A = \sum^{n_A} \frac{F_3(x_3 = h)}{wt} \tag{8.2}$$

where F_3 is the component of the nodal force vector $\boldsymbol{F}$ corresponding to x_3 and n_A the number of nodes on the top face of the cube where $x_3 = h$. The average normal strain components are

$$\bar{\varepsilon}_2 = \frac{1}{h} \int_A \frac{u_2(x_1, x_2 = w', x_3) - u_2(x_1, x_2 = 0, x_3)}{ht} \mathrm{d}A \tag{8.3}$$

$$\bar{\varepsilon}_3 = \frac{1}{w} \int_A \frac{u_3(x_1, x_2, x_3 = w') - u_3(x_1, x_2, x_3 = 0)}{wt} \mathrm{d}A \tag{8.4}$$

where $A = wt$. See also Fig. 8.2.

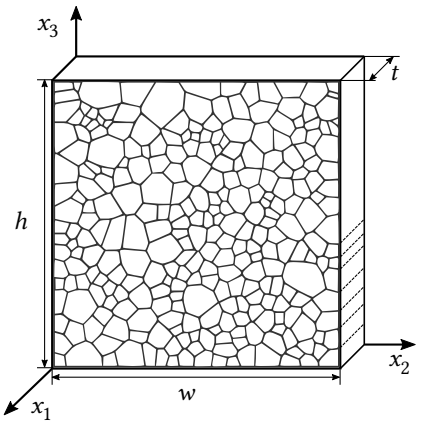

Fig. 8.2: Typical grain geometry and coordinate system in the 2D case, i.e., no change in grain shape in x_1-direction.

Evaluating Eqs. (8.3) and (8.4) was also done by using the nodal displacement information from the finite element solution.

[1] Prescribing no tractions corresponds to a zero traction boundary condition.

In the reference, both grain anisotropy, i.e., the orientation of grains, as well as the elasticity was varied. Elvin stated that the representative volume area needs to include approximately 230 grains to homogenize elastic properties. Furthermore he used an average grain area $\bar{a} = 1.31\ \text{mm}^2$, which with Eq. (7.20) yields an average grain diameter of $\bar{d} = 1.29$ mm. As standard deviation of grain size, a value of $\sigma_\text{d} = 4 \cdot 10^{-4}$ mm was used, which is based on a value given in [140] but scaled according to the average grain diameter. The grain stiffness (Eq. (3.7)) was rotated about the x_1 axis (indicated in Fig. 8.2) according to the process described in Sect. 7.2, hence the c-axes are in the x_2-x_3 plane. Stiffness values are given in Table 8.1. Though it is not explicitly stated, negligible deformation is assumed so the initial

Table 8.1: Single grain stiffness values

Symbol	Value
C_{11}	13.93 ± 0.04
C_{12}	7.08 ± 0.04
C_{13}	5.76 ± 0.02
C_{33}	15.00 ± 0.05
C_{44}	3.01 ± 0.01

C_{ij} as in Eq. (3.7). Values taken from [79]. All values in GPa at −16 °C.

cross-section *wt* is used to calculate the averaged properties (see Sect. 4.3).

In this work, the above-described reference was followed as much as possible. Implicit solving with LS-Dyna was used since computation was faster compared to explicit solving. With respect to discretization, a 2D quadrilateral mesh was extruded to a 3D hexahedron solid mesh. Since for a homogenization study such as this one many models have to be created, the mesh generation needs to be automated as much as possible while maintaining high mesh quality. Therefore triangular and pentahedron elements were permitted sparingly since this lead to better overall mesh quality without the need of manually correcting areas or single elements with low-quality elements. Elvin used a finite thickness t in his models, but did not indicate its value. Here, a thickness corresponding to ≈ 3 % of the edge length was used yielding $3 - 5$ solid elements in thickness direction (x_1 in Fig. 8.2) with good aspect ratios close to one. As elements, the LS-Dyna type "−2" was used since it is a solid element suitable for thin walled structures [30] and implicit solving [59, p. 33].

Regarding a reference solution, Nanthikesan and Sunder [199] calculated Voigt and Reuss bounds for effective elastic constants of S2 ice as

$$9.431\ \text{GPa} \leq E \leq 9.726\ \text{GPa} \tag{8.5}$$

$$0.320 \leq \nu \leq 0.334 \tag{8.6}$$

The effective values for a true RVE should satisfy the above inequalities. Eq. (8.5) can be used to estimate elastic properties through simple averaging such that $E^\text{est} = 9.579$ GPa and $\nu^\text{est} = 0.327$.

Results

To be consistent with the reference [63], averaged properties where calculated according to Eqs. (8.1) to (8.4). Different model sizes corresponding to a varying number of grains were simulated, the results are given in Fig. 8.3. The elastic properties show scatter, but the spread of values –indicated with two times the standard deviation of the sample– decreases with increasing number of grains. The mean value does not vary much and is always between the bounds (Eq. (8.5)). Using mean and standard deviation is justified by the QQ plots (Appendix, Figs. A.3 and A.4) which show that the values approximately follow a normal distribution.

Two aspects differ from the reference: firstly, the spread of values decreases slower. This is possibly related to the generation of polycrystal geometry. In the reference, the size and sphericity of grains appear to be more uniform than in the current approach. A more homogeneous morphology likely decreases scatter of apparent elastic properties. Secondly, the current model was slightly softer than the reference, where this model's mean of E^* values for 279 grains is about $\approx$ 0.8 % less than Elvin's. This model's mean of ν^* differs less than $\approx$ 0.5 % from the reference. This is probably related to the discretization; here, roughly 25 elements were used per grain area (75 per grain with three layers of elements in thickness direction), which is about four times what Elvin used. Hence the slightly softer response.

Briefly, the 2D model works as expected. More grains lead to less scatter of apparent elastic properties. For grain numbers $n_g > 300 - 400$ most simulations give apparent properties within the Reuss-Voigt bounds. With respect to element sizes for isotropic elasticity modeling and assuming uniform distribution of grain sizes, this would mean $\sqrt{300} \approx 17$ grains per edge of a quadrilateral element. This is close to the 14 elements estimated based on the original results in [63], see Sect. 4.

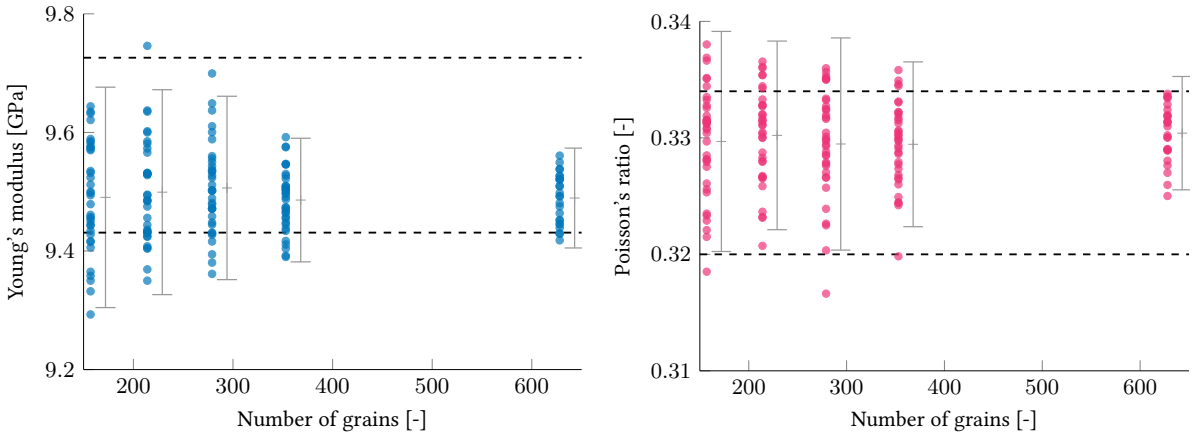

(a) Young's modulus

(b) Poisson's ratio

Fig. 8.3: Apparent elastic properties of the 2D model for different model sizes. (**a**) Young's modulus and (**b**) Poisson's ratio. Each dot represents one simulation run with a different geometry and stiffness tensors randomly rotated about the x_1 axis. Error bars represent mean $\pm$ 2SD with $n = 35$ for all model sizes except the largest with 628 grains where $n = 25$.

8.1.2 RVE size in 3D

Next, the RVE size in 3D is investigated. The model setup is an extension of the 2D model (Sect. 8.1.1). In contrast to the 2D model, the elasticity tensors of the single grains are rotated about random axes and not just within one plane. The stiffness values are the same as in Table 8.1. An exemplary polycrystal geometry is shown in Fig. 8.4.

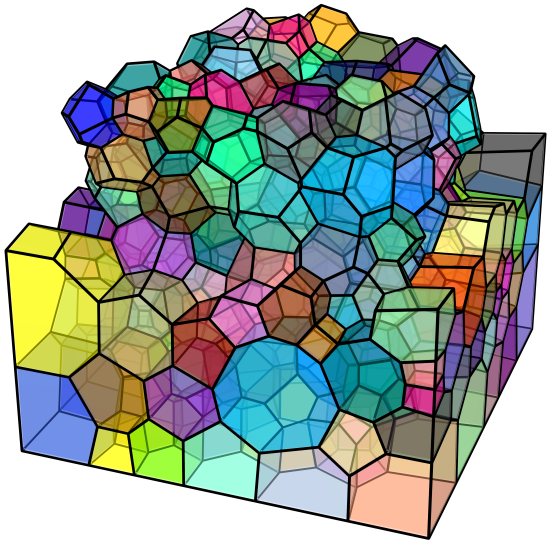

Fig. 8.4: Exemplary polycrystal morphology for a cube with 346 grains and an edge length of 0.008 m. Some grains on the surface are removed for a better visualization of the inner grains.

Preliminaries

The model is discretized with tetrahedral elements. The element size was chosen based on preliminary runs. As elements, the LS-Dyna formulation "13" was used as it is a standard formulation and suitable for implicit simulations [59]. Higher-order element formulations are too computationally expensive for the desired number of simulation runs.

Regarding boundary conditions, the mixed configuration in Fig. 8.5 was used. On the top side $\partial\Omega_3^{\mathrm{t}}$ a prescribed displacement $u_{3\mathrm{t}}$ in x_3-direction was applied, whereas on the bottom side $u_{3\mathrm{b}}$ is zero. One node at $(0, 0, 0)$ was completely fixed to suppress rigid body motions. No tractions were applied on the remaining sides of the cube, which is equivalent to a zero-traction boundary condition. This resembles the setup of a uniaxial test as for instance described in [271].

Regarding a reference solution, [199] give the following Voigt-Reuss bounds for isotropic

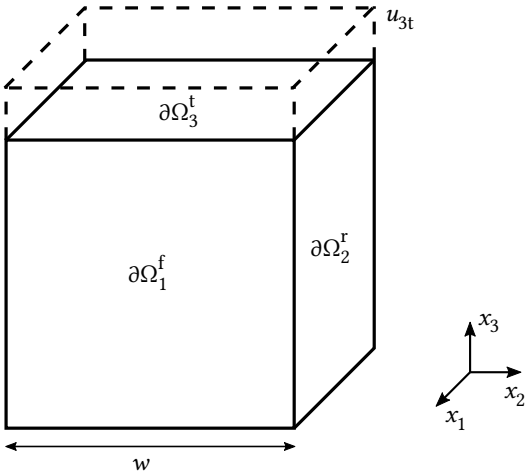

Fig. 8.5: Mixed uniform boundary conditions on a cuboid domain. For the boundaries $\partial\Omega$ the subscript indicates the boundary normal with respect to the coordinate system, the superscript indicates the side, e.g., $(\cdot)^{t,f,r}$ for the top/front/right side.

granular ice based on data for single crystal elasticity from [79] at −16 °C

$$9.09\ \text{GPa} \leq E \leq 9.3\ \text{GPa} \tag{8.7}$$

$$0.325 \leq \nu \leq 0.329 \tag{8.8}$$

These bounds are confirmed with the approach by Cowin [43] as described in Sect. 4.3 and can be used to estimate effective properties through simple averaging giving $E^{\text{est}} = 9.195$ GPa and $\nu^{\text{est}} = 0.327$.

Results

Several points were studied with the 3D RVE model: the RVE size, the distribution of stresses, and the difference between choosing an anisotropic over an isotropic material model. To begin with, a study on RVE size similar to the 2D case was done. That is, the size and number of elements were varied and the apparent elastic properties computed with Eqs. (4.13) to (4.18). Initially, grain size and element size were fixed and only the model size was varied. Since this is computationally expensive for larger models, the model with edge length 0.008 m was used a second time with a lower average grain diameter to achieve a higher number of grains without significantly increasing the number of elements in the model.

The apparent elastic properties are shown in Fig. 8.6. The properties show scatter but the spread of values (mean ± 2SD) decreases with increasing number of grains. The corresponding QQ plots are given in the appendix Figs. A.5 and A.6. The values approximately follow a normal distribution. Small deviations are probably due to a too low number of simulation runs with respect to the scatter of values. The spread decreases from the model with $L = 0.006$ m and a number of grains $n_g \approx 145$ to the model with $L = 0.008$ m and $n_g \approx 346$. For cases with $L > 0.008$ m and $n_g > 346$ the spread only decreases moderately. Moreover,

for cases with more than about 250 grains, the average of apparent values hardly changes. In all, a rough estimate of required grains per edge length of a hexahedron is $\sqrt[3]{346} \approx 7$.

Next, in Fig. 8.6a the dashed line shows the *upper* bound of the Reuss-Voigt bounds (Eqs. (8.7) and (8.8)), indicating that the overall model is too stiff. If the effective value is assumed to be exactly in between the bounds ($(9.09 + 9.3)/2 = 9.195$ GPa), the relative error between the mean of the model with the highest n_g would be $|9.195 - 9.426|/9.195 = 2.5\,\%$. In Fig. 8.6b the dashed line shows the *lower* bound. Here, the same calculation gives an estimated effective Poisson's ratio of 0.327 and the relative error regarding the average apparent value is 1.9 %. Hence the majority of apparent values is not within the given bounds, but the differences between the averages of apparent values and an estimate of the effective values, calculated based on the bounds, are small.

All considered the 3D model works as expected. More grains lead to less scatter of apparent elastic properties, after about 350 grains the spread of values decreases significantly. Nonetheless, still higher numbers of grains do not equally decrease the spread, for $L > 0.008$ m and $n_g > 300$ the passage from statistical- (SVE) to representative volume element (RVE) ($\delta \to \infty$) slows down. When it comes to the global reaction, i.e., the average properties of a SVE, even the largest error is unlikely to be more than a few percent if $n_g > 300$.

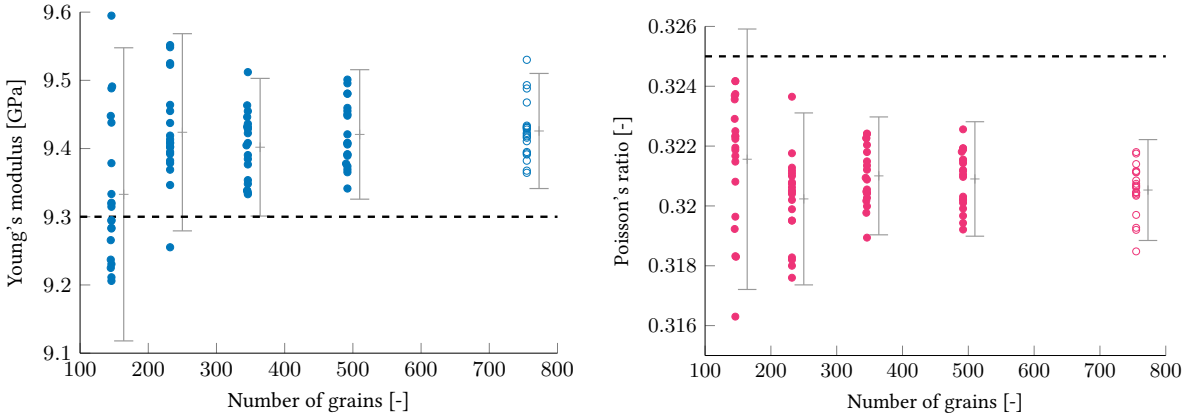

(a) Young's modulus

(b) Poisson's ratio

Fig. 8.6: Apparent elastic properties in 3D for different model sizes. (**a**) Young's modulus and (**b**) Poisson's ratio. Filled dots indicate edge lengths of (left to right) 0.006 m, 0.007 m, 0.008 m, 0.009 m. Circles indicate an edge length of 0.008 m but with lower average grain diameter $\bar{d}$. Each marker represents one simulation run with stiffness tensors rotated about a random axis. Error bars are mean ± 2SD with $n = 20$. Note that in (**a**) the dashed line is the *upper*- and in (**b**) the *lower* bound.

What error is introduced by ignoring minimum RVE sizes, i.e., using an isotropic material model where it is strictly not valid? First, the focus is on average properties. The worst case from the above study on RVE size in 3D would be using $E^* = 9.6$ GPa instead of the lower bound of 9.09 GPa, which gives a relative error of 5.6 %. This error increases with smaller

elements, but it is small for a worst-case scenario. Moreover, this is a local error between a micromechanically modeled volume and *one* averaged element.

Secondly, the error on element-level is analyzed to quantify how much the averaging of properties smears over local stress peaks. A medium sized model with $L = 0.008$ m was solved three times: (i) with an anisotropic material model, (ii) with an isotropic material model where the elastic properties were the same as the apparent properties E^* and ν^* from the anisotropic model, and (iii) with properties from the average of the bounds (8.7) and (8.8). Fig. 8.7 illustrates the difference between models (i) and (ii) for von Mises stress on the surface of the cube. In the isotropic case, all grains experience a stress of about 23 MPa, whereas for the anisotropic model the stresses range from 18 MPa to 30 MPa. Hence this simple comparison already reveals differences of more than 20 %.

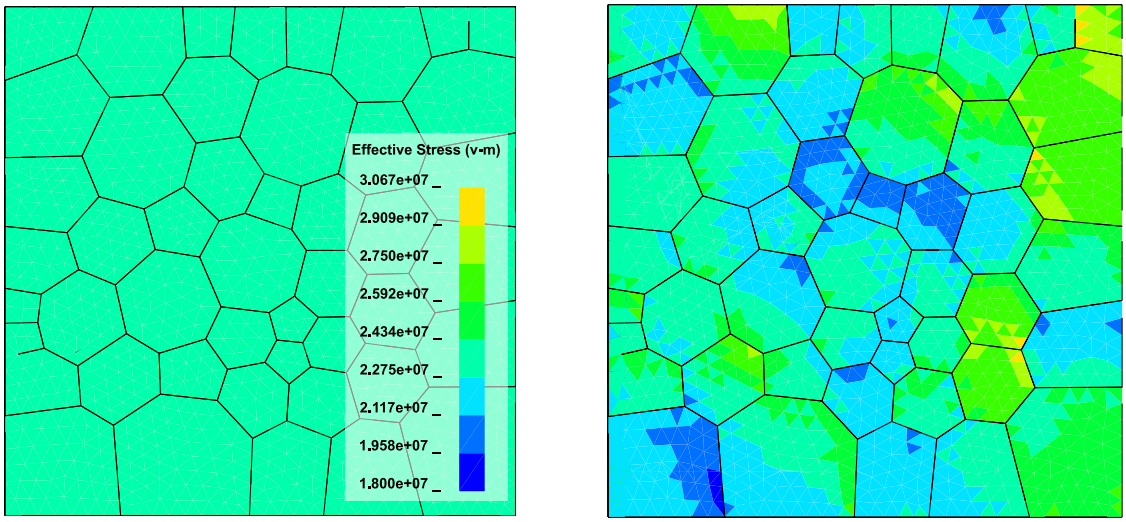

(a) Isotropic

(b) Anisotropic

Fig. 8.7: Von Mises stresses for the same model, i.e., mesh and morphology, but with isotropic and anisotropic elasticity. The isotropic model was run with apparent properties E^* and ν^* from the anisotropic model. Stresses are per element, the fringe scale from (**a**) is the same for (**b**).

The maximum differences in stresses per element are given in Table 8.2. Since these are maximum values it is a worst-case scenario, but the table shows that significant differences in stresses exist in all stress components. Moreover, due to the compression, the only non-zero *average* stress component is $\langle \sigma_{33} \rangle = -23$ MPa (Eq. (4.13)). Hence the anisotropy results in significant stresses in directions other than the global load.

Additionally, Fig. 8.8 shows the differences between stresses of the anisotropic and isotropic model for all elements and two stress components. Roughly 25 % of elements have almost identical stresses, as seen from the first bar at $\Delta\sigma = |\sigma^{\text{iso}} - \sigma^{\text{aniso}}| = 0$. The remaining $\Delta\sigma$ values are distributed such that the higher $\Delta\sigma$, the lower the number of elements. Nonetheless, as seen from the maximum values in Table 8.2, these distributions have long tails. To

conclude, stress components that are parallel to the global load, here σ_{33}, had a difference up to 36 %. Regarding stress components that are not parallel to the global load, here, as an example, σ_{11}, about 75 % of elements show a difference in the order of a couple of MPa. Since $\langle\sigma_{11}\rangle \approx 0$, this means that some elements exhibit significant stresses where their isotropic counterparts are essentially stress-free.

Table 8.2: Maximum of element-wise absolute differences in stresses

Comparison of	$\Delta\sigma_{11}$	$\Delta\sigma_{22}$	$\Delta\sigma_{33}$	$\Delta\sigma_{12}$	$\Delta\sigma_{23}$	$\Delta\sigma_{13}$
Models (i) and (ii)	5.262	5.652	8.502	3.109	4.187	3.811
Models (i) and (iii)	5.262	5.652	8.769	3.109	4.187	3.811

All values in MPa. Model (i) is anisotropic. Model (ii) is isotropic with apparent properties from (i). Model (iii) is isotropic with properties estimated based on Reuss-Voigt bounds.

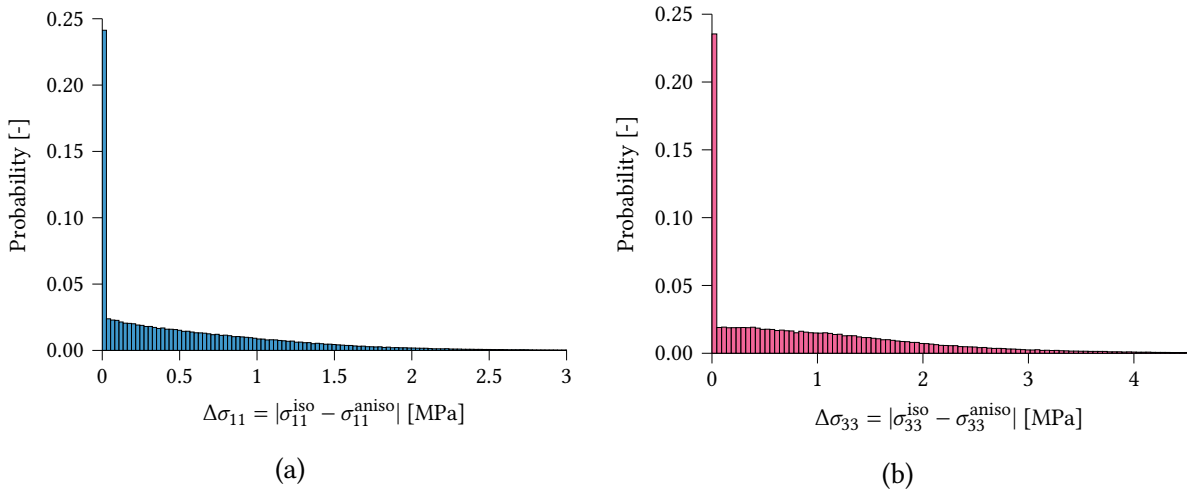

Fig. 8.8: Histograms of absolute differences in stress components (**a**) σ_{11} and (**b**) σ_{33} between anisotropic and isotropic model. X-axes values were cut off for clarity.

Lastly, regarding computational effort, the anisotropic and isotropic models required identical CPU time and memory. Naturally, using RVE-sized elements in the elastic regime would significantly decrease computational effort.

8.1.3 Discussion of results

The results confirm that the speed of passage from SVE to RVE ($\delta \to \infty$) depends on morphology, discretization, desired accuracy and the physics of the problem itself, for instance linear- or nonlinear phenomena, fracture etc. Such dependencies are expected and have been discussed in the literature, see, e.g., [141, 204, 214]. Together with the results of this study, this corroborates that stating a single number as the minimum requirement for the number

of grains in a RVE is misleading. Bearing this in mind, a rough estimate of $15 - 20$ and 7 grains per edge in 2D and 3D, respectively, can be given but such estimates should be treated cautiously. These numbers are also dependent on the element type. The size of the 2D RVE is larger than its 3D equivalent which is in line with studies on other materials, for example viscoplastic composite [181] or porous metal [270].

Besides the minimum RVE size, a critical aspect is the error introduced when choosing an isotropic, averaged material model over an anisotropic one. Globally, a comparison between a true RVE with properties based on Reuss-Voigt bounds showed little deviation. Any local disagreement between micromechanical and averaged model was likely smeared. Locally, however, a different story unfolds. Not only were stresses parallel to the global load different for the majority of elements, anisotropy also created significant local stresses in directions that are globally zero. This is an issue for any modeling of localized phenomena. If for instance crack nucleation immediately leads to crack propagation, as is possible for ice under tension, an undetected local stress peak will result in a higher overall failure load.

Briefly, if elements are larger than the minimum RVE size, and stress concentrations due to mismatch between grains are not expected to significantly affect results, an isotropic model can be used. More generally, no further scale-dependence of both isotropic- and anisotropic model are expected. Nevertheless, grains in sea ice can reach sizes of several centimeters [297] which could result in large RVEs that cannot accurately resolve stress gradients.

8.2 Small-scale tensile splitting test

The tensile splitting test was developed to indirectly test tensile strength of rock and concrete specimens as an alternative to direct uniaxial tensile tests. Briefly, a disc-shaped specimen is compressed between plane blocks or jaws with a prescribed displacement, see Fig. 8.9. The maximum force can be used to analytically calculate a theoretical tensile strength. This however, does not work for ice. Nonetheless, the test gives consistent results, often with only one or two clearly visible cracks, and is easier to perform than uniaxial tensile tests on ice. Furthermore, it captures statistical scatter of test results [140]. Therefore it is a useful test for validating fracture models including stochastic modeling aspects. For a complete discussion of the tensile splitting test see [188].

8.2.1 Preliminaries

The tests used for validation were carried out at the Institute for Ship Structural Design and Analysis and are for instance described in [99]. Discs had a diameter of 98.5 mm, a thickness of 19.7 mm and were cut from a polycrystalline, i.e., granular ice with an average grain size of 2.59 mm. A crosshead speed of $(7.35 \pm 1.11)\,\mathrm{mms}^{-1}$ lead to a mean maximum force of about $(1260 \pm 121)\,\mathrm{N}$. This mean value is for straight cracks only, whereas some cracks were slightly curved. In general, this did not significantly impact the maximum forces. The displacement between initial contact (plate and specimen) and splitting was about 0.15 mm, i.e., the specimens failed ≈ 0.02 s after initial contact. In addition to the behavior seen in the tests, these numbers also indicate brittle behavior. Initially, whitish areas appeared at the top

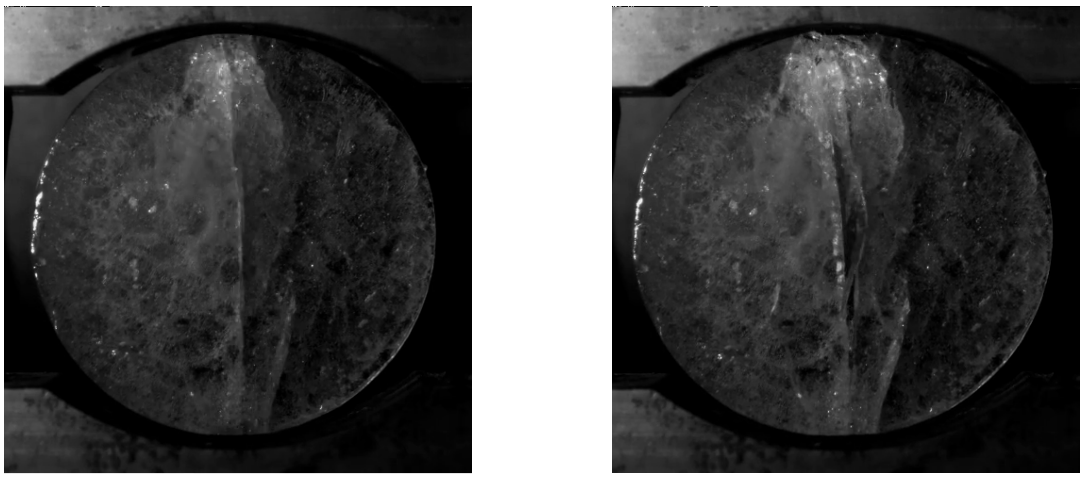

(a) (b)

Fig. 8.9: Snapshots from a high-speed camera video of a tensile splitting test with jaws. (**a**) freshly propagated crack, likely initiated from microcracks in the contact area. (**b**) a couple of milliseconds later, the disc is split in two halves, accompanied by extensive micro- and macrocracking. Images: Eric Grove, with kind permission.

and bottom of the disc which indicates microcracking. Subsequently, one or few macrocracks developed and split the specimens.

Generally, the model setup was done similarly as described before, see Sect. 4.1 and Fig. 8.1. For simplicity, the diameter was slightly increased to 100 mm. It is expected that similar fracture mechanisms are active in both ice types [251]. Therefore, to reduce computation time and meshing effort, the model was built as a quasi-2D model with columnar instead of granular ice. The model thickness was set to 5 mm which is about one fourth of the original thickness. The columnar ice had c-axes randomly distributed in the plane of the disc-shaped specimen. Stiffness values are again given in Table 8.1. To reduce the number of necessary parts, only 180 different c-axis orientations were used and randomly assigned to the $\approx$ 1480 grains. Average grain size, i.e., column diameter, was set to $\bar{d} = 2.59$ mm, the same value as measured in the experiments. Measurements on the standard deviation of the grain size were not available, so a value of 0.1 mm was used. This resulted in a relatively homogeneous grain size distribution, similarly to photographs of thin sections. The tessellation commands in Neper are given in the Appendix, Sect. A.10.

The setup is similar to the RVE study in Sect. 8.1.1. As boundary conditions, both jaws were translated with a symmetrically prescribed displacement to match the crosshead speed of the experiment. The symmetric displacement was used because it lowered the vibrations caused by the initial contact. Damping was introduced to decrease vibrations due to the initial contact, see [173, p. 13-6].

The discretization was done with hexahedral solid elements and quadrilateral cohesive elements on the interfaces between grains. A preliminary mesh study showed that results barely changed for element edge lengths between 0.5 mm to 0.9 mm. Yet due to the relatively small grain size (2.59 mm) a final edge length of 0.6 mm was chosen to accurately resolve the

grain geometry. The depth of the ice disc and the crosshead jaws were eight and ten elements, respectively, which results in an aspect ratio close to one. Cohesive model parameters were the same as in Table 7.1 without further or a priori calibration, respectively. Isotropic elastic material parameters were the same as in Sect. 8.1.1, namely $E^{\text{est}} = 9.579\,\text{GPa}$, $\nu^{\text{est}} = 0.327$, and $\rho = 900\,\text{kgm}^{-3}$. For the steel jaws, an elastic steel material model was used, namely 'mat_elastic' or 'mat_001' as described in [173, p. 2-94], with Young's modulus of $2.1 \cdot 10^{11}$ Pa, a density of $7850\,\text{kgm}^{-3}$ and a Poisson's ratio of 0.33. The parameters for the contact algorithm were also based on experience and are given in the Appendix, Table A.1. Generally, the simulation results were robust with respect to numerical parameters such as those from the contact algorithm.

Table 8.3: Cohesive model parameters, tensile splitting

Parameter	Symbol	Abbreviation	Value	Unit
Density	ρ_{czm}	RO	0.02	kg m^{-3}
Stiffness	K_{coh}	EN, ET	$1.8 \cdot 10^{13}$	Pa m^{-1}
Energy release rate	G_{c}	GIC, GIIC	4	Pa m
Exponent of mixed mode criterion		XMU	1	-
Peak traction in normal direction	σ	T	$6 \cdot 10^5$	Pa
Peak traction in tangential direction	τ	S	$1.2 \cdot 10^6$	Pa

Parameter 'names' and abbreviations are as used by LS-Dyna. Symbols are those used in this work. All values not given are the default values. Density is set to an arbitrary small value to avoid unphysical additional weight. As material model "mat_cohesive_mixed_mode", also called "mat_138", was used. For more information see [173].

8.2.2 Results

Ten models were simulated with the same setup. Initially, both grain geometry and elasticity were varied, i.e., an anisotropic model was simulated. Fig. 8.10 exemplarily shows lateral stresses during the simulation for one case. From the stresses in Fig. 8.10a it can be seen that the grain geometry and elasticity results in a more heterogeneous stress field. In Fig. 8.10b the crack propagates through the disc with a stress concentration ahead of the physical crack tip (with clearly separated crack faces), marking the notional crack tip and the end of the cohesive zone. Generally, the first elements typically fail to the left or right of the upper contact zone, followed by a complete splitting of the disc.

For a quantitative comparison of the anisotropic model and experiment, forces and crosshead displacement at time of failure are given in Table 8.4. Forces are multiplied by four since the thickness of the model geometry was reduced by this factor. On average, the model showed peak forces of $(1351 \pm 158)\,\text{N}$, the displacement at failure was $(0.0572 \pm 0.0056)\,\text{mm}$.

In the isotropic case, the ice material model is isotropic elastic, where the constants were taken as the average of the bounds for S2 ice (see Eqs. (8.5) and (8.6)) hence Young's modulus is 9.759 GPa, Poisson's ratio is 0.327, and density is $900\,\text{kgm}^{-3}$. The remaining model setup

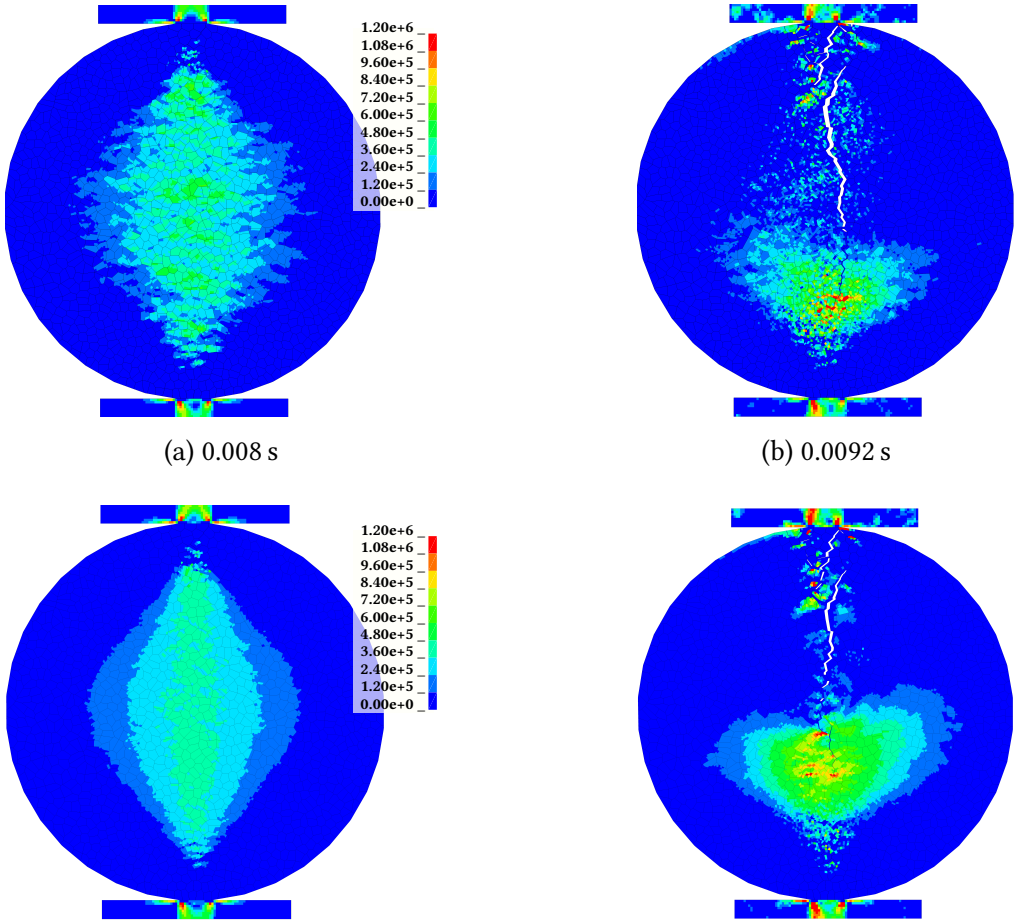

(a) 0.008 s

(b) 0.0092 s

(c) 0.008 s

(d) 0.0093 s

Fig. 8.10: Fringe plots of stress in y-direction, i.e., lateral stress, in tensile splitting simulation for the (**a**), (**b**), anisotropic- and (**c**), (**d**) isotropic case. Stresses in Pa, stress range is limited to 0 Pa $\leq \sigma_y \leq 1.2 \cdot 10^6$ Pa, which corresponds to the maximum tensile stresses of the cohesive elements. Lateral displacement is scaled with factor 50 for a better visualization of cracks. (**a**) and (**c**), prior to cracking. (**b**), (**d**), during crack propagation.

is a copy of the anisotropic case. The stress fields in the isotropic case are given in Fig. 8.10. Stress gradients are smoother than in the anisotropic case, but the stress fields remain locally heterogeneous. The forces in Figs. 8.10b and 8.10d are the same, yet in the isotropic case Fig. 8.10d was taken at a slightly later time step to achieve this. The mean peak force (isotropic) was (1374 ± 165) N and the mean displacement was (0.00574 ± 0.00054) mm. These numbers closely match the anisotropic model results.

With respect to forces, both models compare well to the experiment where peak forces were (1260 ± 121) N [99]. The model results are close, but both models overpredicted forces by 7 % (anisotropic) and 9 % (isotropic), respectively. The displacement at failure of both models is much lower than in the experiments where the specimens failed on average at (0.149 ± 0.044) mm.

Table 8.4: Tensile splitting simulation results

Anisotropic		Isotropic	
Force [N]	Displacement [mm]	Force [N]	Displacement [mm]
1404	0.0565	1384	0.0561
1548	0.0663	1596	0.0636
1548	0.0640	1560	0.0641
1352	0.0584	1376	0.0591
1396	0.0583	1388	0.0587
1284	0.0543	1276	0.0539
1032	0.0450	1068	0.0458
1284	0.0548	1320	0.0556
1164	0.0543	1180	0.0539
1500	0.0600	1588	0.0636
1351 ± 158	0.0572 ± 0.0056	1374 ± 165	0.0574 ± 0.0054

Force is peak force (at failure), values are multiplied by four. Displacement is the crosshead displacement at failure. Last row indicates mean ± standard deviation. The mean force during the experiments was (1260 ± 121) N, mean displacement was (0.149 ± 0.044) mm [99].

8.2.3 Discussion of results

Qualitatively and quantitatively, the model results were similar to what was observed during the experiments. Regarding forces and fracture paths, the models seem to capture the dominant processes. Only the displacement at failure deviated significantly between model and experiments, though values were of the same magnitude. This could be related to both the modeling and the experimental setup.

First, the model does not capture microcracking which could be seen in the contact area during experiments (see Fig. 8.9). This microcracking likely increases compliance in that area, which may delay the specimen's failure and lead to higher displacements. Furthermore, in

reality some viscoelastic response is expected, which would also delay failure, whereas the model is elastic-brittle only.

However, the experimental results are also not as expected. Usually, an increase in displacement speed should lead to a decrease of the displacement at failure, that is, a more brittle behavior. Instead a ten-fold increase of the displacement speed from $(7.35 \pm 1.11)\,\mathrm{mms}^{-1}$ to $(89.9 \pm 5.0)\,\mathrm{mms}^{-1}$ increased the displacement by about 21 % from $(0.149 \pm 0.044)\,\mathrm{mm}$ to $(0.181 \pm 0.042)\,\mathrm{mm}$. Moreover, the experimentally determined displacements varied between 30 % and 23 % standard deviation (SD), compared to the variation of SD of model displacements which were roughly 10 %, see Table 8.4. This suggests that there were some experimental artifacts at play, e.g., related to boundary conditions or control of the hydraulic actuator, which influenced the results more than viscoelasticity or microcracking.

Consequently, a meaningful comparison of model and experiment with respect to displacement at failure is currently not possible. More detailed experimental data is needed.

Next, globally, switching from an anisotropic to an isotropic material model barely affected results. Table 8.4 shows that forces and displacements at failure are very similar for the same grain geometry (the same row in the table). Hence for simulations of this kind of test the irregular grain geometry appears to drive the results, not the anisotropic material model. Possibly, the tensile splitting test resembles a uniaxial tensile test such that once a crack nucleated it is highly likely that it will also propagate and lead to failure. That is, for brittle behavior, the stress required to nucleate a crack is higher than the stress required to propagate it: $\sigma^{\mathrm{N}} > \sigma^{\mathrm{P}}$, see also Fig. 3.2.

In a uniaxial tensile test the initially nucleated crack may appear almost anywhere in the specimen. In the tensile splitting test, the first cracks are mostly observed in the contact area, see Fig. 8.9. In the simulation, the first cracks almost always appeared to the right or left of the contact area. The necessary stress concentration is likely caused by high shear stresses between the compressed and uncompressed material and little influenced by geometric or elastic mismatch between grains. This could explain that, although locally the anisotropic material models leads to a more heterogeneous stress field, globally it does not much affect the results.

In short, the influence of the microstructure on the simulation results was small. Using an anisotropic material model may not be worth the effort for simulations where crack nucleation and propagation is driven by aspects other than elastic mismatch between grains. At any rate, the anisotropic model does not increase computational effort as all elastic material models are efficient and simulation time is mainly driven by cohesive elements.

Regarding the geometric mismatch, theoretically it is energetically preferable for a crack to propagate along element faces in a structured- than in an unstructured mesh [233]. Running multiple simulations with an unstructured mesh, by means of a realistic polycrystal geometry or other, and averaging forces probably gives more realistic results than using a structured mesh.

8.3 Small-scale uniaxial compression

Ice under compression is fundamental to ice-structure interaction processes as described in Sect. 2.2. During full-scale interaction, the stress state of ice is generally triaxial. Nevertheless, modeling uniaxial compressive failure of ice is a first step toward models that can also account for triaxial stress states. Moreover, since uniaxial compression tests require less effort to carry out compared to triaxial tests, they are done more often, see Sect. 6.4. Therefore here the focus is on modeling the brittle behavior of ice during uniaxial compression tests.

8.3.1 Preliminaries

A study by Schulson [251] is taken as a reference. The tests chosen for comparison represent typical testing features: Granular freshwater ice Ih was loaded uniaxially at a temperature of $-10°$, and with a strain rate of $10^{-1}\,\mathrm{s}^{-1}$. The strain rate is on the higher end of typical testing strain rates but was chosen to save computation time. As there is no time dependency in the material model, it is not expected to have a significant influence on the model results. Grain sizes in the experiments were between 1 mm and 10 mm. Cylindrical specimens were used with a diameter of 96 mm and a length of 230 mm. Specimens were either bonded to end caps during freezing or the ice was compressed between longitudinally stiff but transversely compliant platens. In the former case, specimens exhibited shear failure whereas in the latter case axial splitting was observed. Lowering the grain size increased the strength: Though the data is scattered, strength was approximately between 6 MPa and 4 MPa for grain sizes between 1.5 mm and 8 mm.

The model setup was done similarly as described before, see Sect. 4.1 and Fig. 8.1. C-axes were randomly distributed in all planes. Stiffness values were as given in Table 8.1. To reduce the number of necessary model parts, only 500 different orientations were used and randomly assigned to each grain. Using the same grain sizes as in the tests (1 mm to 10 mm) would result in more than 20000 grains which makes the model creation process unwieldy. That is, the model creation may take longer than the actual simulation time. Due to this, average grain sizes were between 12 mm and 20 mm to keep computational and modeling effort acceptable. What is more, the data-based analysis in Ch. 6 showed that overall grain size might not be very influential with respect to strength. At least not for the ranges used here where model grain size is roughly twice the experimental grain size. Similarly to the RVE study (Sect. 4.1), a log-normal distribution of grain sizes was used. Measurements on variability of the grain sizes in the reference were not available, hence a standard deviation of approximately 5 % of mean grain size was used. This resulted in a relatively homogeneous grain size distribution. The tessellation commands in Neper are given in the Appendix, Sect. A.10.

As boundary conditions, the bottom nodes were fixed in all directions, whereas the top nodes were constrained in lateral directions to mirror the bond between ice and platens. In addition, a prescribed displacement with an average speed of $23\,\mathrm{mm\,s}^{-1}$, corresponding to a strain rate $10^{-1}\,\mathrm{s}^{-1}$, was applied to the top nodes. To reduce unlikely inertial effects, the displacement was prescribed with a smooth curve such as the one shown in Fig. 8.14. Due to using this type of curve, the speed of compression and the strain rate only matches the above-given values on average.

The discretization was done with tetrahedral solid elements and pentahedral cohesive elements. Element size was prescribed for 2D triangle elements on the grain boundaries. The 3D tetrahedral mesh was then built according to the existing triangle mesh. A preliminary study showed that results barely changed for elements with element sizes[2] 2.5 mm to 7.5 mm. A final size of 5 mm was chosen to accurately resolve the grain geometry, even for smaller grain sizes. An exception were models with a grain size of 10 mm where an element size of 4 mm was used. Cohesive model parameters are given in Table 8.5. Compared to the parameters for the tensile splitting test simulation (Table 8.3), the energy release rate is increased. A preliminary study showed that otherwise the stress at failure was too low. Moreover, for $G_c = 4$ Pa m, the cohesive elements failed on several planes simultaneously, whereas for $G_c = 30$ Pa m, as used by [96], the failure reflected the shear faulting or axial splitting observed in the experiments. K_{coh} was lowered by factor 10 as changing from $1.8 \cdot 10^{13}$ Pa m to $1.8 \cdot 10^{12}$ Pa m did not affect results but may increase time step size.

Lastly, a contact algorithm was employed in a preliminary study. The parameters are given in Table A.1 in the Appendix. However, whether contact was included or not did not make a difference regarding initial failure stress and strain, and the type of failure. For now, we are interested in the initial brittle failure and less in subsequent behavior. Furthermore, adding a contact algorithm increases computation time. Hence for the compression study, no contact algorithm was used.

Table 8.5: Cohesive model parameters, uniaxial compression

Parameter	Symbol	Abbreviation	Value	Unit
Density	ρ_{czm}	RO	0.02	kg m^{-3}
Stiffness	K_{coh}	EN, ET	$1.8 \cdot 10^{12}$	Pa m^{-1}
Energy release rate	G_c	GIC, GIIC	30	Pa m
Exponent of mixed mode criterion		XMU	1	-
Peak traction in normal direction	σ	T	$6 \cdot 10^5$	Pa
Peak traction in tangential direction	τ	S	$1.2 \cdot 10^6$	Pa

Parameter 'names' and abbreviations are as used by LS-Dyna. Symbols are those used in this work. All values not given are the default values. Density is set to an arbitrary small value to avoid unphysical additional mass. As material model "mat_cohesive_mixed_mode", also called "mat_138", was used. For more information see [173].

8.3.2 Results

Different model sets were simulated. The main result of interest is the overall suitability of the model and the comparison between isotropic and anisotropic models. That is, the same model setup was simulated for different grain sizes, once with anisotropic- and once with

[2] In HyperMesh, these were computed as the shortest distance between a corner node and the shortest distance of a line perpendicular to the opposite leg of the triangle. This is also called minimal normalized height.

isotropic grains. The results are summarized in Table 8.6 showing that using an anisotropic elasticity model barely changes results. Both stress and strain at failure are almost identical and, at least globally, the influence of the microstructure on the results is small.

Moreover, in the reference compressive strength was (5.2 ± 0.6) MPa (mean ± standard deviation, SD) for grain sizes between 1.8 mm and 9.2 mm, which compares well to the strength values in Table 8.6. Strain was not systematically documented in the reference, but an exemplary value is given as 10^{-3} which is close to the values in Table 8.6.

Failure modes were evaluated by looking for patterns in failed cohesive elements. These were also very similar for anisotropic- and isotropic elasticity. Fig. 8.11 shows two exemplary cases of mixed- and shear faulting. In Fig. 8.11b the first cohesive elements that failed are oriented rather vertically, subsequently more elements fail in a 30° angle with respect to the direction of compression. Fig. 8.11b shows a shear fault. In general, the models failed either in shear or in some type of mixed shear faulting and axial splitting.

Table 8.6: Uniaxial compression results aniso- and isotropic

	Anisotropic		Isotropic	
Grain size [mm]	Strength [MPa]	Strain [-]	Strength [MPa]	Strain [-]
20	5.10	$9.04 \cdot 10^{-4}$	5.04	$9.17 \cdot 10^{-4}$
18	4.70	$8.35 \cdot 10^{-4}$	4.70	$8.61 \cdot 10^{-4}$
16	4.68	$8.83 \cdot 10^{-4}$	4.72	$9.17 \cdot 10^{-4}$
14	4.92	$9.39 \cdot 10^{-4}$	4.95	$9.65 \cdot 10^{-4}$
12	4.95	$1.09 \cdot 10^{-3}$	4.89	$1.07 \cdot 10^{-3}$

Grain size are average values ($\bar{d}$). Strength and strain at point of failure, strength is force divided by cross-sectional area. Experimental reference strength for grain sizes between 1.8 mm and 9.2 mm is (5.2 ± 0.6) MPa (mean ± SD), reference strain roughly $1 \cdot 10^{-3}$ [251].

Lastly, ten models with $\bar{d} = 14$ mm were simulated to assess the influence of varying grain geometry and elasticity on strength and failure mode. Results are given in Table A.5. Strength and displacement at failure was (4.92 ± 0.11) MPa and $(9.87 \pm 0.40) \cdot 10^{-4}$ (mean ± SD). In both cases the average results are close to the reference. The low standard deviation shows that the stochastic effect of varying grain geometry and elasticity is small. Similar to the results with different grain sizes, almost all models failed with one or more shear faults, two models showed mixed faults.

8.3.3 Discussion of results

Overall, the model results match the experimental reference [251]. Strength values were slightly lower but the model grain sizes were higher, hence a lower strength value is expected (see Eq. (3.8a) and [251]). The influence of grain size was not the focus of this study for two reasons: Firstly, the data-based analysis showed a small influence of grain size (see Ch. 6).

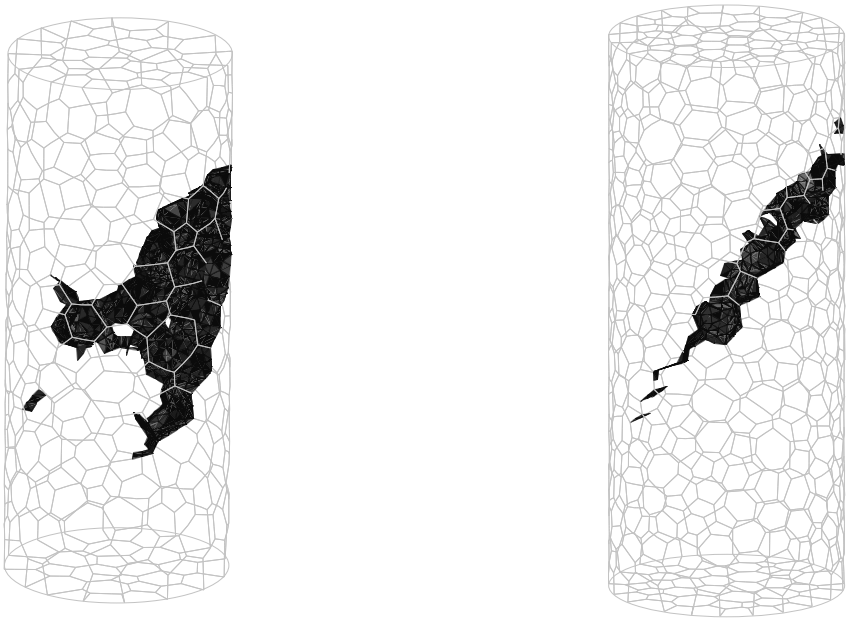

(a) $\bar{d} = 18$ mm (b) $\bar{d} = 14$ mm

Fig. 8.11: Failed cohesive elements for two exemplary cases of uniaxial compression and different grain sizes. (**a**) Mixed shear and axial failure, and (**b**) shear failure.

Secondly, in [96] a similar methodology was used, albeit with an isotropic model, showing that the expected increase of strength with decreasing grain size can be achieved.

Strain values were not systematically documented in the experimental reference, but were of the order of $1 \cdot 10^{-3}$. The simulation strain values match the reference and confirm brittle behavior of the model.

In the reference the specimens failed either via axial splitting or shear faulting. The failure mode is expected to depend on the type of bonded caps. The stronger the bond between specimen and caps, the more lateral confinement, which in turn suppresses cracking in the specimen's end zones. In the model, lateral movement of the end nodes was restricted which should have prevented axial splitting. Yet the model exhibited both failure modes, albeit with a strong tendency toward shear faults.

Regarding Cohesive Zone Model (CZM) parameters, values were taken from [96], only the peak tractions were slightly lower than in the reference. No further calibration was done. Though in [96] a different Cohesive Zone Model was used, overall results in the present study are good, suggesting that these parameters are well-suited for using the CZM in compression. Moreover, the high energy release rate in comparison to the tensile splitting model (see Table 8.3) did not result in ductile behavior. Possibly, in setups where tensile failure dominates, the peak tractions are more important than the energy release rate, whereas when compressive failure dominates the energy release rate is more important. This could be due to the strong link between friction and fracture under compression, see discussions in, e.g., [249, 250, 262].

There were no significant differences between anisotropic- and isotropic model results.

Similarly to the tensile splitting model results, introducing randomly oriented and anisotropically elastic grains did not significantly influence global results. Hence, if the focus is not on local behavior, and given a polycrystal geometry, the additional effort of creating anisotropic grains might not be worth the effort. Nevertheless, the grain geometry itself remains crucial to enable quasi-random fracture paths.

Lastly, numerical effort was acceptable with each simulation taking about a day with parallel processing on six CPUs and requiring few GBs of RAM. There is a trade-off between grain size and numerical effort: For grain sizes below 12 mm the model creation process became unwieldy. Two bottlenecks were identified: The creation of polycrystal geometries in Neper, which is already highly optimized and cannot be sped up significantly, and the scripted 'drawing' of the polycrystal geometry in HyperMesh. The python codes (see Fig. 8.1) on the other hands were not the limiting factor. Nevertheless, as grain size was not identified as a strongly influential feature in the data-based analysis (Ch. 6), using higher grain sizes in the model than in the experiment is likely acceptable.

To sum up, the presented model setup is well-suited to simulate uniaxial compression tests with reasonable numerical effort. Open-ended questions are the effect of triaxial stress, friction, and numerical effects such as the element size with respect to the grain size and the Cohesive Zone Model's parameters.

8.4 Edge crack in a square plate

Previous sections showed that the proposed elastic-brittle material model is, in principle, suited to simulate small-scale experiments. Moreover, with respect to applying the elasticity model to larger geometries, no scale dependency is expected, the exception being the minimum size for an isotropically elastic representative volume element, see Sect. 4.1. By contrast, fracture related mechanical properties are scale-dependent. Therefore this section discusses the brittle-fracture part of the model, the Cohesive Zone Model (CZM), with respect to scale.

As described in Sect. 7.4.3, the CZM has two desirable properties. It is theoretically applicable to all scales and captures the size effect, that is, the variation of material strength P/tL with the size L/λ_{L} of a geometrically similar structure. Furthermore, it should be able to resolve the fracture process zone (FPZ), or cohesive zone, ahead of the crack tip. The first point is important for future full-scale applications of the fracture model and upscaling of laboratory fracture test results. The second point is required for quasi-brittle materials such as ice, but this depends on the actual size of the FPZ in comparison to the geometry's characteristic length (see Sect. 7.4.1 and [18], not to be confused with the material's characteristic length). These points are assessed with a numerical model of an edge-cracked square plate. This study has been published in [145]. Here, these results are reassessed and extended.

8.4.1 General setup and reference solutions

The general setup is shown in Fig. 8.12: A pre-crack in a square plate with length L and thickness t is loaded with a symmetrical force P on both sides. If a sufficient force is applied,

the crack starts to propagate through the plate. Between physical (A) and cohesive (or notional) crack tip (B), the cohesive stress Σ_{coh} acts on the cohesive crack, and is given by the traction-separation law (TSL) which relates Σ_{coh} to the half-crack-opening displacement U. Both U and Σ_{coh} generally depend on the position along X as well as A and B. Two TSLs were considered, one for rectangular- and one for linear softening, where the normal tensile tractions in the fracture process zone (FPZ) Σ_{coh} are

$$\Sigma_{\mathrm{coh}}(A, B, X) = \begin{cases} 0 & ; 0 < X < B \\ \Sigma_0 & ; B \leq X \leq A \end{cases} \tag{8.9}$$

$$\Sigma_{\mathrm{coh}}(A, B, X) = \begin{cases} 0 & ; 0 < X < B \\ \Sigma_0 \left(1 - \frac{U(A,B,X)}{U_{\mathrm{cr}}}\right) & ; B \leq X \leq A \end{cases} \tag{8.10}$$

with U_{cr} half of the critical separation at which cohesive elements are deleted, and maximum traction Σ_0. The shapes of Eqs. (8.9) and (8.10) are exemplarily shown in Fig. 7.3.

For the above-described case, analytical solutions have been established with both linear elastic fracture mechanics (LEFM) and the Cohesive Zone Model (CZM) [175, 307, 308]. For the LEFM, the solutions include the splitting load P, and in the CZM case for infinite plates additionally the size of the FPZ $R = A - B$. These solutions were compared to the numerical model. To do this, and following [308], the results were normalized. CZM-based results were normalized with either L such that $\alpha = A/L$, $\beta = A/L$ or with the characteristic length[3] λ. For λ the following definitions hold; Generally

$$\lambda_{\mathrm{L}} = \frac{EG_{\mathrm{c}}}{\Sigma_0^2} \tag{8.11}$$

which is independent of the TSL shape and used for describing lengths. The critical fracture energy, or energy release rate, is calculated as $G_{\mathrm{c}} = 0.5\Sigma_0 2U_{\mathrm{cr}} = \Sigma_0 U_{\mathrm{cr}}$ for the linear-, and $G_{\mathrm{c}} = 2\Sigma_0 U_{\mathrm{cr}}$ for the rectangular case. Using this with the definition

$$\lambda = \pi \frac{EU_{\mathrm{cr}}}{2\Sigma_0} \tag{8.12}$$

from [308] gives $\lambda = \frac{\pi}{2}\lambda_{\mathrm{L}}$ for linear- and $\lambda = \frac{\pi}{4}\lambda_{\mathrm{L}}$ for rectangular softening. If the FPZ size is unknown it is often estimated with variations of Eq. (8.11) [299] as indicated in Table 8.7.

In addition, the numerical model results were compared to large-scale experiments from Dempsey et al. [51]. They conducted fracture tests with an edge-notched square plate, with a thickness of $t = 1.8$ m and plate sizes L between 0.5 m and 80 m, giving a size range of $1 : 160$. Material parameters are as follows: Young's modulus E between 4 GPa to 6 GPa, a critical fracture energy G_{c} of 15 Pa m, and a strength σ of 0.4 MPa to 0.47 MPa. With Eq. (8.11)

[3] A different but commonly used notation for the characteristic length is l_{ch}

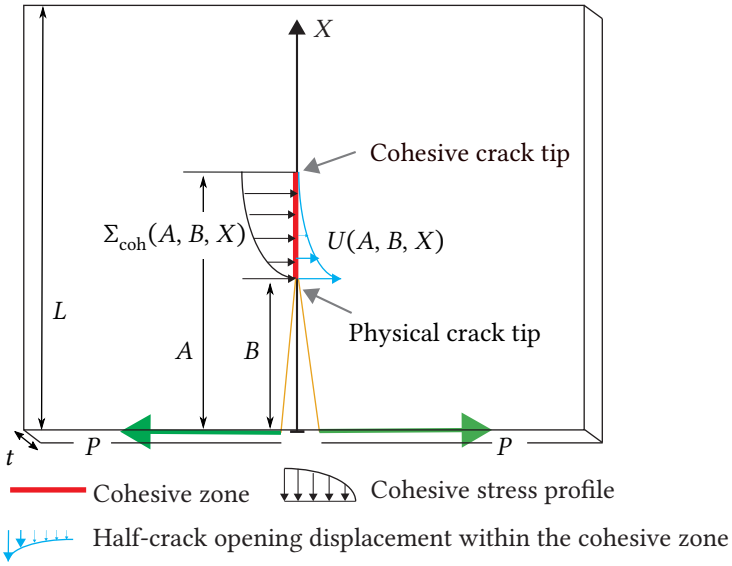

Fig. 8.12: Sketch of the cohesive edge crack in a square plate. For the model with intrinsic cohesive elements, the stress profile $\Sigma_{coh}(A, B, X)$ resembles the one in Fig. 8.15. Sketch adapted from [145, 175].

and taking the middle values of E and σ we can estimate $\lambda_L = 0.4$ m. Taking the different thickness and λ_L into account, the numerical and experimental results can be compared. Moreover, Dempsey et al. fitted a Bažant size effect law to the nominal strength

$$\sigma_n = \frac{2P(2L + B)}{t(L - B)^2} \tag{8.13}$$

with splitting load P, physical crack tip B, thickness t and plate size L. The Bažant size effect law is given as

$$\sigma_n = \frac{c_1}{\sqrt{1 + \frac{L}{c_2}}} \tag{8.14}$$

with fitted constants $c_1 = 0.59$ MPa and $c_2 = 0.37$ m. Inserting Eq. (8.13) into (8.14) yields the normalized splitting load

$$\frac{P}{tL} = \frac{c_1}{\sqrt{1 + \frac{L}{c_2}}} \frac{(L - B)^2}{2L(2L + B)} \tag{8.15}$$

To sum up, different solutions to the edge-cracked square plate problem exist: (i) An analytical LEFM-based solution for large plates or perfectly brittle behavior, (ii) an analytical CZM-based solution for infinite plates, (iii) large-scale experimental results from [51], and lastly (iv) a Bažant size effect law fitted to the experiments from (iii). All these are compared to the numerical model described next. Furthermore, the FPZ size estimates in Table 8.7 are compared to the computed sizes from the numerical model.

Table 8.7: Fracture process zone size estimates

Source	Equation	Value [m]	Value norm. [-]
Hui et al. [127]	$\frac{2}{3\pi} E \frac{G_c}{\sigma^2}$	0.24	0.21
Irwin [81]	$\frac{1}{\pi} E \frac{G_c}{\sigma^2}$	0.35	0.32
Dugdale [57], Barenblatt [9]	$\frac{\pi}{8} E \frac{G_c}{\sigma^2}$	0.44	0.39
Rice [230], Falk et al. [68]	$\frac{9\pi}{32} E \frac{G_c}{\sigma^2}$	0.98	0.88
Hillerborg et al. [119]	$E \frac{G_c}{\sigma^2}$	1.11	1.0
Mulmule and Dempsey [197]	$0.3 \ldots 0.5 \cdot E \frac{G_c}{\sigma^2}$	0.33 to 0.55	0.3 to 0.5

Table partially reproduced from [299]. Normalized values divided by λ_L. E, G_c, σ and λ_L as in Table 8.8.

8.4.2 Numerical model setup

The numerical model is shown in Fig. 8.13 and mimics the setup from Fig. 8.12 with finite- and cohesive elements. The software LS-Dyna was used with an explicit time integration because future use of similar models aim at simulations of dynamic scenarios, e.g., the collision between a ship and an ice floe. In addition, though results are normalized, the parameter values used in the numerical model resemble those for ice, see Table 8.8.

The plate consists of shell elements with unit thickness and one through-thickness integration point. Cohesive elements were inserted along the prescribed crack path through the middle of the plate and connect the shell elements' edges. The cohesive elements were small ($\approx 0.007\lambda_L$) to ensure that the high stress gradients along the crack are correctly resolved. Elements around the crack path are rectangular shells whereas farther away from the crack path, triangular shells were used since they allow a rapid increase of element size. Element formulations are given in [173]. For plates of size $L \leq 30\lambda_L$ the crack path spans the whole plate. Correspondingly, the length along which cohesive elements are inserted D equals L. For larger plates D is limited to $30\lambda_L$. The reason is that the number of cohesive elements drives the number of total elements.

A small pre-crack corresponding to a length of 6 to 11 cohesive elements was used to apply the crack mouth opening displacement. The prescribed displacement function is given in Fig. 8.14: The displacement speed is gradually increased to avoid any inertia effects. The force necessary to achieve this displacement is the sought splitting load P. One node in the middle of the far-end side of the plate was fixed.

An isotropic-elastic material model was used for the shell elements with parameters as given in Table 8.8. The Poisson's ratio of the plate material was set to zero to suppress any deformation normal to the plate. The CZM material models (Eqs. (8.10) and (8.9)) were programmed as user material subroutines to enable the generation of an output with time, posi-

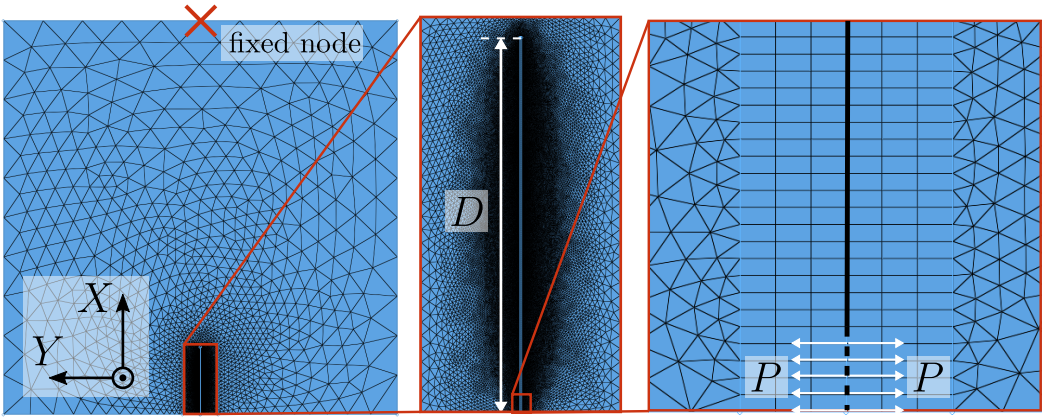

Fig. 8.13: Exemplary model setup and mesh where $D \neq L$ with D the length along which cohesive elements were inserted. Left: complete mesh, in the middle of the top side one node is fixed. Middle: magnification of the mesh around the crack. Right: further magnification, the thick solid black line indicates cohesive elements, the dashed black line indicates the pre-crack where force P is applied over several nodes. Figure from [145].

tion and element ID when a cohesive element reached peak traction or the critical separation (α and β in Fig. 8.15). See also material model description in the Appendix, Sect. A.4.

During postprocessing, whenever an element failed, the closest point in time where any other element reached maximum traction was identified along with the current splitting load. The two elements' positions were then used to calculate $R = A - B$. An exemplary stress distribution along the crack is given in Fig. 8.15. It shows the high stress gradient at the physical crack tip and the long 'tail' of reversibly loaded cohesive elements to the right of α, see also Fig. 7.4.

Table 8.8: Parameter values for finite plate model

Symbol	Parameter	Value	Unit
Material and cohesive zone parameters			
G_c	Critical fracture energy	10	Pa m
E	Young's modulus	10^{10}	Pa
ν	Poisson's ratio	0	-
ρ	Density	900	kg m^{-3}
Σ_0	Maximum traction	$3 \cdot 10^5$	Pa
K_{coh}	Initial TSL slope	$1.8 \cdot 10^{12}$	Pa m^{-1}
K_{Ic}	Fracture toughness[a]	316 227.766	Pa m$^{0.5}$
λ	Charact. length linear softening	1.7453	m
λ	Charact. length rectangular softening	0.8727	m
λ_L	Charact. length	1.1111	m
Tvergaard-Hutchinson model parameters			
u_1	Separation at reaching peak traction	$1.67 \cdot 10^{-7}$	m
$u_2 = u_{fail}$	Critical separation	$3.317 \cdot 10^{-5}$	m
Geometry			
t	Thickness of the plate	1	m

[a] Calculated for plane stress and a linear elastic material as $\sqrt{G_c E}$ [203, p. 113].

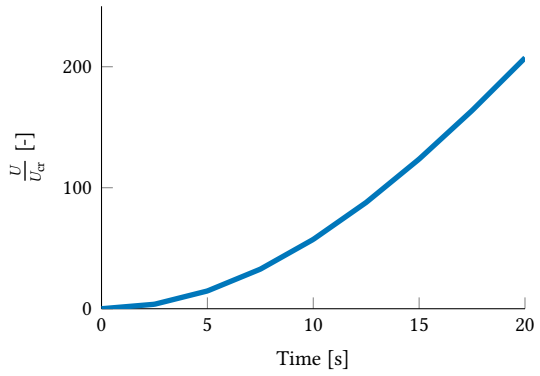

Fig. 8.14: Prescribed displacement at crack mouth, normalized. Adapted from [145].

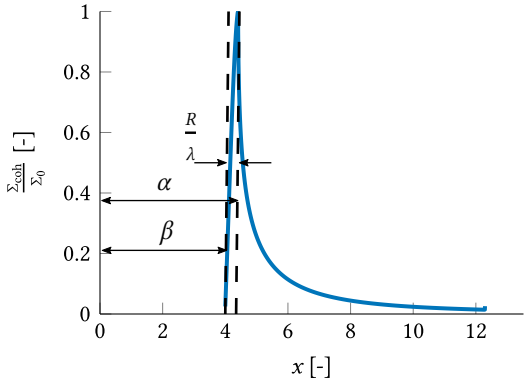

Fig. 8.15: Exemplary cohesive stress along crack, normalized ($x = X/\lambda$). Adapted from [145].

8.4.3 Results

First of all, the simulated splitting load is compared to an analytical solution from linear elastic fracture mechanics (LEFM) for finite plates. The aim is to validate the numerical model and show the difference between LEFM and CZM. As the size L/λ_L increases, it is expected that the numerical CZM (i.e., the Cohesive Element Method, CEM) results approach those by LEFM. In Fig. 8.16, a normalized splitting load $P/tK_{Ic}\sqrt{L}$ is plotted vs. a normalized crack tip position B/L. As mentioned, and contrasting LEFM, the fracture process in the CZM is not concentrated in one point. Therefore, for the CEM-based results, the physical crack tip position B was used as a crack length.

The analytical solutions for the finite and semi-infinite plate diverge after about $B/L = 0.1$. For the infinite plate, the load required to propagate the crack increases, whereas for a finite plate, the load plateaus and decreases after about $B/L = 0.2$. The larger the plate, the closer the CEM-based results to the analytical LEFM solution. For smaller plates the results do not match. For plates $L > 30\lambda_L$ and $D \neq L$, the results are not independent of D anymore and not shown in Fig. 8.16. All other results are generated before the stress distribution along the crack reaches D. Briefly, the CEM-based model was successfully validated with a LEFM-based analytical solution for large plates.

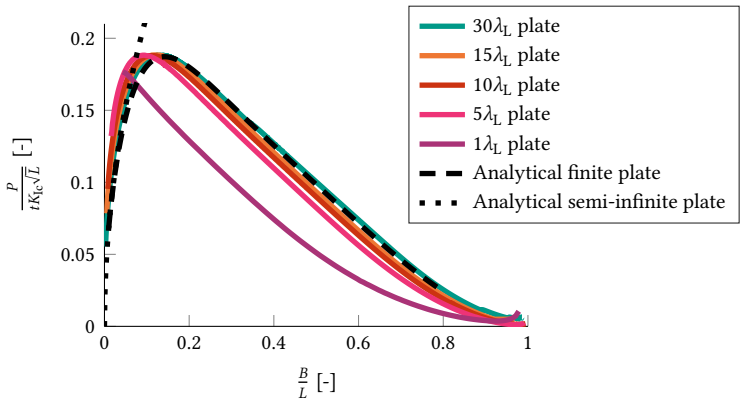

Fig. 8.16: Splitting load P vs. crack tip position B, both normalized. Plot adapted from [145].

Secondly, a size effect regarding the splitting load is assessed. Fig. 8.16 illustrates that solutions based on LEFM and CZM, respectively, only match for large plate sizes. For a plate of arbitrary size, the numerical CZM results were compared to an analytical CZM solution from [307, 308]. In particular, Fig. 8.17 compares the splitting load, or material strength P/tL [17, p. 14], over the plate size L/λ_L for three solutions; CZM-based analytical, CEM-based numerical with linear and rectangular softening, and LEFM-based. The comparison is done for a fixed physical crack length of $B = 0.043L$, but the same trends are found for other physical crack lengths as well, see Fig. 8.19 and [175]. Generally, the CZM numerical and analytical solutions match, thereby showing the correct CEM-based implementation. The LEFM solution is a straight line. The CZM-based curves for the numerical and analytical solution (plot in Fig. 8.17) follow the LEFM-based solution for large plates $L/\lambda_L > 10^2$ but begin to deviate for smaller plates. For plates smaller than $L/\lambda_L = 10^0$ the CZM-based

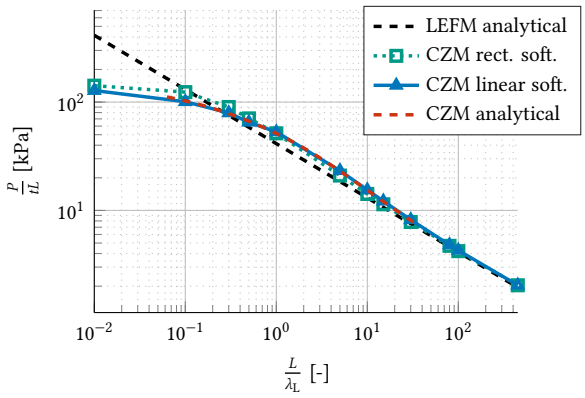

Fig. 8.17: Splitting load over plate length for fixed $B/L = 0.043$. CZM curves are normalized with λ_L as given in Table 8.8. Adapted from [145].

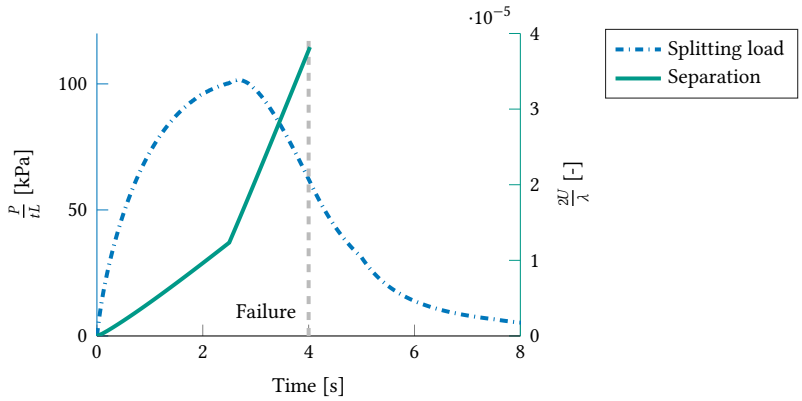

Fig. 8.18: Splitting load (left axis) vs. separation of leading cohesive element (right axis), both normalized. Left axis normalized with λ for linear softening. Vertical dashed line indicates point of failure of leading cohesive element. Adapted from [145].

curves appear to converge.

For small plates the splitting load already decreases before the leading cohesive element reaches critical separation, see Fig. 8.18. From the point where the maximum splitting load is reached, between 2 s to 3 s, the separation U of the leading cohesive element accelerates. Therefore in Fig. 8.17 for plates with $L \leq 0.3\lambda_L$ the maximum load is taken as a splitting load instead.

Similarly, Fig. 8.19 gives the splitting load vs. plate length for $B/L = 0.3$, i.e., when the crack propagated through almost a third of the plate length. Due to the above-mentioned issue with the crack tip approaching D, the largest plate with $100\lambda_L$ is not shown. Furthermore, similarly to Fig. 8.17, for the smallest plates the maximum force is taken as splitting force. The numerically determined loads are shown along with experimental results from [51] and a Bažant size effect law fitted to the experimental results (Eq. 8.15). For comparison, the experimental and Bažant-law results are normalized: Plate lengths are divided by $\lambda_L = 0.4$ m (Eq. (8.11)) and the splitting load values from [51, 175] are divided by L and t.

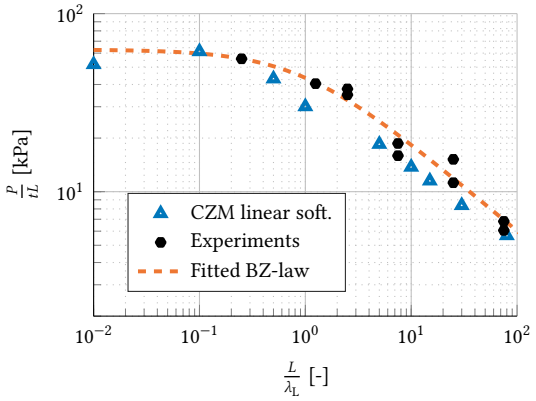

Fig. 8.19: Splitting load over plate length for fixed $B/L = 0.3$. CZM curve is normalized with λ_L as given in Table 8.8. Experimental data originally from [51] and used as prepared by [175]. Fitted Bažant-law (BZ-law) from [51], repeated in Eq. (8.15).

Fig. 8.19 indicates that the results compare well to experiments, though material parameters as well as plate thickness are different. Note that the Bažant-law and experimental results are sensitive with respect to the choice of λ_L, but in any case the trends are the same.

A more detailed comparison of CZM-based numerical (CEM) and analytical model is given in Fig. 8.20. To additionally validate the splitting load, Fig. 8.20a gives P over β for different plate sizes. For all plate sizes but $1\lambda_L$ the load increases to a maximum and slowly decreases. For the $1\lambda_L$ plate, there is a maximum load at the beginning which immediately decreases once the crack propagates. The analytical solution is for a semi-infinite plate, hence it is only matched partially by the largest plates.

The last result of interest is the cohesive zone or fracture process zone (FPZ) size. In Fig. 8.20b, the development of the FPZ is plotted over the crack tip position. The results are cut off for $L = 100\lambda_L$ and $L = 80\lambda_L$ once the crack tip reaches the end of D. Generally, the FPZ increases, plateaus and decreases once the crack tip approaches the opposite end of the plate. The horizontal line indicates the limiting case for a fully developed FPZ, i.e., when the half crack opening displacement at the traction free crack tip reaches the cohesive model's critical separation. As in Fig. 8.20a, the analytical solution for a semi-infinite plate is only matched partially by the largest plates. Results for rectangular softening are similar and given in Fig. A.8 in the Appendix.

Moreover, in Fig. 8.21a the maximum FPZ sizes (R_{max}) are plotted as percentage of plate size over plate size. The FPZ size relative to the plate size strongly increases for plates smaller than $L/\lambda_L = 5$ m until it almost includes the whole plate. Fig. 8.21b gives absolute maximum FPZ size vs. plate size. This shows that for plate sizes of approximately $L > 10\lambda_L = 11.11$ m, both softening types converge to the limiting cases of 0.81 m for linear- and 0.44 m for rectangular softening [308]. The curves in Fig. 8.21b give lower- and upper bounds for the FPZ size due to the choice of TSL [145]. Finally, the estimates of R_{max}/λ_L in Table 8.7 range from 0.21 to 1.0 whereas those from Fig. 8.21b can be much smaller.

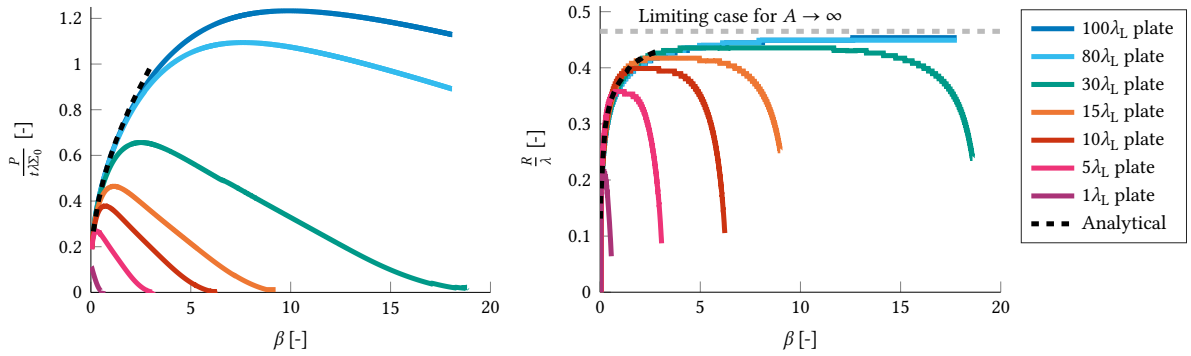

(a) Force (b) Cohesive zone size

Fig. 8.20: (**a**) Force P and (**b**) cohesive zone size over crack tip position β for different plate sizes. All results normalized, λ is for linear softening (Eq. 8.12). Analytical solutions for infinite plates from [308]. Adapted from [145].

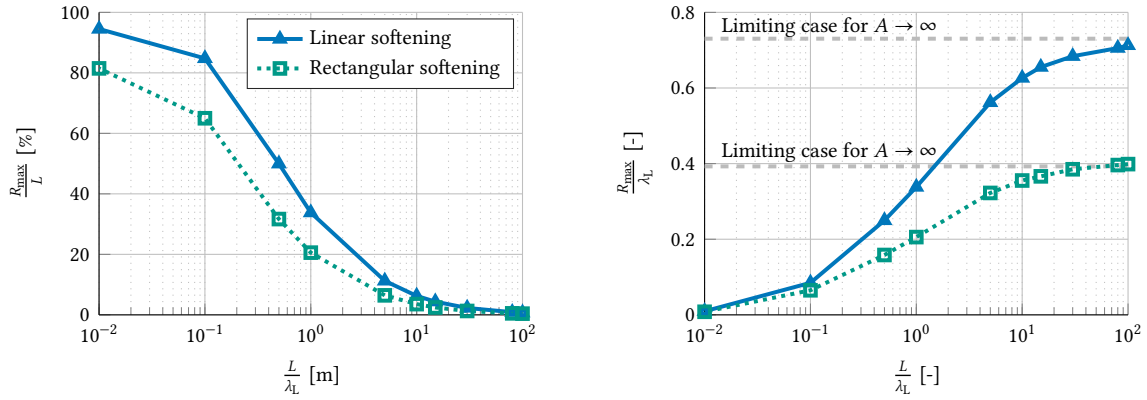

(a) (b)

Fig. 8.21: (**a**) Maximum cohesive zone size as fraction of plate size for linear- and rectangular softening and different plate sizes, and (**b**) the same plot but with absolute cohesive zone size and limiting cases for both softening types and for infinite plates. (**b**) adapted from [145].

8.4.4 Discussion of results

Overall, the Cohesive-Zone-Method (CZM)-based numerical model works as intended. Two limitations apply: Once the stress distribution along the crack reaches D the fact that no further cohesive elements exist in the numerical model distorts results. Moreover, the strong acceleration of separation of the leading cohesive elements for small plates ($L \leq 0.3\lambda_{\mathrm{L}}$, see also Fig. 8.18) necessitated taking the the maximum load over the load corresponding to the fixed $B/L = 0.043$ as the splitting load for Fig. 8.17.

The objective of this study was to assess the scalability of the fracture model and its ability to reflect the fracture process zone. First of all, the CZM-based numerical model does indeed capture the size effect. The plot (Fig. 8.17) illustrates this. In general, LEFM predicts that as $L \to \infty$, the (nominal) strength scales such that

$$\frac{P}{tL} \sim 1/\sqrt{L} \quad \text{or} \tag{8.16}$$

$$\log \frac{P}{tL} = \text{constant} - \frac{1}{2} \log L \tag{8.17}$$

hence the $-1/2$ slope of the LEFM curve [16]. This slope is valid for brittle materials and large geometries. It is matched by the CZM-based curves for large plates. For smaller plates, the CZM-based curves diverge from the LEFM curve, as it is expected for quasi-brittle behavior [16], but match a curve from a CZM-based analytical model. The plot in Fig. 8.19 shows that the CZM-based numerical model also matches experimental results. Moreover, a recommended size above which LEFM is applicable is $12\lambda_{\mathrm{L}} = 13.33$ m [197], which is supported by Fig. 8.17.

Hence, as already shown analytically by Lu et al. [175], the CZM is numerically confirmed as another tool for extrapolating laboratory-scale measurements to full-scale. More so since the parameters of the traction-separation law were the same for all model sizes, similar to results from a study by Ha et al. [101]. This supports that a CEM-based model can possibly be calibrated with small-scale fracture experiments and –cautiously– be applied to full-scale scenarios. However, here, to minimize the influence of the discretization, (cohesive) elements were chosen to be too small for full-scale simulations. Nevertheless it should be possible to execute similar simulations with a coarser discretization, in particular if the aim is not to accurately compute FPZ sizes [299]. Furthermore, for very small plates, the immediate softening (Fig. 8.18) makes it difficult to compare splitting loads over several magnitudes of plate sizes. This indicates that achieving a stable crack growth for very small plates is challenging. Though here the approach of simply taking the maximum load appears to yield good results, more research is needed, e.g., with even smaller elements sizes or a slower loading process.

Next, for this setup and finite plates, the fracture process zone (FPZ) size was computed for the first time. It was confirmed that as $A \to \infty$ the maximum FPZ size converges to 0.5λ and 0.465λ for rectangular and linear softening, as stated in [308]. Moreover, the maximum FPZ size is influenced by the plate size and the physical crack length. Consequently estimating a single value for the FPZ size with formulas from the literature, see, e.g., [299], can be misleading. The estimated maximum FPZ values in Table 8.7 are, compared to the computed

values, of the correct magnitude, but only for larger plates. For small plates these estimates overpredict FPZ size and may lead to too few elements in the FPZ. What is more, the FPZ is much smaller at crack initiation and close to the limit of crack propagation, see the beginning and end of the curves in Fig. 8.20b. In these two situations it is likely that any other than an extremely fine discretization is too coarse to accurately resolve the FPZ.

Regarding the comparison between LEFM and numerical CZM, the results show that when the FPZ spans more than 10 % to 20 % of the plate, the numerical CZM is more accurate. For laboratory testing below the recommendation of $L = 12\lambda_{\mathrm{L}}$, any upscaling should be done with scaling laws that are suitable for quasi-brittle behavior (termed transitional laws by Bažant, see Fig. 3.4) or the presented CZM-based numerical model.

Regarding the objectives of this work, the scalability of the fracture model based on the CZM is confirmed. Through choosing a different characteristic length λ the results should also be applicable to other (quasi-)brittle materials. However, these results are strictly speaking only valid for tensile cracks. Additional studies are necessary on fracture under shear and compression.

8.5 Discussion of the numerical model

The proposed numerical model for elastic-brittle behavior of ice successfully addresses various modeling issues from a physical and a numerical point of view. Specifically, it reflects a polycrystal geometry and anisotropic elasticity as well as intergranular fracture.

In a first study the polycrystal model, i.e., with polycrystal geometry and anisotropic elasticity but without fracture, was used to identify the minimum size for an elastic 3D representative volume element (RVE). Below the minimum size, average elastic properties exhibited notable but small scatter. This is as expected from earlier studies in 2D [63, 272] and the overall moderate elastic anisotropy of ice crystals [254]. Hence when looking at volume-averaged stress or strain fields, the resulting error of using too small volumes with isotropic (homogeneous) elastic properties is not expected to be significant. Once volumes are larger than the minimum RVE size, volume-averaged results based on elasticity are independent of using a polycrystal- or a homogeneous model. If the focus is on non-averaged local stresses or strains, e.g., for a failure criterion, element-wise differences due to elastic or geometric mismatch between grains can be high.

Modeling only elasticity is not useful when looking at brittle behavior. Hence the model was extended to include intergranular fracture with a cohesive-element-based approach. Two further studies applied this model to small-scale tests, one dominated by tensile and one by compressive failure. The extended model captured these tests with good accuracy and feasible numerical effort. Furthermore, the influence of polycrystal geometry and elasticity when fracture is included was analyzed. In both studies, the influence of using anisotropically elastic grains was small. This is in line with the literature, e.g., [77, 309], where elastic mismatch between grains is stated to be less important than for instance inclusions. However, the polycrystal geometry (with or without anisotropic grains) is a good way to achieve more realistic fracture patterns compared to structured meshes. In addition, the polycrystal geometry allows to model only intergranular fracture, which is an assumption based on the

experimental observations in [87]. The good results not only support this assumption, modeling only intergranular fracture also drastically reduces the number of cohesive elements compared to inserting cohesive elements between all volume elements. This circumvents known CZM numerical issues such as artificial compliance, see, e.g., [289], and strongly reduces computational effort.

Whereas the RVE study analyzed the relationship between polycrystal elasticity and model size, the fourth study addressed scaling behavior of fracture modeling with the Cohesive Element Method (CEM). Based on the edge-cracked square plate (ECSP) problem it was shown that the CEM solution matches experiments and analytical solutions for plate sizes that span several magnitudes. Hence, at least for tensile cracks, the CEM should be applicable to different model sizes without changing its parameters. The method is furthermore applicable when FPZs are large compared to specimen size. The study was done with ice material parameters, but these findings should be valid for other (quasi-)brittle materials too.

Overall, the proposed model was successfully applied to a range of studies which included real test setups as well as more theoretical problems to identify, e.g., the minimum elastic RVE size. These studies demonstrate that both the elasticity- and fracture part of the model can be applied to different scales. Nonetheless, open-ended questions remain: Regarding the polycrystal elasticity and geometry, no parameter study was done on the distribution of grain sizes. With respect to the CZM, parameters from previous studies were taken without further analysis of their influence. Moreover, no research was done on the scaling of fracture under compression or shear. Also, currently, the proposed model is limited to uniaxial or two-dimensional scenarios with brittle behavior. Further influential factors identified by the data-based analysis (Ch. 6), such as triaxial stress state, or described in the literature, e.g., inclusions [77], are not considered.

However, the way this model was built gives a lot of flexibility and hence room for adaptations. The CZM in particular is remarkably flexible, both with respect to numerical methods as well as the material modeling. For instance, cohesive elements cannot accurately reflect 3D stresses or strains but this information may be collected from neighboring volume elements. This would enable the consideration of triaxial stress states. Moreover, each cohesive element could be assigned with slightly different parameters to include artificial inclusions. For instance, inclusions could be artificially inserted by randomly assigning low-traction values to certain cohesive elements. Also, methods that alleviate numerical issues are continuously being developed, for example the Discontinuous Galerkin formulation [200, 324].

Furthermore, using Neper as a starting point for the polycrystal model offers a range of possibilities to create the microstructure. This includes, e.g., columnar grains or different grain size and shape distributions. In addition it is possible to include transgranular fracture with multiscale tessellations where each grain is further divided by tessellation. Thus created 'child-grains' could inherit all properties from the parent grain. Hence within the parent grain, material properties would be homogeneous, yet the child grains would allow for more options of fracture paths. Additionally, the python script used to create anisotropically elastic grains can be adapted to for example to not only vary the elasticity tensor orientation but also its elastic constants.

9 Final remarks

This final chapter gives a summary, and discusses the method and results in terms of the objectives given in Ch. 1. Furthermore an outlook for future research is presented.

9.1 Summary and conclusion

The leitmotif of this work was an improved understanding of ice mechanics and to advance ice material modeling based on calibration and validation with small-scale tests but with the perspective of future applications to full-scale ice-structure interaction (ISI) scenarios, see Ch. 1 and Sect. 2.4. Driven by this motif, two complementary approaches were pursued.

Firstly, a large database of small-scale tests was used to synthesize a broad range of experimental studies. Explainable machine learning (ML) models were applied to this data to emulate a multivariate study. These models accurately predicted two targets which are key to understanding ice: compressive strength and behavior type (Chs. 5 and 6). The explanations of these predictions make sense in terms of ice mechanics: Known feature relations could be confirmed, quantified and compared by impact. Moreover, some relationships that were less visible or discussed until now were revealed, for instance the impact of columnar loading on behavior. Lastly, analysis results may be used as an alternative means for the validation of other ice-related models. Hence, the first objective of an improved understanding of ice mechanics through an analysis of experimental data was achieved.

Secondly, an ice material model consisting of two submodels was created: one model for polycrystal elasticity and geometry, and a fracture model based on the Cohesive Zone Method (CZM) (Ch. 7). The former was used to identify the minimum elastic representative volume element (RVE) size as 300 to 400 grains per 2D and 200 to 300 grains per 3D element. In addition, the combination of polycrystal and fracture model was able to reproduce small-scale tests which reflect features of ISI. With these small-scale simulations, it was also shown that using polycrystal elasticity over a model with homogenized elastic properties did not introduce a significant error. To be more specific, the influence of the microstructure was small globally, at least for the tensile splitting and uniaxial compression tests. Nonetheless, locally the influence of the microstructure was high. Furthermore, the polycrystal geometry was essential to achieve a more realistic crack pathing. With this, the second and third objective were accomplished, namely identifying the minimum size for an elastic RVE and the development of an elastic-brittle ice material model for small-scale tests (Ch. 8).

Finally, the scalability of the numerical implementation of the CZM was confirmed, at least for tensile cracks. It was also shown that process zones can span more than 60 % of the overall size for small plates. Hence the fourth objective, assessing the scalability of the

CZM-based fracture model and identifying fracture process zone sizes, was achieved. This supports the application of models that incorporate the process zone to ice and other quasi-brittle materials over models that cannot, e.g., based on linear-elastic fracture mechanics.

To conclude, the presented ice material model reflects typical features of ISI and is scalable. This shows that, within the limits of the model and simulations shown here, ice material modeling based on small-scale tests with future upscaling is possible. Nevertheless, the addition of new model aspects should always entail an analysis of scaling effects both from a numerical- as well as ice mechanics perspective. Furthermore, the use of data-based analyses can support ice-related modeling, e.g., material models for numerical simulations, and complement the classic approach of deriving mechanical laws through hypotheses and experiments.

9.2 Outlook

Various open-ended questions and improvements to the current methodology remain. Regarding the data analysis, more balanced and complete data is desirable. It is also conceivable to include more-dimensional data, such as stress-strain curves or 2D pressure area measurements in the analysis. From the machine-learning model perspective, other types of models could be explored, for instance causal or Bayesian machine learning. Furthermore, additional explainable AI capabilities could generate further insights, e.g., by separating main and interaction effects through SHAP interaction values.

With respect to the material model, the fracture model probably has the most potential for improvement. Both crack nucleation and propagation could be modeled in more detail, for example by including transgranular fracture or inclusions. Instead of using a single phenomenological fracture model, more detailed submodels could be used, e.g., one for Coulombic- and another for Plastic faulting together with a criterion for the switch between the two. Moreover, post-failure processes such as fragmentation and friction between fragments were not treated here, but likely have a large influence, especially in ice-structure interaction. Also, fracture through shear and the corresponding scaling has been little studied until now.

Finally, the link between the material model parameters, the model size, and the discretization is critical to fracture modeling but was not studied systematically. Such numerical aspects deserve attention, particularly with the future aim of full-scale simulations with models with a high number of elements. As was shown, the scaling and homogenization of elasticity will probably not be an issue as long as the ratio between grain size and model size remains small. However, an efficient way of achieving realistic fracture paths and multiple fractures in full-scale models remains to be found. Using the Cohesive Zone Method together with massively parallel processing could be an option, but needs further research and development.

Bibliography

[1] M. Abadi et al. "Tensorflow: a system for large-scale machine learning". In: *OSDI'16: Proceedings of the 12th USENIX Conference on Operating Systems Design and Implementation*. USENIX Association, 2016.

[2] M. Ambati, T. Gerasimov, and L. de Lorenzis. "A review on phase-field models of brittle fracture and a new fast hybrid formulation". In: *Computational Mechanics* 55.2 (2015), pp. 383–405. DOI: 10.1007/s00466-014-1109-y.

[3] M. Arakawa and N. Maeno. "Mechanical strength of polycrystalline ice under uniaxial compression". In: *Cold Regions Science and Technology* 26.3 (1997), pp. 215–229. DOI: 10.1016/S0165-232X(97)00018-9.

[4] D. Arthur and S. Vassilvitskii. "k-means++: The advantages of careful seeding". In: *Proceedings of the Eighteenth Annual ACM-SIAM Symposium on Discrete Algorithms*. New York: Society for Industrial and Applied Mathematics and Association for Computing Machinery, 2007, pp. 1027–1035.

[5] E. Arzaghi et al. "An ecological risk assessment model for Arctic oil spills from a subsea pipeline". In: *Marine Pollution Bulletin* 135 (2018), pp. 1117–1127. DOI: 10.1016/J.MARPOLBUL.2018.08.030.

[6] A. Atkins. "Icebreaking modeling". In: *Journal of Ship Research* 19.1 (1975), pp. 40–43.

[7] E. Bailey Dudley et al. "Using Discrete Element Model to simulate keel-gouging: A sensitivity analysis". In: *Proceedings of the ASME 2017 36th International Conference on Ocean, Offshore and Arctic Engineering*. 2017. DOI: 10.1115/OMAE2017-62479.

[8] O. Banda et al. "Winter navigation at the Baltic Sea: An analysis of accidents occurred during winters 2002–2003 & 2009–2013". In: *Safety and reliability: Methodology and applications*. Ed. by T. Nowakowski et al. Vol. 1. London: CRC Press, 2015, pp. 83–92. DOI: 10.1201/b17399-14.

[9] G. Barenblatt. "The mathematical theory of equilibrium cracks in brittle fracture". In: *Advances in applied mechanics*. Ed. by H. L. Dryden et al. Vol. 7. New York: Academic Press, 1962, pp. 55–129. DOI: 10.1016/S0065-2156(08)70121-2.

[10] S. Bargmann et al. "Generation of 3D Representative Volume Elements for heterogeneous materials: A review". In: *Progress in Materials Science* 96 (2018), pp. 322–384. DOI: 10.1016/j.pmatsci.2018.02.003.

[11] A. Barredo Arrieta et al. "Explainable Artificial Intelligence (XAI): Concepts, taxonomies, opportunities and challenges toward responsible AI". In: *Information Fusion* 58 (2020), pp. 82–115. DOI: 10.1016/j.inffus.2019.12.012.

[12] R. Batto and E. Schulson. "On the ductile-to-brittle transition in ice under compression". In: *Acta Metallurgica et Materialia* 41.7 (1993), pp. 2219–2225. DOI: 10.1016/0956-7151(93)90391-5.

[13] Z. P. Bažant and M. T. Kazemi. "Determination of fracture energy, process zone length and brittleness number from size effect, with application to rock and concrete". In: *International Journal of Fracture* 44.2 (1990), pp. 111–131. DOI: 10.1007/BF00047063.

[14] Z. P. Bažant. "Concrete fracture models: Testing and practice". In: *Engineering Fracture Mechanics* 69.2 (2002), pp. 165–205. DOI: 10.1016/S0013-7944(01)00084-4.

[15] Z. P. Bažant. "Fracture analysis and size effects in failure of sea ice". In: *The mechanics of solids*. Ed. by M. H. Santare and M. J. Chajes. Newark: University of Delaware Press, 2008, pp. 151–170.

[16] Z. P. Bažant. "Scaling laws in mechanics of failure". In: *Journal of Engineering Mechanics* 119.9 (1993), pp. 1828–1844. DOI: 10.1061/(ASCE)0733-9399(1993)119:9(1828).

[17] Z. P. Bažant. *Scaling of structural strength*. 2nd ed. Oxford: Elsevier Butterworth Heinemann, 2005.

[18] Z. P. Bažant. "Scaling theory for quasibrittle structural failure". In: *Proceedings of the National Academy of Sciences of the United States of America* 101.37 (2004), pp. 13400–13407. DOI: 10.1073/pnas.0404096101.

[19] E. Bélisle et al. "Evaluation of machine learning interpolation techniques for prediction of physical properties". In: *Computational Materials Science* 98 (2015), pp. 170–177. DOI: 10.1016/j.commatsci.2014.10.032.

[20] J. Bergstra et al. "Algorithms for hyper-paramater optimization". In: *NIPS'11: Proceedings of the 24th International Conference on Neural Information Processing Systems*. Ed. by J. Shawe-Taylor and R. S. Zemel. Advances in neural information processing systems. Red Hook, N.Y.: Curran Associates Inc., 2012.

[21] J. Bergstra et al. "Hyperopt: A Python library for model selection and hyperparameter optimization". In: *Computational Science & Discovery* 8.1 (2015). DOI: 10.1088/1749-4699/8/1/014008.

[22] M. Bjerkås. "Ice actions on offshore structures: With applications of continuous wavelet transforms on ice load signals". PhD thesis. Trondheim: Norwegian University of Science and Technology, 2006.

[23] N. Blal et al. "Criteria on the artificial compliance inherent to the intrinsic cohesive zone". In: *Comptes Rendus Mécanique* (2011). DOI: 10.1016/j.crme.2011.10.001.

[24] N. Blal et al. "Micromechanical-based criteria for the calibration of cohesive zone parameters". In: *Journal of Computational and Applied Mathematics* 246 (2013), pp. 206–214. DOI: 10.1016/j.cam.2012.10.031.

[25] BMWi. *Eckpunkte für die Reform des EEG*. 2014.

[26] R. U. F. von Bock und Polach. "The mechanical behavior of model-scale ice: Experiments, numerical modeling and stability". PhD thesis. Aalto University, 2016.

[27] R. U. F. von Bock und Polach et al. “State of the art and knowledge gaps on modelling structures in cold regions”. In: *Proceedings of the ASME 2019 38th International Conference on Ocean, Offshore and Arctic Engineering*. American Society of Mechanical Engineers, 2019. DOI: 10.1115/OMAE2019-95085.

[28] R. U. F. von Bock und Polach et al. “The non-linear behavior of aqueous model ice in downward flexure”. In: *Cold Regions Science and Technology* 165 (2019). DOI: 10.1016/j.coldregions.2019.05.001.

[29] R. U. F. von Bock und Polach, V. Janardanan, and S. Ehlers. “Ice model tests in context of the investment value of an offshore vessel”. In: *Proceedings of the ASME 31st international conference on ocean, offshore and arctic engineering–2012*. New York, N.Y.: ASME, 2012, pp. 545–554. DOI: 10.1115/OMAE2012-83854.

[30] T. Borrvall. “A heuristic attempt to reduce transverse shear locking in fully integrated hexahedra with poor aspect ratio”. In: *Proceedings of the 7th European LS-DYNA Conference*. 2009.

[31] R. de Borst. “Numerical aspects of cohesive-zone models”. In: *Engineering Fracture Mechanics* 70.14 (2003), pp. 1743–1757. DOI: 10.1016/S0013-7944(03)00122-X.

[32] G. Brys, M. Hubert, and A. Struyf. “A robust measure of skewness”. In: *Journal of Computational and Graphical Statistics* 13.4 (2004), pp. 996–1017. DOI: 10.1198/106186004X12632.

[33] M. Buchanan. “The limits of machine prediction”. In: *Nature Physics* 15.4 (2019), p. 304. DOI: 10.1038/s41567-019-0489-5.

[34] G. T. Camacho and M. Ortiz. “Computational modelling of impact damage in brittle materials”. In: *International Journal of Solids and Structures* 33.20-22 (1996), pp. 2899–2938. DOI: 10.1016/0020-7683(95)00255-3.

[35] CENELEC European Committee for Electronical Standardization. *Wind turbines: Part 3: Design requirements for offshore wind turbines (IEC 61400-3:2009)*. 2009.

[36] H. Chen et al. *True to the Model or True to the Data?* 2020. URL: http://arxiv.org/pdf/2006.16234v1.

[37] T. Chen and C. Guestrin. “XGBoost: A scalable tree boosting system”. In: *Proceedings of the 22nd ACM SIGKDD International Conference on Knowledge Discovery and Data Mining - KDD ’16*. Ed. by B. Krishnapuram et al. New York, USA: ACM Press, 2016, pp. 785–794. DOI: 10.1145/2939672.2939785.

[38] D. Chicco. “Ten quick tips for machine learning in computational biology”. In: *BioData Mining* 10.1 (2017), p. 205. DOI: 10.1186/s13040-017-0155-3.

[39] F. Chollet. *Keras*. keras.io. URL: https://github.com/fchollet/keras.

[40] D. Cole. *Effect of grain size on the internal fracturing of polycrystaline ice: CRREL Report 86-5*. 1986.

[41] D. M. Cole. “Strain-rate and grain–size effects in ice”. In: *Journal of Glaciology* 33.115 (1987), pp. 274–280. DOI: 10.1017/S0022143000008844.

[42] D. M. Cole. "The microstructure of ice and its influence on mechanical properties". In: *Engineering Fracture Mechanics* 68.17-18 (2001), pp. 1797–1822. DOI: 10.1016/S0013-7944(01)00031-5.

[43] S. C. Cowin. "Properties of the anisotropic elasticity tensor". In: *The Quarterly Journal of Mechanics and Applied Mathematics* 42.2 (1989), pp. 249–266. DOI: 10.1093/qjmam/42.2.249.

[44] G. F. N. Cox, J. Richter-Menge, and W. Weeks. *Mechanical properties of multi-year sea ice: Phase I: Test results. Report 84-9*. 1984.

[45] J. Currier and E. Schulson. "The tensile strength of ice as a function of grain size". In: *Acta Metallurgica* 30.8 (1982), pp. 1511–1514. DOI: 10.1016/0001-6160(82)90171-7.

[46] J. S. Dai. "Euler–Rodrigues formula variations, quaternion conjugation and intrinsic connections". In: *Mechanism and Machine Theory* 92 (2015), pp. 144–152. DOI: 10.1016/j.mechmachtheory.2015.03.004.

[47] C. Dávila and P. Camanho. "Decohesion elements using two and three-parameter mixed mode criteria". In: *American Helicopter Society Conference*. 2001.

[48] J. Dempsey. "Research trends in ice mechanics". In: *International Journal of Solids and Structures* 37.1-2 (2000), pp. 131–153. DOI: 10.1016/S0020-7683(99)00084-0.

[49] J. Dempsey. "Scale effects on the fracture of ice". In: *The Johannes Weertman Symposium*. Ed. by R. Arsenault et al. 1996.

[50] J. Dempsey. "The fracture toughness of ice". In: *Ice-Structure Interaction*. Ed. by S. Jones et al. Berlin, Heidelberg: Springer, 1991.

[51] J. Dempsey, R. Adamson, and S. Mulmule. "Scale effects on the in-situ tensile strength and fracture of ice: Part II: First-year sea ice at Resolute, N.W.T". In: *International Journal of Fracture* 95.1/4 (1999), pp. 347–366. DOI: 10.1023/A:1018650303385.

[52] J. Dempsey, D. Cole, and S. Wang. "Tensile fracture of a single crack in first-year sea ice". In: *Philosophical transactions. Series A, Mathematical, physical, and engineering sciences* 376.2129 (2018). DOI: 10.1098/rsta.2017.0346.

[53] J. Dempsey et al. "Scale effects on the in-situ tensile strength and fracture of ice. Part I: Large grained freshwater ice at Spray Lakes Reservoir, Alberta". In: *Fracture Scaling*. Ed. by Z. Bažant and Y. Rajapakse. Dordrecht: Springer Netherlands, 1999, pp. 325–345. DOI: 10.1007/978-94-011-4659-3_18.

[54] J. Dempsey et al. "The cyclic and fracture response of sea ice in McMurdo Sound: Part II". In: *Proceedings of the 17th International Conference on Port and Ocean Engineering under Arctic Conditions*. Trondheim, 2003.

[55] A. Derradji-Aouat. "Multi-surface failure criterion for saline ice in the brittle regime". In: *Cold Regions Science and Technology* 36.1-3 (2003), pp. 47–70. DOI: 10.1016/S0165-232X(02)00093-9.

[56] F. Doshi-Velez and B. Kim. *Towards A Rigorous Science of Interpretable Machine Learning*. 2017. URL: http://arxiv.org/pdf/1702.08608v2.

[57] D. Dugdale. "Yielding of steel sheets containing slits". In: *Journal of the Mechanics and Physics of Solids* 8.2 (1960), pp. 100–104. DOI: 10.1016/0022-5096(60)90013-2.

[58] P. Duval, M. Ashby, and I. Anderman. "Rate-controlling processes in the creep of polycrystalline ice". In: *The Journal of Physical Chemistry* 87.21 (1983), pp. 4066–4074. DOI: 10.1021/j100244a014.

[59] Dynamore Nordic. *Guideline for implicit analyses using LS-DYNA*. 2018.

[60] J. Effelsberg et al. "On parameter identification for the GISSMO damage model". In: *Proceedings of the 12th International LS-DYNA Users Conference*. 2012.

[61] S. Ehlers et al. "Scenario based risk management for arctic shipping and operations". In: *Proceedings of the 33rd International Conference on Ocean, Offshore and Arctic Engineering*. American Society of Mechanical Engineers, 2014. DOI: 10.1115/OMAE2014-23112.

[62] M. Elices et al. "The Cohesive Zone Model: Advantages, limitations and challenges". In: *Engineering Fracture Mechanics* 69.2 (2002), pp. 137–163. DOI: 10.1016/S0013-7944(01)00083-2.

[63] A. Elvin. "Number of grains required to homogenize elastic properties of polycrystalline ice". In: *Mechanics of Materials* 22.1 (1996), pp. 51–64. DOI: 10.1016/0167-6636(95)00024-0.

[64] B. Erceg et al. "A response comparison of a stiffened panel subjected to rule-based and measured ice loads". In: *Proceedings of the ASME 2014 33rd International Conference on Ocean, Offshore and Arctic Engineering*. 2014.

[65] T. Erhart. "An overview of user defined interfaces in LS-DYNA". In: *Proceedings of the 8th European LS-Dyna Conference*. 2011.

[66] Å. Ervik et al. "A continuum model of large deformation continuous ductile ice crushing". In: *Proceedings of the 24th International Conference on Port and Ocean Engineering under Arctic Conditions*. 2017.

[67] R. Ettema. "Research needs for physical modelling in ice engineering: Reflections from a university ice tank". In: *Cold Regions Science and Technology* 13.1 (1986), pp. 57–65. DOI: 10.1016/0165-232X(86)90007-8.

[68] M. Falk, A. Needleman, and J. Rice. "A critical evaluation of Cohesive Zone Models of dynamic fracture". In: *Le Journal de Physique IV* 11.PR5 (2001), pp. 43–50. DOI: 10.1051/jp4:2001506.

[69] A. Fantilli, B. Chiaia, and B. Frigo. "Analogies in fracture mechanics of concrete, rock and ice". In: *Procedia Materials Science* 3 (2014), pp. 397–407. DOI: 10.1016/j.mspro.2014.06.067.

[70] Finnish Transport Safety Agency. *Ice Class Regulations and the Application Thereof*. 2017.

[71] N. Fletcher. *The chemical physics of ice*. Cambridge monographs on physics. London: Cambridge U.P, 1970.

[72] C. Forbes. *Statistical distributions*. 4. Oxford: Wiley, 2011.

[73] A. L. Fortt and E. Schulson. "The resistance to sliding along coulombic shear faults in ice". In: *Acta Materialia* 55.7 (2007), pp. 2253–2264. DOI: 10.1016/j.actamat.2006.11.022.

[74] R. Frederking et al. "Overview of the Molikpaq multi-year ice load reanalysis 2007 JIP". In: *Proceedings of the 21th International Conference on Port and Ocean Engineering under Arctic Conditions*. 2011.

[75] J. H. Friedman. "Greedy function approximation: a gradient boosting machine". In: *The Annals of Statistics* 29.5 (2001), pp. 1189–1232.

[76] J. H. Friedman. "Stochastic gradient boosting". In: *Computational Statistics & Data Analysis* 38.4 (2002), pp. 367–378. DOI: 10.1016/S0167-9473(01)00065-2.

[77] H. Frost. "Mechanisms of crack nucleation in ice". In: *Engineering Fracture Mechanics* 68.17-18 (2001), pp. 1823–1837. DOI: 10.1016/S0013-7944(01)00036-4.

[78] R. Gagnon. "A numerical model of ice crushing using a foam analogue". In: *Cold Regions Science and Technology* 65.3 (2011), pp. 335–350. DOI: 10.1016/j.coldregions.2010.11.004.

[79] P. Gammon, H. Klefte, and M. Clouter. "Elastic constants of ice samples by Brillouin spectroscopy". In: *The Journal of Physical Chemistry* 87 (1983), pp. 4025–4029.

[80] R. J. Geelen et al. "A phase-field formulation for dynamic cohesive fracture". In: *Computer Methods in Applied Mechanics and Engineering* 348 (2019), pp. 680–711. DOI: 10.1016/j.cma.2019.01.026.

[81] George Irwin. "Plastic zone near a crack and fracture toughness". In: *Proceedings of the Seventh Sagamore Ordnance Materials Research Conference*. 1960.

[82] Germanischer Lloyd. "Guideline for the construction of fixed offshore installations in ice infested waters". In: *Rules & Guidelines*. Germanischer Lloyd, 2016.

[83] A. Géron. *Hands-on machine learning with Scikit-Learn, Keras, and TensorFlow: Concepts, tools, and techniques to build intelligent systems*. Second Edition. Sebastopol, CA: O'Reilly, 2019.

[84] I. Gitman, H. Askes, and L. Sluys. "Representative volume: Existence and size determination". In: *Engineering Fracture Mechanics* 74.16 (2007), pp. 2518–2534. DOI: 10.1016/j.engfracmech.2006.12.021.

[85] *Global Wind Report: Annual Market Update*. 2017.

[86] L. W. Gold. "Statistical behaviour of the deformation for first loading of polycrystalline ice". In: *Journal of Glaciology* 49.164 (2003), pp. 37–49. DOI: 10.3189/172756503781830935.

[87] L. W. Gold. "Statistical characteristics for the type and length of deformation-induced cracks in columnar-grain ice". In: *Journal of Glaciology* 43.144 (1997), pp. 311–320. DOI: 10.3189/S0022143000003269.

[88] N. Golding. "Compressive shear faulting in ice loaded triaxially: The influence of confinement". PhD thesis. 2011. DOI: 10.1349/ddlp.344.

[89] N. Golding, E. Schulson, and C. Renshaw. "Shear faulting and localized heating in ice: the influence of confinement". In: *Acta Materialia* 58.15 (2010), pp. 5043–5056. DOI: 10.1016/j.actamat.2010.05.040.

[90] N. Golding, E. Schulson, and C. Renshaw. "Shear localization in ice: Mechanical response and microstructural evolution of P-faulting". In: *Acta Materialia* 60.8 (2012), pp. 3616–3631. DOI: 10.1016/j.actamat.2012.02.051.

[91] N. Golding et al. "Plastic faulting in saltwater ice". In: *Journal of Glaciology* 60.221 (2014), pp. 447–452. DOI: 10.3189/2014JoG13J178.

[92] S. Graham and N. Yang. "Representative volumes of materials based on microstructural statistics". In: *Scripta Materialia* 48.3 (2003), pp. 269–274. DOI: 10.1016/S1359-6462(02)00362-7.

[93] E. Gratz and E. Schulson. "Brittle failure of columnar saline ice under triaxial compression". In: *Journal of Geophysical Research* 102.B3 (1997), pp. 5091–5107. DOI: 10.1029/96JB03738.

[94] F. Grennerat et al. "Experimental characterization of the intragranular strain field in columnar ice during transient creep". In: *Acta Materialia* 60.8 (2012), pp. 3655–3666. DOI: 10.1016/j.actamat.2012.03.025.

[95] I. Gribanov, R. Taylor, and R. Sarracino. "Application of Cohesive Zone Model to the fracture process of freshwater polycrystalline ice under flexural loading". In: *IOP Conference Series: Earth and Environmental Science* 193 (2018). DOI: 10.1088/1755-1315/193/1/012013.

[96] I. Gribanov, R. Taylor, and R. Sarracino. "Cohesive zone micromechanical model for compressive and tensile failure of polycrystalline ice". In: *Engineering Fracture Mechanics* (2018). DOI: 10.1016/j.engfracmech.2018.04.023.

[97] I. Gribanov et al. "Investigation of mixed mode fracture of L-shaped sea ice beams". In: *Proceedings of the 25th International Conference on Port and Ocean Engineering under Arctic Conditions*. 2019.

[98] M. Gross. "Arctic shipping threatens wildlife". In: *Current Biology* 28.15 (2018), R803–R805. DOI: 10.1016/j.cub.2018.07.053.

[99] E. Grove. "Review and experiments of splitting tensile tests for ice". Project Thesis. Hamburg, Germany: Hamburg University of Technology, 2020.

[100] H. Hendrikse. "Ice-induced vibrations of vertically sided offshore structures". PhD thesis. Delft University of Technology, 2017. DOI: 10.4233/uuid:325ebcfb-f920-400c-8ef6-21b2305b6920.

[101] K. Ha, H. Baek, and K. Park. "Convergence of fracture process zone size in cohesive zone modeling". In: *Applied Mathematical Modelling* 39.19 (2015), pp. 5828–5836. DOI: 10.1016/j.apm.2015.03.030.

[102] K. Ha et al. "On the size effect of interfacial fracture between concrete and fiber reinforced polymer". In: *Cement and Concrete Composites* 93 (2018), pp. 99–106. DOI: 10.1016/j.cemconcomp.2018.07.003.

[103] P. Hall and G. Navdeep. *Introduction to Machine Learning Interpretability*. Sebastopol, USA: O'Reilly Media, Inc., 2018.

[104] K. Hammonds and I. Baker. "Quantifying damage in polycrystalline ice via X-Ray computed micro-tomography". In: *Acta Materialia* 127 (2017), pp. 463–470. DOI: 10.1016/j.actamat.2017.01.046.

[105] S. Hänninen. *Incidents and accidents in winter navigation in the Baltic Sea, winter 2002-2003: Research Report Nr. 54*. Helsinki, 2005.

[106] P. W. Harper and S. R. Hallett. "Cohesive zone length in numerical simulations of composite delamination". In: *Engineering Fracture Mechanics* 75.16 (2008), pp. 4774–4792. DOI: 10.1016/j.engfracmech.2008.06.004.

[107] M. C. N. Hartmann et al. "Investigation of nonlinear wave–ice interaction using parameter study and numerical simulation". In: *Journal of Offshore Mechanics and Arctic Engineering* 142.2 (2020), p. 2847. DOI: 10.1115/1.4045625.

[108] T. Hastie, R. Tibshirani, and J. Friedman. *The elements of statistical learning: Data mining, inference, and prediction*. Second edition, corrected at 12th printing 2017. Springer series in statistics. New York, NY: Springer, 2009.

[109] F. Häusler. *Dreidimensionales Bruchkriterium für Meer-Eis: Bericht Nr. E 113/81*. 1981.

[110] I. Hawkes and M. Mellor. "Deformation and fracture of ice under uniaxial stress". In: *Journal of Glaciology* 11.61 (1972), pp. 103–131. DOI: 10.1017/S002214300002253X.

[111] F. Haynes. *Effect of temperature on the strength of snow ice: CRREL Report 78-27*. Hanover, 1978.

[112] F. Haynes and M. Mellor. "Measuring the uniaxial compressive strength of ice". In: *Journal of Glaciology*. Vol. 19. 1977, pp. 213–223.

[113] S. Hazanov. "Hill condition and overall properties of composites". In: *Archive of Applied Mechanics* 68.6 (1998), pp. 385–394. DOI: 10.1007/s004190050173.

[114] S. Hazanov and M. Amieur. "On overall properties of elastic heterogeneous bodies smaller than the representative volume". In: *International Journal of Engineering Science* 33.9 (1995), pp. 1289–1301. DOI: 10.1016/0020-7225(94)00129-8.

[115] S. Hazanov and C. Huet. "Order relationships for boundary conditions effect in heterogeneous bodies smaller than the representative volume". In: *Journal of the Mechanics and Physics of Solids* 42.12 (1994), pp. 1995–2011. DOI: 10.1016/0022-5096(94)90022-1.

[116] H. Herrnring et al. "Experimental investigation of an accidental ice impact on an aluminium high speed craft". In: *Progress in the Analysis and Design of Marine Structures*. Ed. by C. Soares and Y. Garbatov. 2017, pp. 695–704. DOI: 10.1201/9781315157368-80.

[117] H. Herrnring, J. M. Kubiczek, and S. Ehlers. "The ice extrusion test: a novel test setup for the investigation of ice-structure interaction – results and validation". In: *Ships and Offshore Structures* 4 (2020), pp. 1–9. DOI: 10.1080/17445302.2020.1713437.

[118] R. Hill. "Elastic properties of reinforced solids: Some theoretical principles". In: *Journal of the Mechanics and Physics of Solids* 11.5 (1963), pp. 357–372. DOI: 10.1016/0022-5096(63)90036-X.

[119] A. Hillerborg, M. Modéer, and P.-E. Petersson. "Analysis of crack formation and crack growth in concrete by means of fracture mechanics and finite elements". In: *Cement and Concrete Research* 6.6 (1976), pp. 773–781. DOI: 10.1016/0008-8846(76)90007-7.

[120] K.-I. Hirayama, J. Schwarz, and H.-C. Wu. "Model technique for the investigation of ice forces on structures". In: *Proceedings of the 2nd Inernational Conference on Port and Ocean Engineering under Arctic Conditions*. 1973.

[121] P. Hobbs. *Ice physics*. Oxford classic texts in the physical sciences. Oxford: Oxford Univ. Press, 2010.

[122] H. Hosni and A. Vulpiani. "Forecasting in light of big data". In: *Philosophy & Technology* 31.4 (2018), pp. 557–569. DOI: 10.1007/s13347-017-0265-3.

[123] K. Høyland. "Morphology and small-scale strength of ridges in the north-western Barents Sea". In: *Cold Regions Science and Technology* 48.3 (2007), pp. 169–187. DOI: 10.1016/j.coldregions.2007.01.006.

[124] K. V. Høyland. "Consolidation of first-year sea ice ridges". In: *Journal of Geophysical Research* 107.C6 (2002). DOI: 10.1029/2000JC000526.

[125] M. Hubert and E. Vandervieren. "An adjusted boxplot for skewed distributions". In: *Computational Statistics & Data Analysis* 52.12 (2008), pp. 5186–5201. DOI: 10.1016/j.csda.2007.11.008.

[126] C. Huet. "Application of variational concepts to size effects in elastic heterogeneous bodies". In: *Journal of the Mechanics and Physics of Solids* 38.6 (1990), pp. 813–841. DOI: 10.1016/0022-5096(90)90041-2.

[127] C.-Y. Hui et al. "Crack blunting and the strength of soft elastic solids". In: *Proceedings of the Royal Society of London. Series A: Mathematical, Physical and Engineering Sciences* 459.2034 (2003), pp. 1489–1516. DOI: 10.1098/rspa.2002.1057.

[128] D. Iliescu and E. Schulson. "The brittle compressive failure of fresh-water columnar ice loaded biaxially". In: *Acta Materialia* 52.20 (2004), pp. 5723–5735. DOI: 10.1016/j.actamat.2004.07.027.

[129] S. Ince, A. Kumar, and J. Paik. "A new constitutive equation on ice materials". In: *Ships and Offshore Structures* (2016), pp. 1–14. DOI: 10.1080/17445302.2016.1190122.

[130] ISO International Organization for Standardization. *Petroleum and natural gas industries – Arctic offshore structures (ISO 19906:2010)*. 2011.

[131] M. Itskov. "On the theory of fourth-order tensors and their applications in computational mechanics". In: *Computer Methods in Applied Mechanics and Engineering* 189.2 (2000), pp. 419–438. DOI: 10.1016/S0045-7825(99)00472-7.

[132] M. Jefferies and W. Wright. "Dynamic response of "Molikpaq" to ice-structure interaction". In: *Proceedings of the 7th international conference on offshore mechanics and arctic engineering*. Ed. by D. S. Sodhi, C. H. Luk, and N. K. Sinha. Vol. 4. 1988, pp. 201–220.

[133] S. Ji, X. Chen, and A. Wang. "Influence of the loading direction on the uniaxial compressive strength of sea ice based on field measurements". In: *Annals of Glaciology* (2020), pp. 1–11. DOI: 10.1017/aog.2020.14.

[134] P. Jochmann. *Full Scale Measurements at Light- house Norströmsgrund -Winter 2001-*. Hamburg, 2003.

[135] P. Jochmann and J. Schwarz. *Ice Force Measurements at Lighthouse Norstrømsgrund Winter 2000: LOLEIF Report No. 9*. 2001.

[136] S. Jones. "A review of the strength of iceberg and other freshwater ice and the effect of temperature". In: *Cold Regions Science and Technology* 47.3 (2007), pp. 256–262. DOI: 10.1016/j.coldregions.2006.10.002.

[137] S. Jones. "High strain-rate compression tests on ice". In: *The Journal of Physical Chemistry* 101.32 (1997), pp. 6099–6101.

[138] S. Jones. "The confined compressive strength of polycrystalline ice". In: *Journal of Glaciology* 28.98 (1982), pp. 171–178. DOI: 10.1017/S0022143000011874.

[139] I. Jordaan. "Mechanics of ice–structure interaction". In: *Engineering Fracture Mechanics* 68.17-18 (2001), pp. 1923–1960. DOI: 10.1016/S0013-7944(01)00032-7.

[140] Z. Kamio, H. Matsushita, and B. Strnadel. "Statistical analysis of ice fracture characteristics". In: *Engineering Fracture Mechanics* 70.15 (2003), pp. 2075–2088. DOI: 10.1016/S0013-7944(02)00255-2.

[141] T. Kanit et al. "Determination of the size of the representative volume element for random composites: Statistical and numerical approach". In: *International Journal of Solids and Structures* 40.13-14 (2003), pp. 3647–3679. DOI: 10.1016/S0020-7683(03)00143-4.

[142] L. Kellner, H. Herrnring, and M. Ring. "Review of ice load standards and comparison with measurements". In: *Proceedings of the ASME 2017 36th International Conference on Ocean, Offshore and Arctic Engineering*. 2017. DOI: 10.1115/OMAE2017-61735.

[143] L. Kellner. *XAI and Ice material modeling v1.1*. 2022. DOI: 10.5281/zenodo.5817768.

[144] L. Kellner et al. "Establishing a common database of ice experiments and using machine learning to understand and predict ice behavior". In: *Cold Regions Science and Technology* (2019). DOI: 10.1016/j.coldregions.2019.02.007.

[145] L. Kellner et al. "Study on the cohesive edge crack in a square plate with the Cohesive Element Method". In: *International Journal of Fracture* (2021). DOI: 10.1007/s10704-021-00560-9.

[146] F. E. Kennedy, E. Schulson, and D. E. Jones. "The friction of ice on ice at low sliding velocities". In: *Philosophical Magazine A* 80.5 (2000), pp. 1093–1110. DOI: 10.1080/01418610008212103.

[147] K. P. Kennedy et al. "Dynamic activity in medium-scale ice indentation tests". In: *Cold Regions Science and Technology* 22.3 (1994), pp. 253–267. DOI: 10.1016/0165-232X(94)90004-3.

[148] A. G. Khan et al. "Numerical investigation of propeller-ice interaction effects". In: *Ocean Engineering* 216 (2020). DOI: 10.1016/j.oceaneng.2020.107716.

[149] E. Kim et al. "Mechanisms governing failure of ice beneath a spherically-shaped indenter". In: *Cold Regions Science and Technology* 78 (2012), pp. 46–63. DOI: 10.1016/j.coldregions.2012.01.011.

[150] A. Kiselev et al. "Active sites in heterogeneous ice nucleation-the example of k-rich feldspars". In: *Science (New York, N.Y.)* 355.6323 (2017), pp. 367–371. DOI: 10.1126/science.aai8034.

[151] R. Kissell and J. Poserina. *Optimal sports math, statistics, and fantasy*. Amsterdam: Academic Press, 2017.

[152] G. Klambauer et al. "Self-normalizing neural networks". In: *Advances in Neural Information Processing Systems 30 (NIPS 2017)*. Ed. by I. Guyon et al. 2017.

[153] K. Kolari. "A complete three-dimensional continuum model of wing-crack growth in granular brittle solids". In: *International Journal of Solids and Structures* 115-116 (2017), pp. 27–42. DOI: 10.1016/j.ijsolstr.2017.02.012.

[154] M. König, L. Radtke, and A. Düster. "A flexible C++ framework for the partitioned solution of strongly coupled multifield problems". In: *Computers & Mathematics with Applications* 72.7 (2016), pp. 1764–1789. DOI: 10.1016/j.camwa.2016.07.031.

[155] M. Kõrgesaar, P. Kujala, and J. Romanoff. "Load carrying capacity of ice-strengthened frames under idealized ice load and boundary conditions". In: *Marine Structures* 58 (2018), pp. 18–30. DOI: 10.1016/j.marstruc.2017.10.011.

[156] A. Kovacs. *Sea Ice: Part II. Estimating the Full-Scale Tensile, Flexural, and Compressive Strength of First-Year Ice*. 1996.

[157] G. Kuehn and E. Schulson. "The mechanical properties of saline ice under uniaxial compression". In: *Annals of Glaciology* 19 (1994), pp. 39–48. DOI: 10.3189/1994AoG19-1-39-48.

[158] G. Kuehn et al. "The compressive strength of ice cubes of different sizes". In: *Journal of Offshore Mechanics and Arctic Engineering* 115.2 (1993), pp. 142–148. DOI: 10.1115/1.2920104.

[159] E.-J. N. Kuiper et al. "Using a composite flow law to model deformation in the neem deep ice core, greenland – Part 1: The role of grain size and grain size distribution on deformation of the upper 2207 m". In: *The Cryosphere* 14.7 (2020), pp. 2429–2448. DOI: 10.5194/tc-14-2429-2020.

[160] J. Kuutti, K. Kolari, and P. Marjavaara. "Simulation of ice crushing experiments with cohesive surface methodology". In: *Cold Regions Science and Technology* 92 (2013), pp. 17–28. DOI: 10.1016/j.coldregions.2013.03.008.

[161] P. Larrañaga et al. "Machine learning in bioinformatics". In: *Briefings in Bioinformatics* 7.1 (2006), pp. 86–112. DOI: 10.1093/bib/bbk007.

[162] Y. LeCun, Y. Bengio, and G. Hinton. "Deep learning". In: *Nature* 521.7553 (2015), pp. 436–444. DOI: 10.1038/nature14539.

[163] R. H. Leicester. *Effect of Size on the Strength of Structures*. Melbourne, Australia, 1973. DOI: 10.4225/08/586e8d12bf30b.

[164] A. Leiserowitz et al. *Politics & Global Warming, April 2019*. New Haven, USA, 2019. DOI: 10.17605/OSF.IO/NBJGS.

[165] D. Lesar. *Modeling and Simulation of Ice Failure Modes During Ice Floe / Ship Structure Collision: NSWCCD-65-TR-2017/12*. 2017.

[166] X. Li and J. Zhao. "An overview of particle-based numerical manifold method and its application to dynamic rock fracturing". In: *Journal of Rock Mechanics and Geotechnical Engineering* 11.3 (2019), pp. 684–700. DOI: 10.1016/j.jrmge.2019.02.003.

[167] J. Lian et al. "Uniaxial compressive strength and fracture mode of lake ice at moderate strain rates based on a digital speckle correlation method for deformation measurement". In: *Applied Sciences* 7.5 (2017), p. 495. DOI: 10.3390/app7050495.

[168] Z. C. Lipton. "The mythos of model interpretability". In: *ACM Queue* 16.3 (2018). DOI: 10.1145/3236386.3241340.

[169] L. Liu and M. Özsu, eds. *Encyclopedia of Database Systems*. Boston, MA: Springer US, 2009. DOI: 10.1007/978-0-387-39940-9.

[170] M. Liu and G. Liu. "Smoothed Particle Hydrodynamics (SPH): An overview and recent developments". In: *Archives of Computational Methods in Engineering* 17.1 (2010), pp. 25–76. DOI: 10.1007/s11831-010-9040-7.

[171] Z. Liu, J. Amdahl, and S. Løset. "Plasticity based material modelling of ice and its application to ship–iceberg impacts". In: *Cold Regions Science and Technology* 65.3 (2011), pp. 326–334. DOI: 10.1016/j.coldregions.2010.10.005.

[172] M. Llorens et al. "Dynamic recrystallisation of ice aggregates during co-axial viscoplastic deformation: a numerical approach". In: *Journal of Glaciology* 62.232 (2016), pp. 359–377. DOI: 10.1017/jog.2016.28.

[173] *LS-Dyna Keyword User's Manual: Volume II Material Models 10/12/18 (r:10572)*. 2019.

[174] *LS-Dyna Theory Manual: 07/24/19 (r:11261)*. 2019.

[175] W. Lu, R. Lubbad, and S. Løset. "In-plane fracture of an ice floe: A theoretical study on the splitting failure mode". In: *Cold Regions Science and Technology* 110 (2015), pp. 77–101. DOI: 10.1016/j.coldregions.2014.11.007.

[176] W. Lu et al. "A large scale simulation of floe-ice fractures and validation against full-scale scenario". In: *International Journal of Naval Architecture and Ocean Engineering* 10.3 (2018), pp. 393–402. DOI: 10.1016/j.ijnaoe.2018.02.006.

[177] W. Lu et al. "Medium-scale consolidation of artificial ice ridge – Part II: Fracture properties investigation by a splitting test". In: *Proceedings of the 25th International Conference on Port and Ocean Engineering under Arctic Conditions*. 2019.

[178] S. M. Lundberg, G. G. Erion, and S.-I. Lee. *Consistent Individualized Feature Attribution for Tree Ensembles*. 2019. URL: http://arxiv.org/pdf/1802.03888v3.

[179] S. M. Lundberg and S.-I. Lee. "A unified approach to interpreting model predictions". In: *Neural Information Processing Systems Proceedings 2017*. 2017.

[180] S. M. Lundberg et al. "From local explanations to global understanding with explainable AI for trees". In: *Nature Machine Intelligence* 2.1 (2020), pp. 56–67. DOI: 10.1038/s42256-019-0138-9.

[181] K. Madi et al. "Estimating RVE sizes for 2D/3D viscoplastic composite materials". In: *Matériaux*. 2006.

[182] G. Marsaglia. "Choosing a point from the surface of a sphere". In: *The Annals of Mathematical Statistics* 43.2 (1972), pp. 645–646. DOI: 10.1214/aoms/1177692644.

[183] H. Mason and C. Wiggins. *A Taxonomy of Data Science*. 2010. URL: http://www.dataists.com/2010/09/a-taxonomy-of-data-science/ (visited on 05/04/2021).

[184] H. Matlock, W. Dawkins, and J. Panak. "A model for the prediction of ice-structure internation". In: *Offshore Technology Conference*. Offshore Technology Conference, 1969. DOI: 10.4043/1066-MS.

[185] C. F. Matta et al. "Can one take the logarithm or the sine of a dimensioned quantity or a unit? Dimensional analysis involving transcendental functions". In: *Journal of Chemical Education* 88.1 (2011), pp. 67–70. DOI: 10.1021/ed1000476.

[186] B. W. Matthews. "Comparison of the predicted and observed secondary structure of T4 phage lysozyme". In: *Biochimica et Biophysica Acta (BBA) - Protein Structure* 405.2 (1975), pp. 442–451. DOI: 10.1016/0005-2795(75)90109-9.

[187] M. Mellor and D. Cole. "Deformation and failure of ice under constant stress or constant strain-rate". In: *Cold Regions Science and Technology* 5.3 (1982), pp. 201–219. DOI: 10.1016/0165-232X(82)90015-5.

[188] M. Mellor and I. Hawkes. "Measurement of tensile strength by diametral compression of discs and annuli". In: *Engineering Geology* 5.3 (1971), pp. 173–225. DOI: 10.1016/0013-7952(71)90001-9.

[189] J. Melton and E. Schulson. "Ductile compressive failure of columnar saline ice under triaxial loading". In: *Journal of Geophysical Research* 103.C10 (1998), pp. 21759–21766. DOI: 10.1029/98JC01266.

[190] A.-S. Milaković et al. "Equivalent ice thickness in ship ice transit simulations: Overview of existing definitions and proposition of an improved one". In: *Ship Technology Research* 291 (2019), pp. 1–17. DOI: 10.1080/09377255.2019.1655260.

[191] Y. Mizuno. "Effect of hydrostatic confining pressure on the failure mode and compressive strength of polycrystalline ice". In: *The Journal of Physical Chemistry B* 102.2 (1998), pp. 376–381. DOI: 10.1021/jp963163b.

[192] C. Molnar. *Interpretable machine learning ; A guide for making black box models explainable*. Leanpub, 2020.

[193] M. Montagnat et al. "Measurements and full-field predictions of deformation heterogeneities in ice". In: *Earth and Planetary Science Letters* 305.1-2 (2011), pp. 153–160. DOI: 10.1016/j.epsl.2011.02.050.

[194] M. Montagnat and E. M. Schulson. "On friction and surface cracking during sliding of ice on ice". In: *Journal of Glaciology* 49.166 (2003), pp. 391–396. DOI: 10.3189/172756503781830647.

[195] P. O. Moslet. "Field testing of uniaxial compression strength of columnar sea ice". In: *Cold Regions Science and Technology* 48.1 (2007), pp. 1–14. DOI: 10.1016/j.coldregions.2006.08.025.

[196] S. Mulmule and J. Dempsey. "Scale effects on sea ice fracture". In: *Mechanics of Cohesive-frictional Materials* 4.6 (1999), pp. 505–524. DOI: 10.1002/(SICI)1099-1484(199911)4:6<505::AID-CFM67>3.0.CO;2-P.

[197] S. V. Mulmule and J. P. Dempsey. "Lefm size requirements for the fracture testing of sea ice". In: *International Journal of Fracture* 102.1 (2000), pp. 85–98. DOI: 10.1023/A:1007603428907.

[198] J. Nadreau, A. Nawwar, and Y. Wang. "Triaxial testing of freshwater ice at low confining pressures". In: *Journal of Offshore Mechanics and Arctic Engineering* 113.3 (1991), p. 260. DOI: 10.1115/1.2919929.

[199] S. Nanthikesan and S. Sunder. "Anisotropic elasticity of polycrystalline ice". In: *Cold Regions Science and Technology* 22.2 (1994), pp. 149–169. DOI: 10.1016/0165-232X(94)90026-4.

[200] V. P. Nguyen. "Discontinuous galerkin/extrinsic cohesive zone modeling: implementation caveats and applications in computational fracture mechanics". In: *Engineering Fracture Mechanics* 128 (2014), pp. 37–68. DOI: 10.1016/j.engfracmech.2014.07.003.

[201] L. Noels and R. Radovitzky. "A general discontinuous galerkin method for finite hyperelasticity: formulation and numerical applications". In: *International Journal for Numerical Methods in Engineering* 68.1 (2006), pp. 64–97. DOI: 10.1002/nme.1699.

[202] T. O'Malley et al. *keras-tuner*. github.com/keras-team/keras-tuner, 2019. URL: keras-team.github.io/keras-tuner/.

[203] A. Öchsner. *Continuum Damage and Fracture Mechanics*. Singapore: Springer Singapore, 2016. DOI: 10.1007/978-981-287-865-6.

[204] M. Ostoja-Starzewski et al. "Scaling to RVE in random media". In: *Advances in Applied Mechanics*. Vol. 49. Advances in Applied Mechanics. Elsevier, 2016, pp. 111–211. DOI: 10.1016/bs.aams.2016.07.001.

[205] M. Ostoja-Starzewski. "Material spatial randomness: from statistical to Representative Volume Element". In: *Probabilistic Engineering Mechanics* 21.2 (2006), pp. 112–132. DOI: 10.1016/j.probengmech.2005.07.007.

[206] D. H. Pahr and P. K. Zysset. "Influence of boundary conditions on computed apparent elastic properties of cancellous bone". In: *Biomechanics and modeling in mechanobiology* 7.6 (2008), pp. 463–476. DOI: 10.1007/s10237-007-0109-7.

[207] A. Palmer and M. Bjerkås. "Synchronisation and the transition from intermittent to locked-in ice induced vibration". In: *Proceedings of the 22th International Conference on Port and Ocean Engineering under Arctic Conditions*. 2013.

[208] A. Palmer and J. Dempsey. "Model tests in ice". In: *Proceedings of the 20th International Conference on Port and Ocean Engineering under Arctic Conditions*. 2009.

[209] A. Palmer and K. Croasdale. *Arctic offshore engineering*. Hackensack New Jersey, USA: World Scientific, 2013.

[210] W. Pan, A. Tartakovsky, and J. Monaghan. "Smoothed Particle Hydrodynamics non-Newtonian model for ice-sheet and ice-shelf dynamics". In: *Journal of Computational Physics* 242 (2013), pp. 828–842. DOI: 10.1016/j.jcp.2012.10.027.

[211] K. Park and G. H. Paulino. "Cohesive Zone Models: A critical review of traction-separation relationships across fracture surfaces". In: *Applied Mechanics Reviews* 64.6 (2011), p. 203. DOI: 10.1115/1.4023110.

[212] K. Park et al. "Prediction of interfacial fracture between concrete and fiber reinforced polymer (FRP) by using cohesive zone modeling". In: *Cement and Concrete Composites* 63 (2015), pp. 122–131. DOI: 10.1016/j.cemconcomp.2015.07.008.

[213] F. Pedregosa et al. "Scikit-learn: Machine learning in Python". In: *The Journal of Machine Learning Research* 12 (2011), pp. 2825–2830.

[214] C. Pelissou et al. "Determination of the size of the Representative Volume Element for random quasi-brittle composites". In: *International Journal of Solids and Structures* 46.14-15 (2009), pp. 2842–2855. DOI: 10.1016/j.ijsolstr.2009.03.015.

[215] J. Petrovic. "Review mechanical properties of ice and snow". In: *Journal of Materials Science* 38.1 (2003), pp. 1–6. DOI: 10.1023/A:1021134128038.

[216] R. C. Picu and Gupta. "Crack nucleation in columnar ice due to elastic anisotropy and grain boundary sliding". In: *Acta Metallurgica et Materialia* 43.10 (1995), pp. 3783–3789. DOI: 10.1016/0956-7151(95)90162-0.

[217] W. Popko. "Impact of sea ice loads on global dynamics of offshore wind turbines". PhD thesis. Hannover, Germany: Gottfried Wilhelm Leibniz Universität Hannover, 2020.

[218] J. P. Poplin and A. T. Wang. "Mechanical properties of rafted annual sea ice". In: *Cold Regions Science and Technology* 23.1 (1994), pp. 41–67. DOI: 10.1016/0165-232X(94)90011-6.

[219] C. Qi et al. "Dynamic compressive strength and failure of natural lake ice under moderate strain rates at near melting point temperature". In: *Latin American Journal of Solids and Structures* 14.9 (2017), pp. 1669–1694. DOI: 10.1590/1679-78253907.

[220] S. Qi and E. Schulson. "The effect of temperature on the ductile-to-brittle transition in columnar ice". In: *Proceedings of the 14th IAHR International Symposium on Ice*. 1998.

[221] R. Quey and L. Renversade. "Optimal polyhedral description of 3D polycrystals: method and application to statistical and synchrotron x-ray diffraction data". In: *Computer Methods in Applied Mechanics and Engineering* 330 (2018), pp. 308–333. DOI: 10.1016/j.cma.2017.10.029.

[222] B. Quinton et al. "Experimental investigation of accidental sliding loads on the response of hull plating". In: *Progress in the Analysis and Design of Marine Structures*. Ed. by C. Soares and Y. Garbatov. 2017, pp. 513–522. DOI: 10.1201/9781315157368-59.

[223] R. Radovitzky et al. "A scalable 3D fracture and fragmentation algorithm based on a hybrid, discontinuous galerkin, cohesive element method". In: *Computer Methods in Applied Mechanics and Engineering* 200.1-4 (2011), pp. 326–344. DOI: 10.1016/j.cma.2010.08.014.

[224] F. Ralph and I. Jordaan. "Local design pressures during ship ram events modeling the ocurrence and intensity of high pressure zones". In: *Proceedings of the ASME 2017 36th International Conference on Ocean, Offshore and Arctic Engineering*. 2017.

[225] P. Refaeilzadeh, L. Tang, and L. Huan. "Cross-validation". In: *Encyclopedia of Database Systems*. Ed. by L. Liu and M. Özsu. Boston, MA: Springer US, 2009, pp. 532–537.

[226] C. Renshaw, N. Golding, and E. Schulson. "Maps for brittle and brittle-like failure in ice". In: *Cold Regions Science and Technology* 97 (2014), pp. 1–6. DOI: 10.1016/j.coldregions.2013.09.008.

[227] C. Renshaw and E. Schulson. "Strength-limiting mechanisms in high-confinement brittle-like failure: Adiabatic transformational faulting". In: *Journal of Geophysical Research: Solid Earth* 122.2 (2017), pp. 1088–1106. DOI: 10.1002/2016JB013407.

[228] C. Renshaw and E. Schulson. "Universal behaviour in compressive failure of brittle materials". In: *Nature* 412.6850 (2001), pp. 897–900. DOI: 10.1038/35091045.

[229] M. T. Ribeiro, S. Singh, and C. Guestrin. "Why should I trust you?" In: *Proceedings of the 22nd ACM SIGKDD International Conference on Knowledge Discovery and Data Mining - KDD '16*. Ed. by B. Krishnapuram et al. New York, USA: ACM Press, 2016, pp. 1135–1144. DOI: 10.1145/2939672.2939778.

[230] J. Rice. "The mechanics of earthquake rupture". In: *Physics of the earth's interior*. Ed. by A. Dziewonski and E. Boschi. Proceedings of the International School of Physics "Enrico Fermi". Amsterdam: North-Holland Publ. Co, 1980.

[231] J. Richter-Menge and K. Jones. "The tensile strength of first-year sea ice". In: *Journal of Glaciology* 39.133 (1993), pp. 609–618. DOI: 10.1017/S0022143000016506.

[232] J. Richter-Menge et al. *Triaxial testing of first-year sea ice: CRREL Report 86-16*. 1986.

[233] J. J. Rimoli and J. J. Rojas. "Meshing strategies for the alleviation of mesh-induced effects in Cohesive Element Models". In: *International Journal of Fracture* 193.1 (2015), pp. 29–42. DOI: 10.1007/s10704-015-0013-6.

[234] M. Rist. "High-stress ice fracture and friction". In: *The Journal of Physical Chemistry B* 101.32 (1997), pp. 6263–6266. DOI: 10.1021/jp963175x.

[235] M. Rist and S. Murrell. "Ice triaxial deformation and fracture". In: *Journal of Glaciology* 40.135 (1994), pp. 305–318. DOI: 10.1017/S0022143000007395.

[236] Robin Härer. "Compression tests of laboratory-made freshwater ice". Project Thesis. Hamburg University of Technology, 2019.

[237] J. Roessiger et al. "Competition between grain growth and grain-size reduction in polar ice". In: *Journal of Glaciology* 57.205 (2011), pp. 942–948. DOI: 10.3189/002214311798043690.

[238] H. Rojas-Romagosa, J. Francois, and E. H. Bekkers. *Melting Ice Caps and the Economic Impact of Opening the Northern Sea Route*. 2016. DOI: 10.7892/boris.89212.

[239] R. Roscher et al. "Explainable machine learning for scientific insights and discoveries". In: *IEEE Access* 8 (2020), pp. 42200–42216. DOI: 10.1109/ACCESS.2020.2976199.

[240] S. Saeb, P. Steinmann, and A. Javili. "Aspects of computational homogenization at finite deformations: A unifying review from Reuss' to Voigt's bound". In: *Applied Mechanics Reviews* 68.5 (2016). DOI: 10.1115/1.4034024.

[241] P. R. Sammonds, S. A. F. Murrell, and M. A. Rist. "Fracture of multiyear sea ice". In: *Journal of Geophysical Research* 103.C10 (1998), pp. 21795–21815. DOI: 10.1029/98JC01260.

[242] T. Sanderson. *Ice Mechanics and Risks to Offshore Structures*. 1st ed. Vol. 1. Cold Region Engineering Studies. Berlin: Springer, 1988.

[243] J. Schmidt et al. "Recent advances and applications of machine learning in solid-state materials science". In: *npj Computational Materials* 5.1 (2019), p. 484. DOI: 10.1038/s41524-019-0221-0.

[244] K. Schneider. "Computational micromechanics of matrix-inclusion composites". PhD thesis. Hamburg University of Technology, 2019. DOI: 10.15480/882.2520.

[245] K. Schneider, B. Klusemann, and S. Bargmann. "Fully periodic RVEs for technological relevant composites: not worth the effort!" In: *Journal of Mechanics of Materials and Structures* 12.4 (2017), pp. 471–484. DOI: 10.2140/jomms.2017.12.471.

[246] E. Schulson. "Brittle failure of ice". In: *Engineering Fracture Mechanics* 68.17-18 (2001), pp. 1839–1887. DOI: 10.1016/S0013-7944(01)00037-6.

[247] E. Schulson. "Compressive shear faults in ice: Plastic vs. coulombic faults". In: *Acta Materialia* 50.13 (2002), pp. 3415–3424. DOI: 10.1016/S1359-6454(02)00154-4.

[248] E. Schulson. "Fracture of ice on scales large and small". In: *IUTAM Symposium on Scaling Laws in Ice Mechanics and Ice Dynamics*. Ed. by J. P. Dempsey and H. H. Shen. Vol. 94. Solid Mechanics and Its Applications. Dordrecht: Springer Netherlands, 2001, pp. 161–170. DOI: 10.1007/978-94-015-9735-7_14.

[249] E. Schulson. "Friction of sea ice". In: *Philosophical transactions. Series A, Mathematical, physical, and engineering sciences* 376.2129 (2018). DOI: 10.1098/rsta.2017.0336.

[250] E. Schulson. "Low-speed friction and brittle compressive failure of ice: Fundamental processes in ice mechanics". In: *International Materials Reviews* 60.8 (2015), pp. 451–478. DOI: 10.1179/1743280415Y.0000000010.

[251] E. Schulson. "The brittle compressive fracture of ice". In: *Acta Metallurgica et Materialia* 38.10 (1990), pp. 1963–1976. DOI: 10.1016/0956-7151(90)90308-4.

[252] E. Schulson. "The fracture of ice Ih". In: *Le Journal de Physique Colloques* 48.C1 (1987), pp. C1-207-C1–220. DOI: 10.1051/jphyscol:1987129.

[253] E. Schulson. "The fracture of water ice Ih: A short overview". In: *Meteoritics & Planetary Science* 41.10 (2006), pp. 1497–1508. DOI: 10.1111/j.1945-5100.2006.tb00432.x.

[254] E. Schulson. "The structure and mechanical behavior of ice". In: *JOM* 51.2 (1999), pp. 21–27. DOI: 10.1007/s11837-999-0206-4.

[255] E. Schulson and S. Buck. "The ductile-to-brittle transition and ductile failure envelopes of orthotropic ice under biaxial compression". In: *Acta Metallurgica et Materialia* 43.10 (1995), pp. 3661–3668. DOI: 10.1016/0956-7151(95)90149-3.

[256] E. Schulson and P. Duval. *Creep and fracture of ice*. Cambridge: Cambridge University Press, 2009.

[257] E. Schulson and A. Fortt. "Friction of ice on ice". In: *Journal of Geophysical Research* 117.B12 (2012). DOI: 10.1029/2012JB009219.

[258] E. Schulson and E. Gratz. "The brittle compressive failure of orthotropic ice under triaxial loading". In: *Acta Materialia* 47.3 (1999), pp. 745–755. DOI: 10.1016/S1359-6454(98)00410-8.

[259] E. Schulson, P. Lim, and R. Lee. "A brittle to ductile transition in ice under tension". In: *Philosophical Magazine A* 49.3 (1984), pp. 353–363. DOI: 10.1080/01418618408233279.

[260] E. Schulson and O. Y. Nickolayev. "Failure of columnar saline ice under biaxial compression: Failure envelopes and the brittle-to-ductile transition". In: *Journal of Geophysical Research* 100.B11 (1995), pp. 22383–22400. DOI: 10.1029/95JB02513.

[261] E. Schulson et al. "Failure envelope of first-year arctic sea ice: the role of friction in compressive fracture". In: *Journal of Geophysical Research* 111.C11 (2006). DOI: 10.1029/2005JC003235.

[262] E. Schulson et al. "On the role of frictional sliding in the compressive fracture of ice and granite: Terminal vs. post-terminal failure". In: *Acta Materialia* 54.15 (2006), pp. 3923–3932. DOI: 10.1016/j.actamat.2006.04.024.

[263] V.-G. Schulze. *Arctic Strategies Round-up 2017*. 2017.

[264] J. Schwarz and W. F. Weeks. "Engineering properties of sea ice". In: *Journal of Glaciology* 19.81 (1977), pp. 499–531. DOI: 10.3189/S0022143000029476.

[265] A. Seagraves and R. Radovitzky. "Advances in cohesive zone modeling of dynamic fracture". In: *Dynamic Failure of Materials and Structures*. Ed. by A. Shukla, G. Ravichandran, and Y. D. Rajapakse. Vol. 143. Boston, MA: Springer US, 2010, pp. 349–405. DOI: 10.1007/978-1-4419-0446-1_12.

[266] J. Segurado, R. A. Lebensohn, and J. LLorca. "Computational homogenization of polycrystals". In: *Advances in Crystals and Elastic Metamaterials, Part 1*. Vol. 51. Advances in Applied Mechanics. Elsevier, 2018, pp. 1–114. DOI: 10.1016/bs.aams.2018.07.001.

[267] Z. Shabir et al. "The role of cohesive properties on intergranular crack propagation in brittle polycrystals". In: *Modelling and Simulation in Materials Science and Engineering* 19.3 (2011), p. 035006. DOI: 10.1088/0965-0393/19/3/035006.

[268] M. Shazly and V. Prakash. *High-Strain-Rate Compression Testing of Ice: NASA/TM—2006-213966*. 2006.

[269] M. Shazly, V. Prakash, and B. A. Lerch. "High strain-rate behavior of ice under uniaxial compression". In: *International Journal of Solids and Structures* 46.6 (2009), pp. 1499–1515. DOI: 10.1016/j.ijsolstr.2008.11.020.

[270] H. Shen and L. C. Brinson. "Finite element modeling of porous titanium". In: *International Journal of Solids and Structures* 44.1 (2007), pp. 320–335. DOI: 10.1016/j.ijsolstr.2006.04.020.

[271] H. Shen and L. C. Brinson. "A numerical investigation of the effect of boundary conditions and Representative Volume Element size for porous titanium". In: *Journal of Mechanics of Materials and Structures* 1.7 (2006), pp. 1179–1204. DOI: 10.2140/jomms.2006.1.1179.

[272] N. Sinha. "Elasticity of natural types of polycrystalline ice". In: *Cold Regions Science and Technology* 17.2 (1989), pp. 127–135. DOI: 10.1016/S0165-232X(89)80003-5.

[273] N. Sinha. "Field test 1 of compressive strength of first-year sea ice". In: *Annals of Glaciology* 4 (1983), pp. 253–259. DOI: 10.3189/S0260305500005565.

[274] M. A. Slawinski. *Seismic waves and rays in elastic media*. Vol. v. 34. Seismic exploration. Amsterdam: Pergamon, 2003.

[275] T. Smith and E. Schulson. "The brittle compressive failure of fresh-water columnar ice under biaxial loading". In: *Acta Metallurgica et Materialia* 41.1 (1993), pp. 153–163. DOI: 10.1016/0956-7151(93)90347-U.

[276] S. Snyder. "Mechanical behavior and elastic properties of prestrained columnar ice". PhD thesis. Hanover, New Hampshire: Dartmouth College, 2015.

[277] S. Snyder, E. Schulson, and C. Renshaw. "Effects of prestrain on the ductile-to-brittle transition of ice". In: *Acta Materialia* 108 (2016), pp. 110–127. DOI: 10.1016/j.actamat.2016.01.062.

[278] S. Snyder, E. Schulson, and C. Renshaw. "The role of damage and recrystallization in the elastic properties of columnar ice". In: *Journal of Glaciology* 61.227 (2015), pp. 461–480. DOI: 10.3189/2015JoG14J225.

[279] T. Soler. "Active versus passive rotations". In: *Journal of Surveying Engineering* 144.1 (2018), p. 06017004. DOI: 10.1061/(ASCE)SU.1943-5428.0000247.

[280] A. Spettl et al. "Parametric representation of 3D grain ensembles in polycrystalline microstructures". In: *Journal of Statistical Physics* 154.4 (2014), pp. 913–928. DOI: 10.1007/s10955-013-0893-7.

[281] J. S. Steenfelt. "Ice loads on structures in the baltic environment". In: *Proceedings of 13th Baltic Sea Geotechnical Conference*. Ed. by J. Medzvieckas. 2016, pp. 129–136. DOI: 10.3846/13bsgc.2016.018.

[282] M. Stender. "Data-driven techniques for the nonlinear dynamics of mechanical structures". PhD thesis. Hamburg University of Technology, 2020. DOI: 10.15480/882.3055.

[283] M. Stender et al. "Explainable machine learning determines effects on the sound absorption coefficient measured in the impedance tube". In: *The Journal of the Acoustical Society of America* 149.3 (2021), p. 1932. DOI: 10.1121/10.0003755.

[284] B. Stone et al. "Experiments on the damage process in ice under compressive states of stress". In: *Journal of Glaciology* 43.143 (1997).

[285] L. Strub-Klein. "A statistical analysis of first-year level ice uniaxial compressive strength in the Svalbard area". In: *Journal of Offshore Mechanics and Arctic Engineering* 139.1 (2017), p. 011503. DOI: 10.1115/1.4034526.

[286] L. Strub-Klein and D. Sudom. "A comprehensive analysis of the morphology of first-year sea ice ridges". In: *Cold Regions Science and Technology* 82 (2012), pp. 94–109. DOI: 10.1016/j.coldregions.2012.05.014.

[287] D. Sudom and G. Timco. "Knowledge gaps in sea ice ridge properties". In: *Proceedings of the 22th International Conference on Port and Ocean Engineering under Arctic Conditions*. 2013.

[288] C. T. Sun and Z.-H. Jin. "Cohesive Zone Model". In: *Fracture Mechanics*. Elsevier, 2012, pp. 227–246. DOI: 10.1016/B978-0-12-385001-0.00009-2.

[289] A. Tabiei and W. Zhang. "Cohesive element approach for dynamic crack propagation: Artificial compliance and mesh dependency". In: *Engineering Fracture Mechanics* 180 (2017), pp. 23–42. DOI: 10.1016/j.engfracmech.2017.05.009.

[290] *Tahoe User Guide: Input Version 3.4.1*. 2003.

[291] R. Taylor and I. Jordaan. "Probabilistic fracture mechanics analysis of spalling during edge indentation in ice". In: *Engineering Fracture Mechanics* 134 (2015), pp. 242–266. DOI: 10.1016/j.engfracmech.2014.10.021.

[292] M. G. Tijssens, B. L. Sluys, and E. van der Giessen. "Numerical simulation of quasi-brittle fracture using damaging cohesive surfaces". In: *European Journal of Mechanics - A/Solids* 19.5 (2000), pp. 761–779. DOI: 10.1016/S0997-7538(00)00190-X.

[293] G. Timco and R. Frederking. "An investigation of the failure envelope of granular/discontinuous-columnar sea ice". In: *Cold Regions Science and Technology* 9.1 (1984), pp. 17–27. DOI: 10.1016/0165-232X(84)90044-2.

[294] G. Timco and R. Frederking. "Confined compression tests: Outlining the failure envelope of columnar sea ice". In: *Cold Regions Science and Technology* 12.1 (1986), pp. 13–28. DOI: 10.1016/0165-232X(86)90016-9.

[295] G. Timco and R. Frederking. "Compressive strength of sea ice sheets". In: *Cold Regions Science and Technology* 17.3 (1990), pp. 227–240. DOI: 10.1016/S0165-232X(05)80003-5.

[296] G. Timco and S. O'Brien. "Flexural strength equation for sea ice". In: *Cold Regions Science and Technology* 22.3 (1994), pp. 285–298. DOI: 10.1016/0165-232X(94)90006-X.

[297] G. Timco and W. Weeks. "A review of the engineering properties of sea ice". In: *Cold Regions Science and Technology* 60.2 (2010), pp. 107–129. DOI: 10.1016/j.coldregions.2009.10.003.

[298] V. Tomar, J. Zhai, and M. Zhou. "Bounds for element size in a variable stiffness cohesive Finite Element Model". In: *International Journal for Numerical Methods in Engineering* 61.11 (2004), pp. 1894–1920. DOI: 10.1002/nme.1138.

[299] A. Turon et al. "An engineering solution for mesh size effects in the simulation of delamination using Cohesive Zone Models". In: *Engineering Fracture Mechanics* 74.10 (2007), pp. 1665–1682. DOI: 10.1016/j.engfracmech.2006.08.025.

[300] P. Vannucci. *Anisotropic elasticity*. Vol. 85. Lecture notes in applied and computational mechanics. Singapore: Springer, 2017. DOI: 10.1007/978-981-10-5439-6.

[301] P. Virtanen et al. "SciPy 1.0: Fundamental algorithms for scientific computing in python". In: *Nature methods* 17.3 (2020), pp. 261–272. DOI: 10.1038/s41592-019-0686-2.

[302] F. von Bock und Polach and S. Ehlers. "On the scalability of model-scale ice experiments". In: *Journal of Offshore Mechanics and Arctic Engineering* 137.5 (2015), p. 051502. DOI: 10.1115/1.4031114.

[303] F. von Bock und Polach and D. Molyneux. "Model ice: A review of its capacity and identification of knowledge gaps". In: *Proceedings of the ASME 2017 36th International Conference on Ocean, Offshore and Arctic Engineering*. 2017. DOI: 10.1115/OMAE2012-84033.

[304] L. Wachter, C. Renshaw, and E. Schulson. "Transition in brittle failure mode in ice under low confinement". In: *Acta Materialia* 57.2 (2009), pp. 345–355. DOI: 10.1016/j.actamat.2008.09.021.

[305] A. M. Walker and J. Wookey. "MSAT—A new toolkit for the analysis of elastic and seismic anisotropy". In: *Computers & Geosciences* 49 (2012), pp. 81–90. DOI: 10.1016/j.cageo.2012.05.031.

[306] Q. Wang et al. "Estimation of the uniaxial compressive strength of Arctic sea ice during melt season". In: *Cold Regions Science and Technology* 151 (2018), pp. 9–18. DOI: 10.1016/j.coldregions.2018.03.002.

[307] S. Wang and J. P. Dempsey. "A cohesive edge crack". In: *Engineering Fracture Mechanics* 78.7 (2011), pp. 1353–1373. DOI: 10.1016/j.engfracmech.2011.02.018.

[308] S. Wang, I. E. Gharamti, and J. P. Dempsey. "Cohesive cracking in negative geometries". In: *Engineering Fracture Mechanics* 221 (2019), p. 106681. DOI: 10.1016/j.engfracmech.2019.106681.

[309] D. H. Warner and J. F. Molinari. "Micromechanical finite element modeling of compressive fracture in confined alumina ceramic". In: *Acta Materialia* 54.19 (2006), pp. 5135–5145. DOI: 10.1016/j.actamat.2006.06.046.

[310] M. Waskom. "seaborn: Statistical data visualization". In: *Journal of Open Source Software* 6.60 (2021), p. 3021. DOI: 10.21105/joss.03021.

[311] W. Weeks and A. Assur. *The mechanical properties of sea ice*. 1967.

[312] J. Weiss and E. Schulson. "The failure of fresh-water granular ice under multiaxial compressive loading". In: *Acta Metallurgica et Materialia* 43.6 (1995), pp. 2303–2315. DOI: 10.1016/0956-7151(94)00421-8.

[313] J. Weiss et al. "(Finite) statistical size effects on compressive strength". In: *Proceedings of the National Academy of Sciences of the United States of America* 111.17 (2014), pp. 6231–6236. DOI: 10.1073/pnas.1403500111.

[314] C. J. Willmott and K. Matsuura. "Advantages of the mean absolute error (MAE) over the root mean square error (RMSE) in assessing average model performance". In: *Climate Research* 30 (2005), pp. 79–82. DOI: 10.3354/cr030079.

[315] M. N. Wright and I. R. König. "Splitting on categorical predictors in random forests". In: *PeerJ* 7 (2019). DOI: 10.7717/peerj.6339.

[316] M. S. Wu and S. Shyam Sunder. "Elastic anisotropy and micro-damage processes in polycrystalline ice: Part I - Theoretical formulation". In: *International Journal of Fracture* 55.3 (1992), pp. 223–243.

[317] X.-P. Xu and A. Needleman. "Numerical simulations of fast crack growth in brittle solids". In: *Journal of the Mechanics and Physics of Solids* 42.9 (1994), pp. 1397–1434. DOI: 10.1016/0022-5096(94)90003-5.

[318] X. T. Xu, J. H. Yuan, and R. Q. Bai. "Laboratory investigation on mechanical behavior of artificial ice under triaxial compression". In: *Advanced Materials Research* 887-888 (2014), pp. 903–906. DOI: 10.4028/www.scientific.net/AMR.887-888.903.

[319] H. Yang et al. "Transport expansion threatens the Arctic". In: *Science (New York, N.Y.)* 359.6376 (2018), pp. 646.3–647. DOI: 10.1126/science.aar5443.

[320] Z. Yu and J. Amdahl. "A numerical solver for coupled dynamic simulation of glacial ice impacts considering hydrodynamic-ice-structure interaction". In: *Ocean Engineering* 226 (2021), p. 108827. DOI: 10.1016/j.oceaneng.2021.108827.

[321] Q. Yue, F. Guo, and T. Kärnä. "Dynamic ice forces of slender vertical structures due to ice crushing". In: *Cold Regions Science and Technology* 56.2-3 (2009), pp. 77–83. DOI: 10.1016/j.coldregions.2008.11.008.

[322] A. Zaoui. "Continuum micromechanics: Survey". In: *Journal of Engineering Mechanics* 128.8 (2002), pp. 808–816. DOI: 10.1061/(ASCE)0733-9399(2002)128:8(808).

[323] L. Zhang et al. "Uniaxial compressive strengths of artificial freshwater ice". In: *Advanced Materials Research* 243-249 (2011), pp. 4634–4637. DOI: 10.4028/www.scientific.net/AMR.243-249.4634.

[324] W. Zhang, A. Tabiei, and D. French. "Comparison between discontinuous Galerkin method and Cohesive Element Method: On the convergence and dynamic wave propagation issue". In: *International Journal for Computational Methods in Engineering Science and Mechanics* 19.5 (2018), pp. 363–373. DOI: 10.1080/15502287.2018.1535527.

[325] Q. Zhao, E. Adeli, and K. M. Pohl. "Training confounder-free deep learning models for medical applications". In: *Nature communications* 11.1 (2020), p. 6010. DOI: 10.1038/s41467-020-19784-9.

[326] L. ZhiJun et al. "Experimental study on the effect of porosity on the uniaxial compressive strength of sea ice in Bohai Sea". In: *Science China Technological Sciences* 54.9 (2011), pp. 2429–2436. DOI: 10.1007/s11431-011-4482-1.

[327] T. I. Zohdi and P. Wriggers. *An introduction to computational micromechanics*. Vol. 20. Lecture Notes in Applied and Computational Mechanics. Berlin: Springer, 2008.

Appendices

A.1 Codes

The software codes that were used for this research are available online in Zenodo and/or GitHub [143]. Feel free to use them. However, note that they will likely not be updated in the future.

A.2 Switching Voigt notation ordering

The order in which stresses and strains are listed in Eq. (3.6) is not universal. If a different ordering of components in Voigt notation is used, any operations with $\boldsymbol{\sigma}$ or $\boldsymbol{\varepsilon}$ has to be preceded by an index mapping. Alternatively, the columns and rows of $\boldsymbol{C}$ have to be swapped. As an example, take strains in the ordering in Eq. (A.1) as used within the structure solver LS-Dyna [174, p. 22-39].

$$\boldsymbol{\varepsilon}' = \begin{bmatrix} \varepsilon_{11} & \varepsilon_{22} & \varepsilon_{33} & 2\varepsilon_{12} & 2\varepsilon_{23} & 2\varepsilon_{13} \end{bmatrix}^\top \tag{A.1}$$

To calculate stresses with matrix $\boldsymbol{C}$, which corresponds to the ordering in Eq. (3.6), the following mapping with index vectors $\boldsymbol{q}$ and $\boldsymbol{q}'$ has to be used

$$\varepsilon_q = \varepsilon'_{q'} \tag{A.2}$$

$$\boldsymbol{q} = \begin{bmatrix} 1 & 2 & 3 & 4 & 5 & 6 \end{bmatrix} \tag{A.3}$$

$$\boldsymbol{q}' = \begin{bmatrix} 1 & 2 & 3 & 5 & 6 & 4 \end{bmatrix} \tag{A.4}$$

yielding stresses corresponding to the same ordering (Eq. (3.6)). Alternatively, the columns and rows of $\boldsymbol{C}$ can be swapped with q and q' to give $\boldsymbol{C}'$, where e.g. the 6th row of $\boldsymbol{C}$ becomes the 4th row of $\boldsymbol{C}'$. Then the stresses $\boldsymbol{\sigma}' = \boldsymbol{C}'\boldsymbol{\varepsilon}'$ are output in the same ordering as the strains from Eq. (A.1).

A.3 Contact algorithm

Table A.1: Contact algorithm parameters

Parameter	Abbreviation	Value
Static coefficient of friction	FS	0.03
Viscous damping coefficient	VDC	20.0
Soft constraint option	SOFT	2
Segment-based contact options	SBOPT	5.0
Search depth in automatic contact	DEPTH	35

Eroding single surface contact. All values not given are the default values. For more information see [174].

A.4 Cohesive zone user material models

User material models, programmed as LS-Dyna subroutines [65], were used to obtain element information at the points of peak stress and failure (α and β). They were validated against existing material models from the LS-Dyna library. The linear softening model was validated against the cohesive mixed mode model (nr. 138 in the library), based on [47]. The rectangular softening was validated against the Tvergaard-Hutchinson model (nr. 185 in the library) based on [290].

The Tvergaard-Hutchinson model computes separation with a dimensionless gap vector Λ. The separation for the initial and final peak tractions are Λ_1 and Λ_2, respectively, the critical separation is termed Λ_{fail}. These variables are related to the material properties through a trapezoid area without right-hand side slope, i.e. $\Lambda_2 = \Lambda_{\text{fail}}$. Separations are normalized with u_{fail} so that $\Lambda/\Lambda_{\text{fail}} = 1$ for the critical separation.

$$u_1 = \frac{\Sigma_0}{K_{\text{coh}}} \tag{A.5}$$

$$\Lambda_1 = \frac{u_1}{u_{\text{fail}}} \tag{A.6}$$

$$u_2 = u_{\text{fail}} = \frac{G_{\text{c}}}{\Sigma_0} + \frac{\Sigma_0}{2K_{\text{coh}}} \tag{A.7}$$

$$\Lambda_2 = \Lambda_{\text{fail}} = 1 \tag{A.8}$$

See also [145].

A.5 ANN model and results

Below, the artificial feed forward neural networks (ANN) are described. Tensorflow along with Keras API was used [1, 39]. Hyperparameter optimization was done with the kerastuner [202]. Parts of the preprocessing were done with the scikit-learn package [213].

The final model architecture is given in Table A.2. Using different optimizers did not significantly impact performance or predictions. The mini-batch gradient descent method from Keras's stochastic gradient descent (SGD) class was chosen since it is commonly regarded as a good standard option. A preliminary study on logarithmizing target values improved ANN performance, hence the data was logarithmized prior to learning. The ANN model cannot handle missing values (NaNs), therefore firstly features with more than 25 % missing values were excluded and then all samples still containing NaNs were deleted. Afterward, training data was standardized such that

$$z = \frac{x - \bar{x}}{SD} \tag{A.9}$$

with x the original feature value, z the new feature value (i.e., the z-score), $\bar{x}$ and SD the mean and standard deviation of the training sample.

Table A.2: ANN model parameters

Parameter	Strength	Behavior
Input layer	Number of features	Number of features
Hidden layers	3 × 64 RELU	3 × 64 RELU
Output layer function	Linear	Sigmoid
Batch size	128	128
Epochs	400	400
Loss objective	MAE	Log-loss
Early stopping patience	5	5
Early stopping metric	MAE	Accuracy
Optimizer	SGD	SGD
Optimizer learning rate	0.1	0.1
Optimizer momentum	0.9	0.9

RELU is REctified Linear Unit, MAE is mean absolute error, SGD is stochastic gradient descent. For further description of parameters see [1, 39, 83].

Table A.3: Performance of ANN behavior classifier

Metric	Freshwater ice	Saltwater ice
ACC CV average	1.0 ± 0.0	0.87 ± 0.01
ACC final model	1.0	0.82
MCC CV average	1.0 ± 0.0	0.69 ± 0.03
MCC final model	1.0	0.56

CV values are average ± SD, $n = 5$ (number of CV folds).

Table A.4: Performance of ANN strength regression model

Metric	Freshwater ice	Saltwater ice
RMSE CV average	6.66 ± 3.95	2.75 ± 0.35
RMSE final model	4.48	2.80
MAE CV average	3.46 ± 1.45	1.50 ± 0.10
MAE final model	2.44	1.66

CV values are average ± SD, $n = 5$ (number of CV folds).

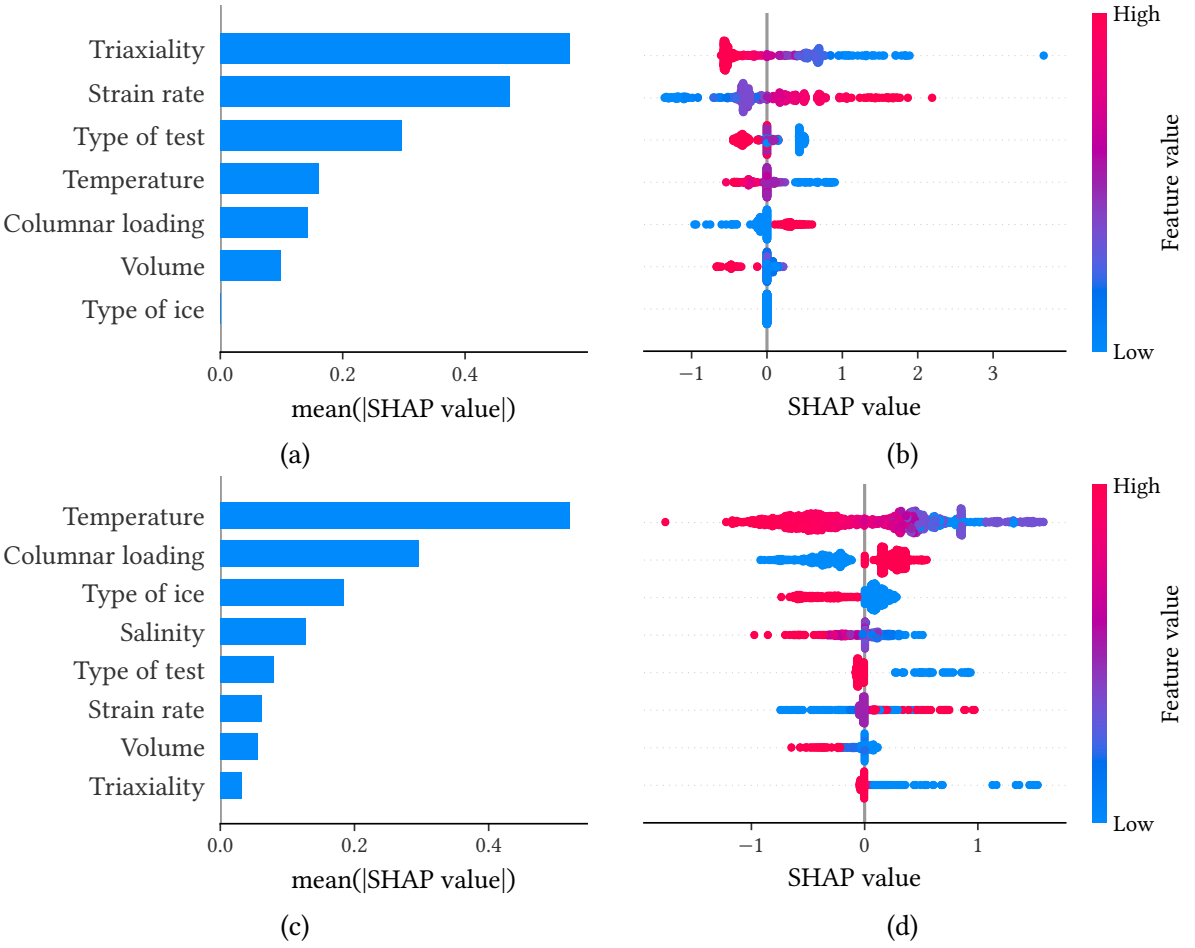

Fig. A.1: Explanation of the ice strength prediction with ANN. (**a, c**) Average SHAP value indicating global feature importance. (**b, d**) Local explanation with beeswarm plots. (**a, b**) For freshwater ice and (**c, d**) for saltwater ice.

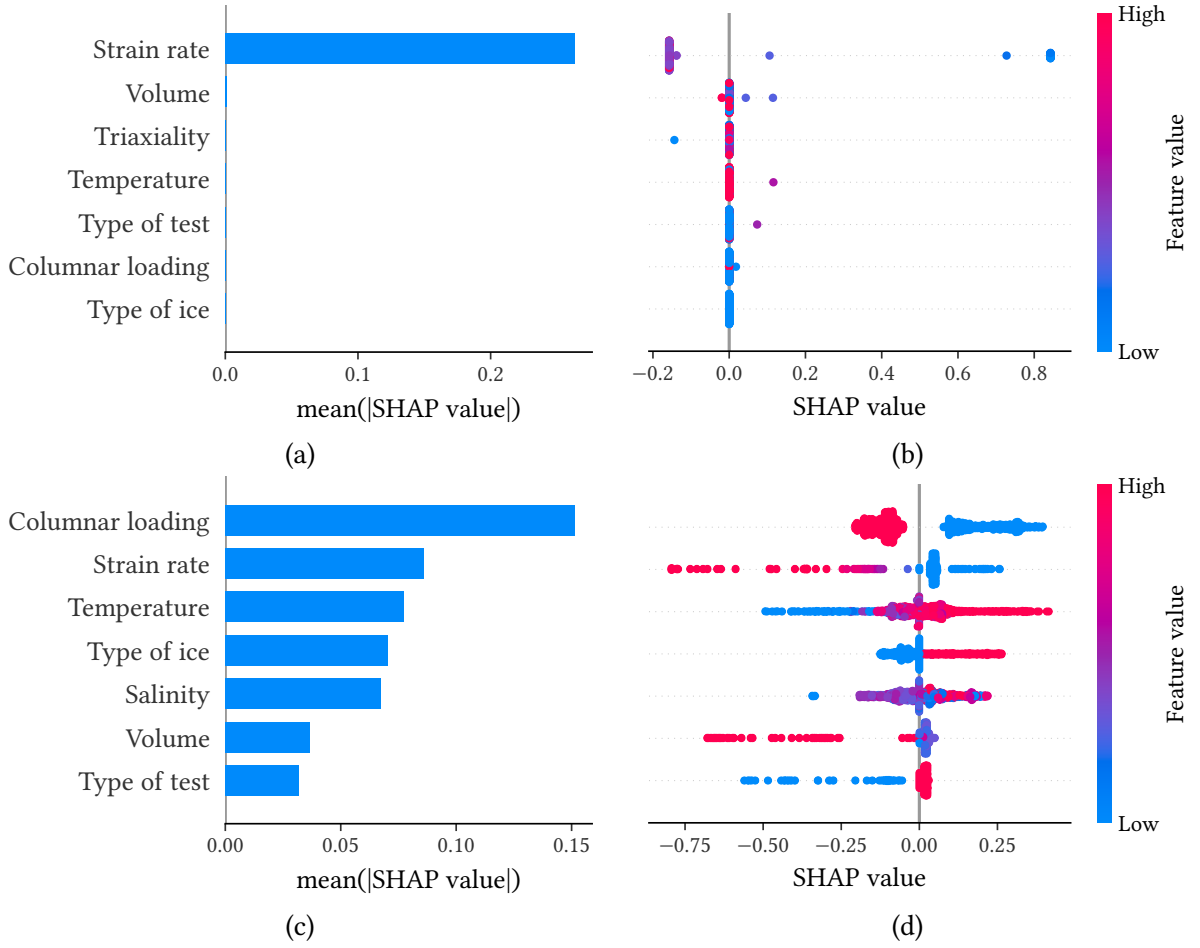

Fig. A.2: Explanation of the saltwater ice behavior prediction with ANN. (**a, c**) Average SHAP value indicating global feature importance. (**b, d**) Local explanation with beeswarm plots. (**a, b**) For freshwater ice and (**c, d**) for saltwater ice.

A.6 QQ plots for RVE study

In Figs. A.3 to A.6 the QQ plots for the 2D and 3D RVE studies are shown. In all cases the dots approach the diagonal lines with an increased number of grains per volume. Hence it is likely that the underlying distribution is normal.

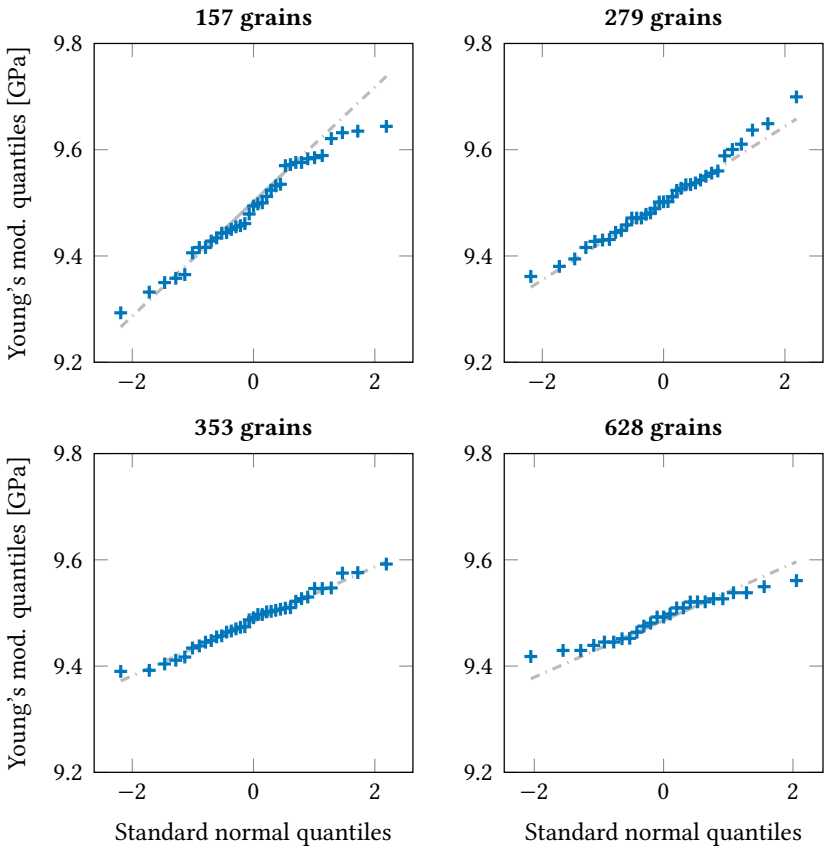

Fig. A.3: QQ plots of Young's modulus for different model sizes for the 2D RVE investigation.

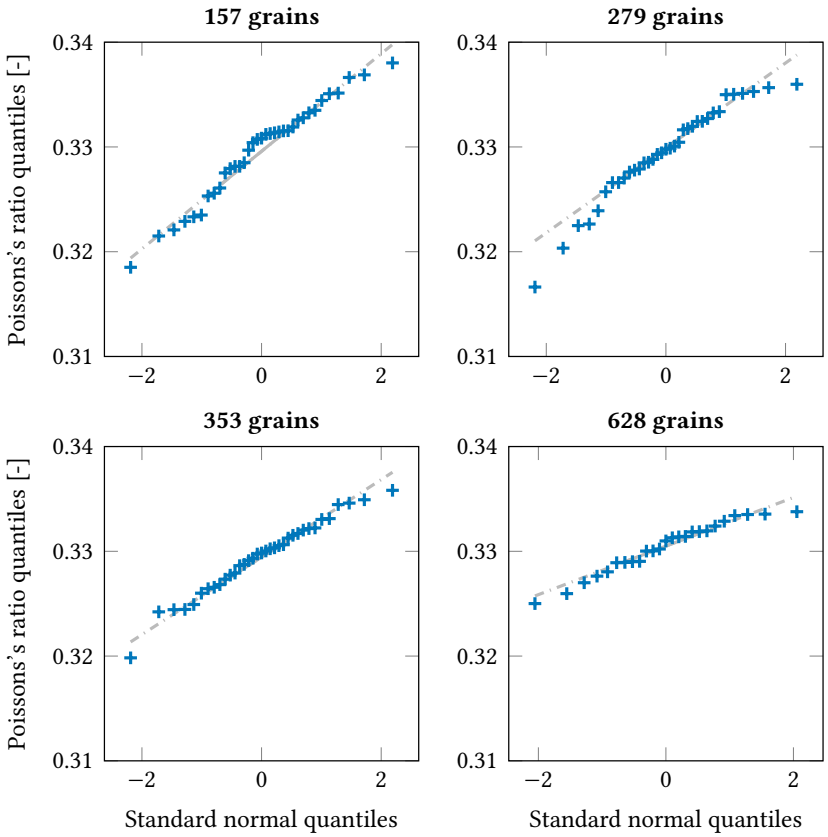

Fig. A.4: QQ plots of Poisson's ratio for different model sizes for the 2D RVE investigation.

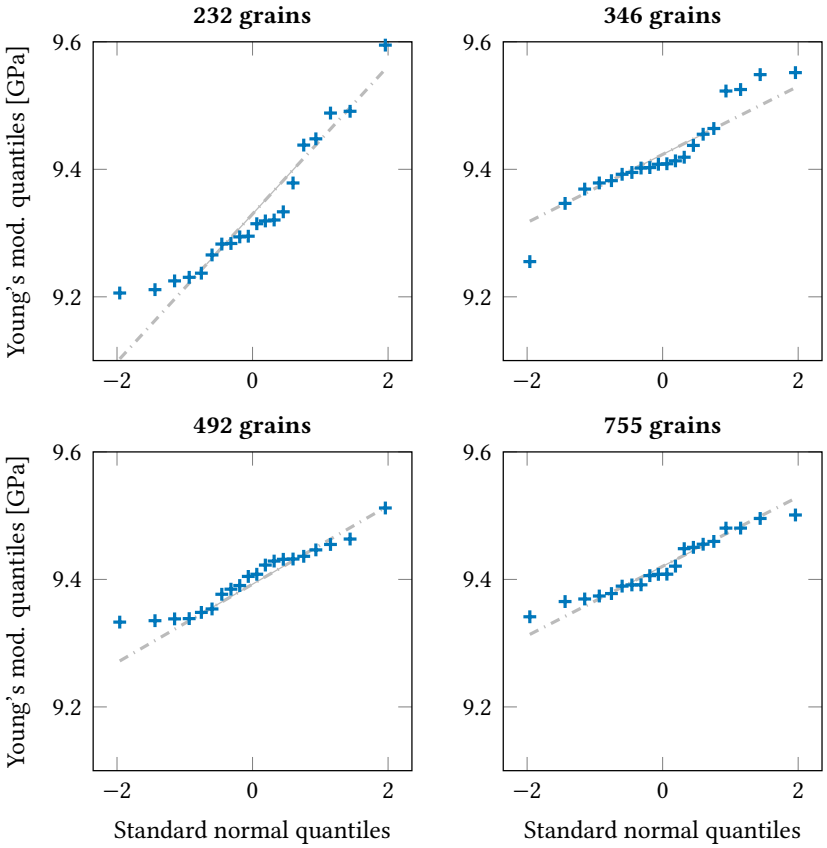

Fig. A.5: QQ plots of Young's modulus for different model sizes for the 3D RVE investigation.

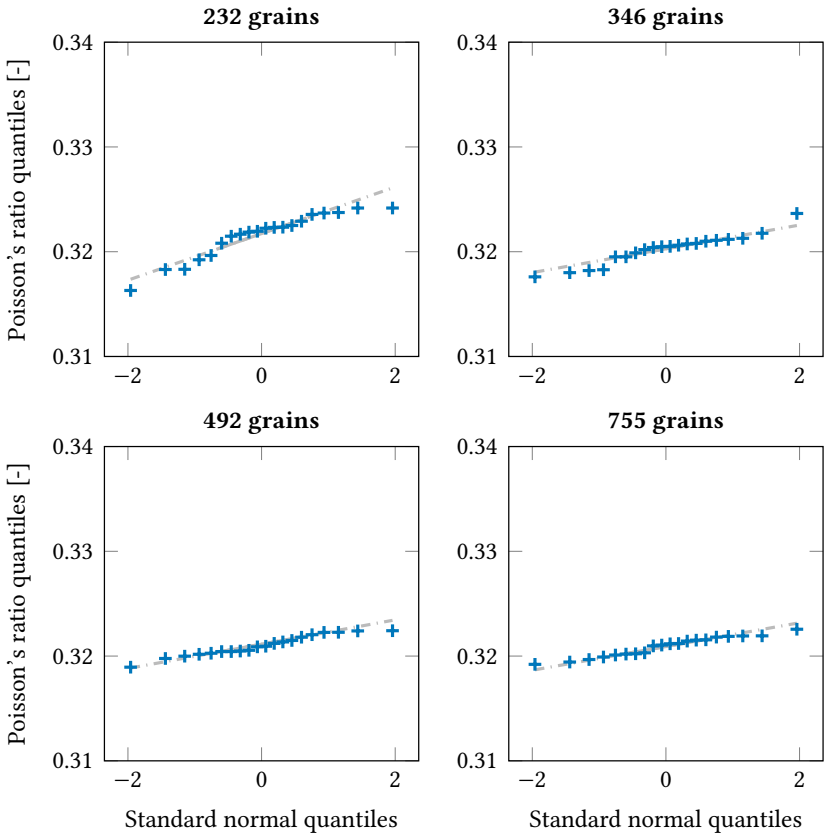

Fig. A.6: QQ plots of Poisson's ratio for different model sizes for the 3D RVE investigation.

A.7 SHAP plots for saltwater ice behavior

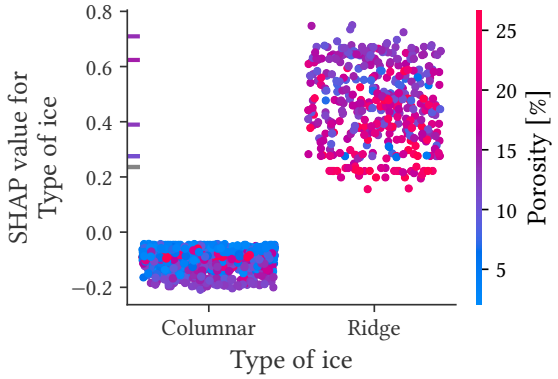

Fig. A.7: SHAP dependence plot for type of ice and porosity.

A.8 Small-scale uniaxial compression results

In Table A.5, grain size was 14 mm. Strength and strain are given at failure, strength is force divided by cross-section area. Last row is mean ± standard deviation. Reference strength for grain sizes between 1.8 mm and 9.2 mm was (5.2 ± 0.6) MPa (mean ± SD), experimental strain about 10^{-3} [251].

Table A.5: Uniaxial compression results anisotropic

Strength [MPa]	Strain [-]
4.92	$9.41 \cdot 10^{-4}$
4.82	$9.41 \cdot 10^{-4}$
4.84	$9.41 \cdot 10^{-4}$
4.86	$9.76 \cdot 10^{-4}$
5.00	$1.03 \cdot 10^{-3}$
4.90	$9.99 \cdot 10^{-4}$
5.06	$1.03 \cdot 10^{-3}$
4.85	$9.64 \cdot 10^{-4}$
5.15	$1.05 \cdot 10^{-3}$
4.84	$9.76 \cdot 10^{-4}$
4.90	$9.99 \cdot 10^{-4}$
4.92 ± 0.11	$(9.87 \pm 0.40) \cdot 10^{-4}$

A.9 Cohesive zone model results for rectangular softening

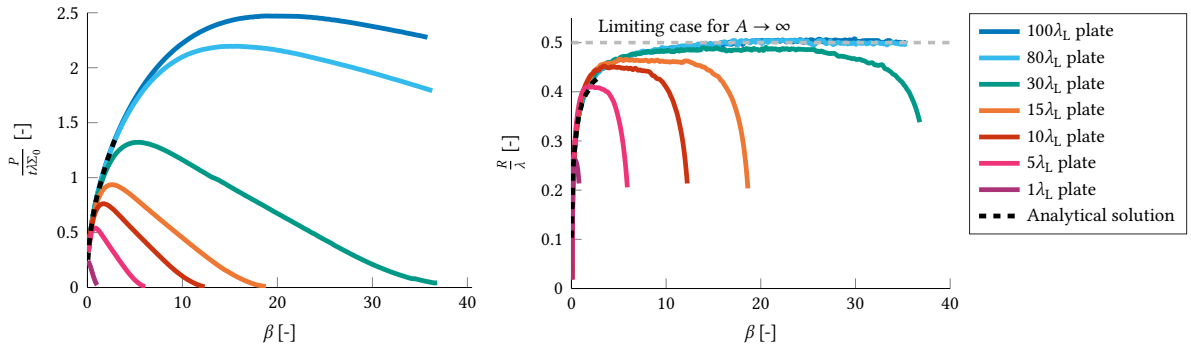

(a) Force

(b) Cohesive zone size

Fig. A.8: Adapted from [145].

A.10 Neper commands

The following exemplary neper commands were used for creating the grain or tessellation geometries, respectively.

RVE 2D

neper -T -reg 1 -id 1 -statcell diameq,sphericity,area -n from_morpho -morpho
”diameq:lognormal(mean=1.29e-3,sigma=4e-4),1-circularity:lognormal(0.1,0.03)”
-dim 2 -domain ’square(0.02,0.02)’ -transform ”rotate(0,1,0,90)” -o square_1

RVE 3D

neper -T -id 1 -statcell diameq,sphericity,vol -n from_morpho -morpho
”diameq:lognormal(mean=1.29e-3,sigma=4e-4),1-circularity:lognormal(0.1,0.03)”
-dim 3 -domain ’cube(0.01,0.01,0.01)’ -o cube_01

Uniaxial compression

neper -T -id 1 -statcell diameq,sphericity,vol -n from_morpho -morpho
”diameq:lognormal(mean=5e-3,sigma=3e-4),1-circularity:lognormal(0.1,0.03)”
-dim 3 -domain ’cylinder(0.23,0.096,24)’ -o cylinder_1

Tensile splitting test

neper -T -reg 1 -id 1 -statcell diameq,sphericity,area -n from_morpho -morpho
”diameq:lognormal(mean=2.59e-3,sigma=1e-4),1-circularity:lognormal(0.1,0.03)”
-dim 2 -domain ’circle(0.1, 36)’ -transform ”rotate(0,1,0,90),translate(-0.05,-0.05,0)”
-o tensile_split_id1 -format tess